

Stony Brook University



OFFICIAL COPY

The official electronic file of this thesis or dissertation is maintained by the University Libraries on behalf of The Graduate School at Stony Brook University.

© All Rights Reserved by Author.

DNA-programmable Nano-systems: Design, Reconfiguration and Optical Properties

A Dissertation Presented

by

Ye Tian

to

The Graduate School

in Partial Fulfillment of the

Requirements

for the Degree of

Doctor of Philosophy

in

Chemistry

Stony Brook University

May 2015

Stony Brook University

The Graduate School

Ye Tian

We, the dissertation committee for the above candidate for the

Doctor of Philosophy degree, hereby recommend

acceptance of this dissertation.

Oleg Gang

Dissertation Advisor

Group Leader, Center for Functional nanomaterials, Brookhaven National Lab

Robert B. Grubbs

Professor

Chemistry Department, Stony Brook University

Nancy S. Goroff

Professor

Chemistry Department, Stony Brook University

Yizhi Meng

Professor

Department of Materials Science and Engineering, Stony Brook University

This dissertation is accepted by the Graduate School

Charles Taber

Dean of the Graduate School

Abstract of the Dissertation

DNA-programmable Nano-systems: Design, Reconfiguration and Optical Properties

by

Ye Tian

Doctor of Philosophy

in

Chemistry

Stony Brook University

2015

One of the main goals of nanotechnology is developing methods for creation of designed nano-scaled systems with ability to control their structures, transformations and dynamic processes. Such full control over the material design will permit achieving the desired functional properties. Approaches based on DNA-driven assembly of nanosystems were recently demonstrated as a powerful route for regulated self-assembly at nanoscale. Metal nanoparticles or quantum dots, functionalized with oligonucleotides are envisioned in this approach to be precisely directed in targeted structures, in bulk, at surfaces or within a cluster. The Watson-Crick recognition between DNA grafted on particle surface allows for programming interparticle interactions with extreme richness and thermodynamical tunability.

Firstly, we extended DNA-assembly methodology for fabrication of dynamically responsive clusters, which were switched between dimer (two-particle) and trimer (three-particle) structures. We developed a simple yet effective approach for the switching the morphology of nanoparticle clusters using a linking particles ‘i-motif’, a DNA sequence that responds to pH stimulation. Our

experiments demonstrate that such cluster switching can be reversibly cycled multiple times. Moreover, by employing both gold nanoparticles (NP) and fluorescent quantum dots, we showed that structural cluster switching induced corresponding changes in the system optical response due to the fluorescence quenching by plasmonic particle. Then, we successfully fabricated three-dimensional superlattices using the ‘i-motif’ sequence as a linker. Our in-situ synchrotron-based small angle x-ray scattering (SAXS) measurements revealed repeatable lattice transformations for the formed body centered cubic (bcc) superlattices. We also uncovered changes in the interparticle distances during pH cycling of simple more complex DNA motifs.

Secondly, we used the DNA-driven assembly strategy to self-assemble a series of clusters with core-shell architecture. The core, gold nanoparticle (AuNP) was surrounded by the shell of DNA-attached colloidal quantum dots (QD), forming AuNP-DNA-QD clusters with tunable optical (photoluminescence) responses, which mimics the architecture of light harvesting complex. By varying the inter-component distance through the DNA linker length we demonstrated precise biasing of the plasmon-exciton interactions, and as such of the optical response of the nanoclusters from photoluminescence quenching to about five-fold enhancement.

Thirdly, considering that DNA sequence has chiral structure, its functionalization onto the surface of plasmonic nanoparticles was predicted theoretically to induce the circular Dichroism (CD) signal in plasmonic area. This effect was observed previously but no significant amplification was detected. However, we demonstrated that for silver nanocube about two orders of magnitudes enhancement of CD signal can be induced. We also confirmed that orientation of DNA played an important role in determining the magnitude of the response.

Furthermore, we reported a novel strategy for assembling 3D nanoparticle clusters: designing a molecular frame with encoded vertices for particles placement. Using a DNA origami octahedron as such frame we positioned specific particles types at the octahedron vertices, which permitted a fabrication of clusters with different symmetries and particles composition. We applied the combination of cryo-EM technique and single particle method to uncover the structure of the DNA frame and to reveal that nanoparticles are spatially coordinated in the prescribed manner. Our strategy is advantageous for nanomaterial engineering because it permits massive and precise assembly of mesoscale 3D clusters by-design. Plasmonic chiral signal can be induced by positioning NP in the desired way.

Lastly, we proposed a new strategy for creating prescribed NP superlattices via coupling DNA frames and NPs into DNA-NP frameworks. We designed several typical frames of polyhedra including cube, square dipyramid, prism, tetrahedron and their variations as the building block for construction of 3-D crystals. Gold nanoparticle, with functional sticky ends on the entire surface, can be treated as ‘universal glue’ for the assembly process. We investigated conditions and designed parameters that lead to the formation ordered DNA-NP frameworks. Using SAXS characterization we reveal several types of well-ordered structures for the frameworks. By programming the DNA frame, we precisely control the positions and numbers of functional DNA sticky ends that permits regulating the topology of connections and result in the formation of different types of arrays.

Table of Contents

Chapter 1 Introduction	1
1.1 Basics of self-assembly	1
1.2 Driving forces for self-assembly	2
1.2.1 Interaction between particles	2
1.2.2 Geometry-driven self-assembly	5
1.2.3 Patchy particles	7
1.3. DNA direct assembly	9
1.3.1 Introduction of DNA	9
1.3.2 DNA nanotechnology	11
1.3.3 DNA origami	12
1.4 DNA-guided assembly of nanomaterials.	16
1.4.1 Short DNA oligos as a template	16
1.4.2 DNA as a linker for assembly of nanoclusters	17
1.4.3 Short DNA linkers for assembly of 3-D crystal	18
1.4.4 DNA structure assembly with nanoparticles	21
1.5 Outline of the Thesis	24
Chapter 2 Reversible Switching of Structure and Optical Response of DNA-assembled Nanoparticle Clusters by pH Stimulation	26
2.1 Introduction	26

2.2 Experimental design	27
2.3 Results and discussion.....	29
2.4 Conclusion.....	34
2.5 Methods.....	34
Chapter 3 Switching of Nanoparticle Superlattices and Dimer Clusters by pH-Regulated ‘i-motif’ DNA.....	36
3.1 Introduction	36
3.2 Experimental design.....	37
3.3 Results and discussions	39
3.4 Conclusion.....	46
3.5 Methods.....	47
Chapter 4 Light Harvesting Nanoparticle Core-Shell Clusters with Controllable Optical Output	49
4.1 Introduction	49
4.2 Nanocluster design and fabrication via self-assembly	52
4.3 Estimation of interparticle distances	54
4.4 Distance-dependent optical response of core-shell nanoclusters	56
4.5 Conclusion.....	64
4.6 Experimental Methods	65
Chapter 5 Discrete Nanocubes as Plasmonic Reporters of Molecular Chirality	68
5.1 Introduction	69

5.2 Experimental design	71
5.3 Results and discussions	75
5.4 Conclusion.....	86
5.5 Methods.....	88
Chapter 6 Prescribed Nanoparticle Cluster Architectures and Low-Dimensional Arrays	93
6.1 Introduction	94
6.2 Experimental design.....	96
6.3 Results and discussion.....	99
6.4 Conclusion.....	122
6.5 Methods.....	124
Chapter 7 Rational Assembly of 3D Superlattices of Nanoparticle via Symmetric DNA Origami Structures	141
7.1 Introduction	141
7.2 The concept of nanoparticle-DNA framework.....	142
7.3 Results and discussion.....	144
7.3.1 Octahedron.....	145
7.3.2 Elongated Square Bipyramid.....	148
7.3.3 Cube.....	149
7.3.4 Tetrahedron.....	151
7.3.5 Triangular Bipyramid	152

7.4 Conclusion.....	153
7.5 Methods.....	155
Chapter 8 Conclusions and Future Work.....	158
References.....	161

List of Figures

- Figure 1.1** Calculate Phase Diagram for binary system for the exponential form of repulsive potential $U(r)$. Reprinted with permission from Reference 13. Copyright 2002, American Physical Society. 5
- Figure 1.2** Calculated map of close-packed structures obtained from corresponding polyhedra. Reprinted with permission from reference 15. Copyright 2012, Science, the American Association for the Advancement of Science. 7
- Figure 1.3** Colloidal kagome lattice after equilibration. Reprinted with permission from Reference 16. Copyright 2011, Nature, Nature Publishing Group. 8
- Figure 1.4** DNA patchy particle fabrication. Reprinted with permission from Reference 17. Copyright 2012, Nature, Nature Publishing Group. 9
- Figure 1.5** Self-assembly of DNA polyhedral. Reprinted with permission from Reference 38. Copyright 2008, Nature, Nature Publishing Group. 13
- Figure 1.6** Design steps of 2-D origami structures. Reprinted with permission from Reference 40. Copyright 2006, Nature Publishing Group. 14
- Figure 1.7** Design of 3-D origami structure. Reprinted with permission from Reference 31. Copyright 2009, Nature Publishing Group. 14
- Figure 1.8** Design principles for controlling twist and curvature in DNA bundles. Reprinted with permission from reference 42. Copyright 2009, Science, the American Association for the Advancement of Science. 15
- Figure 1.9** caDNAno interface and design pipeline. Reprinted with permission from reference 43. Copyright 2009, Nucleic Acids Research, Oxford University Press. 16
- Figure 1.10** The assembly and encoding steps to fabricate the dimer cluster and asymmetric Janus clusters. Reprinted with permission from Reference 10. Copyright 2009, Nature Materials, Nature Publishing Group. 19
- Figure 1.11** Assembly processes of DNA-capped nanoparticles into crystalline (a). Detailed picture of five systems used for assembly (b). Reprinted with permission from Reference 44. Copyright 2008, Nature, Nature Publishing Group. 20
- Figure 1.12** Crystallization pathway for system IV and structure of crystalline DNA-nanoparticle system. Reprinted with permission from Reference 44. Copyright 2008, Nature, Nature Publishing Group. 20
- Figure 1.13** Creating trimer nanoclusters using DNA origami triangles as the template. Reprinted with permission from Reference 57. Copyright 2010, Nature Nanotechnology, Nature Publishing Group. 23
- Figure 2.1** Schematic illustration of the cluster change between dimer and trimer. 28
- Figure 2.2.** Population percentage yield and representative SEM image of dimer nanoclusters. 30

- Figure 2.3** Assembly of trimers in different pH. (a) Analysis of assembled nanoclusters using SEM statistical analysis. (red or left: pH=8.0; blue or right: pH=5.0) (b&c) Representative SEM image for the sample in pH=8.0 (b) and pH=5.0 (c). 30
- Figure 2.4** Model and Analysis (b) of cluster size change by cycling for dimer-trimer switch (red line, circle point) and control experiment which cannot form trimers (black line, square point).31
- Figure 2.5** Control experiment for hydrodynamic diameter of dimer and after adding non-complementary NP4. 32
- Figure 2.6** Fluorescence intensity of dimer-QD in different pH values. 33
- Figure 3.1** Cartoon of structure transformation of 'i-motif' sequence alone (a); in 3-D crystalline (b) and in dimer system (c). 38
- Figure 3.2** Structure factor (left) and cartoon (right) for 'i-motif' linked 3D-crystalline structure (a) and dimer system (b) with different pH values. Blue lines are fitted data by a dumbbell model. 40
- Figure 3.3** Structure factor (left) and cartoon (right) for L30 DNA (all poly dT) linked 3D-crystalline structure with different pH values. 41
- Figure 3.4** Representative SEM images for dimer clusters. 43
- Figure 3.5** DLS data of hydrodynamic size of monomers (black) and assembled dimers (red). 43
- Figure 3.6** Structure factor (left) and cartoon (right) for L30 DNA (all poly dT) linked dimer system with different pH values. 44
- Figure 3.7** Cartoon (right) of two 'i-motif' separated by 15bp double strand, and its structure upon different pH values; structure factor (left) for 3-D nanocrystalline and dimer clusters linked by two 'i-motif' DNA. 45
- Figure 3.8.** Interparticle distance in pH cycles for 3-D nanocrystalline and dimer clusters. 46
- Figure 4.1** **Figure 4.1** a) A core-shell AuNP-Qdot nanocluster with satellite-like architecture in which a core AuNP and several CdSe/ZnS Qdots are linked by DNA (purple). b) Predicted photoluminescence enhancement for a coupled AuNP-point dipole system as a function of AuNP-dipole separation distance, and of optical pumping (excitation) wavelength calculated for a 50 nm size AuNP and a point dipole emitting at 605 nm in air. Calculations adapted from^{1,2}. Also shown (left) is the predicted PL enhancement for optical pumping at surface plasmon resonance (@530 nm). 51
- Figure 4.2** Left. AuNP-Qdot surface-to-surface intercomponent distances for a series of AuNP-DNA-Qdot core-shell nanoclusters named herein NC1 through NC7, as estimated based on DNA model (square and line) and SAXS measurements (dots and dash). Right: DNA linker designs for nanoclusters NC1, NC2, NC3 (a), NC4 (b), NC5 (c) and NC6, NC7 (d). 55
- Figure 4.3** a) Optical scattering spectrum for 50 nm AuNP nanoparticles (black) and Uv-vis absorption (red) and photoluminescence (blue) spectra for CdSe/ZnS Qdots in aqueous solution.

b) Optical scattering spectrum of core/shell AuNP/Qdot nanoclusters with varying DNA linker length. Inset shows the SPR peak vs DNA linker length monotonic dependency. 56

Figure 4.4 a) PL intensity vs AuNP-Qdot separation distance (dots and line). Data are normalized to the value corresponding to the longest linker where quenching is absent. b) Energy transfer rate (k_{ET}) vs AuNP-Qdot separation distance (dots and dash). (c) Energy transfer efficiency (E) vs AuNP-Qdot separation distance (dots) and fits according to various energy transfer models and eq.3: NSET model with $n=4$ (dash line) and $n=3.5$ (line) and FRET model with $n=6$ (dotted line) yielding critical distances $R_0=12.7$ nm, 12.4 nm and 13.4 nm, respectively. 58

Figure 4.5 a) PL enhancement (EF_{PL}) vs separation distance (triangle and line) following optical pumping at 440 nm (square and line), 490 nm (triangle and line) and 530 nm (dots and line). b) and c) are normalized PL lifetime vs separation distance for AuNP/Qdot nanoclusters optically pumped at 440 nm and 530 nm, respectively. 62

Figure 4.6 Fluorescence measurements of the nanoparticle solution before assembly and the supernatant after assembly and centrifugation. 66

Figure 5.1 Individual plasmonic chiral nanoparticle based on silver nanocube. **a.** Structure design of “individual plasmonic chiral nanoparticle” that is based on a gold/silver (Au/Ag) core-shell nanocube (namely, Ag NC) modified with chiral molecules (e.g. DNA) on its surfaces, theoretically expected to exhibit a plasmon-induced circular dichroism (CD) response. Structural characterizations of single-strand (ss) DNA-functionalized Ag NCs (**b-e**). **b.** Low-magnification scanning electron microscopy (SEM) and **c.** transmission electron microscopy (TEM) images show size and shape uniformity of nanocubes with edge length of 42 ± 2 nm. **d** and **e.** Scanning transmission electron microscopy (STEM) and the corresponding energy diffraction X-ray scanning (EDX) map images demonstrate the nanocube is made of an octahedral Au core embedded with thick cubic shell of Ag. 72

Figure 5.2 Representative electron microscope (EM) images of deposited nanocubes showing their two-dimensional projections. **a.** SEM. **b.** TEM. A gold-core octahedron is visible in the TEM image. 74

Figure 5.3 Dynamic light scattering (DLS) of ssDNA-functionalized Ag NCs. 74

Figure 5.4 Optical response of chiral ssDNA, non-chiral Ag NCs, and plasmonic chiral DNA-functionalized Ag NCs. **a.** UV-vis absorption spectra taken from two individual components of ssDNA-functionalized Ag NCs, ssDNA (illustration in a black frame) and virgin Ag NC (illustration in a red frame) respectively. The ssDNA strands (black curve) show one characteristic UV peak at 264 nm and the virgin silver nanocubes (red curve) show three characteristic peaks at 452 nm (P1), 378 nm (P2), and 349 nm (P3), respectively. **b.** The CD spectra were recorded from the virgin Ag NCs of 0.18 nM (**b₁**), ssDNA of 0.1 μ M (**b₂**) and 20 μ M (**b₃**). No CD signal in **b₁** is observed from the virgin non-chiral Ag NCs without DNA modification (framed illustration beside **b₁**). Due to the detector resolution limitation of instrument, natural chirality from little amount of DNA at 0.1 μ M concentration (framed illustration beside **b₂**) cannot be presented in the CD spectrum of **b₂**. Observable CD signal from chiral ssDNA requires much more strands (framed illustration beside **b₃**). A thick specimen of

ssDNA (20 μM) exhibits the characteristic bisignated CD peaks with maxima at 249 and 275nm, respectively, in the spectrum of **b**₃. **c**. UV-vis absorption and CD spectra of ssDNA-functionalized Ag NCs. The Ag NCs functionalized with ssDNA (red curve) show similar absorption features as the virgin ones do (red curve in **b**₁). However, the CD spectrum recorded from 0.18nM NCs in 10mM phosphate buffer (PB) (blue curve) exhibits novel features different from the spectral plateau of virgin Ag NCs: two positive cotton effects are observed at 345nm and 378nm, respectively, together with a negative cotton effect at 355nm; the positive peak at 378nm and another negative-cotton-effect-induced split peak centered at 350nm are well corresponding to two plasmonic resonance peaks of Ag NCs (P2 and P3). An enhancement factor (A_{CD}) of 85~103 is achieved from the ssDNA of 0.088~0.106 μM that are grafted onto the Ag NCs of 0.18nM due to the plasmon-induced CD resonance mechanism. 76

Figure 5.5 a-f. CD spectra, the representative TEM images and corresponding shape illustrations of 30ssDNA-functionalized nanoparticles: **a**. Au nano-spheres of 10nm in diameter (2nM); **b**. Au nano-spheres of 45nm in diameter (0.2nM); **c**. Au nano-cubes with edge length 45nm (0.2nM); **d**. Au nano-octahedra of 45nm in edge length (0.2nM); **e**. Ag nano-spheres of 20nm in diameter (1nM); **f**. Ag nano-spheres of 40nm in diameter (0.2nM). **g**. CD spectra, the representative TEM image and shape illustration of 50ssDNA-functionalized Ag NC with edge length 42nm (0.18nM). The corresponding CD signal is weaker than observed from 30ssDNA-functionalized Ag nanocubes, which is attributed to the lower coverage of NC with longer-chain DNAs. **h**. The normalized UV-vis absorption spectra of nanoparticles shown in **a-g**. Scale bars in the insets of **a, b, e, and f**: 20nm. Scale bars in the insets of **c, d, and g**: 50nm. 79

Figure 5.6 a. (Upper) Normalized UV-Vis absorption spectra of 30ss-DNA (blue curve) and the 20nm Ag nanospheres functionalized with 30ss-DNA (red curve). The 30ss-DNA shows the characteristic UV peak at 264nm and the 20nm Ag nanospheres functionalized with 30ss-DNA show a surface plasmon resonance (SPR) peak at 404nm in the visible range, respectively. (Lower) CD spectrum of 20nm Ag nanospheres functionalized with 0.78 μM of 30ss-DNA (3.4nM of spheres) displays one negative peak at 277nm in the UV range and the other at 398nm in the visible range. An enhancement factor (A_{CD}) of 1.6 is estimated. **b.** (Upper) Normalized UV-Vis absorption spectra of 30ss-DNA (blue curve) and the 40nm Ag nanospheres functionalized with 0.196 μM of 30ss-DNA (0.4nM of spheres) (red curve). The 30ss-DNA functionalized 40nm Ag nanospheres show a SPR peak at 415nm in the UV-Vis spectrum (red curve, upper), but no signal in the CD spectrum (black curve, lower) is observed. 80

Figure 5.7 Spectral dependence of circular dichroism on salt concentration. **a**. Scheme illustrating an evolution of ssDNA alignment status on a cube surface after adding salt. **b**. salt-dependent CD spectra evolution of ssDNA-functionalized Ag NCs with the ionic strength increasing from 0 (deionized water, DIW) to 0.06 (10mM PB), 0.07, 0.08, 0.11, and 0.16M (0.1M phosphate buffer saline, PBS) in the order indicated by black arrow. **c**. Comparison of the CD spectral dependence on Na^+ concentration between ssDNA-functionalized Ag NCs (orange-squares-dash) and pure ssDNA system (blue-square-dash). CD signal intensity monitored at 378nm is normalized by the associated DNA concentration, 0.106 μM for orange-squares-dash plots and 20 μM for blue-squares-dash plots, respectively. With the ionic strength increase, plasmon-induced CD signal of nanocubes fades down gradually whereas no obvious decline in CD signal is observed from pure ssDNA system, which reveals different CD resonance origin from two systems. 82

Figure 5.8 Reboots of plasmon-induced CD resonance in a salted solution. **a.** Scheme illustrating the change of DNA profiles on a cube surface in 0.1M PBS: from flexible ssDNA (black-dotted frame) to relatively rigid double helixes (red-dotted frame) by hybridized with complementary strands. **b.** CD spectral comparison in 0.1M PBS system between before (black curve) and after (red curve) making ssDNA on nanocubes become more rigid double helixes (blue curve of inset is the CD spectrum from pure dsDNA of 20 μ M). 84

Figure 5.9 The calculated 3D profiles for the electric field enhancement $P = |\vec{E}|^2 / |\vec{E}_0|^2$ at Ag nanocube surface for three resonance modes, corresponding to peaks P1 (**a**), P2 (**b**) and P3 (**c**), as shown in UV-Vis absorption spectra in Fig. 2. 86

Figure 6.1 Scheme of three designer clusters assembled from functionalized gold nanoparticles (NPs) on a designer octahedral DNA origami frame. (A) The designer octahedral origami structure. Red numbers mark the six corners or apexes of the octahedron. One apex is zoomed in the lower panel to show the end-on view of the designed structure comprised of four six-helix bundles (6HB). Each 6HB contains one encodable ssDNA sticky end (dotted blue line). (B) An octahedron with all sticky ends being encoded to coordinate 7-nm NPs into the symmetric 6-NP cluster P₆. (C) The P₄(1234) cluster structure may form if the ssDNA at apexes 1-2-3-4 of the octahedral frame is programmed with sequence complementary to the ssDNA on the 10-nm gold NPs. (D) The P₁₂(12)P₂₂(34)P₃₂(56) cluster structure may assemble if the ssDNA at apexes 1-2, 3-4, and 5-6 are programmed to complement the ssDNA on the 7-nm, 15-nm, and the 10-nm NPs, respectively. 98

Figure 6.2 The agarose gel electrophoresis separation of DNA octahedra and DNA octahedra-NP assemblies. (Top) The UV image of the 1% agarose gel. Symbols ‘L’ is for a 1kb ladder, ‘M13’ is for M13 DNA as described in the text, ‘Oct’ is for the folded origami, ‘Free NP’ is for the mixture of 7 nm, 10 nm, 15 nm NPs, and ‘S1’, ‘S2’ and ‘S3’ correspond to the clusters P₆, P₄ and P₁₂P₂₂P₃₂ respectively. (Bottom) The white-light image of the same gel. 100

Figure 6.3 Cryo-EM and 3D reconstruction of the self-assembled DNA origami octahedron. (A) A cryo-EM micrograph with representative views of DNA octahedron boxed by a black square. Only cluster structures that were embedded in the vitreous ice and suspended over the irregular holes in the carbon film substrate were selected for further analysis. (B) Comparison of 2D reprojections of the reconstructed 3D density map (top row), with reference-based class averages (second row), reference-free class averages (third row), and with the corresponding views of the 3D design model (bottom row). (C) Surface-rendered 3D density map of the DNA octahedron, as viewed from the 4-fold (left), 3-fold (middle), and 2-fold (right) symmetry axis. The density surface is colored radially from interior red to outer blue. The color key is shown on the right. The value in the color key indicates the distance in angstrom from the octahedral center. 102

Figure 6.4 The size distribution of the assembled and purified octahedral DNA origami as obtained using dynamic light scattering measurement. 103

Figure 6.5 3D cryo-EM structure of the DNA origami octahedron. The 6 helix bundle (6HB) atomic model (504 bp, 84bp x 6) is fitted into one strut of the 12-strut EM density as a single rigid body. Left panel shows the surface-rendered DNA octahedron 3D density. The strut docked with atomic model is enlarged and shown in an end view (upper right) and a side view (lower right), respectively. 104

Figure 6.6 The estimated resolution for the cryo-EM map of the DNA origami octahedron. Gold standard Fourier shell correlation of two 3D maps calculated from the two halves of the final data set suggests a resolution of ~ 23.5 Å at the correlation threshold of 0.143. 105

Figure 6.7 The P_6 cluster structure as revealed by cryo-EM and 3D reconstruction. (A) A representative EM image of the P_6 cluster structure. Inset shows the histogram of assembled clusters with observed NP numbers. (B) Ten selected cryo-EM images of the fully assembled P_6 octahedron-NP clusters (second and fourth rows), in comparison with the 3D design model in corresponding views (first and third rows). (C) 3D reconstruction of the DNA portion of the P_6 cluster by excluding the high intensity NPs in cryo-EM images. The density surface is colored in the same way as Figure 6.3C. (D) 3D reconstruction of the six NPs of the P_6 cluster by using only the high intensity NP scattering signals in the cryo-EM dataset. (E) The composite 3D EM structure of the P_6 cluster derived by computationally combining the structures shown in (C) and (D). The left, middle, and right panel in (C-E) shows 4-fold, 3-fold, and 2-fold views of the respective structure. 106

Figure 6.8 Surface-rendered 3D cryo-EM density map of Au nanoparticles (NPs) organized by DNA octahedron as viewed from 4-fold (left), 3-fold (middle), and 2-fold (right) symmetry axis, respectively. This density map was derived from the same raw dataset that was used to generate 3D maps shown in Figure 6.7, but without selective image intensity modification. The rendering level was chosen to show the DNA densities (blue). At this low display threshold, the NP densities (golden) are exaggerated in size due to their extremely strong electron scattering power. The shape of the NPs is an artifact due to the combined effect of density mismatch between the DNA and the NP, and the octahedral symmetry applied during 3D reconstruction. 108

Figure 6.9 Structure of the $P_4(1234)$ cluster. (A) The cluster population histogram. (B) Six selected raw cryo-EM images of the assembled DNA-NP cluster (bottom row) in comparison with the design model in corresponding views (top row). (C) A composite density map derived by combining 3D reconstruction of the DNA octahedron (Figure 6.3C) with 3D reconstruction of the four 10-nm NPs organized by octahedral DNA frame. The rendering threshold of the later is set to show the NP densities. Left, middle, and right panel show view along the four-fold, three-fold, and two-fold symmetry axis of octahedron. 110

Figure 6.10 3D density map of the Four 10-nm NPs organized by the DNA octahedron. The surface-rendering threshold was set to show the high density gold NPs. DNA molecule has much lower electron density and is invisible at this display level. 111

Figure 6.11 A representative electron micrograph of the cluster $P_4(1234)$ showing many well disperse clusters each having 4 NPs. Isolated NPs are occasionally visible, for example, near the center of the picture. The white ribbons are aggregated DNA material. 111

Figure 6.12 Electron tomography of individual hetero-cluster, $P^1_2(12)P^2_2(34)P^3_2(56)$, assembled with three types of NPs. (A) Statistical analysis of the NP cluster population. The design model and a representative cryo-EM image of the assembled cluster (untilted view) are shown as insets. (B) Reconstructed 3D structure of the NP cluster shown on the inset of (A). The distance between the diagonally paired 7-nm, 10-nm, and 15-nm NPs are denoted by d_7 , d_{10} , and d_{15} , respectively. α is the angle centered around the 15-nm NPs, and β around the 10-nm NPs, respectively. (C) Images obtained by tilting the cluster shown in (A) at different angles (from left

to right: -20° , -10° , 20° , 40° , 60°) (top row), in comparison with corresponding views of the reconstructed 3D structure. (D) Averaged distances between the diagonally paired 7-, 10-, and 15-nm NPs measured from 12 independently reconstructed $P^1_2P^2_2P^3_2$ clusters. $d_{15} = 58.0 \pm 4.8$ nm, $d_{10} = 55.1 \pm 5.6$ nm, and $d_7 = 53.3 \pm 5.3$ nm. (E) Averaged values of the basal ($\alpha = 89.4^\circ \pm 10.9^\circ$) and apex ($\beta = 54.5^\circ \pm 10.0^\circ$) angles. 113

Figure 6.13 A representative electron micrograph of the cluster $P^1_2(12)P^2_2(34)P^3_2(56)$. This picture contains six fully assembled clusters. Each intact cluster has two small (7 nm), two middle (10 nm), and two large (15 nm) NPs. Isolated individual NPs and partially assembled clusters are also visible. 115

Figure 6.14 Twelve selected raw EM images of the $P^1_2(12)P^2_2(34)P^3_2(56)$ clusters in comparison with the design model in the corresponding views. The coordinating DNA octahedra (gray bars in the 3D model) are virtually invisible in the EM images. The shape of the 15-nm NPs can significantly deviates from the ideal sphere to the elongated or even triangular shapes. 116

Figure 6.15 Variation of the basal and apex bond angles, α (red) and β (blue) respectively (defined in the Figure 6.12), in the assembled cluster $P^1_2P^2_2P^3_2$, as measured from the 3D cryo-EM tomograms. 117

Figure 6.16 CD spectra of octahedron based non-chiral cluster $P^2_2(34)P^3_2(56)P^4_2(12)$ (denoted as $P^2_2P^3_2P^4_2$) and chiral cluster $P^2_2(26)P^3_2(35)P^4_2(14)$ (denoted as $P^2_{c2}P^3_{c2}P^4_{c2}$). (A). Model of non-chiral cluster $P^2_2P^3_2P^4_2$ with its top view. (B). Model of chiral cluster $P^2_{c2}P^3_{c2}P^4_{c2}$ with its top view. (C). Red line is the CD spectrum for cluster $P^2_2P^3_2P^4_2$. The representative TEM image and the model with same orientation are shown at the right top corner. Black line is the CD spectrum for cluster $P^2_{c2}P^3_{c2}P^4_{c2}$ and the blue line is the Lorentzian fit. The representative TEM image and model with same orientation are shown at the low left corner. The CD peaks for both clusters at about 270 nm are from DNA. 119

Figure 6.17 UV-vis spectra of the cluster ‘ $P_1P_2P_3$ ’ (red line) and ‘ $P^c_1P^c_2P^c_3$ ’ (black line). Lorentz fitting was applied to obtain the peak positions of the two curves. 120

Figure 6.18 Encoded octahedra link NPs with 2-fold or 4-fold symmetries for corresponding assembly of low-dimensional, linear 1D and square 2D, NP arrays. (A). Model of octahedral DNA origami with 2-fold symmetry NP binding for assembly of 1D array. (B). The model of 1D array (upper) and the representative negative stained TEM image of formed 1D array (below). (C). Extracted structure factor $S(q)$ for 1D array from in-situ SAXS pattern (red points is a measurement, and the blue line is fitting as described in the text). (D). The model of octahedral DNA origami with 4-fold symmetry NP binding for assembly of 2D square array. (E). The model of 2D square array and the representative negative stained TEM image of formed 2D NP-octahedra array (inset is a zoomed picture of selected area; bar scale is 20nm). (F). Extracted structure factor $S(q)$ for 2D NP array (red line) and the simulated 2D scattering pattern (black lines with diffraction peak indexes). 123

Figure 6.19 Dynamic process by detecting the size of participates after mixing NPs and octahedron for the formation of 2D array crystals by DLS. Sample was annealed from 50 °C to

room temperature with the rate of 4 °C /h. Melting temperature was around 39 °C for the 2D array system. 124

Figure 7.1 10nm gold nanoparticle (NP) assembly with DNA origami polyhedral frames including octahedral, cubic, prism, hexagonal etc. in the position of every corner for each origami shape to form 3D framework. Specially, the octahedral frame was encoded into another two frames with 2-fold and 4-fold symmetry for further assembly. 144

Figure 7.2 Octahedral DNA origami assembled with 10nm NPs to form a crystal and its scattering pattern. (A). Model of DNA origami. Each edge was composed of a six-helix-bundle with the same length. (B). Representative negative stained TEM image of octahedral origami. (C). Model of the assembled superlattice by octahedral origami and NPs. (D). Extracted structure factors $S(q)$ v.s. q for different octahedral/NP superlattice systems (left). Distance from NP to octahedron (d) decreases from top (pink) to bottom (blue). Black line is the fitted lines for f.c.c structure. Right parts show corresponding SAXS images for each system. 146

Figure 7.3 Elongated square bipyramid DNA origami (ESB) assembled with 10nm NPs to form crystal and its scattering pattern. (A). Model of ESB with different length as marked. (B). Representative negative stained TEM image of ESB. (C). SAXS image of the scattering. (D). Extracted structure factors $S(q)$ v.s. q for ESB/NP superlattice system. Inserted is the model of the assembled superlattice by ESB and NP. 149

Figure 7.4: Cubic DNA origami assembled with 10nm NPs to form crystal and its scattering pattern. (A). Extracted structure factors $S(q)$ v.s. q for cubic/NP superlattice system. Inserted is the model of the cube (left) and SAXS image for the system (right). (B). Representative negative stained TEM image of octahedral origami. Inserted is the model of tilted cubic model. (C). Model of the assembled superlattice by cubic frames and NPs. 150

Figure 7.5 Tetrahedron DNA origami structure assembled with 10nm NPs. (A). Extracted structure factor $S(q)$ v.s. q for tetrahedron/NP superlattice system (inserted is the model of tetrahedron). (B). Representative TEM image for tetrahedron. (C). Model of formed f.c.c. structure by tetrahedron/NP system. 152

Figure 7.6 Prism DNA origami structure assembled with 10nm NPs. (A). Extracted structure factor $S(q)$ v.s. q for tetrahedron/NP superlattice system (inserted is the 1D ring image of the SAXS result). (B). Representative TEM image for tetrahedron (inserted is the model of the prism). (C). Model of formed hexagonal structure by prism/NP system. 153

Figure 7.7 DLS results for all the origami structures discussed in this chapter. 155

List of Tables

Table 5.1 Comparison on CD enhancement factors, A_{CD} , from different nanoparticles functionalized with 30ssDNA. N/A indicates that no plasmon-induced CD signal was observed at the measured concentrations.	87
Table 5.2 Average Ag nanoparticle sizes, major SPR peak position, extinction coefficient at SPR peak λ_{ext} , and the measured number of 30ssDNA strands on per particle for studied systems.	88
Table 7.1 Summary of all the frames and relevant models discussed in this chapter.	145
Table 7.2 Summary of building blocks and corresponding assembled frameworks.	155
Table 7.3 Summary of melting temperatures for all frames assembly with 10nm NPs by DLS measurement.	156

Acknowledgments

Firstly, I would like to thank my Ph.D advisor, Dr. and Prof. Oleg Gang, for his mentoring and supporting during the years I am living and studying in Stony Brook University. His patience in interpreting, unique ability in analyzing and creative thinking, and most importantly, the skill in mastery of the research trends keep me benefited and highly motivated all the time. He is also care for my life and gives many suggestions and help. Remarkably, he always considers things from students' aspect and keeps his concerns for us to make sure we are living and studying happily and fruitfully.

I am grateful to Professor Robert Grubbs, Professor Nancy Goroff and Professor Yizhi Meng for kindly serving as committee members for my defense and suggestions for improving my thesis and my future career. I would also want to thank Katherine Hughes and Professor Dale Dreuckhammer (also Professor Nancy Goroff in the first several years) in helping with the affairs regarding enrollment, writing letters and instructions for my graduation and so on.

I would like to thank Dr. Dazhi Sun and Dr. Cheng Chi. They helped me get started in the lab and cooperated with me for some projects. I also thank Dr. Dmytro Nykypanchuk for helping me with instruments in BNL and ordering stuff. I would like to thank all the members in our group and other colleagues in CFN for their scientific support.

I am very lucky to be surrounded by a huge group of friends in America, especially the roommates in Selden. They made my life oversea very joyful.

Finally, I would like to dedicate all the work in SBU to my loving family: my parents, my parents-in-law, my wife and especially, my daughter.

Chapter 1

Introduction

1.1 Basics of self-assembly

Self-assembly means the process by which same or different components in a system organize spontaneously, and in the meanwhile, form ordered structures. The forces driving the assembly come from the intra-object interactions, such as attraction, repulsion including non-covalent bond or chemical bond. Environment also plays an important role in determining the process and final structure, for example, pH, temperature, evaporation rate *et al.* Recently, the topic of self-assembly attracts much attention because it could potentially provide a kind of bottom up route for constructing different atoms, molecules and large structures into macroscopic frameworks^{3,4} and even designed structures. Typically, self-assembly is closely related to the principle of thermodynamic equilibrium which is reached by minimizing the system's free energy⁵. A precise control over the related parameters during the self-assembly process is significant, since we need to exploit self-assembly in various applications and more remarkably, make sure that target structures have grown efficiently. More specifically, in nanomaterial area, many unique and interesting properties may emerge after formation of crystalline or low-dimensional cluster organizations⁶. How to take advantage of these properties to benefit our daily life is still an important but urgent issue in nanotechnology. Ordered assemblies are usually built by weak interactions between nanomaterials to form the advanced structures. These interactions are mostly non-covalent interactions such as hydrogen bonds, electrostatic interaction, hydrophobic interaction *et al.* For self-assembly of nanoparticles, the first step would be the decoration of the hard core with polymers, surfactants, or biomolecules, which would serve as the functional part

by providing spacers or strong binding forces with other nano-objects. One of the most commonly used functional parts includes proteins (protein-protein recognition), and DNA (hybridization of A/T and G/C), which provide special and convenient ways to assemble functional nano-objects⁷. By carefully designing these interactions as ‘glues’ in special ratio of these functional objects, self-assembly progress can be programmed and well controlled.

1.2 Driving forces for self-assembly

In order to create ordered assemblies from different nanoscale particles, we should understand how the particles interact with each other and these interactions result in the phase formation. For example, colloidal nanocrystals contain dipole moments, electric charges, polarizabilities, van der Waals and might have ligand-induced interactions. Understanding different modes of interactions between particles would be beneficial for researchers to design and control the assembly process. Thus, we first discuss different types interaction model and their effect on the particle assembly.

1.2.1 Interaction between particles

In a simple system, for example, a fluid of non-polar atoms or molecules, the interaction between them could be presented by Lennard-Jones 12-6 potential^{8,9}:

$$u(r) = 4\epsilon \left[\left(\frac{\sigma}{r} \right)^{12} - \left(\frac{\sigma}{r} \right)^6 \right] \quad \text{for } r > 0$$

The r^{-12} term is repulsive term presented by Pauli repulsion at short range because of electron orbitals of the atoms or molecules overlapped with each other. The r^{-6} term is the attractive term for long range interactions, for example, van der Waals force or dispersion force. This model is

in good approximation to describe gases, but for collision system which was composed of many atoms, it would be not accurate.

In liquid state, pair distribution function (PDF) could be used to describe the distance distribution of particles with a certain volume. It was described as follows:

$$g(r) = e^{-\beta\omega(r)}$$

It means the possibility to find the second particle within the distance r . Likewise, $\omega(r)$ could be presented as the reversible potential when two particles moved from a finite separation to a certain distance r . We should point out here that the function of $\omega(r)$ is much more complicated than the function of pair potential $u(r)$. Only when the limit of particle concentration is close to 0, these two functions would equal to each other.

When the attraction force of the particles could overcome the repulsion forces, the particles could ‘meet’ with each other and assemble into clusters or aggregations. For example, in the dimer system we would describe in detail in chapter 2 when two gold nanoparticles were separated by DNA linker, the reversible binding energy E was created by these two nanoparticles. In the meanwhile, these two nanoparticles would repel to each other.

Despite numerous efforts the relationship between the isotropic interaction potential and the resulting type of structural order in a lattice is not well understood. Systematic methods to find the type of interparticle interactions for a given structure were not developed until 2005, when Salvatore Torquato put forward computational tools based on inverse statistical mechanics^{10,11}. In general, these tools could find optimal interaction potentials between particles in a many-body system when its ground state was an isotropic structure. He employed two kinds of optimization schemes, called ‘zero-temperature’ scheme and ‘near-melting’ scheme, in order to find suitable

interaction potentials. The first one means that since the lattice was linearly stable, the desired target lattice energy should be minimized. Also, in order to take account anharmonic behavior, the Lindemann parameter of the potential is minimized. Essential part of his study was to explore the limitations of isotropic interactions and the difficulty in finding the potential curve for a certain structure was related to its coordination number. Take close-packed lattice (f.c.c. or h.c.p.) for example. They have 12-fold coordination number and the specific volume is $0.7071 n^3$ (n means the nearest neighbor distance). They could be assembled by oft-cited Lennard-Jones potential, with Gaussian-core model at low intensity and also the simple $1/r^{12}$ potential. While for bcc structure, the specific volume was $0.7698n^3$ with Gaussian core model at high densities including also the Coulomb potential.

In a more complicate case, if we consider a binary system of hard sphere with the same diameter d . These two kinds of particles are belonging to different type (A and B)¹². Same particles had a repulsion potential as described above $U(r)$ while different particles had a binding energy $-E$. It may difficult to identify all the possible morphologies for this system. However, we can limit the search by some assumptions. First, nearest neighbors were consisted of opposite types because of repulsion force. Second, all the neighbors had same bond length. Third, we only consider crystalline morphologies when they possessed a high symmetry and all the sites were equivalent. The formed morphologies could be identified by changed coordination numbers (N): for example, BCC ($Z=8$), SC ($Z=6$), honeycomb ($Z=5$), or diamond ($Z=4$). The phase diagram of the function between E and d was obtained as Figure 1.1.

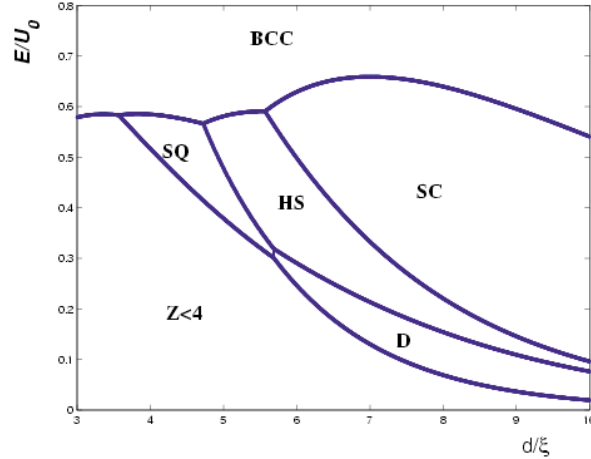


Figure 1.1 Calculate Phase Diagram for binary system for the function of repulsive potential $U(r)$. Reprinted with permission from Reference 12. Copyright 2002, American Physical Society.

More specifically, in our case, when nano-meter sized colloidal particles were coated with DNA shells, there would be four possible interaction energies¹³: van der Waals interaction, electrostatic interaction, steric interaction and depletion interaction. In order to achieve stable nanoparticle suspensions, we should try best to avoid particles approach too closely. Among these four interactions, van der Waals interaction would be the dominant compared to depletion attraction of free polymers. To counteract the attractive energies, electrostatic and steric stabilization should be used by proper selecting of polymer chain length and so on.

1.2.2 Geometry-driven self-assembly

Besides the weak interaction-driven self-assembly, special building blocks with certain shapes also can direct the self-assembly process¹⁴. In this case, packing of colloidal nanoparticles with different shapes could be understood through entropy maximization packing efficiency. Models for dense packing of different polyhedral shapes have been employed to investigate the frameworks of low-temperature systems, for example, crystals, glasses, heterogeneous materials,

and granular media. Packing efficiency is an important parameter in determining the preferential alignment of the flat facets, and in the meanwhile, increasing the entropy of the systems. By increasing the contact area and packing efficiency, we can put the suitable faceted polyhedra to form ordered structure in large scale. The understanding of directional entropic force and the special particle faceting could predict assembled structures of polyhedral framework.

Figure 1.2 shows an example of simulated self-assembled polyhedral structures. Pablo F. Damascene reveals a remarkable propensity for diverse shapes from thermodynamic performance and structural variations¹⁴. Polyhedra are separated into four categories of organization, as shown in Figure 1.2 by different colors: liquid crystals, plastic crystals, crystals, and disordered (glassy) phases. All structures formed by construction from disordered fluid phases with packing fractions range from 0.49 to 0.63 as reported. They revealed a special tendency for geometry-driven assembly. First, if the polyhedral is closer to the sphere, it would have no-directional or weakly-directional entropic interactions, and would prefer to form a FCC or BCC crystal. Second, a polyhedral with more shaped facets usually has strong-directional entropic bonding. Moreover, a polyhedron which could form liquid crystals always has an axial shape as shown in Figure 1.2. The diverse structures of polyhedra can also be constructed by DNA nanotechnology. Later in this thesis, we will discuss methods for designing these DNA polyhedra and how to construct them experimentally.

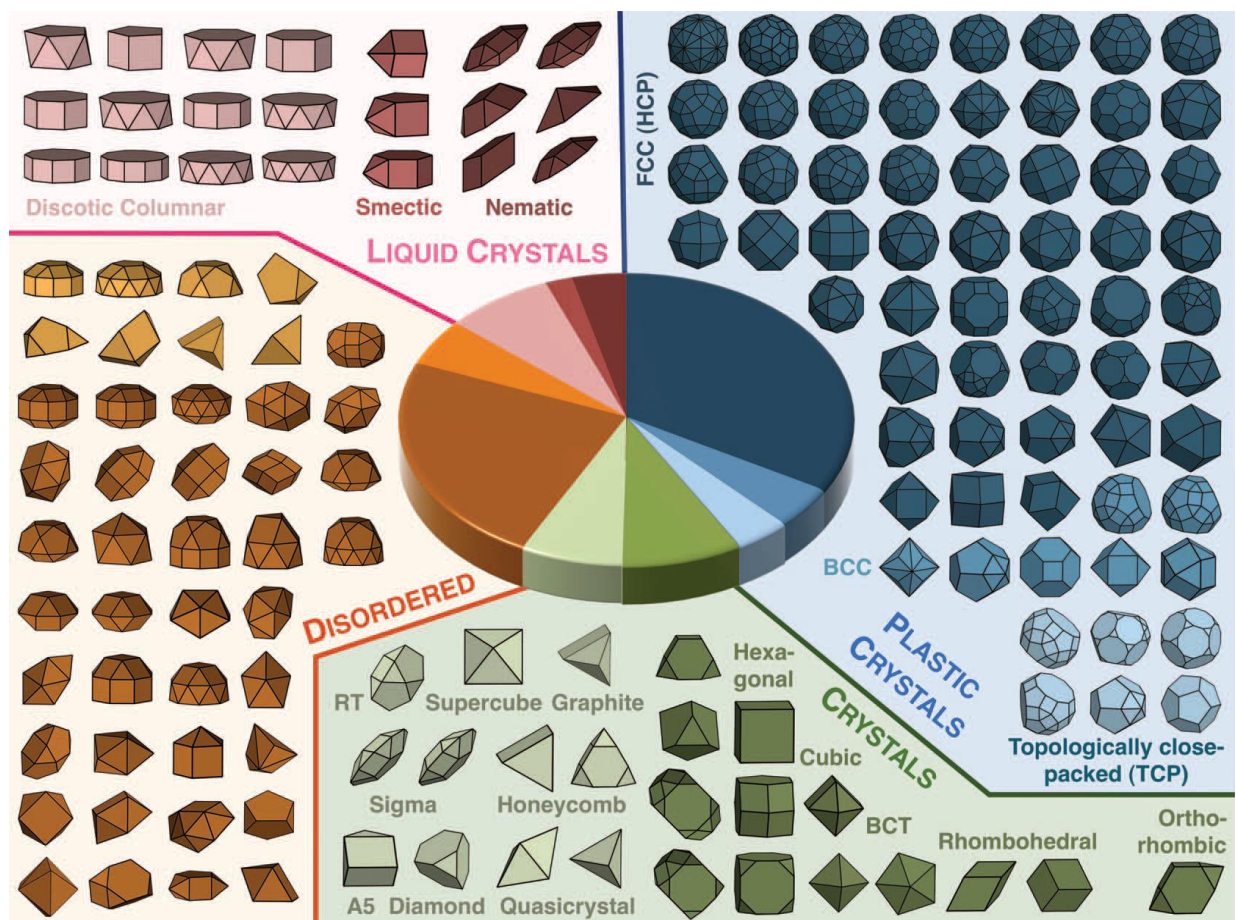


Figure 1.2 Calculated map of close-packed structures obtained from corresponding polyhedra. Reprinted with permission from reference 14. Copyright 2012, Science, the American Association for the Advancement of Science.

1.2.3 Patchy particles

Unlike geometry-driven assembly, atoms and molecules could control the assembly orientations through valence. For example, methane, each covalence orbital adopt sp^3 hybridization, so the four binding mode is in tetrahedral arrangement. In colloids, it would be more difficult to control the binding site and orientations since the colloidal particles should be valent, We called these special particles as ‘patchy particles’^{15,16}.

Glotzer and Solomon introduced an anisotropic nano- and micro- colloids several years ago ¹⁷. The anisotropy nomenclature had eight basic anisotropy dimensions including surface coverage, aspect ratio and so on ¹⁸. Janus particle is named for two-faced patchy particles. In the last two decades, many assembly and fabrication techniques have been developed ¹⁹. They have been used into many new areas such as electronic paper ²⁰, sensors ²¹, micro-rheological probes ²² et al.

More recent work was done in 2011, when Steve Granick's group successfully built a new material with three valences, as described in Figure 1.3 ¹⁵. The particle composed of three parts with different hydrophobic properties. White parts could push each other while black parts attract each other. When salt was applied into the water system, these interactions took place and forming a large scaled lattice.

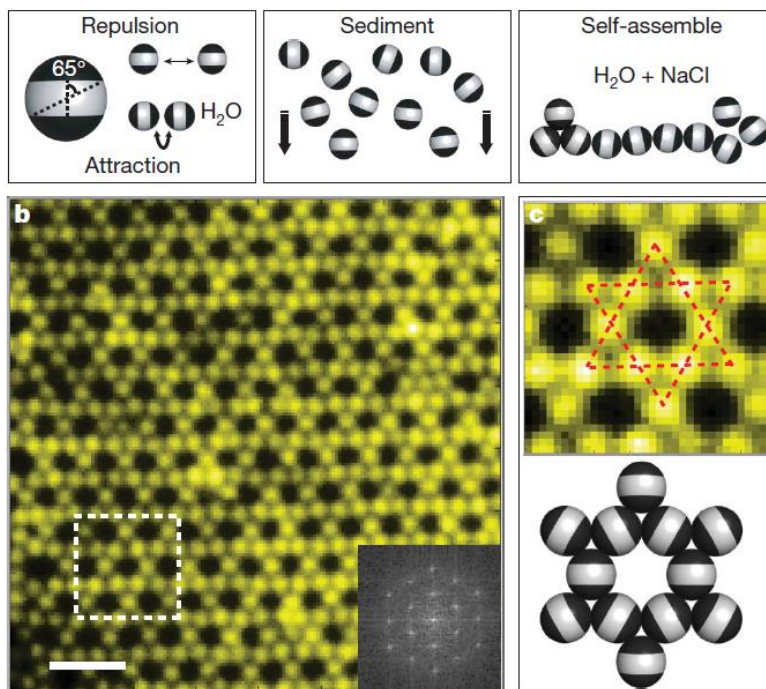


Figure 1.3 Colloidal kagome lattice after equilibration. Reprinted with permission from Reference 15. Copyright 2011, Nature, Nature Publishing Group.

Similar work was also done in David Pine's group in 2012, as shown in Figure 1.4¹⁶. Clusters with different symmetry were prepared first. Then they were swollen by styrene with only symmetric points protruded out. Function groups were selectively grafted onto these points. These functional groups can lead to further assembly with certain directions.

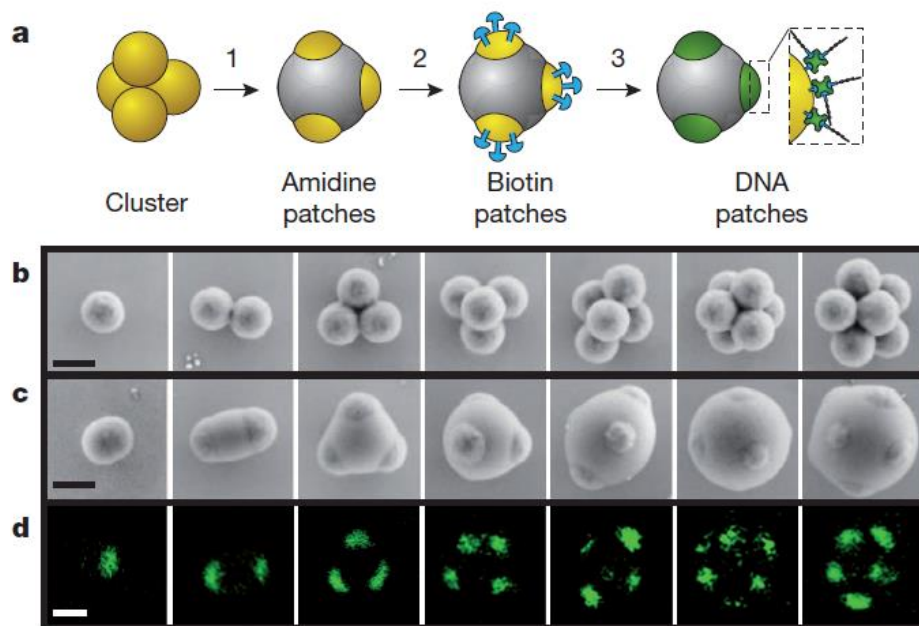


Figure 1.4 DNA patchy particle fabrication. Reprinted with permission from Reference 16. Copyright 2012, Nature, Nature Publishing Group.

1.3. DNA direct assembly

1.3.1 Introduction of DNA

Deoxyribonucleic acid (DNA) is a kind of polymer with a large molecular weight that encodes the genetic information in organisms. It is always found with a double-helix conformation, which is composed of two single strands coiled around each other. Each single strand DNA is called 'polynucleotides,' because it was composed of units of nucleotides. For each nucleotide, it

contains a monosaccharide sugar, a phosphate group, and a nitrogen nucleobase. There are four kinds of nitrogen nucleobases in life: guanine (G), adenine (A), thymine (T) and cytosine (C). Among them, there are two special complementary bindings: A with T and C with G. Hydrogen bonds are the essential driving force for the special interaction between nucleotides. The two single strand polynucleotides run in opposite directions (5' or 3') to form the double strand DNA, known as an 'anti-parallel' orientation. The special sequences along the backbone determine the genetic information for each species. Basically, DNA is a long polymer composed of repeated nucleotides. It was first identified by Friedrich Miescher. James Watson and Francis Crick²³ first discovered the double helix structure. Two single strands in a certain double helix have the same axis and the pitch for each strand is around 3.4nm. The radius of the anti-parallel structure is around 1nm. Though the unit of the DNA polymer is very small, they can form large molecules in life.

According to the description above, DNA could be an ideal matter for assembly by its base-pair interaction. By designing and synthesizing specific DNA chains, a new research area came out: DNA nanotechnology. Seeman, who was considered to be the founder of DNA nanotechnology, proposed the first structural material for bottom up assembly²⁴. Great accuracy and control was organized based on this technique, and was fulfilled on a nanometer scale. Since the 1980s, he and his group members have constructed various kinds of DNA structures as building blocks for further assembly: from Holliday junction²⁵, cubic cage²⁶ to two dimensional lattices²⁷ and three dimensional DNA crystals²⁸.

1.3.2 DNA nanotechnology

In 1973, Cohen and his group members used the base-pair interaction of two double strands to link them together. By ligation, two separate double strand DNA can bind covalently^{29,30}. New and exciting research about DNA structure design came after this report. Branched DNA structures flanked by 3-6 arms are designed with the same logic³¹. Two properties of the branched DNA are important; first, it is hard to control the angle of the branched junctions because of the flexibility of the double stand. More rigid structures need to be designed to obtain the geometrical control. Second, DNA double helix is a helical molecule. By careful design, we can control the orientation of the base in the end. This provides the possibility to construct more complex structures. Based on this property, Seeman and his group members modified Holliday junctions with sticky ends in the tiles. By complementary force between the sticky ends from Holliday junctions nearby, they built two-dimensional structures²⁴.

Three-dimensional DNA discrete structures have attracted researchers since the report of the 2-D pattern of DNA. The first report of a 3-D DNA structure was also published by Seeman's group in 1999^{26,32}. They designed a topological cube with same length of edges. The yield of the product is very low from the report, but it demonstrates the possibility to construct 3D structures by single strand DNA.

Approximately ten years later, Chengde Mao from Purdue University, and his group members reported the construction of a series of highly symmetric DNA polyhedra,³³⁻³⁹ including tetrahedral, cubic, octahedral and more complex structures by hierarchical approach that was based on the construction of a finite number of star motifs, as shown in Figure 1.5. These DNA

motifs are more rigid compared with the one designed in Seeman's group, because each edge of the structure was composed of two double strands.

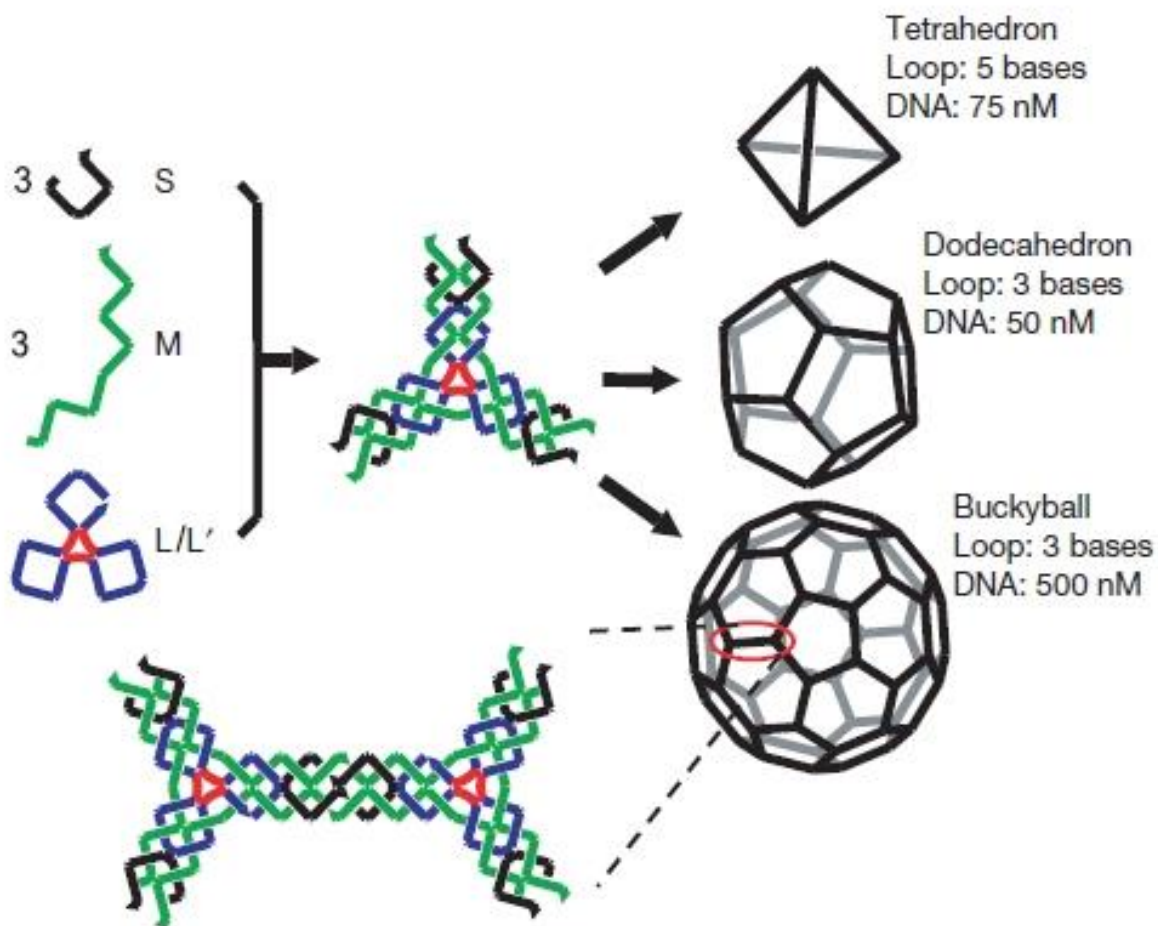


Figure 1.5 Self-assembly of DNA polyhedral. Reprinted with permission from Reference 38.

Copyright 2008, Nature, Nature Publishing Group.

1.3.3 DNA origami

The complexity and the size of the self-assembled DNA structures were greatly increased after 2006 when Rothemund published the first report regarding DNA origami technology⁴⁰. He divided the design process of DNA 2-D structures into 5 steps, as shown in Figure 1.6. According to the desired shape, he firstly built a geometric model of the DNA structure. From

top to the bottom, the shape was then filled by an even number of parallel double strands, called ‘cylinders’. The helices were then cut to fit the shape in individual pairs, which was an integer number of DNA turns. A periodic array of DNA crossovers was then applied to hold the helices together, which linked the designated positions where strands switch to the adjacent helix. In the second step, a single strand DNA (9000 nucleotides) was folded back and forth to comprise one of the two strands in every helix. Another crossover called ‘scaffold crossover’ will be created indicated by the red mark in Figure 1.6b. Designing the folding path is crucial here because the crossover can only be located at the tangent point between helices. Then, in the third step, they designed a set of short strands called ‘staple strands,’ which can provide the Watson-Crick complements for the scaffold as designed. In the fourth step, which is the most complicated step, they need to deal with the crossovers and minimize the strains to a certain length. In order to maximize the domains for staple strands with the scaffold DNA, efforts to merge the pairs of adjacent staple DNAs would be contributed to yield fewer and longer short staple DNAs.

The designing of a 3-D DNA origami structure was first reported in 2009 by William Shih’s group from Harvard Medical School ⁴¹. Different and difficult part here is also the linking of crossovers. As shown in Figure 1.7, the first step is also to design the target 2-D plane before folding. For example, in order to design a 3-D solid cubic, they flat it into a plane structure as shown in Figure 1.7a. Unlike the design of 2-D structures, crossovers from one double strand will not only link to adjacent double helix, but would bond far away to fold the final structure. Much attention must be paid to the orientation of the crossovers to successfully bind them.

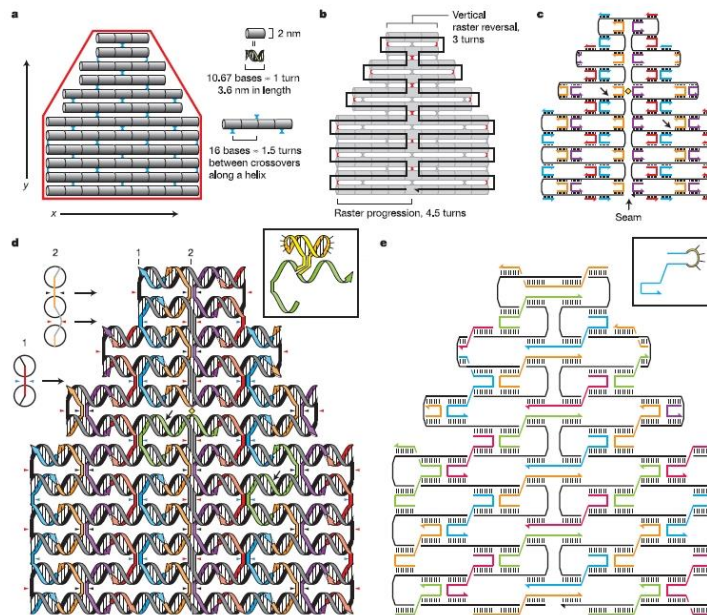


Figure 1.6 Design steps of 2-D origami structures. Reprinted with permission from Reference 40.

Copyright 2006, Nature Publishing Group.

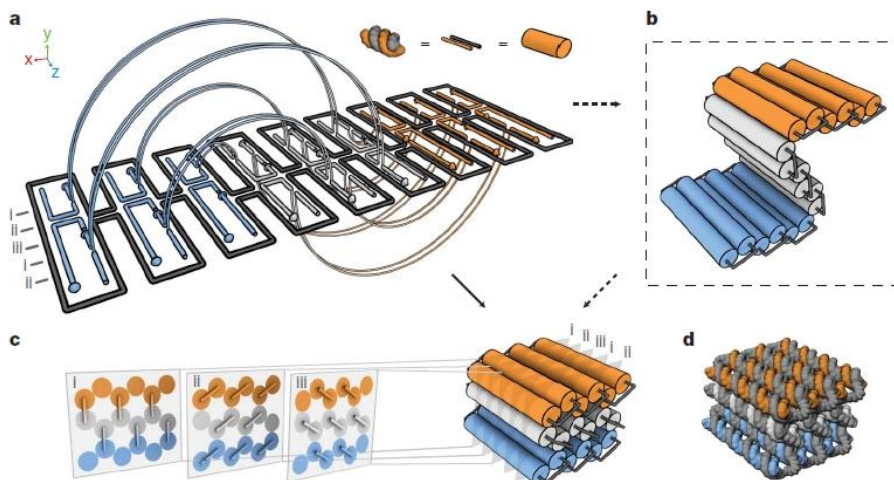


Figure 1.7 Design of 3-D origami structure. Reprinted with permission from Reference 41.

Copyright 2009, Nature Publishing Group.

More complicated 3-D structures were also successfully designed by William Shih's group in the year of 2009⁴². As shown in Figure 1.8, twist bundles with smooth surfaces were created, which

would be essential for investigation of mechanical properties of DNA origami nanotechnology. When the double helix is constrained to a honeycomb arrangement, the crossovers between helices would be spaced at 7-bp intervals. From left to right, each crossover was rotated around 240° to fit the orientation to each other. This would not bring any stress on its neighbors. However, when the intervals are not 7-bp, for example 5-bp or 9-bp, they would exert a right-hand or left-hand torque individually and push on its neighbors, which would bring twist to the final structure.

Although the design principle of DNA origami is well-understood, the designing process can be quite complicated particularly for complex shapes. Douglas, from William Shih's group⁴³, made the design process simpler and easier to operate. He developed a software 'caDNAno' (www.cadnano.org) which simplifies the most complicated part of the design process (arrangement of crossovers) into one bottom click as shown in Figure 1.9.

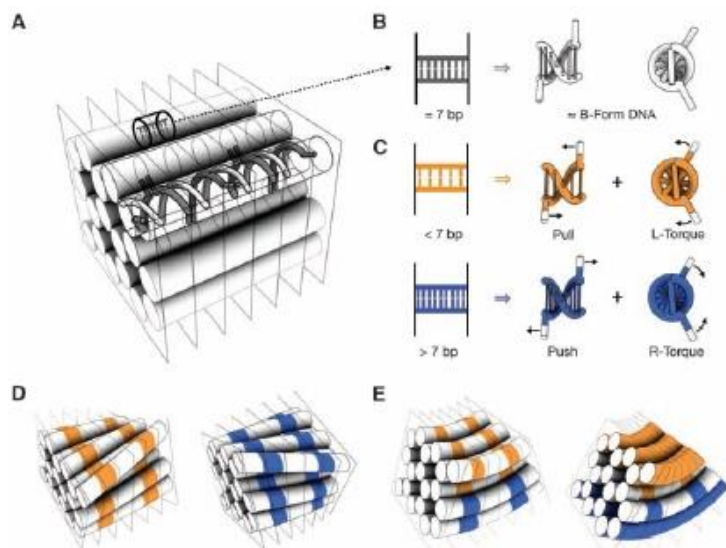


Figure 1.8 Design principles for controlling twist and curvature in DNA bundles. Reprinted with permission from reference 42. Copyright 2009, Science, the American Association for the Advancement of Science.

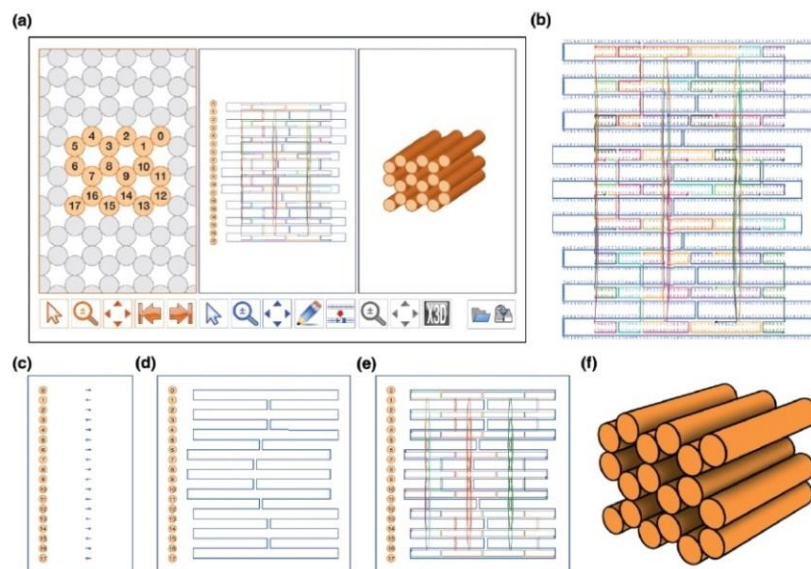


Figure 1.9 caDNAno Interface and design pipeline. Reprinted with permission from reference 43. Copyright 2009, Nucleic Acids Research, Oxford University Press.

1.4 DNA-guided assembly of nanomaterials.

1.4.1 Short DNA oligos as a template

DNA-functionalized nanoparticles were first reported in 1996 by Mirkin and Alivisatos^{44,45}. Synthesized DNA oligonucleotides modified with an alkane-thiol group were mixed with citrate attached gold nanoparticles (13nm). A stepwise salting process can result in the thio-group-functionalized DNA attaching on the gold nanoparticles by replacing the citrate. The number of oligonucleotides capped on the surface of the NPs is strongly dependent on the ratio of DNA to AuNP added to the system, final salt concentration, and the size of the NPs⁴⁶. Alivisatos's group also developed a strategy to coat the DNA oligonucleotides to the surface of gold nanoparticles. A special point for his experiment is that he can control the DNA numbers on the gold nanoparticle by gel electrophoresis. Their contributions on the DNA/NP system lead the way for DNA-based assembly of nanomaterials.

Basically, there are two different methods to generate 1-D assembly of DNA/NP systems⁴⁷. The first one is to immobilize the NPs along the DNA backbone by DNA complementary interactions. NPs would be functionalized with special sequences of oligonucleotides and bind to the DNA double helix template. The second method is to metallize DNA double strands by reducing the positive charged cations which were adsorbed on the surface of the DNA by electrostatic interactions, such as Ag^+ , Pd^{2+} and so on. Alivisatos and his group members showed for the first time that water-soluble gold nanoparticles with one *N*-propylmaleimide ligand can couple to a thio group. With the help of this reaction, linear alignment of gold nanoparticles can be formed with the center-to-center distance ranging from 2nm-6nm⁴⁸.

Direct metallization of DNA has been achieved by Braun and his group⁴⁹. Gold electrodes were first functionalized with disulfide oligonucleotides containing two 12-base sticky ends, with each end complementary to another and attached to different end of the electrodes. Then, Ag^+ was mixed into the system, inducing the charge replacement of Na^+ by Ag^+ . Adding with hydroquinone can cause the Ag^+ to be reduced by the formation of Ag aggregates on the DNA strand. Further reaction can provide the growth of silver, leading to a final size of around 100nm. Measurement of the electrical properties of the grown silver wire showed that the differential resistance at voltages varies between 7 and 30 M Ω .

1.4.2 DNA as a linker for assembly of nanoclusters

Compared with 1-D assembly of nanowire or nanoarrays, nanoclusters with finite size can be treated as analogous to molecules at nanoscale level, which could provide new properties from attractive effects. For example, when a quantum dot and a gold nanoparticle were placed next to each other, the quantum dot could be either quenched or enhanced, depending on the center-to-

center distance as placed^{50,51}. The size of the nanoparticle also played an important role in determining the final properties. The strategy from Alivisato's group provided an easy way to fabricate nanoclusters with only one single-strand DNA attached on the nanoparticles⁵². A dimer can be produced by mixing two kinds of nanoparticles attached with complementary sequences. Different lengths of the oligonucleotides can cause different lengths for the dimer. Fabrication of heterogeneous systems is also possible by replacing one of the gold nanoparticles with a quantum dot or silver nanoparticle. Another way to fabricate gold nanoparticle dimers was reported in 2009 using a stepwise assembly method⁵³. Maye *et al.* used a magnetic surface to block the self-assembly from one direction of the gold nanoparticle to fabricate a Janus particle. Reaction of another end of the gold nanoparticle for further assembly can result in the fabrication of dimer clusters. The Janus particle can also be used to create more complicated clusters by choosing different sizes of nanoparticles, as shown in Figure 1.10.

1.4.3 Short DNA linkers for assembly of 3-D crystal

Successful construction of 3-D superlattice by DNA-functionalized gold nanoparticles was first described by our group and Mirkin's group^{44,45}. As shown in Figure 1.11, two kinds of DNA-capped nanoparticles with complementary recognition sequences can hybridize into amorphous aggregates. Increasing temperature above the DNA melting temperatures in Au-DNA system can disassemble the aggregates, but the following cooling process can re-assemble the system into long-ranged ordered crystals. This process is called annealing. For system I to System V, crystalline phases can only be obtained in system IV and V. It means longer flexible spacers give more organized assembly results. That is to say, systems with shorter spacers or more rigid spacers can only yield amorphous states upon the cycle of heating above T_m , followed by cooling down to the room temperature slowly. The authors took system IV as an example. An ordered

crystalline structure can only be obtained after the annealing process. That is, heating the system above $T_m=60\text{ }^\circ\text{C}$, and then cooling down slowly until the temperature is below T_m . Ordered structures can be signified by the sharp diffraction peaks in SAXS images shown in Figure 1.11 below.

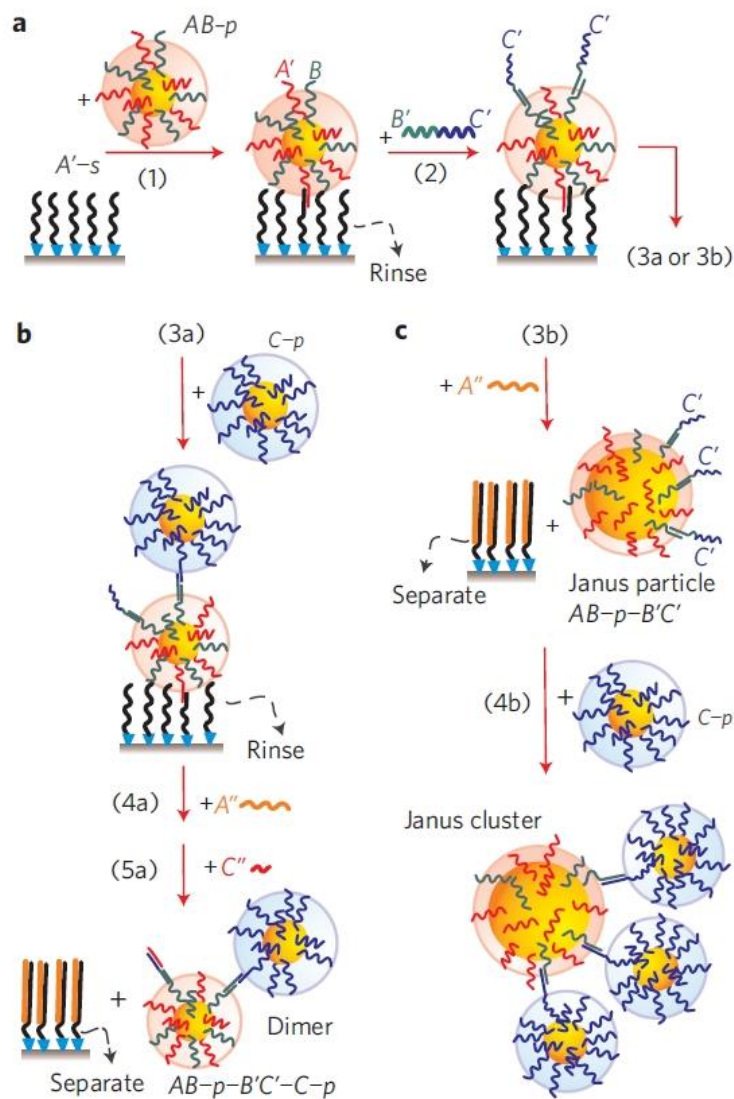


Figure 1.10 The assembly and encoding steps to fabricate the dimer cluster and asymmetric Janus clusters. Reprinted with permission from Reference 10. Copyright 2009, Nature Materials, Nature Publishing Group.

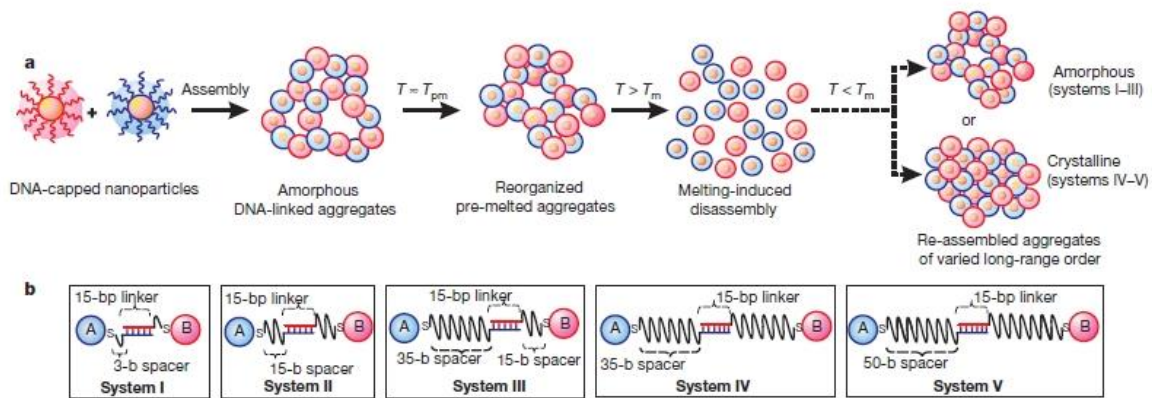


Figure 1.11 Assembly processes of DNA-capped nanoparticles into crystalline (a). Detailed picture of five systems used for assembly (b). Reprinted with permission from Reference 44. Copyright 2008, Nature, Nature Publishing Group.

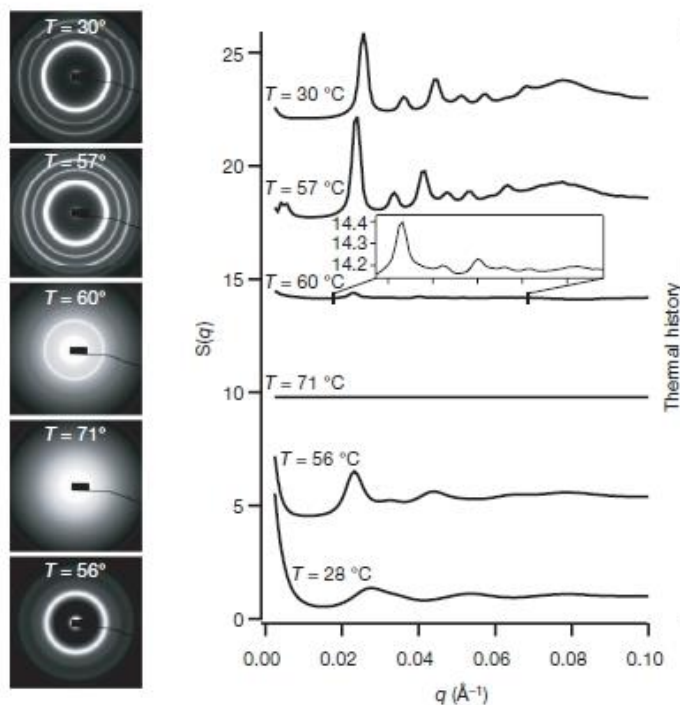


Figure 1.12 Crystallization pathway for system IV and structure of crystalline DNA-nanoparticle system. Reprinted with permission from Reference 44. Copyright 2008, Nature, Nature Publishing Group.

The same experiment was done for system V. These formed crystalline structures are also reversible. They can be obtained by multiple assembly-disassembly cycles. The peak positions from Figure 1.12 demonstrate that the crystalline phase belongs to the $Im\bar{3}m$ space group—body-centered cubic structure (BCC). This binary superlattice can also be obtained by heterogeneous species. Oleg Gang and Dazhi Sun recently introduced a system of Quantum dots and gold nanoparticles connected by DNA, instead of using gold nanoparticles and DNAs only⁵⁴. SAXS was also used to demonstrate the formed crystalline structures. Compared to the Au-DNA-Au system, the Au-DNA-QD system with similar particle sizes shows that simple cubic (SC) arrangement was formed with QDs located in the body position of BCC structure. Thermal cycle test for SAXS of these two kinds of systems showed that QD-DNA-Au system gives a slight broadening of the melting transition, and shows a lower melting temperature of about 3 °C due to the lower DNA density on QDs.

The lattice structures of the assembled nanoparticles with DNA attached are also determined by the size ratio of nanoparticles. Mirkin and coworkers reported in detail about how the structures and lattice parameters were determined by changing the ratios of particle size in their binary system⁵⁵. Instead of sphere nanoparticles, anisotropic nanomaterials can also be assembled and crystallized into 3-D structures, including nano-cubic, nano-rods and prisms⁵⁶.

1.4.4 DNA structure assembly with nanoparticles

From the description of DNA technology discussed previously in this thesis, we also want to explore the assembly of DNA structures with nanoparticles. In this concept, DNA is not only used as a linker, but also as the shape controller or the structure controller. A tetrahedral-shaped DNA structure was designed by Nicholas Kotov's group as the construction platform for

assembly of nanoparticles. Each nanoparticle contains one long DNA which could bind to another two different nanoparticles. These four nanoparticles are designed to be four different ones in size or material, which could bring chirality for the structure. The positions of CD signals could be changed in a wide range from 350-550nm, depending on what materials are chosen for assembly. However, because of the softness of short DNA, the application of DNA structures as a template for further assembly of nanomaterials is limited. The DNA origami technique provides us a better way to fold DNA strands into large and solid structures, and thus attracts research on assembly of DNA origami with nanoparticles.

Hung et. al.⁵⁷ reported assembly of nanoparticles on a triangle origami structure. The triangle was first created by designing and mixing relevant staple strands. After careful annealing, triangles with middle holes were obtained with sticky end sequences on three edges for further assembly. Gold nanoparticles with oligonucleotides attached which were complementary to the sticky ends were mixed into the origami solution. Beautiful nanoparticle patterns were created as shown in Figure 1.12. Baoqian Ding and his co-authors⁵⁸ also used the triangle origami structure as the template to create a series of organized nanoparticle chains to demonstrate that nanoparticles can be precisely positioned at the place desired. Three-dimensional origami structures were also applied as the template to assemble nanoparticles. Zhao and his co-workers⁵⁹ designed a hollow cubic with the diameter of the hole around 10nm which could capture a 10nm gold nanoparticle inside. Sticky ends designed inside the hollow could catch the nanoparticles with complementary sequences attached. Combined with functional positions outside, 3-D nanoclusters can be designed and created.

DNA origami structures can also be transformed by adding additional staple sequences. Baoqian⁶⁰ designed a 2-D origami structure with sticky ends outside to bind with nanoparticles.

Interestingly, after adding some staple sequences which can bind to both edges, the 2-D structure can roll up the plane into a bundle. Nanoparticles arranged along the diagonal line of the 2-D structures now form a spiral pattern, which turned the non-chiral alignment into chiral structures. Since the origami structure can control the position of the attached nanoparticle better than soft double strands, studies of distance-dependent photoluminance could be performed better with origami systems. Acuna et. al. created a 2-D origami platform with precise position of sticky ends stretched out for binding nanoparticles ⁶¹. By varying dye to particle distance, they got a more practical fitting, yielding 50% quenching at the interparticle distance of 10.4nm (as precisely as 0.1nm). More complicated and heterogeneous clusters using a DNA origami structure as the template were reported by Robert etc. in 2014. He proved that different sizes of gold nanoparticles can bind with different numbers of DNA origami bundles, even if the bundles have already attached other small nanoparticles. However, constructing crystal frameworks by DNA nanostructures is still offers many challenges for the scientist, which will be discussed further in this thesis.

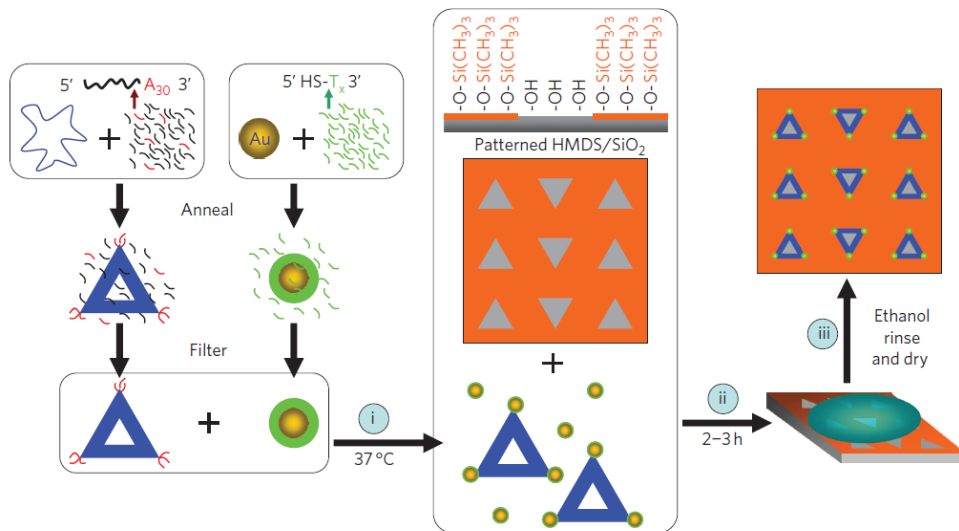


Figure 1.13 Creating trimer nanoclusters using DNA origami triangles as the template. Reprinted with permission from Reference 57. Copyright 2010, Nature Nanotechnology, Nature Publishing Group.

1.5 Outline of the Thesis

The work presented in this thesis focused on the DNA template and functionalized nanostructures including nanoclusters and more complicated nanocrystals. In chapter 2 and 3, we designed a pH sensitive i-motif DNA sequence as the linker for building dimer nanoclusters and nanocrystals.

First, in the dimer system, we encoded the 3rd gold nanoparticle into the solution which was partly complementary with the imotif linker. By switching pH values between 5 and 8, a dynamic transformation of dimer and trimer nanoclusters was detected by SEM statistics, DLS, and fluorescent spectroscopy.

Then, in the crystal system, cycling of pH between 5 and 8 by titration could result in different lattice parameter of the formed BCC structure by SAXS. Similar phenomenon could also be observed in dimer systems when the imotif was encoded in the middle of the linker. These changes could be cycled by at least 3 cycling.

In chapter 4, we designed a core-shell structure with difference surface-to-surface distance controlled by DNA length. Core is 50nm gold nanoparticle, while shell is the 5nm quantum dots. We have shown that the optical output can be controlled by optical excitation from quenched to enhanced state in a step-wise manner.

Moreover, we developed shaped non-chiral nanoparticles acted as plasmonic reporters of chirality for attached molecules by providing a giant, two orders of magnitude CD enhancement in near-visible region. Salt effect of the system was also investigated.

Last but not least, we designed octahedral DNA origami structures and bond different sizes of nanoparticles in designed positions. By cryo-EM technology, we can observe not only both DNA and nanoparticles in the raw micrographs but also sub-nanometer resolution of their 3D structures reconstructed using single particle technique. We also showed that chiral activities can be controlled by simply moving different sizes of NPs into targeted positions. Low dimensional arrays including 1D and 2D can also be obtained using these clusters as the building block.

In chapter 7, we designed polyhedral DNA origami structures with high symmetry and further assembly with NPs to form 3D superlattice frameworks. This is the first report of the formation of 3D DNA origami structures in micro-scale by the help of nanomaterials. Because the advantage of DNA origami in accurate decision of the linking position, simpler and more effective controlling of different crystal superlattice will be more accessible.

Chapter 2

Reversible Switching of Structure and Optical Response of DNA-assembled Nanoparticle Clusters by pH Stimulation

Abstract

DNA-driven self-assembly of nanoparticles is an effective and promising way for nanoclusters fabrication. However, such cluster is typically static or undergoes only conformational changes. We extend DNA-assembly methodology for fabrication of dynamically responsive clusters which are switched between dimer (two-particle) and trimer (three-particle) structures. We developed a simple yet effective approach for the switching the morphology of nanoparticle clusters using a linking ‘i-motif’ DNA sequence that responds to pH stimulation. Our experiments demonstrate that such cluster switching can be reversibly cycled multiple times. Moreover, by employing both gold NP and fluorescent quantum dots, we show that structural cluster switching induces corresponding changes of optical response in the system due to the fluorescence quenching by plasmonic particle.

2.1 Introduction

Self-assembly of nanometer-sized building blocks, especially metallic nanoparticles and quantum dots into various kinds of structure provides a route for exploring their collective functions⁶²⁻⁶⁴. Functionalization of nanoparticles by biomolecules has been demonstrated to be an effective way for construction into these structures^{52,53}. Based on the specific Watson-Crick base-pairing interaction, DNA has been designed for generating more sophisticated nanoclusters such as dimers and more complicate 2-D clusters with extremely high throughput. Moreover,

considering the advantages of conformational polymorphism and programmable sequence recognition for DNA, further demanding for controlling of these different nanoclusters with freedom has been involuntarily put forward. As is well known, pH value is one important factor in determining the structure or morphology of polymers including protein and DNA, especially for the application of drug delivery and chemical sensors. For example, Jing Su *et al.* employed a pH-sensitive catechol containing polymeric carrier for delivery of the anticancer drug bortezomib to cancer cells⁶⁵. Herein, we present a well-designed approach with special i-motif DNA sequence as the linker for achieving dimer and trimer nanoclusters switch by changing pH value of the system. Fluorescent blinking could also be observed when we used Quantum Dots (QDs) as the third nanoparticles in the formation of trimers.

2.2 Experimental design

Our artificial designing route is depicted schematically in Fig. 2.1. Gold nanoparticles (with diameter around 10nm) were functionalized with oligonucleotides firstly for further assembly. According to different oligonucleotides applied, we named relevant NP/DNA building blocks as NP1, NP2 and NP3 which has different DNA strands A, B and C attached respectively. The ssDNA strands (A, B and C) contain an outer recognition part with a poly dT spacer. A linker DNA L_i was designed with two ends complementary to the recognition part of NP1 and NP2 for the formation of dimers. The central region of the linker has 21-base nucleotides (CCCATTCATTCATTCATTC) for binding NP3 while its rest is poly dT. In particular, this region is cytosine-rich, containing four units of triple C, which was called as “i-motif” sequence. NP3 was functionalized with single strand C which was complementary to the “i-motif” part of the linker DNA, but with three mismatches, in order to prevent the formation of G-quartet. Briefly, dimer nanoclusters composed of NP1 and NP2 linked by L_i were firstly prepared by

stepwise surface encoding introduced in the previous paper⁵³. Then adding NP3 into the above solution, hybridization between the end strands on NP3 and L_i took place, leading to the formation of trimer nanoclusters as described in Fig. 2.1. In this process, pH value of the buffer solution should be larger than 7 (~7.5 in our case) to make sure the “i-motif” sequence was unfolding. While the pH was changed to 5-6 by adding HCl (1M), cytosine in “i-motif” sequence will be partially protonated (C^+), and the sequence will form a DNA quadruplex structure by a special intramolecular base-pairing between C/C^+ . pH titration of the i-motif sequence showed a sharp transition point at pH=6.5. NP3 will therefore be “kicked off” from the trimer nanoclusters, and dimer nanoclusters reoccurred, accompanying with more single nanoparticles (NP3). Continuous altering pH value between ~8 and ~5 would transform the state of “i-motif” between intra-molecular quadruplex and inter-molecular duplex of DNA, resulting in the conversion between dimer and trimer nanoclusters.

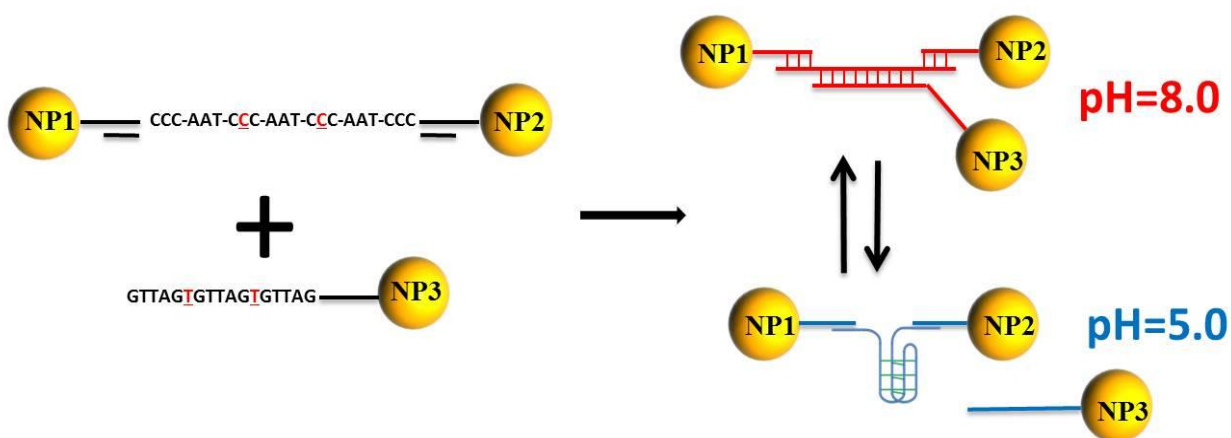


Figure 2.1 Schematic illustration of the cluster change between dimer and trimer

2.3 Results and discussion

We probed the assembled dimer and trimer nanoclusters as discussed above by scanning electron microscopy (SEM). For the samples of dimer nanoclusters prepared freshly before adding NP3, a representative statistical analysis revealed a morphological yield of ~70% dimers (particle percentage for 613 particles), ~28% monomers and only ~2% clusters with more than two particles (Fig. 2.2). This statistical result was similar to the previous paper reported by our group.⁷ When NP3 was added into the prepared dimer solution at pH = 7.4 with a low final concentration, as shown in Fig. 2.3(a), ~41% of the total nanoparticles (760 particles) in the solution was transformed to trimers with ~22% single particles, ~32% dimers and only ~5% clusters composed of more than 3 particles. When pH of the trimer solution is decreased to below 6.0, as described above, 'i-motif' sequence in the central region of L_i will form quadruplex structure, resulting in the disconnection of NP3 from trimer nanoclusters and formation of dimers and single nanoparticles. A representative statistical analysis showed that this process resulted in ~49% single particles (601 particles), ~43% dimers, ~5% trimers and ~3% higher ordered clusters. This result indicated nearly eightfold decrease of the yield percentage of the formed trimer nanoclusters, accompanying with the increase of the corresponding percentage of dimers and single particles.

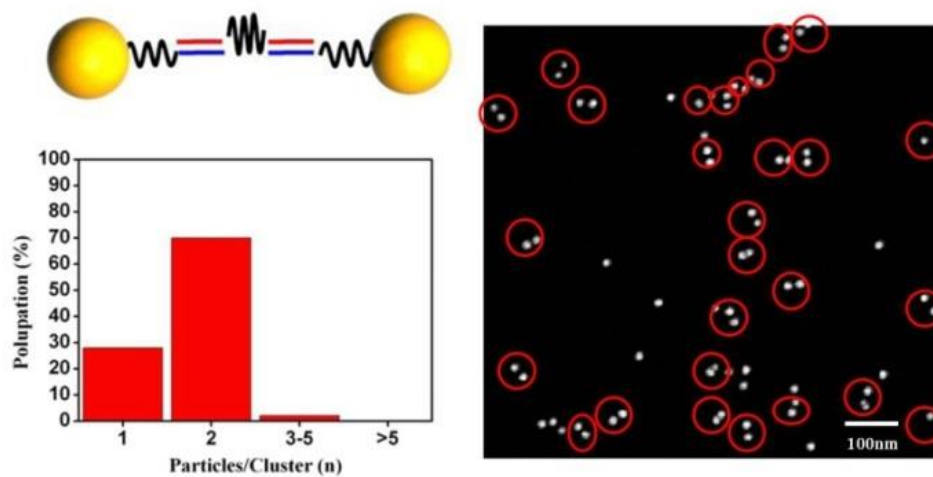


Figure 2.2 Population percentage yield and representative SEM image of dimer nanoclusters.

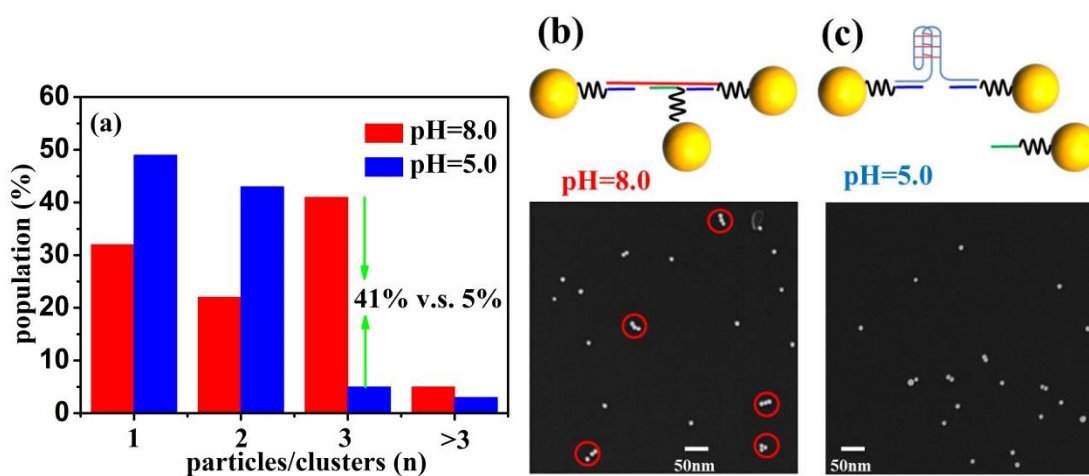


Figure 2.3 Assembly of trimers in different pH. (a) Analysis of assembled nanoclusters using SEM statistical analysis. (red or left: pH=8.0; blue or right: pH=5.0) (b&c) Representative SEM image for the sample in pH=8.0 (b) and pH=5.0 (c)

Dynamic Light Scattering (DLS) reveals the number-averaged hydrodynamic diameter (D_h) population for the switching process between dimers and trimers, as illustrated in Fig. 2.4. The dimer nanoclusters possessed a $D_h \approx 30\text{nm}$, in contrast to $D_h \approx 20\text{nm}$ for isolated DNA capped NP1 (Core size + DNA shell). By adding the additional NP3, D_h was increased to $\approx 39\text{nm}$, demonstrating that trimers were formed. If we further changed the pH value of trimer solution below 6 by adding additional HCl (1M), D_h would decrease to $\approx 22\text{nm}$, smaller than dimers. This was attributed by the formation of single nanoparticles (NP3) accompanying with dimers. Returning pH value back to around 7 by titration of NaOH (1M) would reversibly result in trimer formation as indicated by $D_h \approx 42\text{nm}$. The reversible D_h between $\approx 20\text{nm}$ and $\approx 40\text{nm}$ was observed by controlling pH between ~ 5 and ~ 8 , as shown in Fig. 2.4. Control experiment was performed by changing NP3 to non-complementary NP4 (poly T attached on NP4). After adding NP4 in pH=7.4, hydrodynamic diameter of the dimer solution was decreased to $\approx 20\text{nm}$ instead of increasing because NP4 cannot bind with the linker of dimers to form trimers, as shown in Fig. 2.4 and Fig. 2.5. pH cycling also could not cause any change in DLS measurement.

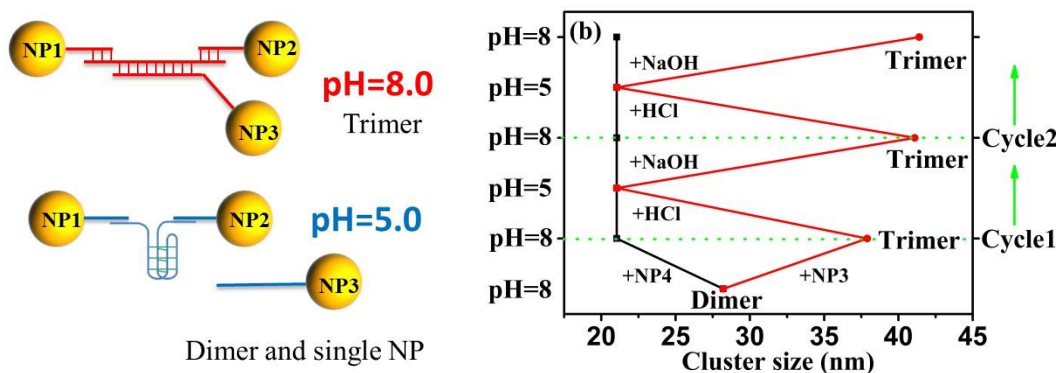


Figure 2.4 Model and Analysis (b) of cluster size change by cycling for dimer-trimer switch (red line, circle point) and control experiment which cannot form trimers (black line, square point);

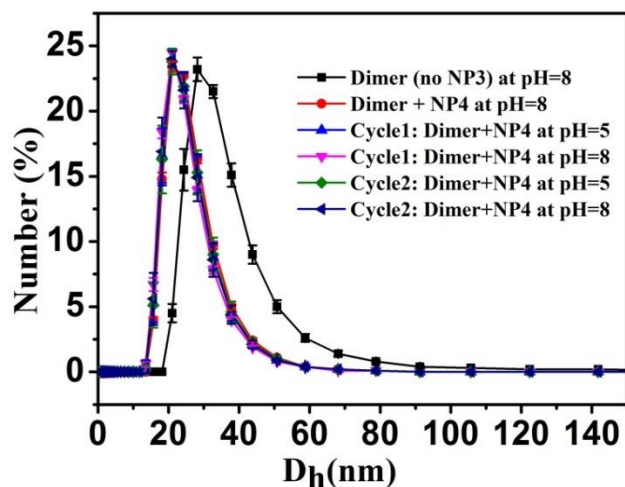


Figure 2.5 Control experiment for hydrodynamic diameter of dimer and after adding non-complementary NP4.

To further demonstrate the switch of dimer and trimer nanoclusters, we changed NP3 into Quantum dots (QDs), with the same DNA sequence (C) attached on the surface. Optical property of QDs near metallic surface such as gold and silver has attract more and more interest recently due to its application in bio-sensors and other optical devices. Fluorescence of QDs can be quenched, even enhanced when they were put near the gold or silver nanoparticles. Hereby, assembly and dis-assembly of QDs with the formed dimer gold nanoclusters can be detected by fluorescent signals. DNA attached QDs were added into freshly prepared dimer clusters linked by ‘i-motif’ DNA with the concentration ratio equaling to 1:1 between QDs and dimers. As illustrated in Fig. 2.6, when pH of the solution was changed between >7 and <6 , quenching and enhancement of fluorescent intensity signals were detected. 10 cycles of fluorescent intensity in different pH values demonstrated the stability of assembly and dis-assembly process. Little decrease for the fluorescent intensity in different cycles (with the same pH value) resulted from dilution of the solution by adding HCl (1M) and NaOH (1M) continuously. In order to reduce the

2.4 Conclusion

In summary, we have successfully fulfilled the switch of dimer nanoclusters and trimer nanoclusters by controlling the pH value of the system. “i-motif” sequence was applied as the “matchmaker” in this designed process. To the best of our knowledge, this is the first example of controlling the structure of sophisticated nanoclusters. By changing the ‘i-motif’ sequence with better-designed DNA ‘glues’ or ‘scaffolds’, more accurate controlling of nanoclusters or nanodevices can be achieved. Dynamic controlling of different nano-structures is also predictable.

2.5 Methods

(1). DNA oligonucleotides were purchased from Integrated DNA Technologies Inc. as lyophilized powders. All the sequences were purified with HPLC. Sequences for the DNA (5’ to 3’) were:

Thiol-ssDNA A: ATTGGAAGTGGATAATTTTTT-C₃H₆-SH;

Thiol-ssDNA B: HS-C₆H₁₂-TTTTTTTAACCTAACCTTCAT;

Thiol-ssDNA C: HS-C₆H₁₂-TTTTTTTTTTTTTTGAATGTGAATGTGAATG;

Thiol-ssDNA D: HS-C₆H₁₂-TTTTTTTTTTTTTTTTTTTTTTTTTTTTTTTTTTT;

Thiol-ssDNA N: ATTGGATTGGAAGTATTTTTTTTTTTTTTTTTT-C₃H₆-SH;

Linker DNA Li: TTATCCACTTCCAATTTCCCATTCCCATTCCCATTCCCTTAT
GAAGGTTACCTTA;

Amino-ssDNA on QDs: NH-C₆H₁₂-TTTTTTTTTTGAATGTGAATGTGAATG;

Biotin-ssDNA N': CTTGTGTCTACTTCCAATCCAATTTTTTTTTTTTTTTTTT-Biotin;

DNA N'': ATTGGATTGGAAGTAGACACAAG

(2). Preparation of DNA attached gold nanoparticles

In a typical experiment, short single strand DNA sequences with thio-group were first mixed with gold nanoparticles (10nm) with a ratio of 1:300. The mixed solution was then buffered to 10nM with phosphate buffer after aging 2 hours. NaCl was then gradually added to the buffered solution to around 0.3M. Aging overnight, we will centrifuge the sample for 4 times to remove the access free DNA (13000 rpm for 1h).

(3). Preparation of SEM sample

The prepared solution was directly dropped on the surface of silicon wafer. After deposit for around 10mins, we remove the solution and washed twice by distilled water. Then it is ready for SEM imaging.

(4). Dynamic Light Scattering

DLS measurements in this thesis were performed on a Malvern Zetasizer ZS instrument which equipped with a 633nm laser source and a backscattering detector at 173° .

Chapter 3

Switching of Nanoparticle Superlattices and Dimer Clusters by pH-Regulated ‘i-motif’ DNA

Abstract

As discussed in chapter 2, ‘i-motif’ DNA sequences are sensitive to pH environment by changing its conformation which can trigger cycling between dimer and trimer clusters. In this chapter, we continued our work by introducing the ‘i-motif’ motor as the linker in three-dimensional crystal structures. Our in-situ synchrotron-based small angle x-ray scattering (SAXS) measurements reveal repeatable and stretchable transformations for the formed nanocrystals during pH cycling and successful realization of this strategy for more complex DNA motifs. Also, dimer structures similar to chapter 2 were also investigated by SAXS measurement upon pH cycling.

3.1 Introduction

DNA was demonstrated to be a useful building block or linker system for the construction of nanoparticles, such as nano-metal particles, quantum dots, and organic nanoparticles, into various kinds of complicated morphologies, including two-dimensional nano-clusters, three-dimensional aggregations or nano-crystals of micrometer-sized colloids based on Watson-Crick interactions^{54,66-68}. Furthermore, DNA can also offer an easy method for post-assembly reconfigurations, such as the DNA robots which can walk⁶⁹, roll⁷⁰ or vibrationally stretch⁷¹. Recently, using DNA to switch the states of nano-clusters has attracted more and more attention, such as dimer-trimer cluster switching and lattice constant change in three-dimensional

superlattices by adding DNA ‘fuels’⁷². Particularly, tuning the lattice constant of superlattices is a great advantage for colloid crystallization, especially when we use DNA as the linker, because DNA is soft, stable, and the length was able to be controlled^{72,73}. However, reported manuscripts only focus on two areas. First, changing the concentration of inorganic salt in the solution of DNA linked colloid crystallization to achieve lattice constant change, but was un-switchable⁷³; Second, using DNA ‘fuels’ for construction of different DNA conformations, to tune the lattice constant, but it consumed raw materials and was not stable enough⁷².

3.2 Experimental design

In this chapter, we introduced one specific DNA sequence, called ‘i-motif’ (CCCAATCCCAATCCCAATCCC) into our systems⁷⁴. Our goal is to tune the parameters of nano-crystal and nano-cluster states by adjusting physical conditions in the solution, in this case, pH value. By tuning the pH value of ‘i-motif’ between ~8.0 and 5.0, this specific sequence can switch its conformation between the chaotic single strand and the specific quadruplex structure (Figure 1a). Simply to say, while the pH of the system was changed to ~5.0, part of cytosine in this DNA linker would be protonated, and bind with another cytosine forming C/C⁺ pair. So the single strand DNA would be transformed to a specific quadruplex structure. When we tune the pH value back to 8.0, cytosine de-protonated and the quadruplex structure unfolded into the normal single strand. The pH sensitive DNA device had three regions in our system, A’, B’ and C’, similar to the one discussed in chapter 2. A’ and B’ are complementary to another two DNA strands (A and B) which were functionalized on gold nanoparticles (10nm) separately (denoted NP1 and NP2). The C’ region is the reconfiguration part which contains the ‘i-motif’ while the rest is poly dT. This designed DNA device was used as the linker for the construction of crystallization and dimer clusters. The linker state here would determine the interparticle

distance d for the formed 3-D structure or the dimer system as designed. In pH~8.0, the ‘i-motif’ DNA would behave as the regular single strand DNA; however, when we changed the pH value to ~5.0, this sequence would shrink into the quadruplex structure, changing the interparticle distance d at the same time. Tuning pH value between ~5.0 and 8.0, we can fulfill the ‘vibration’ of nano-crystals (Figure 3.1b) or dimer clusters (Figure 3.1c) by oscillating the lattice parameter or the inter-particle distance between NP1 and NP2 in dimer systems.

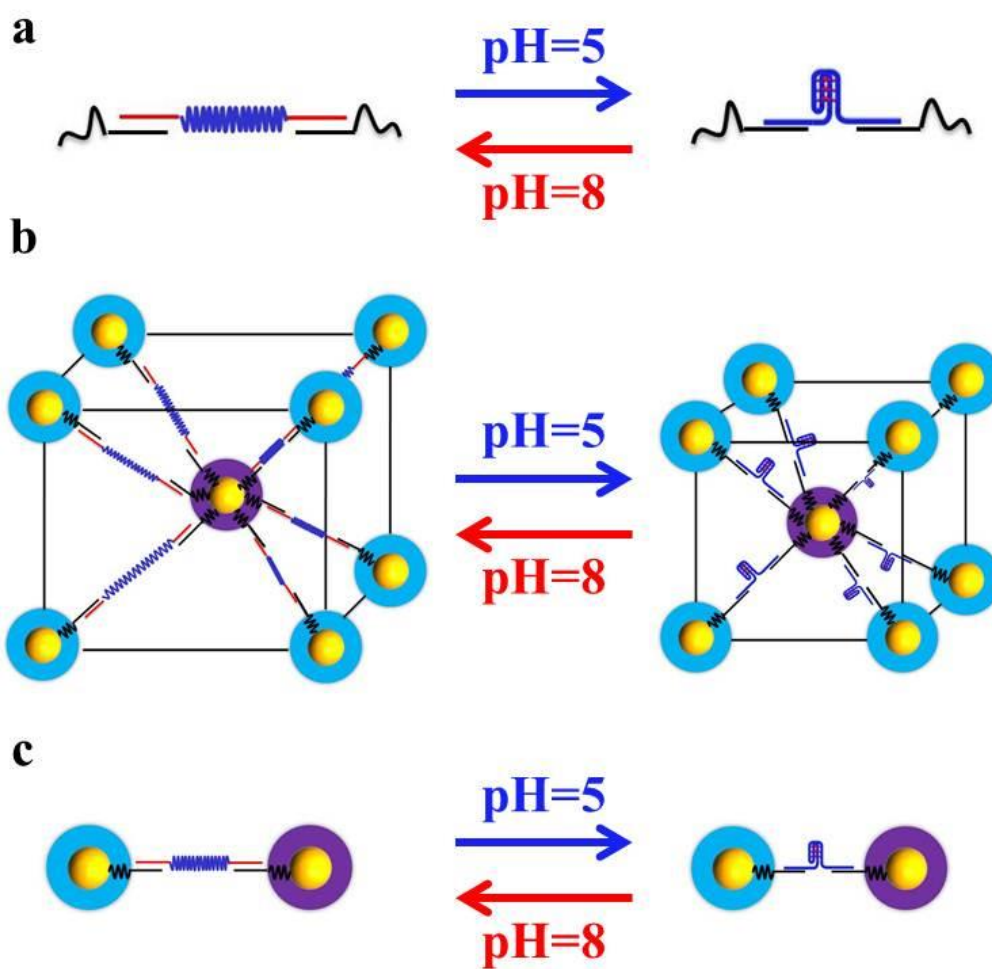


Figure 3.1 Cartoon of structure transformation of i-motif’ sequence alone (a); in 3-D crystalline (b) and in dimer system (c).

3.3 Results and discussions

We first explored the 21-base ‘i-motif’ sequence as the C’ part of the linker for the assembly of DNA-capped nanoparticles into three dimensional polycrystalline aggregations by means of structural probing using in situ synchrotron-based small-angle X-ray scattering (SAXS), while a sample phase is reflected in a scattering pattern. Linker strands containing the ‘i-motif’ sequence were added into a solution of NP1 and NP2 with a ratio [DNA]/[NP]=36 for inducing assembly of particles. The solution here is composed of 10mM phosphate buffer and 100mM NaCl salt with pH=7.5. Figure 3.2a illustrates that after the annealing process, the system exhibits a body-centered cubic (bcc) crystal structure. For this symmetry, the first scattering peak in pH=7.5 corresponds to (110) crystalline plane of the bcc structure with a lattice constant $a=38.6\text{nm}$ ($q_1=0.02319\text{\AA}^{-1}$). The obtained surface-to-surface distance between NP1 and NP2 is around 23.4nm ($d_{1,2}=\frac{\sqrt{3}a}{2}-d_{\text{NP}}$), where $d_{\text{NP}}=10\text{nm}$ is the nanoparticle diameter. This is relatively large volume compared to single nanoparticles or DNA linkers, which indicates that the superlattice framework is extremely open in which 90% of the inner volume is occupied by solvent, facilitating penetration of inorganic ions and small organic compounds for molecular stimuli. We then changed the pH value of the superlattice solution to 5.8 by rinsing the buffer. The structure factor from SAXS results still revealed a bcc superlattice structure with the q_0 value shifted to larger value ($q_0=0.02524$), corresponding to the shrinking of the unit cell to $a=34.7\text{nm}$. The surface-to-surface distance was around 20.6nm after titration of the solution to pH around 5.0. Compared with 23.4nm in the case when pH=7.5, a 2.8nm difference was calculated in two different states. This result matches the simulation for these two different structure lengths. Switching pH value back to 7.5 and repeating the cycles could give a perfect recovery of the unit cell and switching of the lattice parameter between two lengths with around 3nm difference

(Figure 3.8). A control experiment (Figure 3.3) was also performed using the same length linker DNA which could also link NP1 and NP2 in two ends while its rest parts are poly dT. BCC structure can also be obtained in pH=7.5 and pH=5.8 as shown in Figure 3.3. However, interparticle distance in this system does not change much even after repeating 3 cycles. This result demonstrated that the distance change for Figure 3.2 (a) came from the transformation of the ‘i-motif’ sequence.

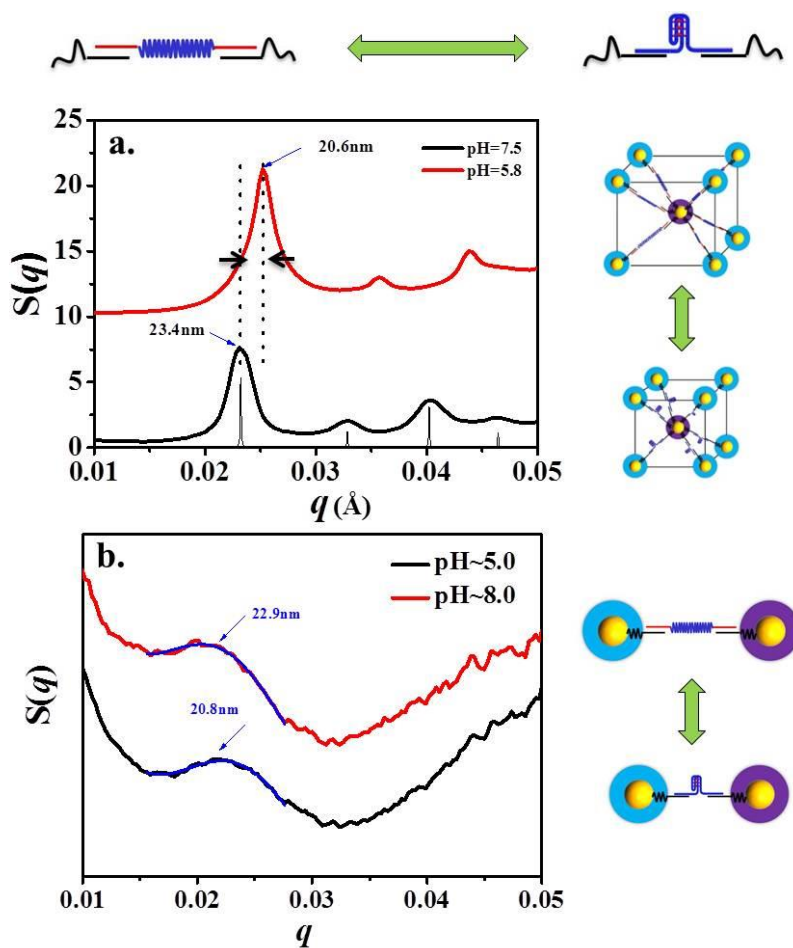


Figure 3.2 Structure factor (left) and cartoon (right) for ‘i-motif’ linked 3D-crystalline structure (a) and dimer system (b) with different pH values. Blue lines are fitted data by a dumbbell model.

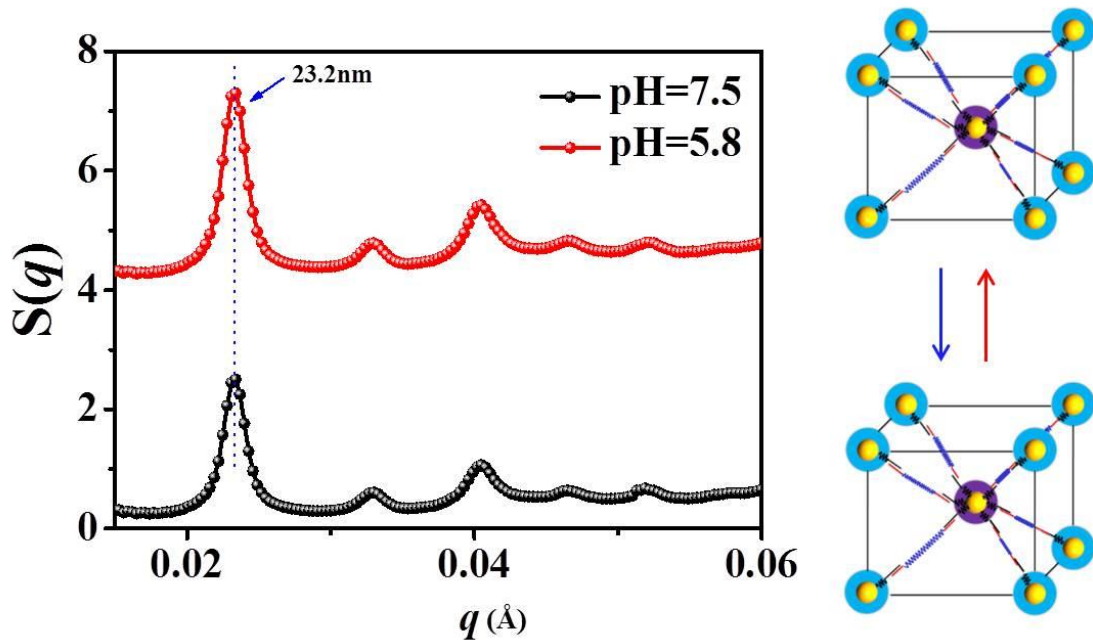


Figure 3.3 Structure factor (left) and cartoon (right) for L30 DNA (all poly dT) linked 3D-crystalline structure with different pH values.

To further check the behavior of this reconfigurable DNA device in similar interparticle environments without the constraint of three-dimensional bulk packing, we introduced the same ‘i-motif’ linker into a dimer cluster system as discussed in chapter 2. Figure 3.4 shows a representative scattering electron microscopy (SEM) image, revealing that around 70% of the nanoparticles formed dimer clusters. Dynamic light scattering (DLS) also shows a representative profile, in which the number-averaged hydrodynamic diameter (D_h) is around 18nm for isolated NP1 and 29nm for dimer with pH=8.0, respectively (Figure 3.5). We used SAXS method to monitor the interparticle distance change for this dimer system in pH~8.0 and pH~5.0 respectively. Figure 3.2b shows the 2-D scattering patterns for two dimer states with different pH values. The first peak q_0 monotonically shifted toward a higher value when the pH value of the dimer solution changed from pH~8.0 to pH~5.0. This clearly indicates a decrease of the

interparticle distance from 22.9nm to 20.8nm when changing pH to a lower value in which the ‘i-motif’ sequence may change its structure from double helix to quadruplex. The $S(q)$ profiles of the dimer clusters here can be described by a dumbbell model:

$$S(q,D) = \frac{\sin(qD)}{2qD} + 0.5$$

where D is the center-to-center distance for nanoparticles. Control experiments (Figure 3.6) reflect that if the linker DNA does not include the ‘i-motif’ sequence (L30 as the linker), there is no distance change while changing the pH. This is also convincing evidence that interparticle distance change in the dimer system also resulted from the structure change of the ‘i-motif’ sequence with different pH values. Similar with what we obtained from bcc nano-crystal structure, repeating the pH value in the same dimer solution between approximately 5.0 and 8.0 can perfectly change the interparticle distance by around 2-2.5nm. Compared with 3nm different in 3D system, dimer clusters assembled with single strand linker DNA show weaker dependence of the interparticle separation due to the greater linker flexibility.

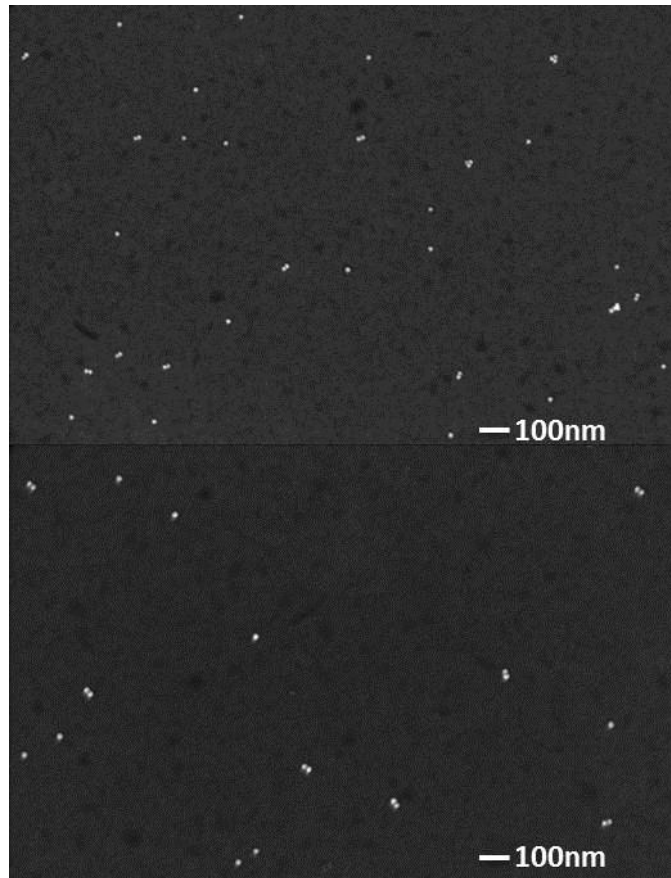


Figure 3.4. Representative SEM images for dimer clusters.

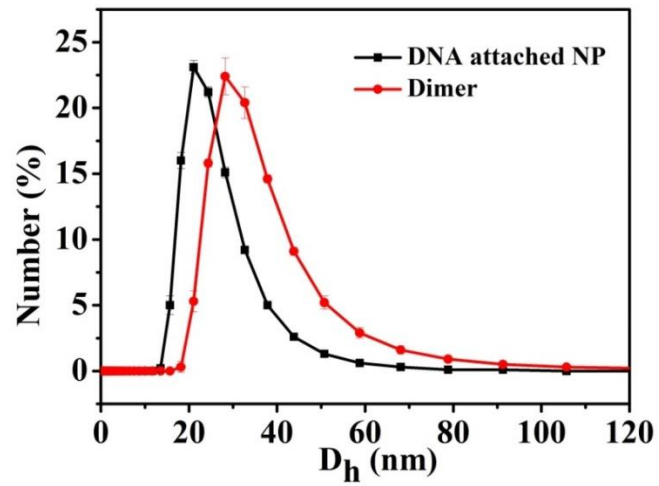


Figure 3.5 DLS data of hydrodynamic size of monomers (black) and assembled dimers (red).

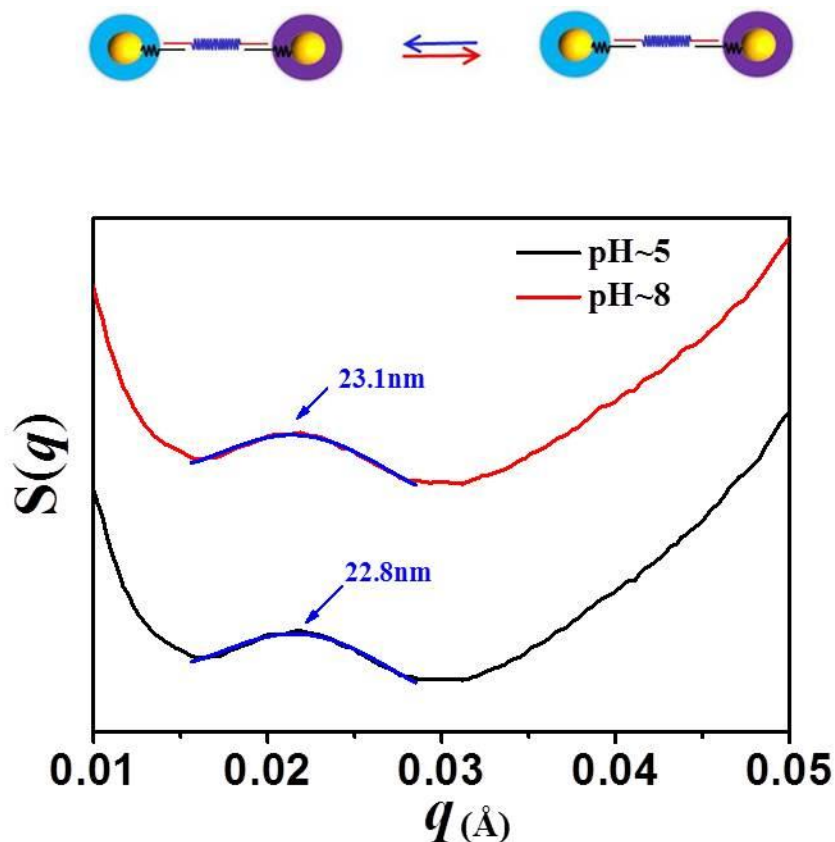


Figure 3.6 Structure factor (bottom) and cartoon (top) for L30 DNA (all poly dT) linked dimer system with different pH values.

In order to control the interparticle distance to some extent by pH tuning for the ‘i-motif’ sequence, we introduced two separate ‘i-motif’ structures in one linker to give a larger effect. Figure 3.7 (top) shows the DNA cartoon image for our design. In region C’ of the linker DNA, two ‘i-motif’ sequences were separated by 15bp DNA, in order to prevent interplay between these two ‘i-motif’ sequences. This ‘twins’ linker was applied to both 3-D nano-crystal and dimer cluster systems. Figure 3.7a showed a larger interparticle distance change (5.2nm) in two different pH states, which is almost twice that for one ‘i-motif’ linker system. Both of the two

states showed a bcc structure. The large distance change can also be perfectly switched for 3 cycles. However, in the dimer system (Figure 3.7b), the ‘twins’ linker can only give a 2.2nm change for interparticle distance between pH=5.0 and 8.0, which is only a little bit larger than the ‘single’ linker system. This may also come from the greater flexibility of the DNA linker between dimer systems and 3-D nano-crystals. This flexibility effect would be more obvious for longer linker DNA.

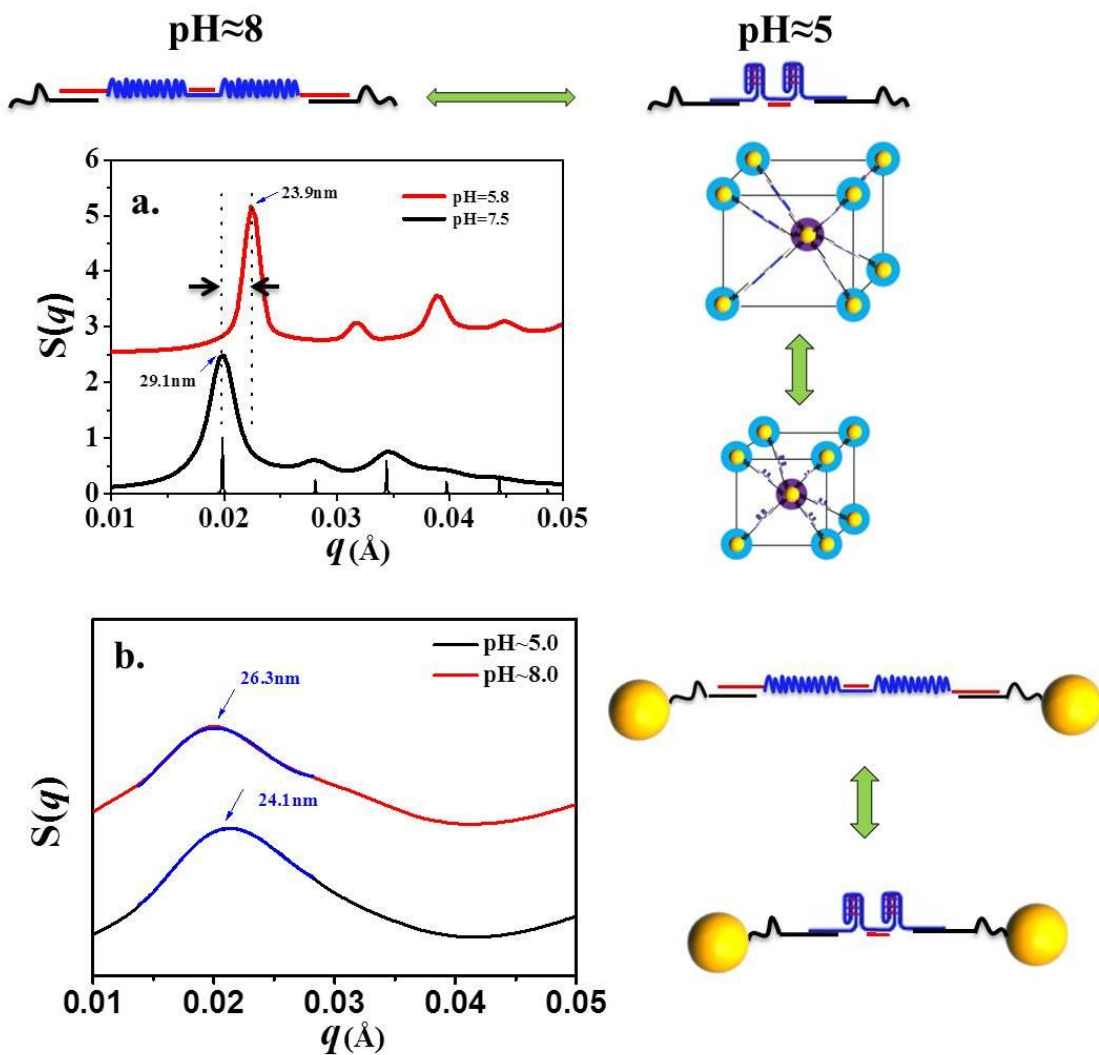


Figure 3.7 Cartoon (right) of two ‘i-motif’ separated by 15bp double strand, and its structure upon different pH values; structure factor (left) for 3-D nanocrystalline and dimer clusters linked by two ‘i-motif’ DNA.

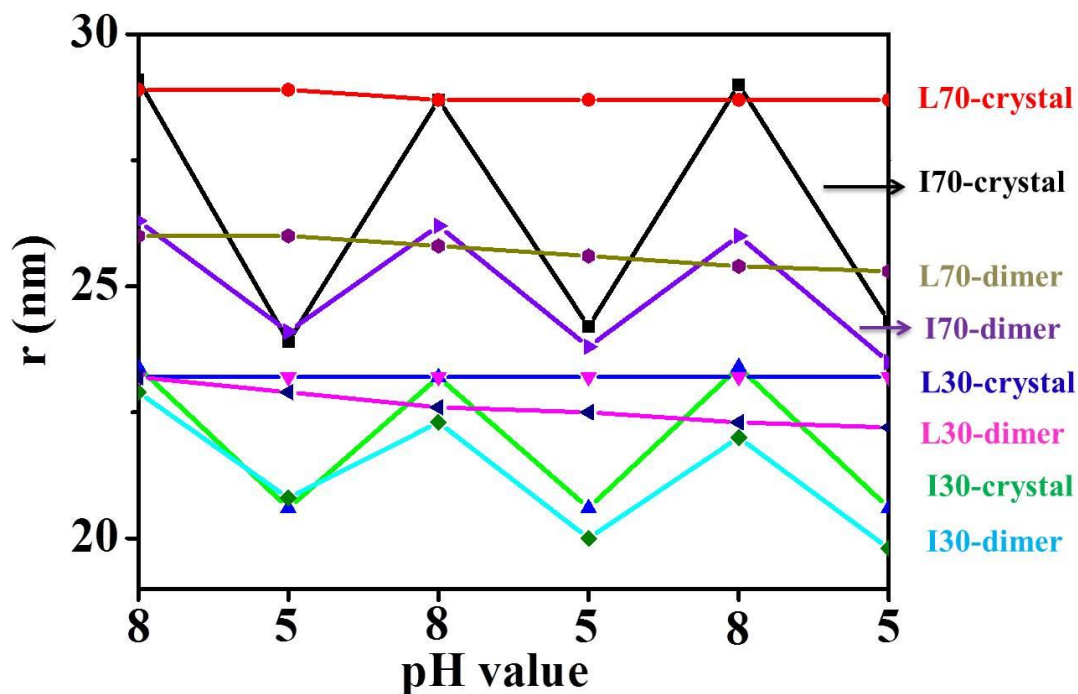


Figure 3.8 Interparticle distance in pH cycles for 3-D nanocrystalline and dimer clusters.

3.4 Conclusion

In summary, we successfully introduced the ‘i-motif’ sequence into our 3-D nano-crystalline and 2-D dimer cluster systems. By tuning the pH value of these two systems between 5.0 and 8.0, structure transformation of ‘i-motif’ can affect a larger scale of colloidal assemblies, mainly reflected in interparticle distance. We also realized the potential of this strategy for more complex DNA motifs.

3.5 Methods

DNA oligonucleotides were purchased from Integrated DNA Technologies Inc. as lyophilized powers. All thio-ended sequences were purified with HPLC, while all linker sequences were purified with standard desalting.

Sequences for the DNA (5' to 3') were:

Thio-DNA (A) on NP1: ATTGGAAGTGGATAA-(T)₁₅-C₃H₆-SH;

Thio-DNA (B) on NP2: HS-C₆H₁₂-(T)₁₅-TAACCTAACCTTCAT;

Thio-DNA (N) on NP1 when preparing dimer clusters: ATTGGATTGGAAGTA-(T)₁₅-C₃H₆-SH

Linker DNA 'i-motif': TTATCCACTTCCAATTTTTTCCCATTCCCATTCCCATTCCCTT
TTTATGAAGGTTAGGTTA;

Linker DNA L30:

TTATCCACTTCCAATTTTTTTTTTTTTTTTTTTTTTTTTTTTTTTTTTTTATGAAGGTTACCTTA;

Linker DNA with two 'i-motif':

TTATCCACTTCCAATTTTCCCTAACCCCTAACCCCTAACCCCTTTTCATGTGTCGATGCTTT
TCCCTAACCCCTAACCCCTAACCCCTTTTATGAAGGTTAGGTTA;

Linker DNA L70:

TTATCCACTTCCAATTTTTTTTTTTTTTTTTTTTTTTTTTTTTTTTTTTTCATGTGTCGATGCTTTTT
TTTTTTTTTTTTTTTTTTTTTTTTTTTTTTTTTTTATGAAGGTTAGGTTA;

Complementary sequence with DNA in the middle of L70 and two 'i-motif' sequence:

AGCATCGACACATGA;

Biotin-DNA N' on Magnetic beads: CTTGTGTCTACTTCCAATCCAATTTTTTTTTTTTT
TTTT-Biotin

Fuel DNA (N'') for releasing dimer clusters: ATTGGATTGGAAGTAGACACAAG;

Small Angle X-ray Scattering was performed at beamline X-9 at National Synchrotron Light Source in Brookhaven National Laboratory. Samples containing aggregation was first injected into a glass capillary which can be placed inside a home-made holder with a small hole for hitting of X-ray beam. 2D rings could be directly obtained from the CCD behind the sample holder.

Chapter 4

Light Harvesting Nanoparticle Core-Shell Clusters with Controllable Optical Output

Abstract

We used DNA self-assembly methods to fabricate a series of core-shell gold nanoparticle-DNA-colloidal quantum dot (AuNP-DNA-Qdot) nanoclusters with satellite-like architecture to modulate optical (photoluminescence) response. By varying the inter-component distance through the DNA linker length designs we demonstrate precise tuning of the plasmon-exciton interaction and as such of the optical behavior of the nanoclusters from regimes characterized by photoluminescence quenching to photoluminescence enhancement. The combination of detailed x-ray scattering and photoluminescence lifetime studies revealed the dependence of the optical output of the cluster structure. Compared to conventional light harvesting systems like conjugated polymers and multichromophoric dendrimers, the proposed nanoclusters bring in enhanced flexibility in controlling the optical behavior towards a desired application, and can be regarded as controllable optical switches *via* the optically pumped color.

4.1 Introduction

Rational design and assembly of colloidal metal and inorganic nanoparticles has stimulated intense research efforts in the past years, especially from the perspective of obtaining nanoclusters with novel optical properties or even with tunable optical response.^{51,75-78} When components like gold nanoparticles and colloidal quantum dots are spaced apart sufficiently so that they do not exchange carriers, the interaction between such nanoparticles is primarily of

Coulomb (dipole-dipole) type in the form of energy transfer, specifically photoluminescence quenching by the metal nanoparticle and electromagnetic enhancement, usually seen as an increase in the emitted photoluminescence of the quantum dots^{51,76,77,79-82}. This so-called plasmon-exciton interaction is determined by several factors, including the type, shape and size of the metal nanoparticles, the electronic properties of the quantum dots, the intercomponent (separation) distance and the nature of the environment between components. Therefore, it is expected that by tuning one or more of such variables in a controlled way one can achieve control and regulation of the optical output from such metal nanoparticle-quantum dot nanostructures.

In this chapter we demonstrate the use of DNA-driven assembly methods for the fabrication of nanoclusters with controllable optical outputs. DNA-based approaches are versatile for creating precisely self-assembled organizations of nanoparticles^{44,83-85}, which is advantageous for fabrication of optically active materials^{78,86-91}. We propose to assemble core/shell gold nanoparticle (AuNP)/quantum dot (Qdot) nanoclusters with satellite-like architecture, as depicted in Fig. 4.1a, where a large (50 nm size) AuNP functions as the core and several CdSe:ZnS quantum dots (Qdots) linked by DNA constitute the shell. DNA was utilized for assembly of both homo- and hetero-nanoclusters (e.g. like the case of AuNPs and Qdots)^{44,51,53,84,92-96} where the positioning of nanocomponents could be regulated with subnanometer (single base-pair) precision. Such architectures mimic the structure of photosynthetic light harvesting complexes. Apart from the assembly role, DNA provides a structural integrity to an assembled nanocluster because hybridized DNA strands behave as a rigid rod at short distances up to 50 nm, a spatial range relevant for the study of plasmon-exciton interactions. We focus on core-shell nanoclusters incorporating rather large (50 nm sized) AuNPs for two particular reasons. First, such AuNPs

can provide electromagnetic enhancement capable to overwhelm the photoluminescence quenching of Qdots by energy transfer to the metal NP when appropriate intercomponent distances are in place (see below). As such, the proposed nanoclusters can be designed to exhibit plasmon-assisted optical regimes in the form of both enhanced and quenched photoluminescence. Second, a large AuNP core offers a relatively large surface on which several Qdots (here 20 on average in our assembly) can be connected *via* DNA linkers of similar length on a single AuNP. As such, the proposed core/shell structure not only represents a model system for the investigation of the distance-dependent plasmon-exciton interaction in the case of AuNP and Qdots but also a plasmon-assisted light harvesting system where Qdots located in the shell harvest the light and transfer it to a “reaction center” represented here by the AuNP core.

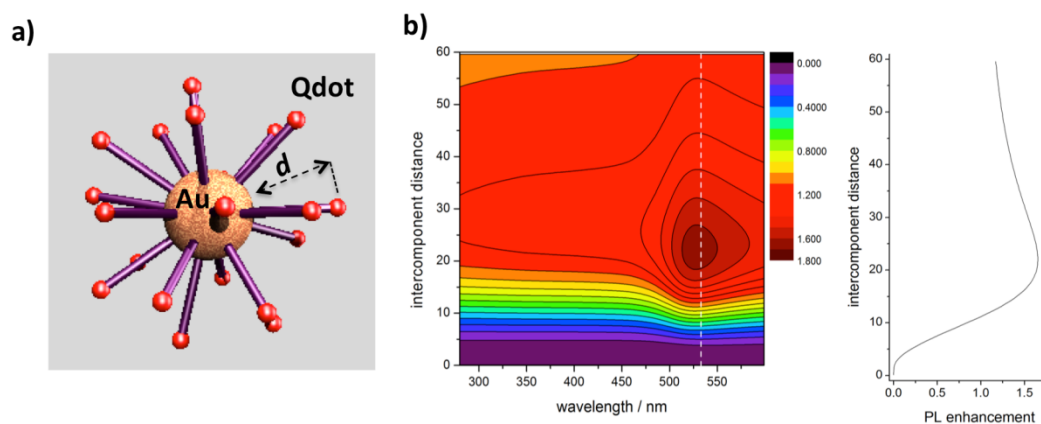


Figure 4.1 a) A core-shell AuNP-Qdot nanocluster with satellite-like architecture in which a core AuNP and several CdSe/ZnS Qdots are linked by DNA (purple). b) Predicted photoluminescence enhancement for a coupled AuNP-point dipole system as a function of AuNP-dipole separation distance, and of optical pumping (excitation) wavelength calculated for a 50 nm size AuNP and a point dipole emitting at 605 nm in air. Calculations adapted from^{1,2}.

Also shown (left) is the predicted PL enhancement for optical pumping at surface plasmon resonance (@530 nm).

The chapter is organized as follows: we first describe the proposed design, the self-assembly procedure and the structural characterization of the AuNP/Qdot core/shell nanoclusters, then demonstrate control (tenability) of the optical signal (photoluminescence, PL) for the nanoclusters, from regimes of PL quenching to PL enhancement, by varying the length of the DNA linker connecting the heterocomponents, and, finally, discuss the origin of plasmon enhanced PL in these cluster architectures.

4.2 Nanocluster design and fabrication via self-assembly

A metal nanoparticle nearby a fluorescent molecule and under light illumination can enhance the excitation rate of the molecule by local field enhancement, it can lower the quantum yield by introducing additional non-radiative channels such as energy transfer, in particular at short metal NP-molecule separation distances, or it can increase the emission rate of the molecule by coupling plasmons and excitons at resonance^{1,2,76}. In the assumption that a Qdot can be approximated with a single point dipole, the electromagnetic field distribution for a coupled metal nanoparticle-dipole system can be calculated using the multiple-multipole method^{1,2}. The predicted PL enhancement for a coupled AuNP-dipole system with the AuNP having 50 nm size and the dipole emitting at 605 nm and with both components residing in air is shown in Fig.4.1b-c. Such coupled hetero-system is expected to exhibit strong PL quenching at separation distances below 20 nm and for any given optical pumping wavelength, and PL enhancement for optical pumping at surface plasmon resonance (SPR) and for separation distances in the 20-45nm range.

Based on the theoretical calculation from Fig.4.1b, we designed a series of core/shell nanoclusters (NC) with intercomponent separation distances (d) ranging from $d \sim 15$ nm to $d \sim 47$ nm (Fig.4.2, left panel, black dots, cluster systems NC1- NC7). Here interparticle separation distances are defined as AuNP-Qdot surface-to-surface distances.

To populate a large range of separation distances for the proposed core/shell nanoclusters, we used three different molecular designs to build the interconnecting DNA linkers. An estimate of AuNP-Qdot surface-to-surface separation distance for each case follows after the assembly description. In the first design, for short separation distances (Fig.4.2a, samples NC1, NC2, NC3), we utilized a direct hybridization of single stranded (ss) DNA attached to both AuNP and Qdot, with ssDNA possessing a 15 base complementary region at the end opposite to the point of attachment to the nanoparticle. For NC1 we used a 30 base ssDNA connecting to each nanoparticle type (Fig.4.2a, $N_{\text{AuNP}} = N_{\text{Qdot}} = 30$), for NC2 we used a 95 base ssDNA for AuNP and a 30 bases ssDNA on Qdot (Fig.4.2a, $N_{\text{AuNP}} = 95$, $N_{\text{Qdot}} = 30$) and for NC3 we used 95 base ssDNA for both types of nanoparticles (Fig.4.2a, $N_{\text{AuNP}} = N_{\text{Qdot}} = 95$). As discussed below, the direct hybridization approach provides separation distances of ~ 15 nm (NC1), ~ 24 nm (NC2) and ~ 36 nm (NC3) (Figure 4.2, left). In the second design, in order to achieve further increase in separation distance, we introduced an additional 18 base-pair dsDNA segment in the linker attached to the AuNP in NC3 (Figure 4.2a) to obtain NC4 (Fig. 4.2b, $N_{\text{AuNP}} = N_{\text{Qdot}} = 95$) with a separation distance now increased to about 40 nm (see discussion below). From NC4 to NC5, the separation distance was further increased to 42 nm by the introduction of an additional 15 base-pair dsDNA segment on the Qdot linker, now having three dsDNA segments on the entire linker connecting the AuNP and Qdots (Fig.4.2c). In the third design, we used a linker-mediated hybridization: AuNP and Qdots were functionalized with non-complementary ssDNA strands,

each of 95 bases, and nanoparticles were connected by a third ssDNA linker (Fig.4.3d, L), with the linker designed with 15 bases complementarity at each end with the strands on the nanoparticles (Fig.4.2d). For NC6 we used a 30 bases linker and for NC7 a 60 bases linker to achieve separation distances of 44 nm and 47 nm, respectively. AuNP and Qdots were mixed with at the ratio of 1:20 and aged for 2-3 hours before the measurements. For systems NC4 and NC5, AuNPs and Qdots were each incubated separately with the DNA linker at a 1:10000 molar ratio of nanoparticle:DNA and for about 1h and the final solutions were mixed. For systems NC6 and NC7, L₃₀ or L₆₀ was first incubated with AuNP for 1h and the resulting solution was further mixed with Qdots.

4.3 Estimation of interparticle distances

Dynamic light scattering (DLS) was used to measure the size of commercial carboxyl-functionalized CdSe/ZnS Qdots with 605 nm photoluminescence emission peak (Qdot605) and provided a hydrodynamic diameter of ≈ 14 nm. A Qdot605 is composed of a CdSe core (≈ 4 nm)^{97,98}, a ZnS shell ($\approx 1.5-2$ nm), and a carboxyl functionalized polymer outer shell, which according to the DLS data is about 2.5-3 nm thick. We then employed a DNA model reported previously by our group^{99,100} to estimate AuNP-Qdot surface-to-surface separation distances for the seven cluster systems. In our approach, we used a Daoud-Cotton (DC) blob model to calculate the thickness of tethered DNA on the particle surface and adopted a worm-like chain (WLC) model to estimate the length of the linker between particles (see Supporting Material for details on calculations). The estimated distances based on the DNA model are plotted in Fig. 4.2, left, (square and line), and the derived AuNP-Qdot surface-to-center distances are 15.3 nm (NC1), 24.3 nm (NC2), 36.0 nm (NC3), 39.5 nm (NC4), 41.8 nm (NC5), 44.2 nm (NC6) and 47 nm (NC7).

We used synchrotron-based SAXS measurements at the beamline X9 at the National Synchrotron Light Source at Brookhaven (Fig.4.2, left, dots and dash) to obtain the detailed information about interparticle separations. In order to obtain sufficient scattering signal, we replaced the Qdots in each of the seven cluster systems with AuNPs of similar diameter (10 nm gold core), thus obtaining core-shell nanoclusters assembled from gold nanoparticles of two different sizes. These homo-nanoclusters of 50 nm AuNP/10 nm AuNP were assembled following an identical recipe as for AuNP-DNA-Qdot nanoclusters, including linker design and assembly procedures, and the corresponding samples are labeled as NC1' through NC7'. We first obtained the 50 nm Au-10 nm Au surface-to-center distance, and then, after substituting 10 nm Au with Qdot, we estimated the AuNP-Qdot surface-to-center distance as 15.1 nm (NC1), 24.1 nm (NC2), 33.2 nm (NC3), 38.1 nm (NC4), 40.0 nm (NC5), 42.9 nm (NC6) and 46.3 nm (NC7) (Fig.4.2, squares and full line). These values match closely with our calculation based on the DNA model discussed above (Fig.4.2, dots and dashed line).

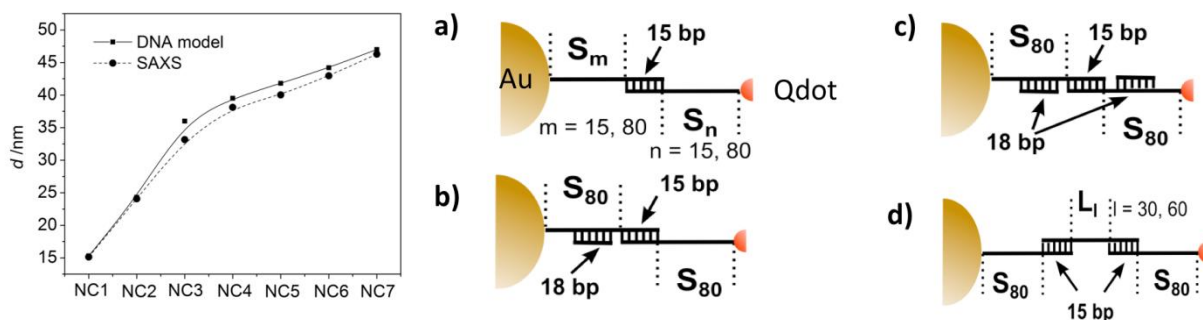


Figure 4.2 Left. AuNP-Qdot surface-to-surface intercomponent distances for a series of AuNP-DNA-Qdot core-shell nanoclusters named herein NC1 through NC7, as estimated based on DNA model (square and line) and SAXS measurements (dots and dash). Right: DNA linker designs for nanoclusters NC1, NC2, NC3 (a), NC4 (b), NC5 (c) and NC6, NC7 (d).

4.4 Distance-dependent optical response of core-shell nanoclusters

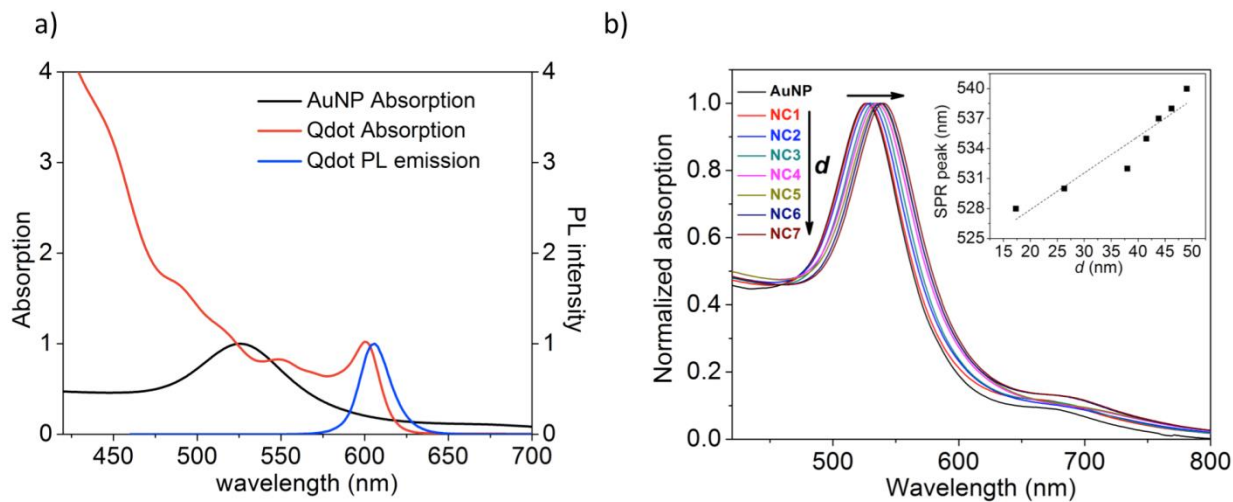


Figure 4.3 a) Optical scattering spectrum for 50 nm AuNP nanoparticles (black) and Uv-vis absorption (red) and photoluminescence (blue) spectra for CdSe/ZnS Qdots in aqueous solution. b) Optical scattering spectrum of core/shell AuNP/Qdot nanoclusters with varying DNA linker length. Inset shows the SPR peak vs DNA linker length monotonic dependency.

Fig.4.3a includes the electronic spectra of the components making up the core-shell nanoclusters, the optical scattering spectrum of the 50nm AuNPs (black color), as well as the Uv-vis absorption (red color) and PL (blue color) spectra of Qdots. The unique shape of Qdot's absorption spectrum, increasing towards higher energy, allows selective excitation of the AuNP-Qdot nanocluster outside gold's surface plasmon resonance (SPR) (for example here @440 nm) and at SPR (@530 nm) while monitoring the spectrally narrow PL emitted by the Qdot. This allows probing the distance dependency for both the nonradiative energy transfer from the photexcited Qdots to the AuNP and the plasmon-assisted PL enhancement. Accounting for changes in the optical density in the Qdot spectrum from 440nm to 530 nm, the overall PL enhancement factor (EF_{PL}) for Qdots in the presence of an AuNP can be calculated using⁵¹

$$EF_{PL} = \frac{PL(@530nm)}{PL(@440nm)} \times \frac{Abs(@440nm)}{Abs(@530nm)} \quad (1)$$

where PL represents the photoluminescence intensity signal measured from the core-shell nanocluster by alternating the optical pumping off and onto SPR resonance. Figure 4.3b are the optical scattering spectra of AuNP-Qdot core-shell nanoclusters of various intercomponent distances, and they feature a monotonic red shift of the SPR peak with increased DNA linker length (Fig.4.3b, inset). DNA's refractive index (1.76) is higher than that of water (1.33), and an increase in the DNA linker length will result in an increase of the amount of DNA as a dielectric material occupying the space between AuNP and Qdots components. Therefore, the medium between the components experiences a monotonic increase in the overall dielectric constant with the increase of the DNA linker length. Because the dielectric constant of the medium between AuNP and Qdot factors in the value of the AuNP's SPR peak, this leads to a monotonic red shift of the SPR peak with increased DNA linker length (Figure 4.3b)¹. Based on the SPR resonance we chose the optical pumping with 530 nm: the changes in the scattering profile across the seven core/shell nanoclusters are minimal at this wavelength, and so are changes in the scattering cross section (see Figure 4.3b, inset).

We probed the AuNP/Qdot nanoclusters with time-resolved confocal PL microscopy using alternate pulsed laser excitation @440 nm/530 nm by employing a time-tagged time-resolved detection mode that measured simultaneously the PL intensity and PL lifetime from photoexcited nanoclusters freely diffusing in an aqueous solution at low (picomolar) concentration.

Optical pumping off-surface plasmon resonance (@440nm). Freely diffusing Qdots (control sample) exhibit an average PL lifetime $\tau_{Qdot} = \sim 10.2$ ns. The dependency for the PL intensity and of the energy transfer rate (k_{ET}) vs DNA linker length (AuNP-Qdot separation distance) for

the seven core-shell nanoclusters following optical pumping off-SPR (440 nm) are shown in Figures 4.4a&4.4b, respectively. The energy transfer rate was calculated as

$$k_{ET} = 1/\tau_{Qdot/AuNP} - 1/\tau_{Qdot} \quad (2)$$

with τ_{Qdot} and $\tau_{Qdot/AuNP}$ PL lifetimes of Qdots (control sample) and AuNP-Qdot nanoclusters, respectively. Both dependencies, and in particular that from Figure 4b demonstrate separation distance-dependent PL quenching, here by energy transfer from photoexcited Qdots to AuNP. The strongest PL quenching (32%) was observed for the shortest DNA linker (= ~15 nm).

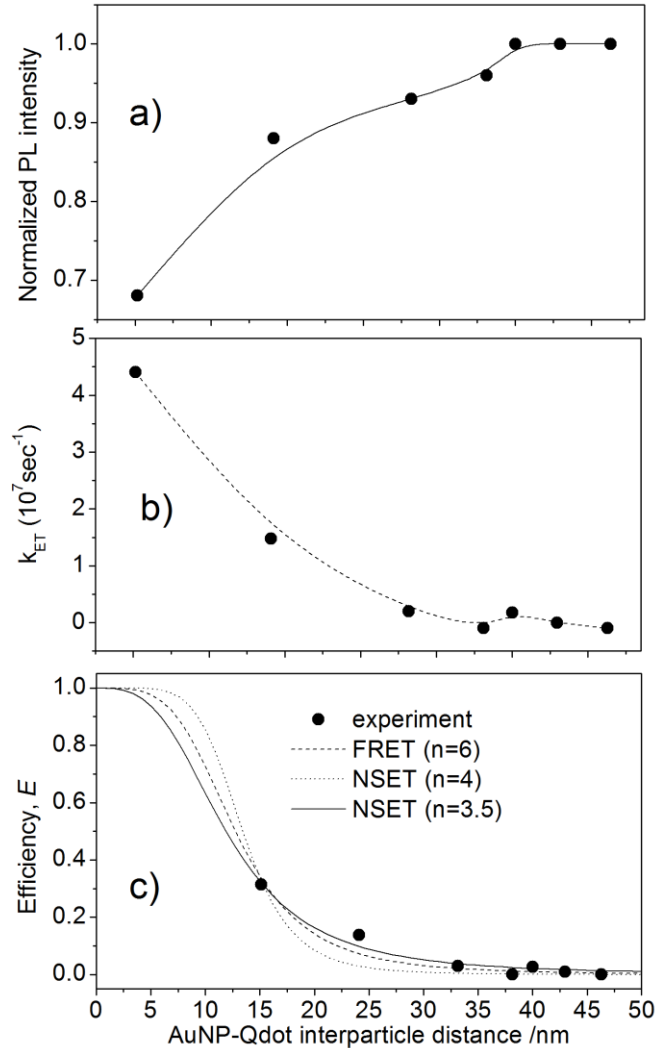


Figure 4.4 a) PL intensity vs AuNP-Qdot separation distance (dots and line). Data are normalized to the value corresponding to the longest linker where quenching is absent. b) Energy transfer rate (k_{ET}) vs AuNP-Qdot separation distance (dots and dash). (c) Energy transfer efficiency (E) vs AuNP-Qdot separation distance (dots) and fits according to various energy transfer models and eq.3: NSET model with $n=4$ (dash line) and $n=3.5$ (line) and FRET model with $n=6$ (dotted line) yielding critical distances $R_0=12.7$ nm, 12.4 nm and 13.4 nm, respectively.

Quenching of fluorescent moieties like colloidal quantum dots and organic fluorescent dyes by proximal metal nanoparticles by energy transfer has been treated analytically by using either a Foerster (FRET) formalism^{92,94,101,102} or a nanosurface energy transfer (NSET) formalism^{95,96,103}, or both¹⁰⁴. Both formalisms are described by a generic formula for the energy transfer efficiency⁹⁶

$$E = \frac{N}{N + (R/R_0)^n} \quad (3)$$

with N , number of metal nanoparticles, R_0 , critical distance where the efficiency $E = 50\%$. FRET assumes a dipole-dipole coupling mechanism between the emitting moiety (donor) and the metal nanoparticle (acceptor), and requires condition of resonance or spectral overlap between donor's emission and acceptor's absorption transitions. FRET is a popular formalism for describing dye-dye and Qdot-dye interactions with components separated at distances 2-10 nm^{105,106}. In FRET, donor-acceptor dipole-dipole interaction leads to a $1/R^6$ energy transfer efficiency vs distance dependency ($n = 6$, eq.3) with the requirement that donor and acceptor components have strong resonance coupling (spectral overlap) and proper (dipole) orientation. The NSET model considers the emitter as a point dipole transferring to an infinite metal surface, leading to a

slower, $1/R^4$ distance dependency ($n = 4$ in eq.3) and without a requirement for resonance coupling. FRET has been found to model AuNP-emitter systems with short separation distances¹⁰², while NSET was found to be more suitable for donor-acceptor pairs with larger intercomponent distances^{95,96,103,104}. Fig. 4.4d (dots) shows the energy transfer efficiency (E) vs separation distance (d) for the seven nanoclusters optically pumped at 440 nm, with the efficiency calculated from the PL lifetimes according to

$$E = 1 - \tau_{Qdot/AuNP} / \tau_{Qdot} \quad (4)$$

A fit to the data from Fig.4.4d according to eq.3 ($N = 1$) yields $n = 3.5$ (full line), close to the NSET model ($n = 4$, dashed line), far from a FRET model (dotted line), and provides a critical distance $R_{0(NSET)} = 12.4$ nm. Our nanoclusters exhibit large donor-acceptor separation distances and a rather poor spectral overlap (Qdot's PL and AuNP's SPR overlap, see Figure 4.2a), and these conditions favor the NSET model against the FRET model in treating the quenching of Qdots PL by AuNP by energy transfer. According to the data in Figs.4.4c&d, energy transfer extinguishes in nanoclusters NC4-NC7, that is, for separation distances around 38 nm and larger. For NSET, the critical distance R_0 is given by^{95,96,103}

$$R_{0(NSET)}^4 = 0.225 \times \frac{cn^2}{4\pi^2 \omega_F k_F} \times \phi_{Qdot} \times \lambda_{Qdot}^2 \quad (5)$$

being a function of donor quantum yield (ϕ_{Qdot}) and PL emission (λ_{Qdot}), of the Fermi frequency (ω_F) and Fermi vector (k_F) of the acceptor, of the refractive index (n) of the embedding medium and of the speed of light (c). Using $k_F = 1.2 \times 10^{10} \text{ m}^{-1}$ and $\omega_F = 8.4 \times 10^{15} \text{ s}^{-1}$ as values defined for bulk gold⁹⁵, and $n = 1.76$ for DNA as the medium filling the space between donor and acceptor and $\phi_{Qdot} \approx 0.5$, the NSET critical distance for the energy transfer from Qdots to AuNP estimated

with eq.5 is $R_{0(NSET)} \approx 10.8$ nm, a value close to that obtained from the fit of the data in Fig.4.4d assuming an NSET model (12.4 nm).

Optical pumping at surface plasmon resonance (@530nm). The PL enhancement (EF_{PL}) vs. AuNP-Qdot separation distance for the seven nanoclusters subjected to optical pumping at SPR (530nm) is shown in Fig.4.5a (dots and line). Also shown in the same graph are the PL enhancements vs. separation distance estimated for two other optical pumping wavelengths, off-SPR @440 nm (square and line) and @490 nm (triangles and line), an intermediate wavelength. At SPR (@530 nm), PL enhancement ($EF_{PL} > 1$) is observed for nanoclusters with separation distances from around 24 nm and up to 43 nm (NC2- NC6, Figure 4.2), with the highest value ($EF_{PL} = 4.3$) observed for nanocluster NC5 (donor-acceptor separation distance of 40 nm). For the shortest separation distance (NC1, 15 nm), $EF_{PL} < 1$, indicating that PL quenching by energy transfer dominates over plasmon-assisted PL enhancement. For the largest separation distance (NC7, 46 nm), $EF_{PL} = 1$, which indicates non-interacting Qdots and AuNP. As such, the designed DNA linkers connecting the donor (Qdot) and acceptor (AuNP) components provide a dynamic range for the plasmon-exciton interaction in our nanoclusters, evolving from regimes of PL quenching to PL enhancement, thus demonstrating the ability to tune the optical output (PL intensity) of an AuNP-Qdot nanocluster by DNA design and DNA self-assembly.

Theoretically, a point dipole emitting at 605 nm and coupled to a 50 nm AuNP in air experiences plasmon-assisted PL enhancement for optical pumping at SPR (530 nm) and for separation distances $d > 12$ nm (Figure 4.1b, left panel, $EF_{PL} > 1$), with a maximum EF_{PL} at $d \approx 22$ nm. Experimentally, we observed $EF_{PL} > 1$ for $d \approx 24$ nm and larger, and maximal EF_{PL} at $d \approx 40$ nm (Fig.4.5a, dots and dash). These differences between theoretical and experimental data may arise here from the theoretical treatment of the plasmon-exciton interaction with a rather simplistic

model² in which we assumed (i) the Qdot is a point dipole with a well-defined transition dipole moment, while recent single particle studies showed that Qdots do not have a well-defined transition dipole moment¹⁰⁷, (ii) the nonradiative energy transfer between Qdots and AuNP is modeled by a FRET formalism, while our nanoclusters were found experimentally to obey a NSET model (Figure 4.4d).

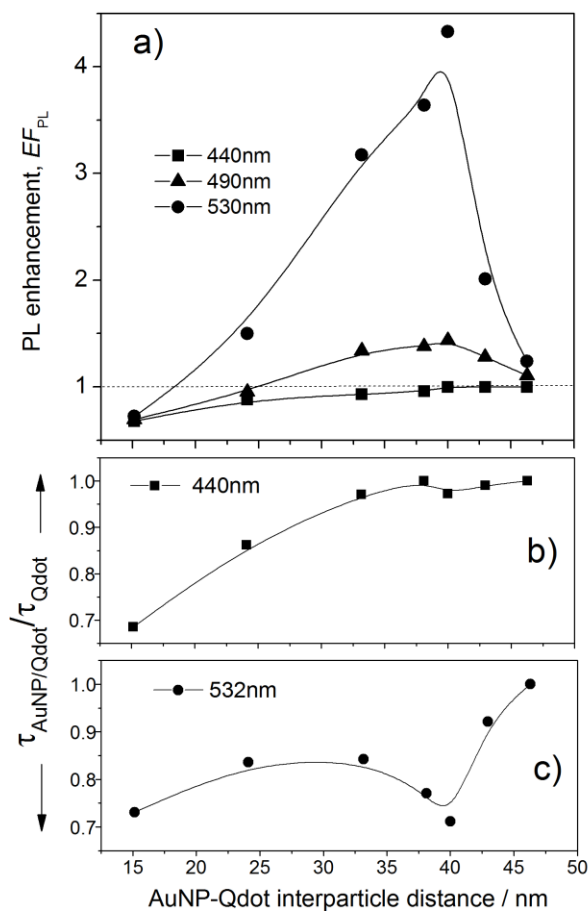


Figure 4.5 a) PL enhancement (EF_{PL}) vs separation distance (triangle and line) following optical pumping at 440 nm (square and line), 490 nm (triangle and line) and 530 nm (dots and line). b) and c) are normalized PL lifetime vs separation distance for AuNP/Qdot nanoclusters optically pumped at 440 nm and 530 nm, respectively.

Figure 4.5c shows the changes in PL lifetime with donor-acceptor separation distance for nanoclusters optically pumped at SPR (@530 nm). A clear anti-correlation is seen between the PL enhancement and PL lifetimes vs separation distance (see Figure 4.5a & 4.5c, dots and line), which could not be observed for optical pumping off-SPR (440 nm (Figure 4.5a – 4.5b, squares and lines)). The PL lifetime of a Qdot is $\tau_{Qdot} = 1/(\gamma_r + \gamma_{nr})$, with γ_r and γ_{nr} radiative and nonradiative rates, while the PL quantum yield is $\phi_{Qdot} = \gamma_r/(\gamma_r + \gamma_{nr})$. To understand the origin of the enhancement in both intensity and decay rates occurring at SPR, we can treat the PL emission from a Qdot as a two-step process that involves (i) optical excitation by the incident electrical field which can be perturbed by the local nanoenvironment and (ii) radiation emission, this later process determined by the quantum yield of the Qdot¹⁰⁸. Assuming for simplicity that excitation and emission occur at similar frequency, $\phi_{Qdot} = \gamma_{em}/\gamma_{exc}$, with γ_{em} PL emission rate and γ_{exc} excitation rate. For a coupled AuNP-Qdot system, the incident light exciting the Qdot will also excite plasmons in the AuNP that can enhance the Qdot's PL quantum yield by increasing the excitation rate, γ_{exc} , and the radiative rate, γ_r . An increase in γ_r requires coupling between Qdot's exciton and AuNP's plasmon which is accomplished by a strong spectral overlap between AuNP's surface plasmon resonance and Qdot's PL emission. In this case, an enhancement in PL intensity is accompanied by an increase in emission rate (decrease in PL lifetime)^{109,110}. Anti-correlated behavior with PL enhancement accompanied by an increase in the emission rate (decrease in PL lifetime) has been observed previously for isolated terrylene molecules interacting with large, 100 nm AuNPs and optically pumped at SPR¹⁰⁹, a behavior explained by the fact that the presence of the nearby nanoparticle alters the excitation electric field at the emitter's position, enhancing the excitation rate γ_{exc} and making both the radiative (γ_r) and nonradiative (γ_{nr}) rates strongly distance and dye (dipole) orientation dependent. In that

study the authors acknowledged the importance of the AuNP plasmon resonance in the enhancement process by performing optical pumping away from resonance to observe a decrease in PL enhancement compared to the condition of SPR resonance. Similarly, we also observed a reduction in the PL enhancement with the change in optical pumping away from SPR, e.g. from 530 nm to 490 nm, with the PL enhancement at optimal separation distance (40nm, Figure4.5a) decreasing from 4.3 ($E_{PL}(530nm) = 4.3$) to 1.44 ($E_{PL}(490nm) = 1.44$), respectively, thus reconfirming the importance of the gold plasmon resonance in enhancing the Qdot's emitted PL. A more recent study¹¹⁰ reported anti-correlated PL enhancement and PL lifetime vs separation distance for CdSe/ZnS Qdots deposited on vertically aligned Au nanorods and optically pumped at SPR. These authors claimed that the PL enhancement resulted from local enhancement of the excitation electric field due to the presence of the nanostructure which in turn enhanced γ_{exc} (absorption) and γ_r (by Purcell effect)¹¹¹. For our AuNP/Qdot nanoclusters, the surface plasmon resonance (530 – 540nm) and the Qdot PL spectrum (605nm) are rather well separated, with little overlap (Fig.4.3a) which is not expected to promote a strong plasmon-exciton resonant interaction. Consequently, most of the PL enhancement is expected to come mainly from an increase in γ_{exc} , and, most probably, that is why changes in PL lifetime from SPR to off-SPR in our case are not as large as those observed in¹⁰⁹ (20 times) and¹¹⁰ (10 times).

4.5 Conclusion

We have shown that by smart design and DNA-self recognition we can create a set of core-shell AuNP-Qdot nanoclusters where the optical output, here photoluminescence, can be controlled by optical pumping color from quenched to enhanced state, in a step-wise manner. For example, optical excitation off-surface plasmon resonance can produce a quenched PL signal with the

quenching rate (efficiency) controlled by the DNA linker length by a $1/d^4$ dependency dictated by non-radiative NSET. For the same set of nanoclusters, optical pumping at surface plasmon resonance enhances the overall PL, maximally ($>4x$) for a component separation distance $d=40$ nm. An anticorrelation between the PL intensity and PL decay rate was observed for optical pumping at surface plasmon resonance and this was attributed to an increase in both excitation and radiative rate, leading to enhanced PL intensity and decreased PL lifetime. Compared to conventional light harvesting systems like conjugated polymers and multichromophoric dendrimers, our nanoclusters bring in enhanced flexibility in controlling the optical output towards a desired application, and can be regarded as controllable optical switches *via* the optically pumped color.

4.6 Experimental Methods

AuNPs (50 nm size, Nanopartz Inc) and carboxyl-functionalized CdSe/ZnS Qdots (Invitrogen, 605nm PL peak, 10nm size including polymer coating) were functionalized with thiolated and aminated ssDNA (Integrated DNA Technologies), respectively, and purified according to literature recipes^{93,112}. We estimated, on average, about 224 strands of DNA attached per 50 nm AuNP and 10 strands per Qdot. Functionalized AuNPs and Qdots dispersed in a 50 mM borate buffer (pH = 8.5, 100 mM NaCl) were mixed at a AuNP:Qdot molar ratio of 1:20, in the presence of appropriate ssDNA linker(s) and depending on the particular sample, and let to self-assembled onto core/shell nanoclusters by annealing at room temperature for at least 3 hours, followed by several washes by centrifugation and finally buffer re-suspension, with the supernatant showing no detectable PL signal, thus indicating all Qdots have bound to AuNPs (Figure 4.6).

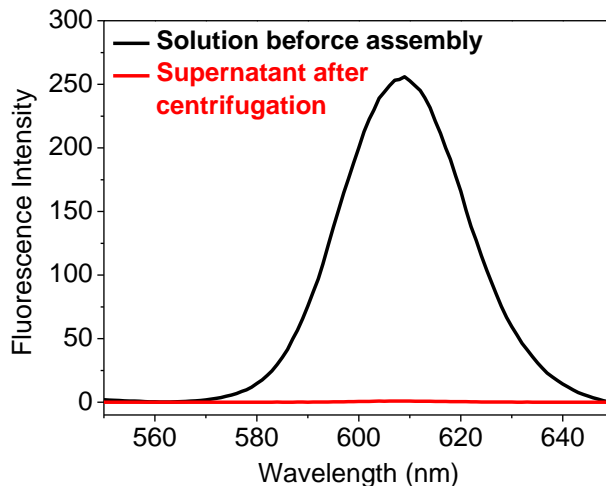


Figure 4.6 Fluorescence measurements of the nanoparticle solution before assembly and the supernatant after assembly and centrifugation.

All spectroscopic experiments reported here were performed at room temperature with both Qdots and core/shell nanoclusters in borate buffer (pH 8.5). Uv-vis and photoluminescence spectra were measured with a Perkin-Elmer Lambda 25 spectrophotometer and a Carry Varian fluorimeter, respectively.

Photoluminescence intensities and lifetimes under laser excitation were measured using an inverted confocal optical microscope equipped with a 1.4 NA, 100x oil immersion objective lens with optical excitation achieved with either a 440 nm or a 530 nm pulsed solid state laser (LDH440/530, Picoquant, GmbH) using a 10 MHz repetition rate @ 1 microW (@440nm) or 1.2 microW (@530nm) average power at sample, thus accounting for differences in photon energy for the two colors. The PL emitted by the sample was collected by the same lens, filtered by a dichroic mirror (Semrock 532DRLP), a long pass filter (Semrock 532 LP) and a 75 microns pinhole before focusing onto a single photon counting avalanche photodiode (SPAD) connected to a PicoHarp300 time analyzer utilized in time-tagged time-resolved mode. PL intensities and

lifetimes were estimated with the Symphotime (Picoquant) software, with PL lifetimes quantified as weighted average values from multi-exponential fits.

DNA used in this chapter was described as follows:

30-b thiol-ssDNA on AuNPs for direct hybridization: TACTTCCAATCCAATTTTTTTTTT
TTTTTT-SH;

30-b thiol-ssDNA on AuNPs for linker-mediated hybridization: ATTGGAAGTGGATAATTT
TTTTTTTTTT TTT-SH;

95-b thiol-ssDNA on AuNPs for direct hybridization:
TACTTCCAATCCAATTCTTGTGTCGATAGGTCGGTTGCTTTTTTTTTTTTTTTTTTTTTT
TTTTTTTTTTTTTTTTTT TTTTTTTTTTTTTTTTTT TT-SH;

30-b amino-ssDNA on Qdots for direct hybridization: ATTGGATTGGAAGTATTTTTTTTTTTT
TTTT-NH₂;

30-b amino-ssDNA on Qdots for linker-mediated hybridization: NH₂-TTTTTTTTTTTTTTTT
TAACCTAACCTTCAT;

95-b amino-ssDNA on Qdots for direct hybridization:
ATTGGATTGGAAGTATCTTGTGTCGATAGGTCGGTTGCTTTTTTTTTTTTTTTTTTTT
TTTTTTTTTTTTTTTTTTTTTTTTTTTTTTTTTTTTTT TT-NH₂;

ssDNA for partially dsDNA spacer in NC4 and NC5: AGC AAC CGA CCT ATC GAC;

ssDNA linker in CN6: TTA TCC ACT TCC AAT-(T)₃₀-ATG AAG GTT AGG TTA;

ssDNA linker in CN7: TTA TCC ACT TCC AAT-(T)₆₀-ATG AAG GTT AGG TTA.

Chapter 5

Discrete Nanocubes as Plasmonic Reporters of Molecular Chirality

Elements reprinted with permission from *Nano Letters*, 13, 3145, 2013. Copyright 2013,

American Chemical Society

Abstract

One of the most intriguing structural properties, chirality, is often exhibited by organic and bio-organic molecular constructs. Chiral spectral signatures, typically appearing in the UV range for organic materials and known as Circular Dichroism (CD), are widely used to probe a molecular stereometry. Such probing has an increasingly broad importance for biomedical and pharmacological fields due to synthesis/ separation/ detection of homochiral species, biological role of chiral organization, and structural response to environmental conditions and enantiomeric drugs. Although CD instrumentation has been progressively evolving, its core methodology is unchanged for about a century. Recently, a theory predicted that CD signal “amplification” can be achieved with detection in the visible band when chiral organic molecules are coupled with plasmonic nanostructures. Although recent experiments have confirmed the presence of the effect, no significant amplification was observed. Here we realize a novel approach for the CD enhancement using shaped nanoparticle, gold/silver core/shell nanocubes. We demonstrate a giant, about two orders of magnitude enhancement of CD signal, detected in near-visible region, from DNA molecules using nanocubes as molecular supports and plasmonic amplifiers. The discovered phenomenon opens novel opportunities in ultrasensitive probing of chiral molecules and for novel optical nanomaterials based on the chiral elements.

5.1 Introduction

Molecular chirality, a basic structural property of many organic molecules, has its origin in the tetrahedral arrangement of carbon bonds¹¹³. Chirality is also often observed in biomolecules due to the formation of secondary and tertiary structures, e.g. helices of nucleic acids and proteins¹¹⁴; such structural organization is crucial for their proper biological functionality¹¹⁵. One of the well-established methods to probe chiral properties relies on the optical signature of chiral molecules due to their different optical absorption of left and right circularly polarized light. The method, known as circular dichroism (CD) spectroscopy, is widely utilized to probe efficiency of synthetic organic reaction and concentration of enantiomers, protein folding and change of conformational states of biomolecules due physical and chemical stimuli, like radiation, temperature, pH, biochemical reactions and drug interactions^{116,117}. The breaking of circular polarization symmetry further provides a promising way for the modulation and encoding of photon polarization states in nanophotonic devices and metamaterials^{118,119}. In this respect, novel approaches for fabrication of chiral nanostructures were recently reported^{83,120}. Nevertheless, for organic molecules CD signal is typically weak, thus, significant amounts of material at relatively high concentrations are required for detectable signal, which is frequently an impediment for a practical use. Moreover, the optical transitions in organic and biological molecules are normally in the ultraviolet (UV) region (150 ~ 300 nm)^{114,116}. Possible probing of optical chirality beyond UV range (> 300 nm) is being actively sought after for a quantitative analysis and for using in pharmacology fields.

Recent advancements in molecular sensing exploit the effects related to plasmon resonances. For example, vibration spectrum of single molecules, observed using Surface Enhanced Raman Scattering (SERS), is related to the amplification of electromagnetic fields by plasmonic

nanoparticle^{121,122}. Also, plasmonic effects lead to the enhanced fluorescence emission of molecular dyes and quantum dots¹²³. Recently, it was theoretically predicted that plasmonic nanostructures under particular conditions might enhance molecular CD signals by orders of magnitude as well as echo its optical signature from UV into plasmonic band. This novel plasmon-induced CD signals far away from the molecular electronic transition may emerge from a hybrid complex, plasmonic nanoparticle–chiral molecule/s, also known as “individual chiral plasmonic nanoparticle”. In such structure, a tiny difference between left- and right-handed refractive indices (n_+ and n_-) slightly shifts the plasmon resonances, which can be detected by CD spectroscopy with a high sensitivity. This effect is analogous to the dielectric sensing by localized surface plasmon resonance¹²⁴. Such realization, if successful, can pave a road for novel biological, pharmaceutical and synthetic applications. Moreover, the observed effect provides a way to enable a chiral optical response for non-chiral plasmonic elements via their functionalization with organic molecules; such elements can be utilized in nanophotonic field. However, to date only a limited number of experimental works have manifested the surface plasmon (SP)-induced CD resonance from individual chiral plasmonic nanoparticles. Comparatively, enhanced CD resonance in the SP region, in despite of being just a few and moderate, are observed generally from the congregate systems of hybrid plasmonic nanoparticles such as dimer, cluster, and aggregates. In the current studies we report experimental scheme, previously not considered theoretically, in which chiral molecules (DNA), attached to silver nanocubes, give rise to a CD signal in silver plasmon band. We observed a giant, about two orders of magnitude, CD enhancement per molecule in the near-visible range in comparison to the DNA native CD signal in the UV region. Through the detailed investigations of single

stranded (ss) and double stranded (ds) DNAs on nanocubes and particles of other shapes we show that the effect originates in the exciton-plasmon interactions.

In the search for a much anticipated plasmonic “amplifier” of CD signal we have considered Ag, whose localized surface plasmon resonances (LSPR) and thus their interaction with light can be fine-tailored across a broad spectral range, from 300 to 1200 nm, by sculpturing nanoparticle size and shape. Recent advances in the solution-phase synthesis of Ag nanoparticles allow for the controllable formation of various shapes (spheres, cubes, octahedrons, and plates, etc) by manipulating a growth of crystalline facets via facet-capping agents (surfactants)¹²⁵⁻¹²⁷. In comparison, LSPR of Au nanoparticles, another typical plasmonic material, is limited to wavelengths longer than 500 nm due to the *d-sp* interband transitions. LSPR of Ag also enjoys a significantly lower loss¹²⁸, which leads to narrower spectral lines and a more detectable spectral fine structure.

5.2 Experimental design

In Fig. 5.1 illustrated our design strategy: we have developed method for synthesizing Au/Ag core-shell nanocube (NC) via a seed-mediated approach and attaching DNA molecules to NC. We choose single-strand and double stranded DNAs as molecular objects with inherent CD signatures in UV region as model systems to study plasmonic effects for molecular constructs with chiral sub-blocks (nucleotides) and overall chiral secondary/tertiary structure (DNA duplex) respectively.

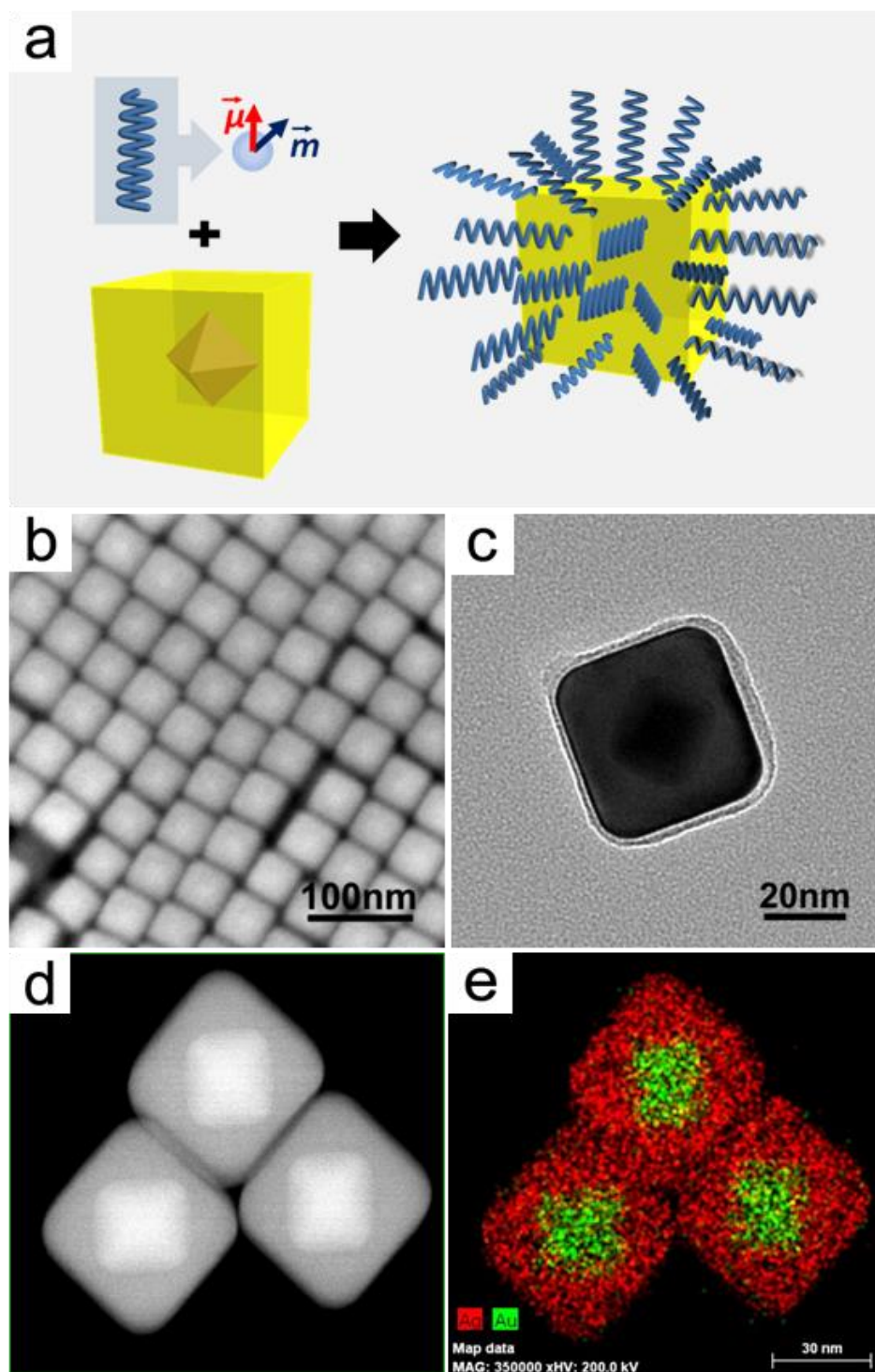


Figure 5.1 Individual plasmonic chiral nanoparticle based on silver nanocube. **a.** Structure design of “individual plasmonic chiral nanoparticle” that is based on a gold/silver (Au/Ag) core-shell nanocube (namely, Ag NC) modified with chiral molecules (e.g. DNA) on its surfaces,

theoretically expected to exhibit a plasmon-induced circular dichroism (CD) response. Structural characterizations of single-strand (ss) DNA-functionalized Ag NCs (**b-e**). **b**. Low-magnification scanning electron microscopy (SEM) and **c**. transmission electron microscopy (TEM) images show size and shape uniformity of nanocubes with edge length of 42 ± 2 nm. **d** and **e**. Scanning transmission electron microscopy (STEM) and the corresponding energy diffraction X-ray scanning (EDX) map images demonstrate the nanocube is made of an octahedral Au core embedded with thick cubic shell of Ag.

The as-synthesized nanocubes are subsequently functionalized with 30 and 50 base long thiol-modified ssDNA. Scanning electron microscopy (SEM) images of ssDNA-functionalized nanocubes (NC) indicate 42 ± 2 nm edge length of the resultant nanocubes (Fig. 5.1b, c). A high size and shape monodispersity of NC results in formation of ordered arrays (Fig. 5.1b). The DNA-functionalized nanocubes show relatively sharp profiles of edges and corners (Fig. 5.2a). The internal structure of NC with its Ag shell and ~ 20 nm Au octahedral core is revealed with transmission electron microscopy (TEM) and scanning TEM (Fig. 5.1c-d, 5.2b). The corresponding energy diffraction X-ray scanning (EDX) (Fig. 5.1e) maps further confirm that an octahedral gold core is embedded in NC, with > 8 nm thick shell of silver. Since, a thick Ag shell primarily determines Ag spectral properties of nanocube, as we show below, we refer here to it as Ag NC. The DNA-functionalized Ag NCs have a good dispersion and stability in the solution without spontaneous aggregation, as shown by dynamic light scattering (DLS) measurements (Fig.5.3).

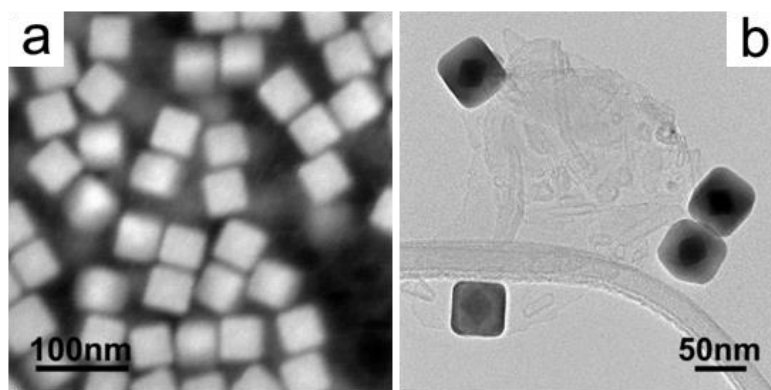


Figure 5.2 Representative electron microscope (EM) images of deposited nanocubes showing their two-dimensional projections. **a.** SEM. **b.** TEM. A gold-core octahedron is visible in the TEM image.

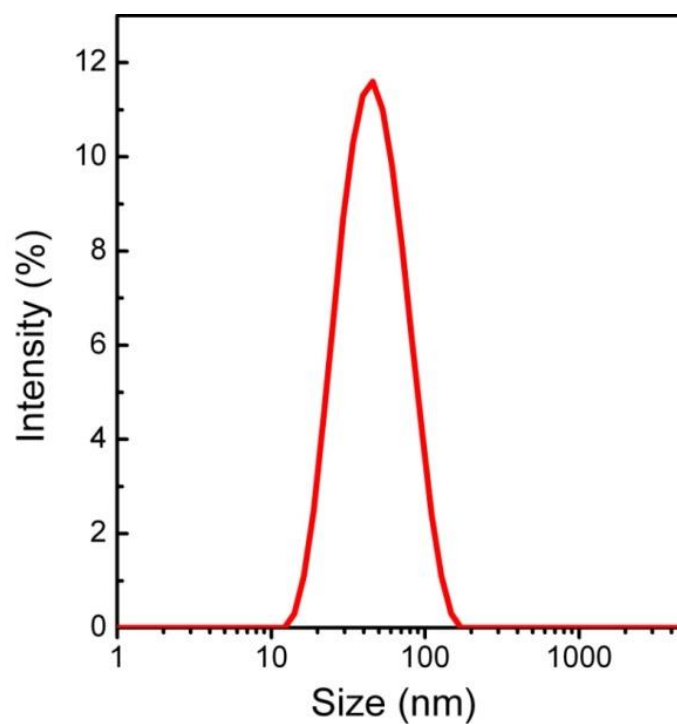


Figure 5.3 Dynamic light scattering (DLS) of ssDNA-functionalized Ag NCs.

5.3 Results and discussions

Fig. 5.4 illustrates typical intrinsic optical extinction features from two individual components of the DNA-NC complex, ssDNA and Ag NC, respectively. The ssDNA show one characteristic UV peak at 264 nm, while virgin Ag NCs, before functionalized with DNA, show three characteristic peaks, a major one at 452 nm (P1, Mode 1), and two shoulder peaks at 378 nm (P2, Mode 2) and 349 nm (P3, Mode 3). These three well-defined LSPR peaks correspond to different dipole resonance modes. The electronic transition of ssDNA is clearly off the SP resonance frequency of Ag NCs. Our CD measurements (using Jasco J-815 instrument) were then performed for three solutions containing only virgin Ag NCs of 0.18 nM, and only ssDNA of two different concentrations, 0.1 μM and 20 μM , respectively. No CD signal is observed from the virgin Ag NCs without DNA functionalization, which is expected for these non-chiral metal nanoparticles (Fig. 5.4b₁). On the other hand, due to the sensitivity limitation of the instrument, a natural chirality from trace amount of ssDNA at 0.1 μM concentration is not observable in their CD spectrum (Fig. 5.4b₂). Observable CD signal from chiral ssDNA requires a significantly larger concentration. Accordingly, as shown in Fig. 5.4b₃, a specimen with a two-hundred fold concentration of ssDNA (20 μM) exhibits the characteristic bisignated CD peaks with maxima at 249 and 275nm, respectively, which falls into the UV region (100~300 nm) and far from the typical plasmon resonance region of the Au and Ag nanoparticles (300 nm~800 nm)¹¹⁴. Recent theoretical work predicted that, CD resonance features, either additional CD signal in plasmonic region or a strong plasmon-induced enhancement, will be activated from the molecule-nanoparticle complex wherein a non-chiral plasmonic nanoparticle is surrounded by chiral molecules¹²⁹⁻¹³¹.

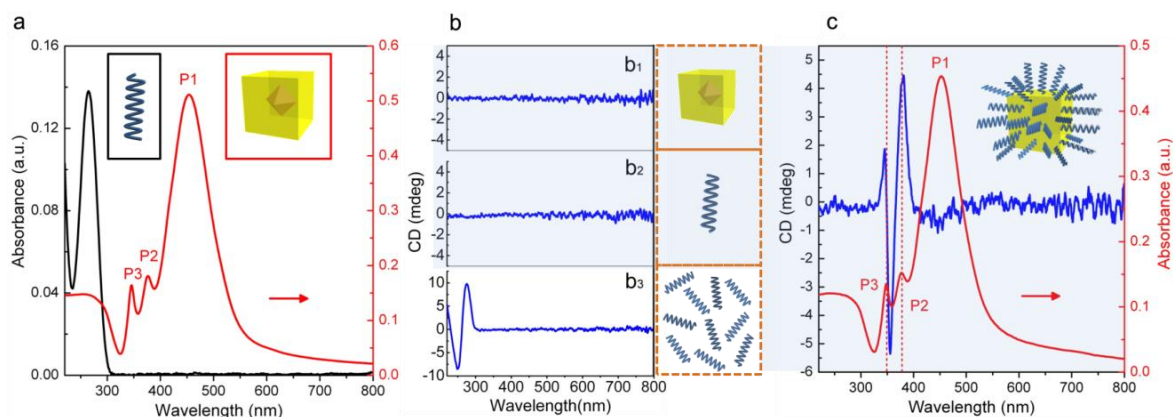


Figure 5.4 Optical response of chiral ssDNA, non-chiral Ag NCs, and plasmonic chiral DNA-functionalized Ag NCs. **a.** UV-vis absorption spectra taken from two individual components of ssDNA-functionalized Ag NCs, ssDNA (illustration in a black frame) and virgin Ag NC (illustration in a red frame) respectively. The ssDNA strands (black curve) show one characteristic UV peak at 264nm and the virgin silver nanocubes (red curve) show three characteristic peaks at 452nm (P1), 378nm (P2), and 349nm (P3), respectively. **b.** The CD spectra were recorded from the virgin Ag NCs of 0.18nM (**b₁**), ssDNA of 0.1 μM (**b₂**) and 20 μM (**b₃**). No CD signal in **b₁** is observed from the virgin non-chiral Ag NCs without DNA modification (framed illustration beside **b₁**). Due to the detector resolution limitation of instrument, natural chirality from little amount of DNA at 0.1 μM concentration (framed illustration beside **b₂**) cannot be presented in the CD spectrum of **b₂**. Observable CD signal from chiral ssDNA requires much more strands (framed illustration beside **b₃**). A thick specimen of ssDNA (20 μM) exhibits the characteristic bisignated CD peaks with maxima at 249 and 275nm, respectively, in the spectrum of **b₃**. **c.** UV-vis absorption and CD spectra of ssDNA-functionalized Ag NCs. The Ag NCs functionalized with ssDNA (red curve) show similar absorption features as the virgin ones do (red curve in **b₁**). However, the CD spectrum recorded from 0.18nM NCs in 10mM phosphate buffer (PB) (blue curve) exhibits novel features different

from the spectral plateau of virgin Ag NCs: two positive cotton effects are observed at 345nm and 378nm, respectively, together with a negative cotton effect at 355nm; the positive peak at 378nm and another negative-cotton-effect-induced split peak centered at 350nm are well corresponding to two plasmonic resonance peaks of Ag NCs (P2 and P3). An enhancement factor (A_{CD}) of 85~103 is achieved from the ssDNA of 0.088~0.106 μ M that are grafted onto the Ag NCs of 0.18nM due to the plasmon-induced CD resonance mechanism.

While there are a range of methods to attach DNA to gold and CdSe nanoparticles^{44,53,93,132,133}, the functionalization of Ag nanoparticles with DNA has proven a challenge owing to inherent lower binding energy of thiols to Ag^{134,135} and due to the blocking of Ag surface by surfactants typically used for nanoparticle synthesis. In particular, for Ag NCs, the main difficulty to realize DNA functionalization is a strong affinity of facet-capping surfactants, such as poly(vinylpyrrolidone) (PVP), required for synthesis¹²⁵⁻¹²⁷. That is, the stubborn surfactant layer usually obstructs DNA from penetrating through and anchoring to particle surfaces in the functionalization process. Herein, we developed a seed-mediated method to synthesize monodisperse Ag NCs with cetylpyridinium chloride (CPC) as shape-controlling surfactant, which is known from our previous work to be easily removable¹³⁶. Effective DNA functionalization of Ag NCs has been achieved through a combination of particle purification and incubation with DNA. The DNA-NC complexes in a low ionic-strength solution (e.g., 10 mM phosphate buffer) might have dandelion-like morphologies wherein electrostatic repulsive DNAs will tend arranging radially around cube (a scheme in Fig. 5.4c) as known for charged polymer brushes¹³⁷. Both DNA-functionalized and virgin Ag NCs have similar absorption profiles, as shown in Fig. 5.4c and Fig.5.4 respectively.

Remarkably, the ssDNA-functionalized NCs exhibit novel CD features (Fig. 5.4c) with resonance bands falling into Ag plasmon region (> 300 nm), which is different from the spectral CD plateau that virgin silver nanocubes at same concentration display. Two positive Cotton effects are observed at 345 nm and 378 nm, respectively, together with a negative Cotton effect at 355 nm, being different from the CD spectra of both pure DNA and virgin NC. The positive signal at 378nm and another negative-Cotton-effect-induced split peak centered at 350 nm are well corresponding to two of the absorption bands of Ag NCs (Modes 2 and 3), which results from the theoretically predicted plasmon-induced CD response. At the same time, no Cotton effect around 240~280 nm, where ssDNA has a native CD signature, was observed from DNA-functionalized NCs, which is due to a low amount of DNA in the solution, i.e. below our detection limit.

Indeed, an estimated surface area of all NCs in the 0.18 nM solution contains about 0.088~0.106 μM of 30 base ssDNA molecules, which is beyond the sensitivity level of conventional detection using our modern CD instrument. Intriguingly, a strong CD signal, up to 4.46 mdeg, at 378 nm indicates a significant enhancement of the optical response of chiral molecular structures. Considering the detected CD intensity (9.74 mdeg) of free ssDNA at 275 nm from a solution of

20 μM (Fig. 5.4b₃), an average CD enhancement factor, defined as $A_{CD} = \frac{CD(\lambda_{plasmon})}{CD_0(\lambda_{UV})}$, was

estimated from multiple measurements and experimental batches as 85~103. Here, $CD_0(\lambda_{UV})$

and $CD(\lambda_{plasmon})$ are the CD signals of freely dispersed molecules and molecule-NC complexes

respectively, as taken at the corresponding wavelengths of molecule electronic transition λ_{UV} and

plasmonic resonance $\lambda_{plasmon}$. This remarkable “amplification” of the native DNA CD signal via

plasmon-induced CD resonance phenomenon strongly depends on the composition and geometry

of nanoparticles supporting chiral molecules. Our experiments show (Table 1) that other DNA-metal complexes including Au nanospheres, nanocubes, nano-octahedron fail to exhibit the detectable CD signal (Fig.5.5a-f), while small-sized Ag nanospheres (Fig.5.5) show only few time enhancements, comparable with other previous reports^{130,138,139}. The evident plasmon-induced CD response was also observed from the Ag NCs functionalized with 50 base ssDNA (Fig.5.5g).

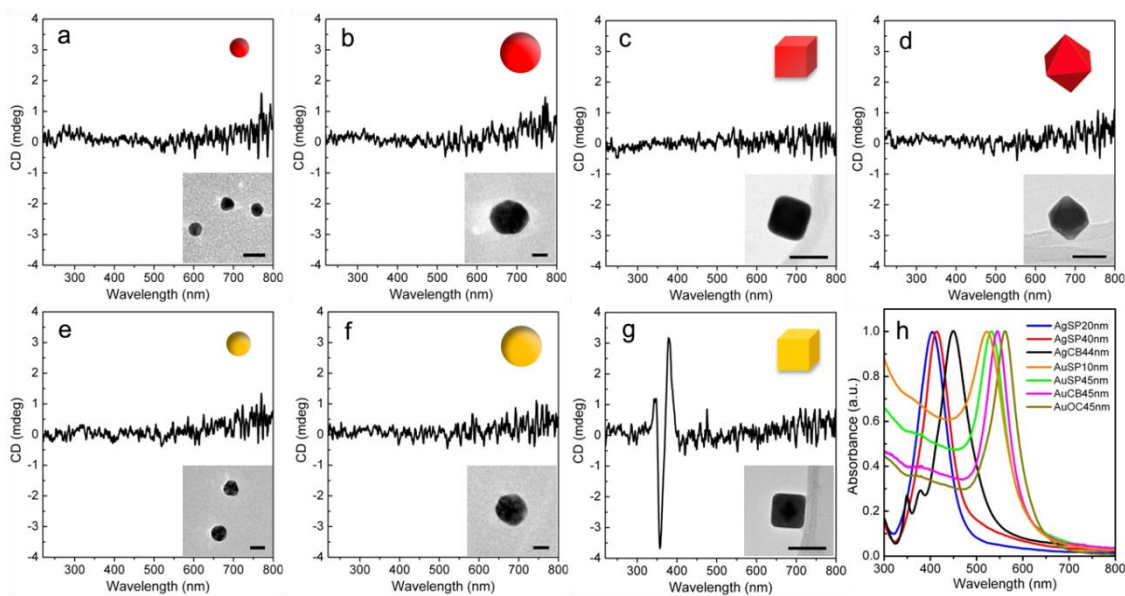


Figure 5.5 a-f. CD spectra, the representative TEM images and corresponding shape illustrations of 30ssDNA-functionalized nanoparticles: **a.** Au nano-spheres of 10nm in diameter (2nM); **b.** Au nano-spheres of 45nm in diameter (0.2nM); **c.** Au nano-cubes with edge length 45nm (0.2nM); **d.** Au nano-octahedra of 45nm in edge length (0.2nM); **e.** Ag nano-spheres of 20nm in diameter (1nM); **f.** Ag nano-spheres of 40nm in diameter (0.2nM). **g.** CD spectra, the representative TEM image and shape illustration of 50ssDNA-functionalized Ag NC with edge length 42nm (0.18nM). The corresponding CD signal is weaker than observed from 30ssDNA-functionalized Ag nanocubes, which is attributed to the lower coverage of NC with longer-chain DNAs. **h.** The

normalized UV-vis absorption spectra of nanoparticles shown in **a-g**. Scale bars in the insets of **a, b, e, and f**: 20nm. Scale bars in the insets of **c, d, and g**: 50nm.

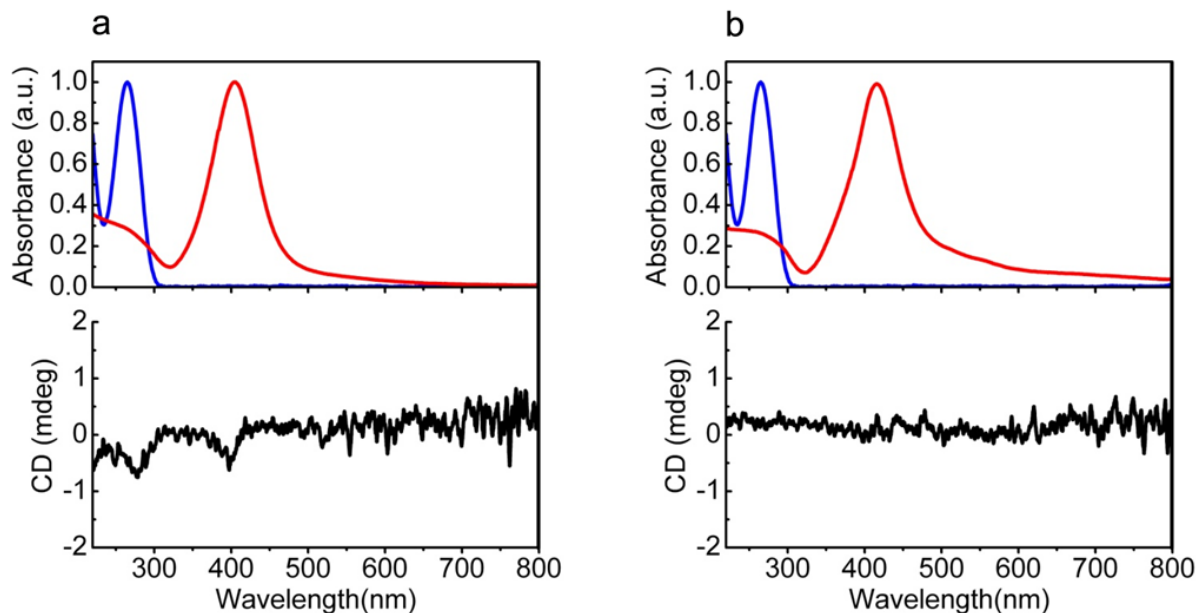


Figure 5.6 a. (Upper) Normalized UV-Vis absorption spectra of 30ss-DNA (blue curve) and the 20nm Ag nanoparticles functionalized with 30ss-DNA (red curve). The 30ss-DNA shows the characteristic UV peak at 264nm and the 20nm Ag nanoparticles functionalized with 30ss-DNA show a surface plasmon resonance (SPR) peak at 404nm in the visible range, respectively. (Lower) CD spectrum of 20nm Ag nanoparticles functionalized with 0.78 μM of 30ss-DNA (3.4nM of spheres) displays one negative peak at 277nm in the UV range and the other at 398nm in the visible range. An enhancement factor (A_{CD}) of 1.6 is estimated. **b.** (Upper) Normalized UV-Vis absorption spectra of 30ss-DNA (blue curve) and the 40nm Ag nanoparticles functionalized with 0.196 μM of 30ss-DNA (0.4nM of spheres) (red curve). The 30ss-DNA functionalized 40nm Ag nanoparticles show a SPR peak at 415nm in the UV-Vis spectrum (red curve, upper), but no signal in the CD spectrum (black curve, lower) is observed.

Recent theoretical studies predicted a strong dependence of the plasmon-induced CD signal in the plasmon range on the degree of ordering of chiral molecules on the surface of a nanocrystal¹²⁹⁻¹³¹. Importantly, molecules, randomly-oriented to the plasmonic surface, may not be able to induce strong plasmonic CD. Besides, the strongest plasmonic CD appears typically for molecular dipoles perpendicular to a nanoparticle surface, when the strongest exciton-plasmon interaction is experienced. In our case, by varying a solution ionic strength the alignment of ssDNAs on cube surfaces can be changed. As illustrated on a scheme in Fig. 5.7a, DNAs on cube surface are reasonably aligned perpendicular to a surface at low/no salt conditions because of electrostatic repulsion of neighboring backbone units within the polyelectrolyte chain and between chains^{137,140}. A salt increase reduces a persistence of ssDNA length, due to the electrostatic screening, thus leading to a deterioration of chains alignment and more pronounced coiling, which, in turn, affects the orientation of chiral nucleotides. Our measurements, Fig. 5.7b and 5.7c, actually show that plasmon-induced CD signal of DNA-functionalized nanocubes fades down gradually when salt added: the CD peak intensity at 378nm decreases from 4.4 mdeg down to 0.2 mdeg with the corresponding ionic strength increase from 0 (deionized water) to 0.16 M (0.1 M phosphate buffer saline). At the same, no change in the spectral position of CD signal is observed. As a reference, pure DNA solution shows no obvious decline in CD signal with a salt concentration increase (Fig. 5.7c); that is due to the averaging of CD signal from randomly oriented nucleotides, which are located either on different freely dispersed ssDNA molecules or within single coiled ssDNA.

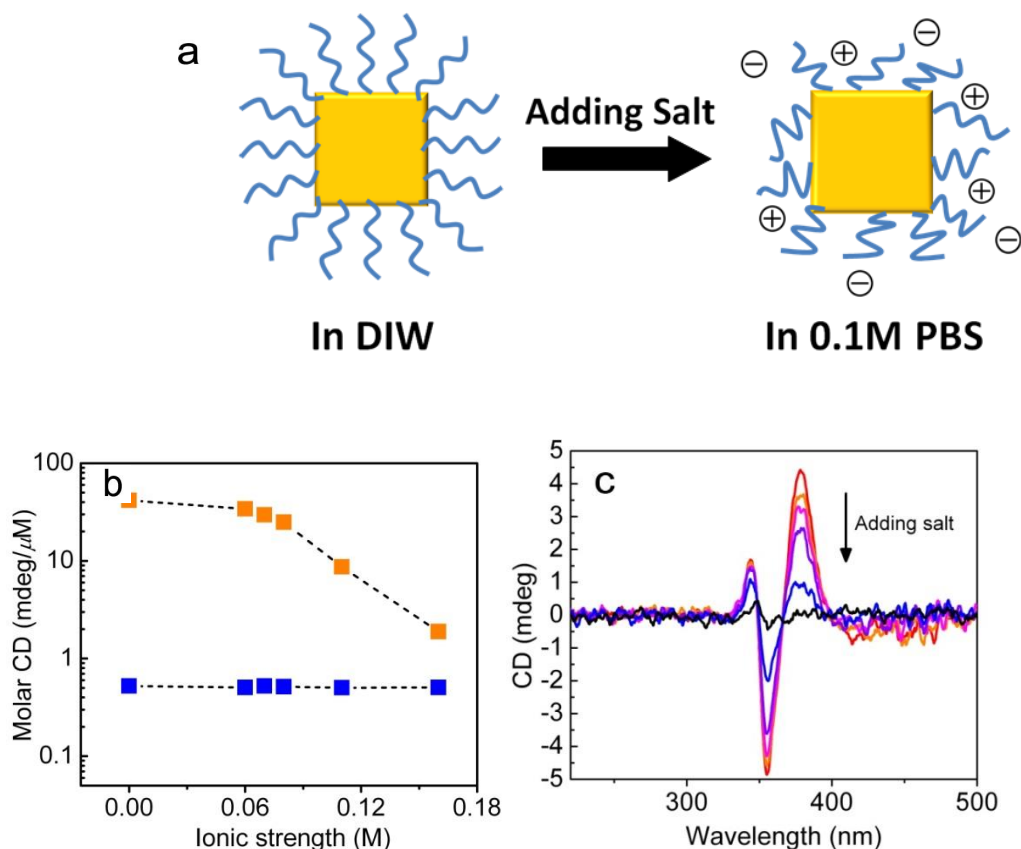


Figure 5.7 Spectral dependence of circular dichroism on salt concentration. **a.** Scheme illustrating an evolution of ssDNA alignment status on a cube surface after adding salt. **b.** salt-dependent CD spectra evolution of ssDNA-functionalized Ag NCs with the ionic strength increasing from 0 (deionized water, DIW) to 0.06 (10mM PB), 0.07, 0.08, 0.11, and 0.16M (0.1M phosphate buffer saline, PBS) in the order indicated by black arrow. **c.** Comparison of the CD spectral dependence on Na^+ concentration between ssDNA-functionalized Ag NCs (orange-squares-dash) and pure ssDNA system (blue-square-dash). CD signal intensity monitored at 378nm is normalized by the associated DNA concentration, $0.106\mu\text{M}$ for orange-squares-dash plots and $20\mu\text{M}$ for blue-squares-dash plots, respectively. With the ionic strength increase, plasmon-induced CD signal of nanocubes fades down gradually whereas no obvious decline in

CD signal is observed from pure ssDNA system, which reveals different CD resonance origin from two systems.

The rigidity of flexible ssDNA drastically increases after hybridization with complementary-strand due to the formation of a double helix in which nucleotides are aligned. Such process, with about 50 times persistence length increase, might restore a DNA orientation on a cube surface for plasmon-enhancement favoring alignment (Fig. 5.8a). Indeed, our results demonstrate that CD signal for ssDNA-functionalized nanocubes becomes undetectable at the ionic strength of 0.16 M. Nevertheless, upon the hybridization with complementary strand CD signal of dsDNA-functionalized nanocubes rises to the well-detectable magnitude of 2.1 mdeg at 376 nm (Fig 5.8b). Besides, in contrast to ssDNA, no significant decline in the magnitude of CD signal for dsDNA-NC complex was observed with a NaCl concentration increase, which is due a high rigidity and stability of dsDNA at those salt concentrations. This observation also supports the discussed mechanism of reduction of CD signal for ssDNA due to the lost of surface alignment. Such high sensitivity of the plasmon-induced CD response to molecular orientation can be further used in the future applications for probing the alignment of chiral molecules at the surfaces and changes in their configurations.

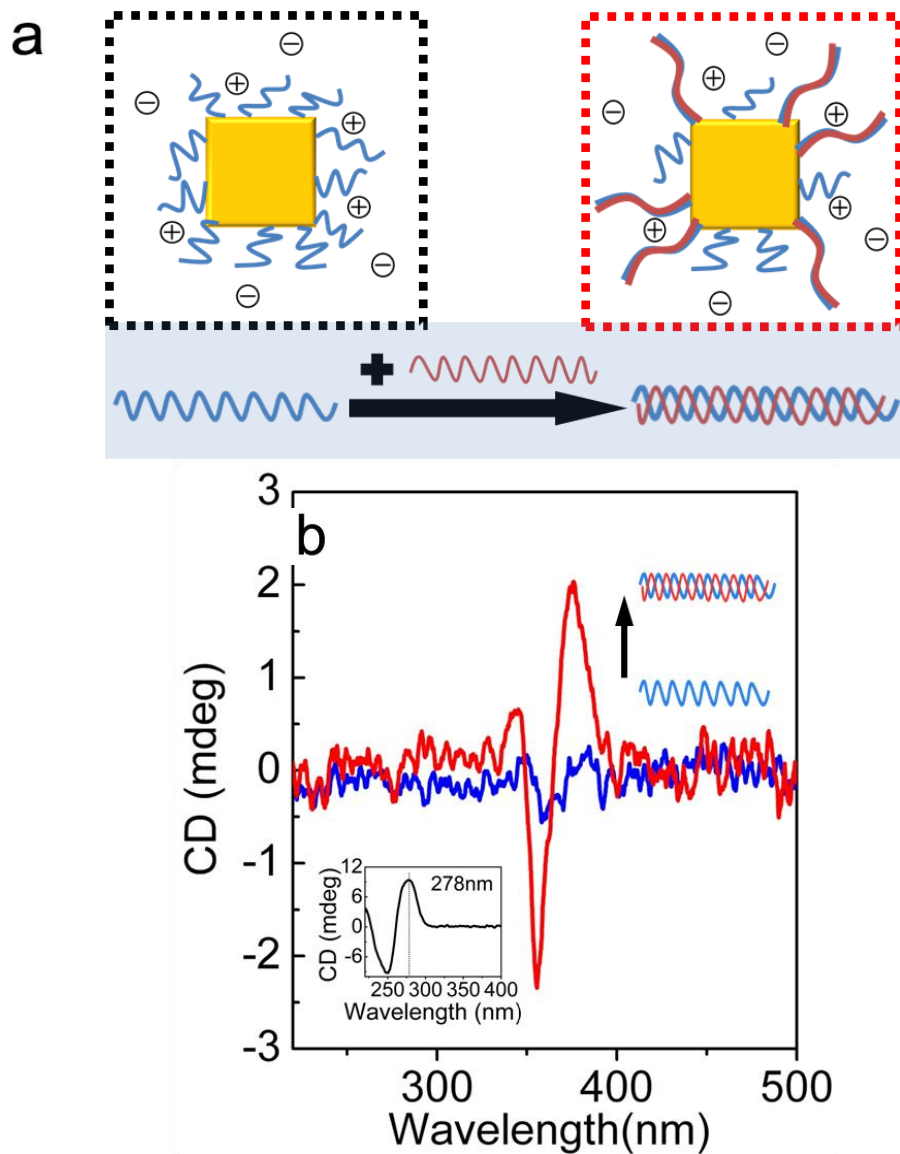


Figure 5.8 Reboots of plasmon-induced CD resonance in a salted solution. **a.** Scheme illustrating the change of DNA profiles on a cube surface in 0.1M PBS: from flexible ssDNA (black-dotted frame) to relatively rigid double helices (red-dotted frame) by hybridized with complementary strands. **b.** CD spectral comparison in 0.1M PBS system between before (black curve) and after (red curve) making ssDNA on nanocubes become more rigid double helices (blue curve of inset is the CD spectrum from pure dsDNA of 20 μ M).

The giant SP-induced CD enhancement reflects the sub-diffraction limit field confinement associated with the SP. As we discussed previously, the tiny difference in the n_+ and n_- (the optical rotary dispersion, ORD) of DNA induces pronounced CD in the LSPR spectrum through the strong near field coupling between the DNA molecules and SP. LSPR mode profiles for the nanocube are calculated using discrete dipole approximation (DDA) method¹⁴¹. Shown in Fig. 5.9 are 3D distributions of the electric field enhancement factor $P = |\vec{E}|^2 / |\vec{E}_0|^2$, where $|\vec{E}|$ and $|\vec{E}_0|$ are respectively the actual and incident electric field amplitudes, for the three SP modes experimentally identified from the nanocubes near a NC surface. For all three modes we observe large electric field enhancements, which are spatially confined to the cube apexes for Mode 1, but it extends to the edges for Modes 2 and 3. For evenly distributed DNA molecules on a nanocube surface the actual plasmon-induced CD signal is predominantly determined by a distribution of the field. Therefore, since the apexes only account for a very small fraction of the nanocube surface, fewer DNA molecules might be located there (assuming their homogeneous spatial placement), resulting in a practically undetectable CD signal at Mode 1. On the other hand, a larger number of DNA molecules is located within field enhancement “hot-spots” at cube edges for Mode 2 and 3. In addition, given a relatively low binding energy of thiol to Ag and an entropic benefit of chains on curved surfaces, edges might have a larger DNA density than NC facets. Furthermore, Modes 2 (378 nm) and 3 (349 nm) are closer to the DNA electronic transition (264 nm) than Mode 1 (452 nm). Considering that the ORD signal at frequency ω is proportional to $(\omega_0 - \omega)^{-1}$, where $\omega_0 > \omega$ is the molecular electronic transition frequency, the difference between n_+ and n_- would be significantly larger for Mode 2 and Mode 3 than Mode 1, which translates to the additional enhancement of CD signals at these two modes.

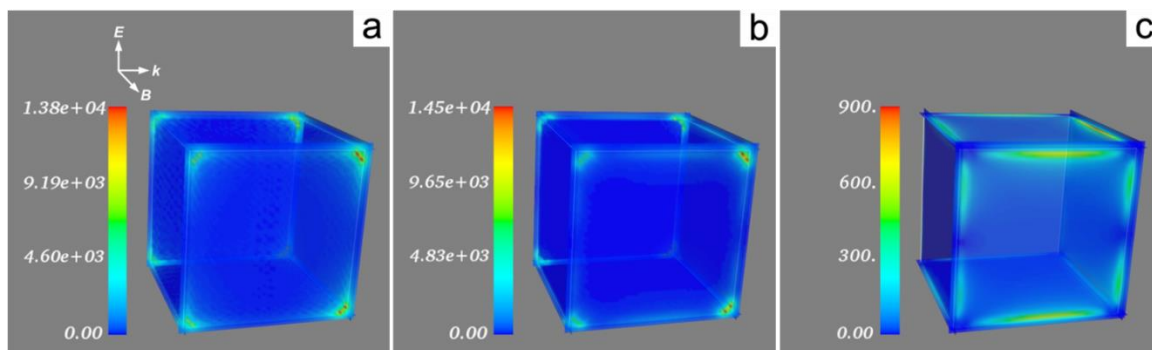


Figure 5.9 The calculated 3D profiles for the electric field enhancement $P = |\vec{E}|^2 / |\vec{E}_0|^2$ at Ag nanocube surface for three resonance modes, corresponding to peaks P1 (a), P2 (b) and P3 (c), as shown in UV-Vis absorption spectra.

Physically, shaped nanoparticle containing sharp feature and the orientation of attached molecules can be crucial for the observation of giant CD for the two reasons: sharp feature NCs have much stronger plasmonic enhancement at the surface, up to about 1000 based on our calculation (Fig. 5.9), and (2) the orientation of molecular components favor the plasmonic CD induction effect (25). In fact, only cubic Ag nanoparticles produce strong plasmonic CD in our study.

5.4 Conclusion

In conclusion, new CD response is observed from the DNA-functionalized Ag NCs, in which the CD bands fall into the plasmon nanoparticle region ($\lambda > 300\text{nm}$). Most remarkably, a giant optical amplification from the DNA on Ag NCs is observed for the first time, with up to 85 ~ 103-fold enhancement per molecule relatively to free DNA with a native CD band at 240~280nm. The observed CD signal is plasmon-induced, although plasmonic particles (NC) have no intrinsic CD signature. The observed “amplification” of CD signal is a consequence of the exciton-plasmon interaction within DNA-nanocube complex. Such a plasmon-induced CD

resonance is sensitive to the molecular orientation with respect to a nanocube surface. A hybrid nanostructure and discovered phenomenon reported here would serve as a promising platform for ultrasensitive sensing of chiral molecules and their transformations in synthetic, biomedical and pharmaceutical applications. Our approach also exhibits a great potential to realize an enhanced and tailorable optical response by combining various shaped non-chiral nanoparticle coupled with chiral molecular components. Such intrinsically non-chiral but optically chiral plasmonic elements might be utilized for optical nanomaterial. Furthermore, the new class of CD “amplifiers”, shaped nanoparticles, calls for more comprehensive theoretical descriptions to reveal the relationship between chiral molecule and its placement, nanoparticle geometry and particle’s material on the plasmon-induced CD signal.

Table 5.1 Comparison on CD enhancement factors, A_{CD} , from different nanoparticles functionalized with 30ssDNA. N/A indicates that no plasmon-induced CD signal was observed at the measured concentrations

Material/shape/size	Au sphere 10nm (diameter)	Au sphere 45nm (diameter)	Au cube 45nm (edge length)	Au octahedron 45nm (edge length)	Ag sphere 20nm (diameter)	Ag sphere 40nm (diameter)	Ag cube 42nm (edge length)
Enhancement factor (A_{CD})	N/A	N/A	N/A	N/A	1.6	N/A	85~103

Table 5.2 Average Ag nanoparticle sizes, major SPR peak position, extinction coefficient at SPR peak λ_{ext} , and the measured number of 30ssDNA strands on per particle for studied systems.

Nanoparticle	SPR peak position (nm)	Extinction coefficient λ_{ext} ($M^{-1} \cdot cm^{-1}$)	DNA strands/particle
20nm-diameter Ag sphere	404	2.9×10^9	230 ± 30
40nm-diameter Ag sphere	415	2.6×10^{10}	490 ± 20
42nm-edge length Ag cube	452	5.5×10^{10}	530 ± 40

5.5 Methods

(1). Chemicals: Gold (III) chloride trihydrate ($HAuCl_4 \cdot 3H_2O$, 99.9+%), silver nitrate ($AgNO_3$, 99.9999%), sodium borohydrate ($NaBH_4$, 99.99%), L-ascorbic acid (AA, 99+%), cetyltrimethylammonium bromide (CTAB, 99.9%), and cetylpyridinium chloride (CPC, 99%) were purchased from Sigma-Adrich and used without further purification. Milli-Q water with a resistivity greater than $18.0 M\Omega \cdot cm$ was used in the preparation of aqueous solutions.

(2). The Au octahedral seeds were prepared using a two-step procedure¹⁴². Firstly, 3nm Au nanoparticles were prepared by quickly injecting 0.60mL of ice-cold, freshly prepared $NaBH_4$ (10mM) into a rapidly stirred mixture of $HAuCl_4$ (10mM, 0.25mL) and CTAB (0.1M, 9.75mL). The resultant solution was stirred for 2 minutes and then left undisturbed for 2 hours. For the synthesis of CTAB-capped Au octahedral seeds, the formerly prepared hydrosol was diluted to

100mL with water, which was used as a seed solution. 0.1mL of 10mM HAuCl₄, 2mL of 0.2M CTAB, and 1.5mL of 0.1M AA were mixed together and the obtained colorless mixture was diluted to 25mL. And then 0.3mL of seed hydrosol was added to the mixture immediately. The reaction mixture was shaken enough, and then left undisturbed at room temperature for 8 hours. Finally, the mixture turned from colorless into light purple, indicating the formation of Au nano-octahedra. The as-prepared products were collected by centrifugation (10min, 15000 rcf), washed with Milli-Q water once, and then re-dispersed into water with a same volume as reaction solution. The finally obtained solution was used as Au octahedral seeds.

(3). In a typical procedure, 10mL of the Au octahedral seeds and 1.6mL of 0.1M CPC aqueous solution were mixed in a 20mL vial. While the mixture was heated up to 60 °C, 0.2mL of 10mM AgNO₃ and 0.8mL of 0.1M AA were added consecutively under magnetic stirring. After 1h reaction, the vial was cooled in an ice-bath. The as-synthesized nanoparticles were spun down (10min, 13400rcf) and re-suspended in deionized water (DIW) twice to remove excess surfactants and get concentrated suspension in DIW.

(4). Thiol-modified single-strand oligonucleotides (see Table 5.2 for sequences) were purchased from Integrated DNA Technologies Inc. with disulfide modification. Before nanoparticle DNA functionalization, the disulfide oligonucleotides were first reduced by dissolving the lyophilized samples (100~300nmoles) in 0.3mL of a 100mM dithiothreitol (DTT) solution in purified water or buffer. The reduced DNA was loaded onto a freshly purified sephadex column (G-25, Amersham Bioscience) and eluted with 2.5mL of 10mM phosphate buffer (pH=7.4). The DNA was quantified using UV-Vis analysis using the known extinction coefficient.

Au/Ag core-shell nanocubes (NC) were functionalized with ssDNA (we have modified a reported procedure¹³²) using a ligand replacement reaction between CPC and thiol-modified oligonucleotides for a high DNA coverage. Briefly, an aliquot of purified DNA solution was added to 1mL aliquot of freshly-dispersed NC (~2 OD₂₆₀ of DNA for per mL of nanoparticle colloid). After allowing 3 hours for thiolated DNAs to react with the silver surface, particle suspensions were brought to 0.01% sodium dodecyl sulfate (SDS) and 10mM sodium phosphate and allowed to sit for overnight. Following literature procedure, the colloidal nanoparticle solutions were then slowly treated with NaCl to allow for electrostatic screening between neighboring DNA strands and denser surface coverage of oligonucleotides. Specifically, NaCl concentration of the solution was brought to 0.5M slowly by adding aliquots of 3M NaCl eight times with ~30min interval for incubation. After reaching the final NaCl concentration, particles were allowed to sit overnight to achieve maximum DNA loading. To remove the excess, unbound DNA from the solution, the mixture was centrifuged, the supernatant was removed, and the pellet was resuspended in washing buffer (0.01% SDS+10mM phosphate buffer, pH=7.4) three times. The final pellet was typically resuspended in 100 μ L to get a concentrated solution of particles. Sodium phosphate and NaCl were added to bring the final suspension to get expected concentrations of sodium phosphate and NaCl, respectively. The product concentration was quantified using the absorbance value at the surface plasmon resonance (SPR) maximum in UV-vis absorption spectra. A molar extinction coefficient of $\sim 5.5 \times 10^{10} \text{ M}^{-1} \text{ cm}^{-1}$ at 452nm SPR peak is used for Au/Ag core-shell nanocubes with ~42nm edge length (see Fig. S6 and the corresponding description of calculations).

In order to get double helix DNA on the surfaces of Au/Ag nanocubes, the 30ssDNA-functionalized nanocubes were firstly hybridized by a 30 base ssDNA that is fully

complementary to that grafted on nanocubes, at a molar ratio of $6000\times$ in 0.2M PBS¹⁴³. This ratio is approximately a 10 fold excess of surface bound 30ssDNA when n of ~ 530 per nanocube is taken into account. The samples were incubated overnight to form dsDNA spacer segments and purified of excess un-hybridized complementary strands by multiple centrifugations and washing with buffer.

(5). Scanning electron microscope (SEM) and transmission electron microscope (TEM) characterizations were conducted on a Hitachi S-4800 Scanning Electron Microscope and a JEOL JEM-2100F high-resolution Analytical Transmission Electron Microscope, respectively. Dynamic light scattering (DLS) measurements were performed on a Malvern Zetasizer ZS instrument. UV-vis spectra were collected on a Perkin-Elmer Lambda 35 spectrometer. CD signals were recorded by the Jasco J-815 spectropolarimeter.

(6). A fluorescence-based method was used to determine the number of DNA loaded on cube surface¹⁴⁴. Firstly, the DNA was chemically displaced from nanoparticle surface using DTT. The displacement was initiated by adding equal volumes of DNA-functionalized nanoparticles and 1.0M DTT in 0.1M PBS, pH=7.4. The oligonucleotides were released into solution during overnight incubation, and the particle precipitate was removed by centrifugation. The concentrations of oligonucleotide in solution were determined by fluorescence spectroscopy. During the fluorescence measurement, the fluorophore was excited at 450nm and the emission was collected from 520 to 640nm.

(7). Sequences

Oligonucleotide

Sequence

30ss-DNA: 5'-SH- C₆H₁₂- (T)₁₅-TAA CCT AAC CTT CAT-3'

50ss-DNA: 5'-SH- C₆H₁₂-(T)₁₂- CGT TGG CTG GAT AGC TGT GTT CTT AAC
CTAACC TTC AT-3'

30ss-DNA-dye: 5'-SH- C₆H₁₂- (T)₁₅-TAA CCT AAC CTT CAT-Cy3-3'

Complementary DNA to 30ss-DNA: 5'-ATG AAG GTT AGG TTA-(A)₁₅-3'

30ds-DNA: 5'- TTT TTT TTT TTT TTT TAA CCT AAC CTT CAT-3'

AAA AAA AAA AAA AAA ATT GGA TTG GAA GTA

Chapter 6

Prescribed Nanoparticle Cluster Architectures and Low-Dimensional Arrays

Abstract

Reliably creating three-dimensional (3D) mesoscale clusters, in which nanoparticles of one or several kinds are spatially arranged in pre-determined positions, is the first step towards arbitrarily designed self-assembled architectures. These engineered clusters would be the mesoscale analogs of molecules and would thus offer tailored nanoparticle properties due to the collective effects. However, establishing a flexible and broadly applicable platform for the fabrication of nanoparticles architectures, as well as probing their 3D non-periodic organizations with high precision, is challenging. Here we report a novel strategy for assembling 3D nanoparticle clusters: designing a molecular frame with encoded apexes for particle placement. Using a DNA origami octahedron as such frame we positioned specific particles types at the octahedron apexes, which permitted a fabrication of clusters with different symmetries and particle composition. We applied the combination of Cryo-EM methods to uncover the structure of the DNA frame and to reveal that nanoparticles are spatially coordinated in the prescribed manner. Employing the demonstrated assembly strategy, we have created nanoclusters with different chiroptical activities based on the specifically encoded center-symmetrical DNA frame and the same set of nanoparticles. We also show that octahedra with particularly designated vertices can serve as interparticle linker, thus, allowing for assembly of 1D or 2D arrays with designed particle arrangements.

6.1 Introduction

The assembly of well-defined particle clusters by design has long been seen as one of the key challenges in rational material fabrication due to their direct analogy with molecules. The designed clusters are not constrained by the orientations of interatomic bonds as in molecules found in the natural world. Therefore, a broad diversity of structures can potentially be generated. Clusters with tailored structures and functions could be used as the designer's blocks to create higher level organizations. Such clusters were recently proposed for addressing the challenge of inverse engineering in self-assembled systems^{145,146}. From a functional perspective, designed meso-clusters from nanoparticles (NP) are attractive for accessing their collective and synergetic effects^{51,147-149} and manipulating their optical response.

Recently, much progress was achieved on micron-scales in understanding and fabrication of clusters from so called patchy particles¹⁵⁰, where the placement of patches determines directional interparticle interactions^{16,151}. For nanoscale particles, the challenges in placing patterns in the specified particle's locations with a high fidelity are significant; therefore, alternative strategies were considered. A number of studies explored the DNA-assembled hetero-clusters¹⁵², the discrete and polymer-like¹⁵³ assemblies using nanoparticles with monovalent and multivalent binding properties^{52,68,147,152,153}, step-wise assembly from molecularly encoded surfaces⁵³, and via templating of molecular motifs^{62,67,154}. Nevertheless, methods for robust and massive assembly of complex yet designed cluster architectures in which nanoparticles of different types can be spatially arranged in pre-determined three-dimensional (3D) arrangements remain challenging. Furthermore, an ultimate goal is a development of universal assembly platform that can be applied to a wide range of nanoparticles materials and their surface functionalities.

In this chapter we propose and demonstrate the experimental realization of the NP cluster assembly platform using a rigid 3D nanoscale molecular frame. We show in the specific implementation using an octahedral DNA frame that nanoparticles can be arranged in 3D in the prescribed locations, which are determined by the frame apexes encoded by the specific DNA sequences (Figure 6.1). We show several representative examples of particles organizations: (i) an octahedral cluster that fully replicates the frame geometry (Figure 6.1B); (ii) a square-like cluster in which subset symmetry of the original frame is used (Figure 6.1C); (iii) an octahedral hetero-cluster in which three types of particles are coordinated in the particular positions (Figure 6.1D). We stress that the discussed approach is conceptually different from the assembly methods based on patchy and patterned particles, since no complex particle fabrication is required. As we show below, the proposed methodology, “the cluster assembly by frame”, streamlines a fabrication of designed 3D meso-architectures and fully support the integration of different nanoparticle types as soon as they contain specific DNAs in their shell ^{100,155}. We choose to use DNA as a frame for the implementation of the concept due to its highly customizable structure ¹⁵⁶ and ease of programmability of interactions between the frame and particles. Over the past decade, DNA has offered a compelling methods towards creation of nanoparticles arrays, either in 2D using DNA tile motifs ^{157,158} by implementing basic design rules ¹⁵⁶ or in 3D using DNA-encoded particle shell interactions ^{44,45}, as well as discrete assemblies and linear arrays ^{83,147,154}. The DNA origami technology allows for the designed fabrication of discrete 2D ⁴⁰ and 3D ⁴² DNA shapes, and the reactive groups can be precisely located ¹⁵⁹. We use here 3D origami construct, shaped as octahedron with DNA-encoded apexes, as frame for assembly of designed clusters from nanoparticles. Moreover, we show that their optical response, a chiroptical activity, can be fully controlled based on the prescribed placement

of nanoparticles of different sizes on the same central-symmetrical frame. By exploiting the octahedron frame as a programmable linker between nanoparticles we demonstrate that low-dimensional, linear 1D and square 2D, nanoparticle arrays can be successfully created in the designed manner.

Revealing 3D structure of mesoscale clusters is a significant challenge, particularly, due to the need for probing clusters both on ensemble and individual cluster levels at different scales. Such probing of frame internal structure, 3D positioning of NPs and a cluster population analysis are important for the realization of high-fidelity assembly and understanding the effects of frame-NP interactions. Traditional TEM provides clear images of metal nanoparticles alone¹⁶⁰, but not of the DNA constructs. Negative staining EM offers a way of observing both metal particles and DNA template^{83,154,159}, but can flatten thus distort the relatively large 3D structure. In contrast, cryo electron microscopy (cryo-EM) preserves samples in their near native states and provides close to nanometer resolution of structures using single particle 3D reconstruction technique^{38,157,161,162} and tomography¹⁶³⁻¹⁶⁵. We show here that cryo-EM can be successfully applied to probe the 3D structure of DNA-NP clusters.

6.2 Experimental design

First, we designed the frame, an octahedral DNA origami structure (Figure 6.1A), using the caDNAno software package (<http://cadnano.org/>)⁴³. Each octahedral edge contains a six-helix-bundle (6HB)¹⁶⁶⁻¹⁶⁸, out of which one helix (blue, Figure 6.1A at the bottom) has a single strand (ss) DNA stretched out of the duplex ends for attaching nanoparticles (NPs). Apex positions (labeled from 1 to 6) could be encoded with distinctive ssDNA “sticky ends”, which can bind the nanoparticles coated with complementary DNA. We designed three routes to assemble different

numbers and sizes of gold nanoparticles (Figure 6.1B-6.1D). When six apexes have the same sticky end, a six-particle cluster is formed after mixing with the corresponding DNA-encoded NPs. The resulting NP cluster, denoted as 'P₆' (Figure 6.1B), has a symmetry O_h. When only four in-plane apexes are encoded and two others are silent, 4-particle cluster (Figure 6.1C) could be formed, denoted as 'P₄(1234)' to indicate the number of particles and their apex locations. The heterogeneous cluster can be created by introduction of different DNA at apexes of choice. Here, we used three distinctive sets of sticky ends, with two of the same kind located at opposite apexes, as shown in Figure 6.1D. Such design allows binding three types of nanoparticles. We used 7 nm (P¹), 10 nm (P²), and 15 nm (P³) gold NP with respectively complementary shells for prescribing this hetero-cluster, labeled as 'P¹₂(12)P²₂(34)P³₂(56)'.

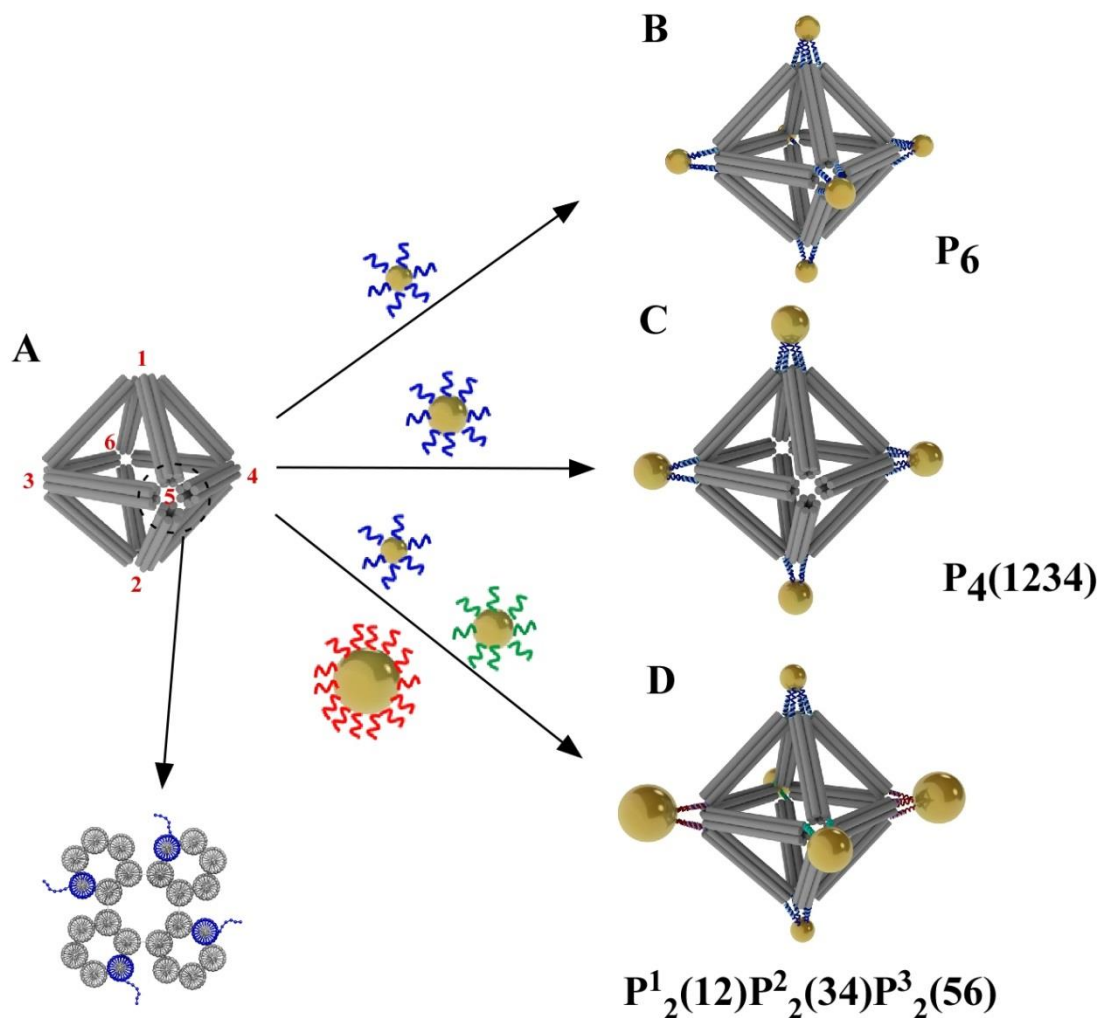


Figure 6.1 Scheme of three designer clusters assembled from functionalized gold nanoparticles (NPs) on a designer octahedral DNA origami frame. (A) The designer octahedral origami structure. Red numbers mark the six corners or apexes of the octahedron. One apex is zoomed in the lower panel to show the end-on view of the designed structure comprised of four six-helix bundles (6HB). Each 6HB contains one encodable ssDNA sticky end (dotted blue line). (B) An octahedron with all sticky ends being encoded to coordinate 7-nm NPs into the symmetric 6-NP

cluster P_6 . (C) The $P_4(1234)$ cluster structure may form if the ssDNA at apexes 1-2-3-4 of the octahedral frame is programmed with sequence complementary to the ssDNA on the 10-nm gold NPs. (D) The $P^1_2(12)P^2_2(34)P^3_2(56)$ cluster structure may assemble if the ssDNA at apexes 1-2, 3-4, and 5-6 are programmed to complement the ssDNA on the 7-nm, 15-nm, and the 10-nm NPs, respectively.

6.3 Results and discussion

The octahedral DNA frame was formed by mixing M13mp18 DNA and hundreds of staple strands^{40,42} and slowly annealed from 90 °C to room temperature which was confirmed firstly by gel electrophoresis (Figure 6.2). According to our design, each six-helix-bundle on the edge has a designed length of 28.6 nm (84 base pairs). To confirm the successful fabrication of octahedron frame after its assembly we carried out a detailed cryo-EM study, in addition to the standard electrophoretic characterization. The high-fidelity octahedral formation (TEM observed yield around 99%) is clearly visible in the raw cryo-EM micrograph (Figure 6.3A). Several representative views of the DNA octahedra are highlighted by the square boxes. The DNA octahedra are randomly oriented in the vitreous ice, have expected dimensions, and appear monodisperse in shape and size. These 2D images permitted computational reconstruction of the 3D structure of the octahedron origami, as we discuss below. 2D class averages of raw particle images are nearly identical to the corresponding re-projections of the reconstructed 3D density model (Figure 6.3B). This demonstrates the quality of the particle images and the reliability of the 3D reconstruction of the DNA octahedron.

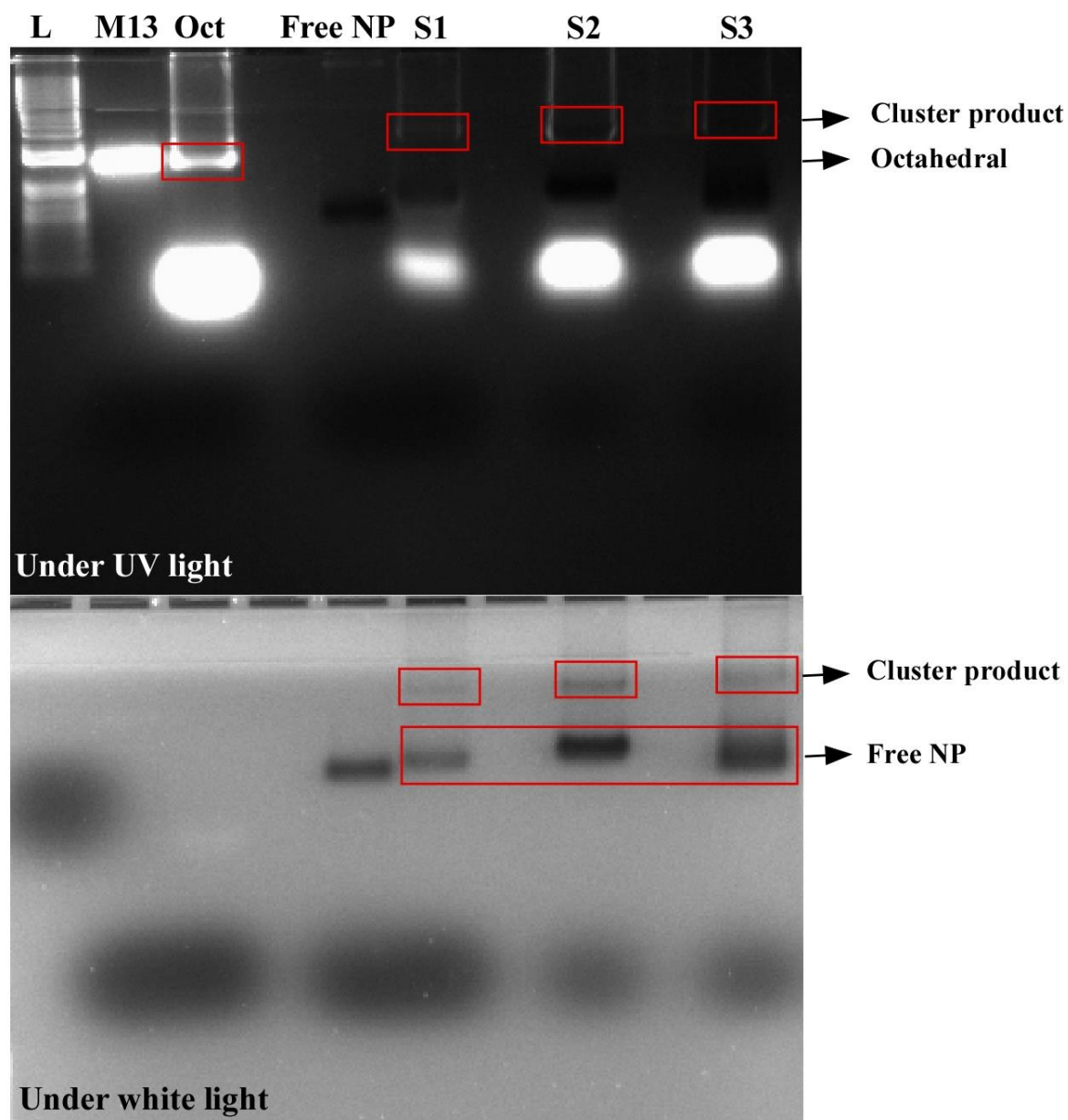


Figure 6.2 The agarose gel electrophoresis separation of DNA octahedra and DNA octahedra-NP assemblies. (Top) The UV image of the 1% agarose gel. Symbols ‘L’ is for a 1kb ladder, ‘M13’ is for M13 DNA as described in the text, ‘Oct’ is for the folded origami, ‘Free NP’ is for the mixture of 7 nm, 10 nm, 15 nm NPs, and ‘S1’, ‘S2’ and ‘S3’ correspond to the clusters P_6 , P_4 and $P^1_2P^2_2P^3_2$ respectively. (Bottom) The white-light image of the same gel.

The DNA octahedron structure was derived from approximately 10,000 manually selected raw particle images (Figure 6.3C). The 3D density map is surface rendered and shown in the typical 4-fold, 3-fold, 2-fold axis views. The octahedral edge in the three-dimensional map is ~29 nm long, in agreement with the designed length. Each edge of the reconstructed DNA octahedron is a hollow structure with a ~2 nm channel in the middle. Again this feature is consistent with our six-helix bundle design for the edge (Figures 6.1 and 6.5). The resolution of the reconstructed DNA octahedron structure is estimated to be ~23.5 Å (Figure 6.6)¹⁶⁹, perhaps limited by the rigidity of the structure. Rigidity is an important design parameter for cluster assembly. The persistence length of double helix is about 50 nm¹⁷⁰; clusters built from the double helix frame may suffer from the edge flexibility. In contrast, the persistence length for 6HB is around 1 μm¹⁷¹, much longer than both DNA duplex and DNA double crossover (DX) design¹⁷². We therefore chose the six-helix bundle (6HB) design to construct octahedron edges. The hollow structure of 6HB and formed octahedral apexes provides housing functionalized moieties, with potential applications in nanotechnology and biomedicine¹⁵⁹. Our success in visualizing the structure of the large, symmetric, and non-space-filling 3D origami constructs by cryo-EM is notable, because this method was previously applied only to the space-filling DNA origami¹⁶² or flexible origami box¹⁶¹ or to the nano-scale non-origami polyhedra^{38,157,161}.

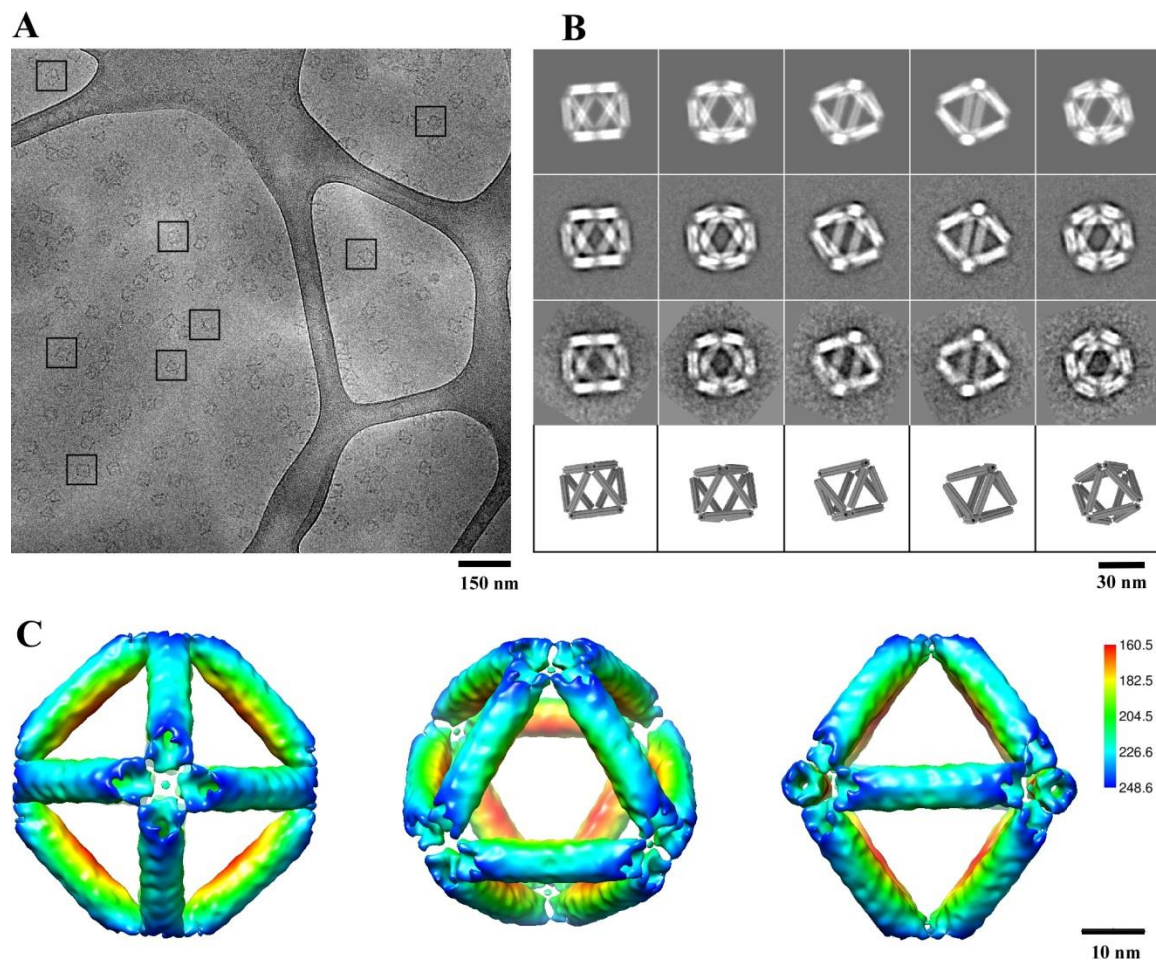


Figure 6.3 Cryo-EM and 3D reconstruction of the self-assembled DNA origami octahedron. (A) A cryo-EM micrograph with representative views of DNA octahedron boxed by a black square. Only cluster structures that were embedded in the vitreous ice and suspended over the irregular holes in the carbon film substrate were selected for further analysis. (B) Comparison of 2D reprojections of the reconstructed 3D density map (top row), with reference-based class averages (second row), reference-free class averages (third row), and with the corresponding views of the 3D design model (bottom row). (C) Surface-rendered 3D density map of the DNA octahedron, as viewed from the 4-fold (left), 3-fold (middle), and 2-fold (right) symmetry axis. The density surface is colored radially from interior red to outer blue. The color key is shown on the right. The value in the color key indicate the distance in angstrom from the octahedral center.

We computationally built a standard B-DNA model with 84 base pairs (bp) in length and manually arranged six copies to form a close-packed 6HB DNA model, leaving a hollow channel in the middle. We then docked the 6HB model as one entity (rigid body) into one edge of the DNA octahedron EM map, and found that the model fitted the density very well (Figure 6.5). The good agreement leads us to conclude that we have succeeded in fabricating the DNA origami octahedron that we have designed for. The central cavity of the octahedron should be able to accommodate a spherical particle up to 20 nm in diameter. Dynamic light scattering measured the hydrodynamic size of the octahedral in solution is around 37.8nm, which also demonstrated the well-formation of the target structure (Figure 6.4).

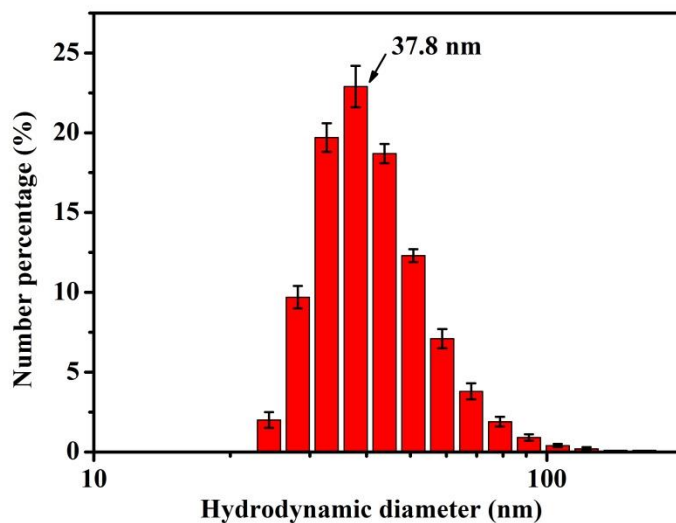


Figure 6.4 The size distribution of the assembled and purified octahedral DNA origami as obtained using dynamic light scattering measurement.

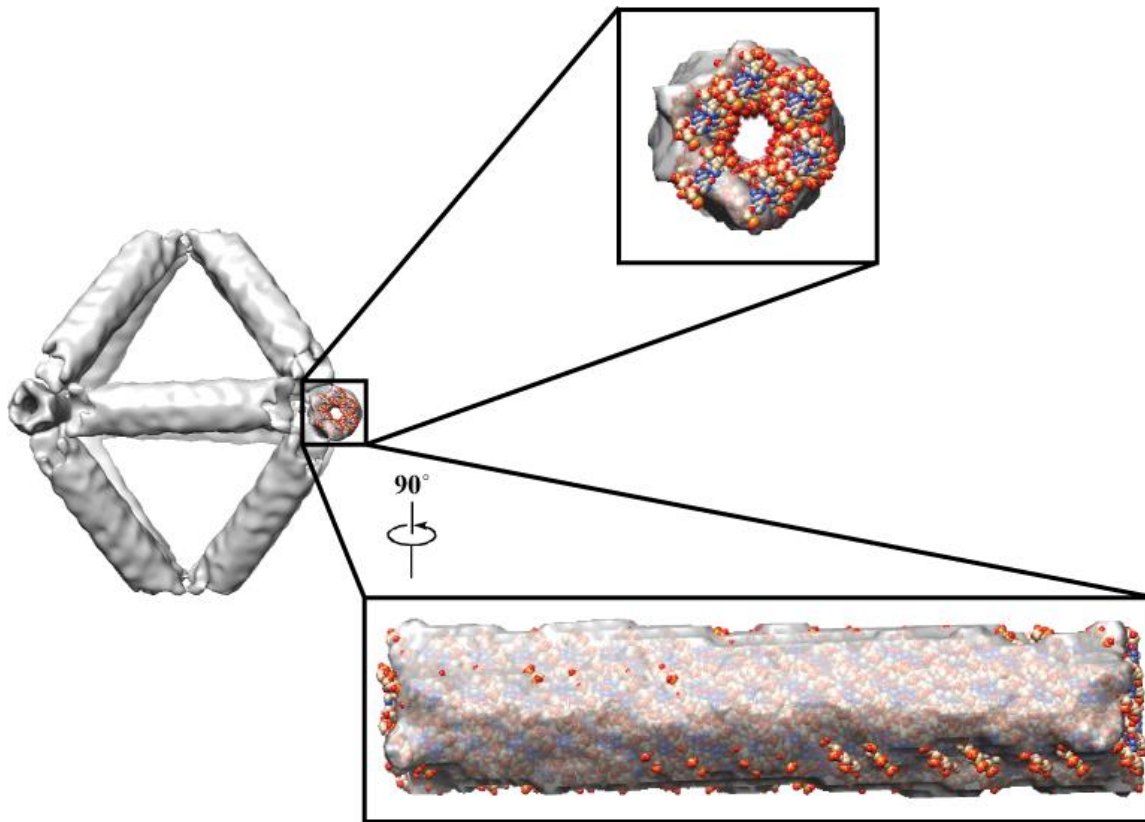


Figure 6.5 3D cryo-EM structure of the DNA origami octahedron. The 6 helix bundle (6HB) atomic model (504 bp, 84bp x 6) is fitted into one strut of the 12-strut EM density as a single rigid body. Left panel shows the surface-rendered DNA octahedron 3D density. The strut docked with atomic model is enlarged and shown in an end view (upper right) and a side view (lower right), respectively.

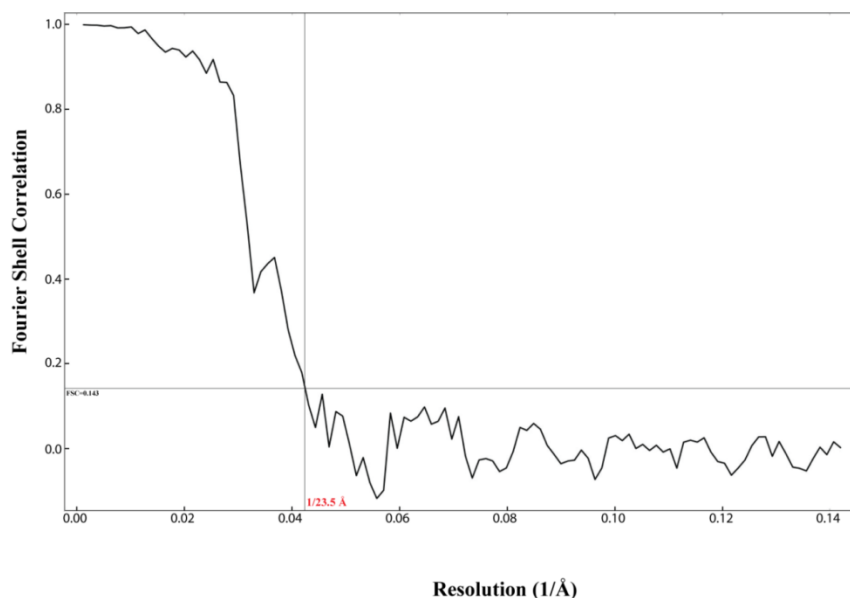


Figure 6.6 The estimated resolution for the cryo-EM map of the DNA origami octahedron. Gold standard Fourier shell correlation of two 3D maps calculated from the two halves of the final data set suggests a resolution of $\sim 23.5 \text{ \AA}$ at the correlation threshold of 0.143.

We then assembled a simple P_6 cluster on the octahedron frame. We first functionalized the 7-nm gold nanoparticles (NP) with the 30-base ssDNA that are complementary in sequence to the sticky ends of the octahedral apices, then mixed the NP with the octahedra at a molar ratio of 1:15 (octahedra:NP; DNA octahedra concentration about 1nM). The mixture was annealed from $50 \text{ }^\circ\text{C}$ to room temperature in 3 hours, concentrated, and loaded into a 1% agarose gel for separation. The gel band containing assembled clusters are cut out, crushed with a pestle, and filtered through a cellulose-acetate spin column, and the collected sample solution was used for negative-staining EM and cryo-EM. In Figure 6.7A is shown a representative raw image of the purified complexes. These clusters are highly homogeneous, with over 90% out of the 460 clusters counted containing the correct number (6) of NPs in the prescribed apex positions in each octahedron (Fig. 6.7A inset).

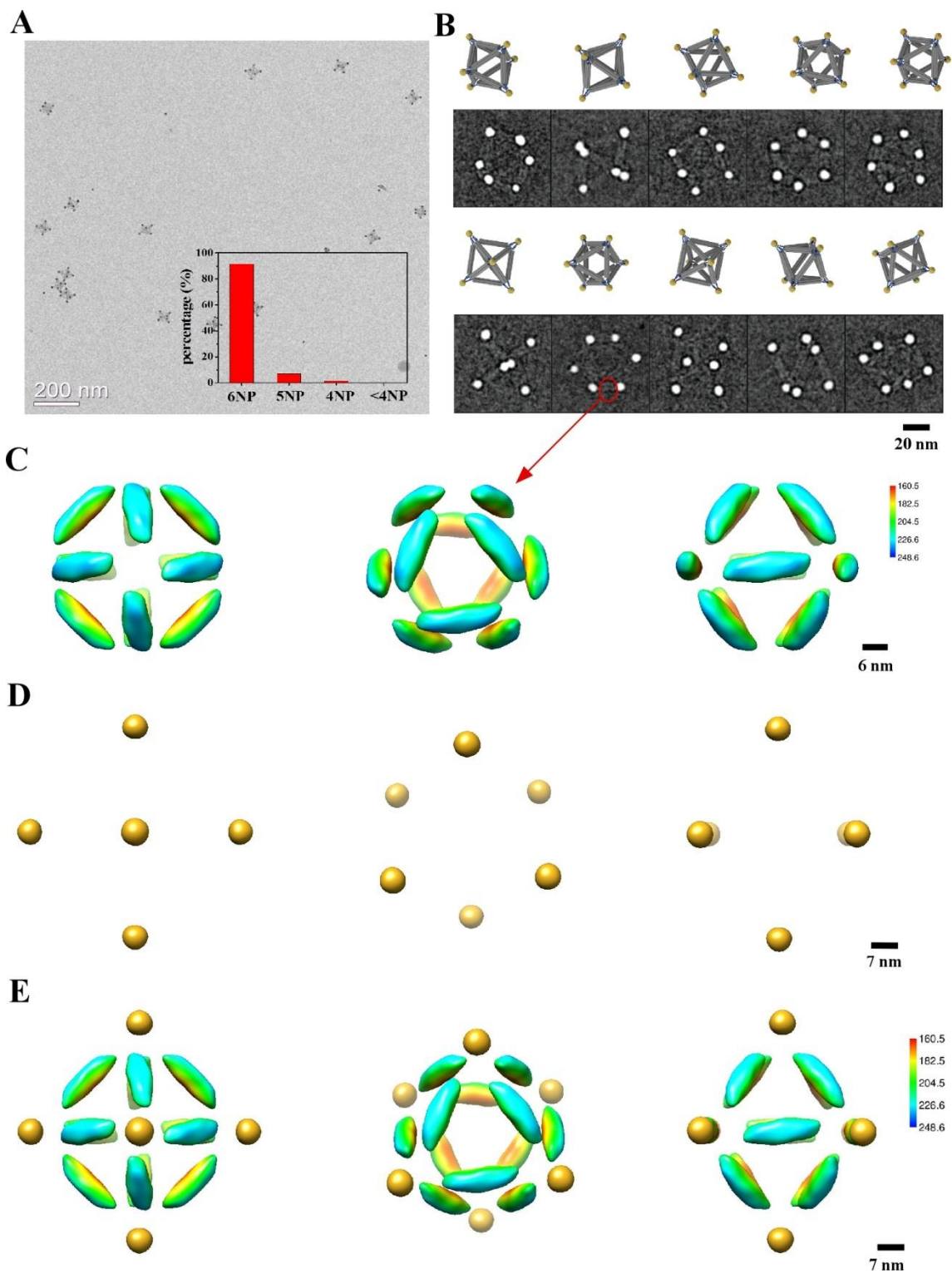


Figure 6.7 The P_6 cluster structure as revealed by cryo-EM and 3D reconstruction. (A) A representative EM image of the P_6 cluster structure. Inset shows the histogram of assembled

clusters with observed NP numbers. (B) Ten selected cryo-EM images of the fully assembled P_6 octahedron-NP clusters (second and forth rows), in comparison with the 3D design model in corresponding views (first and third rows).. (C) 3D reconstruction of the DNA portion of the P_6 cluster by excluding the high intensity NPs in cryo-EM images. The density surface is colored in the same way as Figure 6.3C. (D) 3D reconstruction of the six NPs of the P_6 cluster by using only the high intensity NP scattering signals in the cryo-EM dataset. (E) The composite 3D EM structure of the P_6 cluster derived by computationally combining the structures shown in (C) and (D). The left, middle, and right panel in (C-E) shows 4-fold, 3-fold, and 2-fold views of the respective structure.

It is clear that the 6 NPs of the individual clusters in the raw cryo-EM images are arranged in a manner that is consistent with the octahedral symmetry (Fig. 6.7B). Notably, the DNA is barely visible, with much weaker contrast than the gold NPs. This is so because the gold NPs are significantly more electron dense than the DNA. 3D reconstruction from the raw particle images reveals the overall size and symmetry of the P_6 cluster (Figure 6.8). However, when the display threshold is set to show the DNA structure, the gold NPs appear to be distorted and much larger than expected. To overcome the problem, we subsequently calculated two independent 3D reconstructions from the same cryo-EM dataset: in the first reconstruction the high NP densities were computationally removed from the raw images, keeping the DNA density intact (Figure 6.7C), and in the second reconstruction the lower intensity DNA density as well as the background noise were removed leaving only the higher intensity NPs (Figure 6.7D). We normalized and then aligned the two reconstructions by their symmetry axes and merged them into a synthetic structure (Figure 6.7E). In this compound map, the diameters of NPs are around 7 nm, consistent with the particle size estimated from the raw images. Six nanoparticles are

precisely positioned at the six apexes of the reconstructed DNA octahedron frame, with the nearest center-to-center NP distance of ~43 nm.

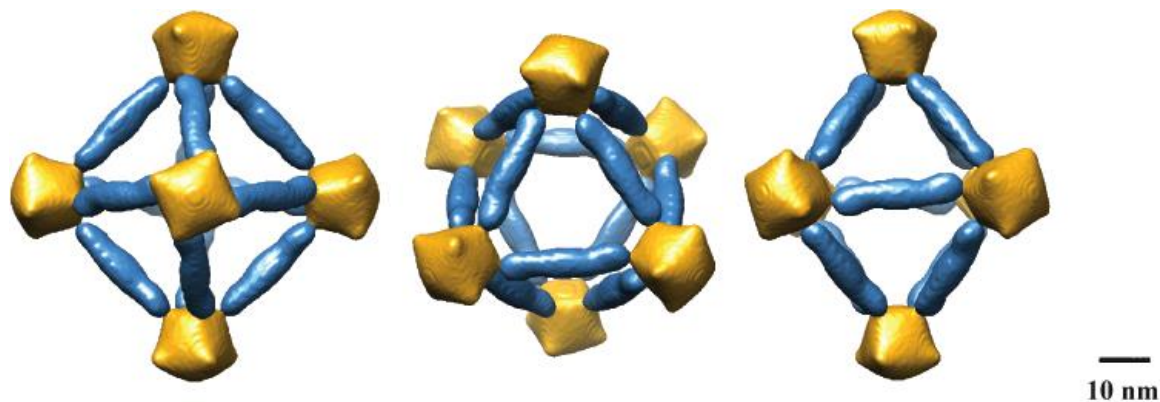


Figure 6.8 Surface-rendered 3D cryo-EM density map of Au nanoparticles (NPs) organized by DNA octahedron as viewed from 4-fold (left), 3-fold (middle), and 2-fold (right) symmetry axis, respectively. This density map was derived from the same raw dataset that was used to generate 3D maps shown in Figure 6.7, but without selective image intensity modification. The rendering level was chosen to show the DNA densities (blue). At this low display threshold, the NPs densities (golden) are exaggerated in size due to their extremely strong electron scattering power. The shape of the NPs is an artifact due to the combined effect of density mismatch between the DNA and the NP, and the octahedral symmetry applied during 3D reconstruction.

The control over the assembly of pre-defined cluster, $P_4(1234)$, with a square-like particle arrangement, was further demonstrated by choosing four co-planar corners of the octahedron with the specific sticky end oligonucleotides (Figure 6.1C). 10nm gold NPs functionalized with complementary DNA were then mixed with the designed octahedra at a molar ratio of 10:1 to form the target cluster. Samples for EM were obtained in the same way as for the P_6 cluster. We

show the representative image of the $P_4(1234)$ clusters in Figure 6.11. The cluster population histogram (Figure 6.9A) demonstrates that close to 80% of the clusters contains the correct number (four) of NPs (out of total number 554). Figure 6.9B compares cryo-EM images of six origami-NP complex with their corresponding views of the 3D model. The DNA density in these images appears even weaker than that in Figure 6.7B because the NPs used are larger; as a result, their density is more predominant in contrast with DNA octahedra. 3D reconstruction of the NP cluster is shown in Figure 6.10, where four well-positioned nanoparticles (gold color) are clearly seen located with 4-fold symmetry. The NP size in the reconstruction is around 10 nm, which is consistent with the estimation from the raw images, and the nearest center-to-center NP distance is about 40 nm. To illustrate the arrangement of the four NPs with the DNA octahedra, we computed a composite map by aligning and merging the gold NPs reconstruction with the DNA octahedron reconstruction as shown in the Figure 6.3C. The composite map shows that four 10-nm NPs are precisely positioned at four apexes of the reconstructed octahedron origami template (Figure 6.9C).

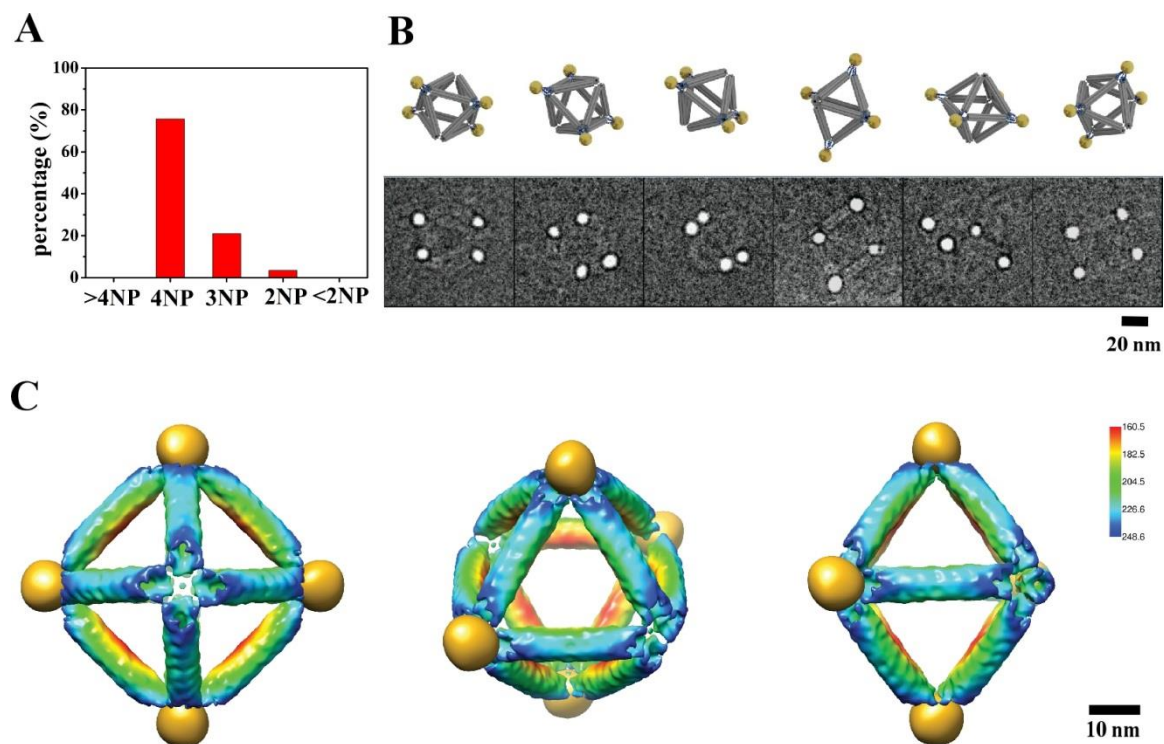


Figure 6.9 Structure of the $P_4(1234)$ cluster. (A) The cluster population histogram. (B) Six selected raw cryo-EM images of the assembled DNA-NP cluster (bottom row) in comparison with the design model in corresponding views (top row). (C) A composite density map derived by combining 3D reconstruction of the DNA octahedron (Figure 6.3C) with 3D reconstruction of the four 10-nm NPs organized by octahedral DNA frame. The rendering threshold of the later is set to show the NP densities. Left, middle, and right panel show view along the four-fold, three-fold, and two-fold symmetry axis of octahedron.

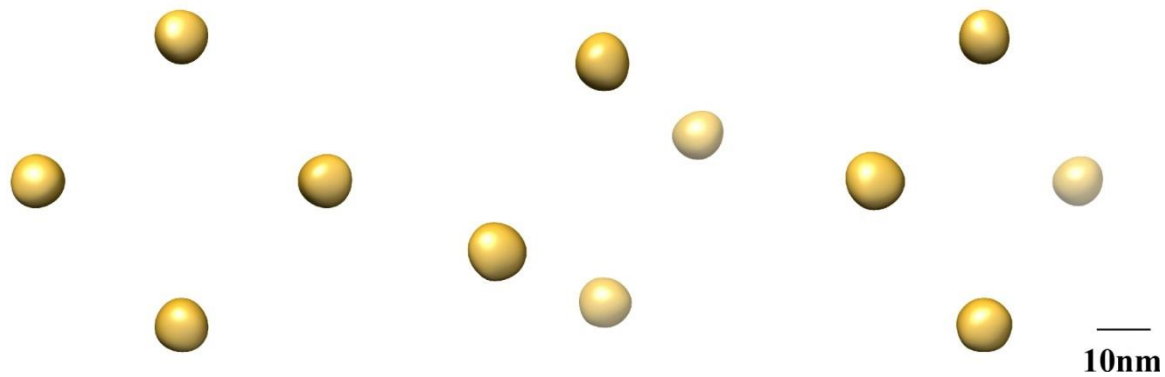


Figure 6.10 3D density map of the Four 10-nm NPs organized by the DNA octahedron. The surface-rendering threshold was set to show the high density gold NPs. DNA molecule has much lower electron density and is invisible at this display level.

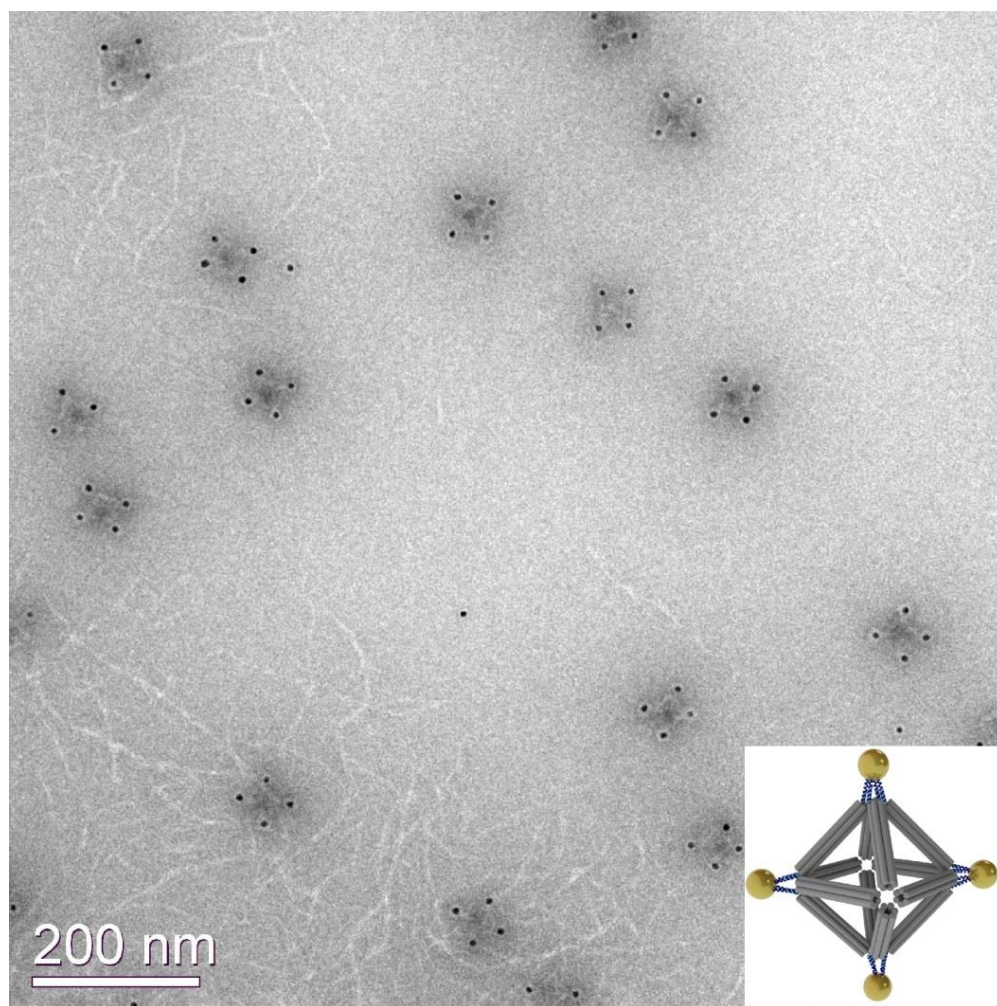


Figure 6.11 A representative electron micrograph of the cluster $P_4(1234)$ showing many well disperse clusters each having 4 NPs. Isolated NPs are occasionally visible, for example, near the center of the picture. The white ribbons are aggregated DNA material.

Next we demonstrate that outlined assembly approach allows for the realization of hetero-clusters containing several types of particles in pre-defined positions. For example, the cluster was designed to coordinate three particles types, $P^1_2(12)P^2_2(34)P^3_2(56)$, as shown in Fig. 6.1D. Six corners of the octahedron were grouped into three diagonal sets. By providing the corresponding DNA encoding, we assign apexes 1 and 2, 3 and 4, and 5 and 6 to bind to 7nm, 10 nm and 15 nm NPs respectively. DNA octahedra were mixed with three kinds of NPs with at the corresponding ratio of 1:5:5:5 and slowly annealed and purified as described above. The representative TEM image of the assembled cluster shows that the majority of these clusters have the correct structure (Figure 6.13). The population histogram, shown in Figure 6.12A, reveals that about 70% of the clusters (out of a total number of 467 clusters), coordinate 6 NPs with about equal fraction of each particle types. For partially assembled clusters (5NP and less), the missing NPs came from 3 different kinds nearly evenly. Figure 6.14 shows twelve raw cryo-EM images in comparison with corresponding 2D projections of a designed model of $P^1_2P^2_2P^3_2$ cluster. We note that due to the high dynamical range of electron densities the DNA is nearly invisible.

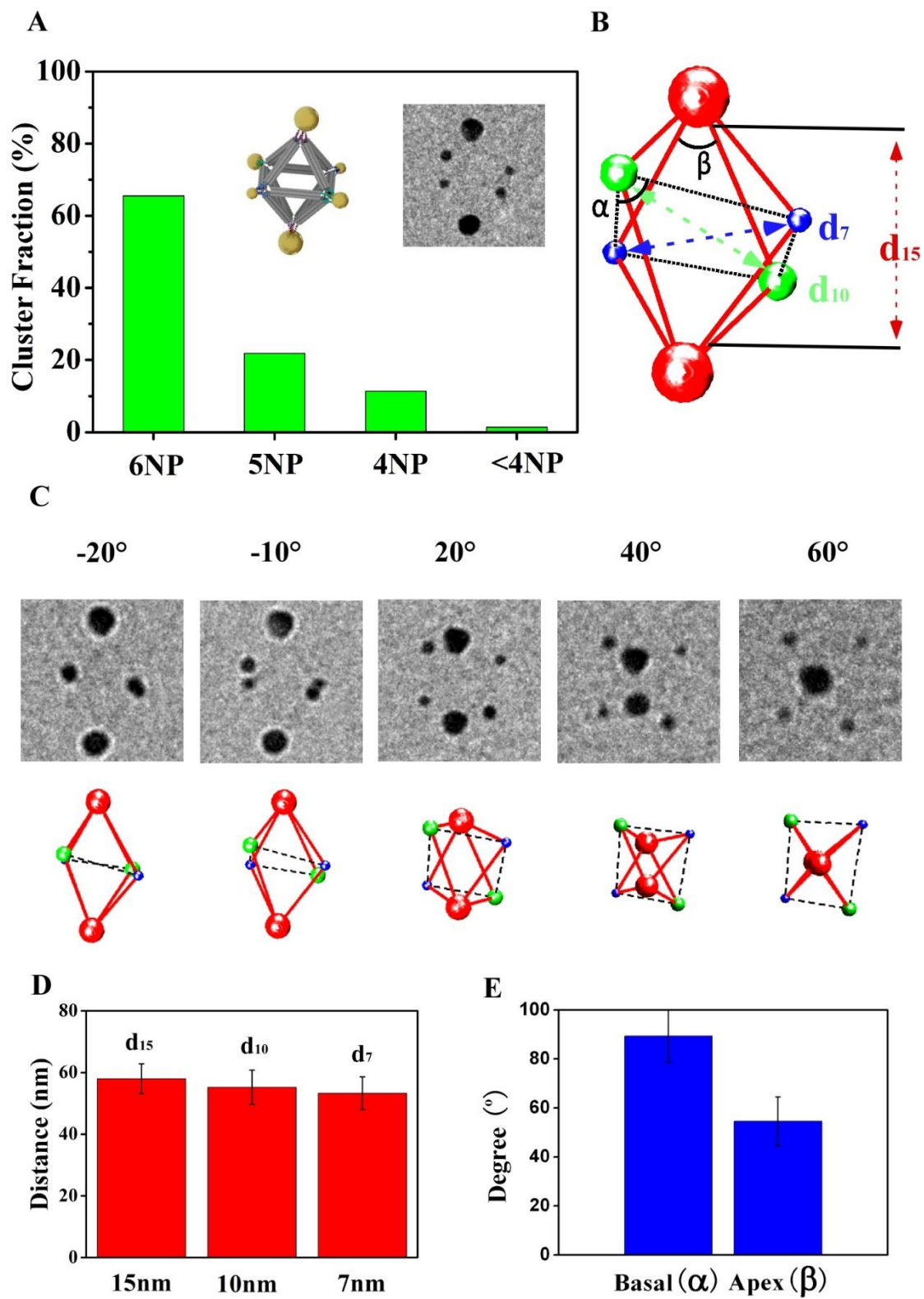


Figure 6.12 Electron tomography of individual hetero-cluster, $P^1_2(12)P^2_2(34)P^3_2(56)$, assembled with three types of NPs. (A) Statistical analysis of the NP cluster population. The design model and a representative cryo-EM image of the assembled cluster (untilted view) are shown as insets. (B) Reconstructed 3D structure of the NP cluster shown on the inset of (A). The distance between the diagonally paired 7-nm, 10-nm, and 15-nm NPs are denoted by d_7 , d_{10} , and d_{15} , respectively. α is the angle centered around the 15-nm NPs, and β around the 10-nm NPs, respectively. (C) Images obtained by tilting the cluster shown in (A) at different angles (from left to right: -20° , -10° , 20° , 40° , 60°) (top row), in comparison with corresponding views of the reconstructed 3D structure. (D) Averaged distances between the diagonally paired 7-, 10-, and 15-nm NPs measured from 12 independently reconstructed $P^1_2P^2_2P^3_2$ clusters. $d_{15} = 58.0 \pm 4.8$ nm, $d_{10} = 55.1 \pm 5.6$ nm, and $d_7 = 53.3 \pm 5.3$ nm. (E) Averaged values of the basal ($\alpha = 89.4^\circ \pm 10.9^\circ$) and apex ($\beta = 54.5^\circ \pm 10.0^\circ$) angles.

To unravel the 3D coordinates of the assembled $P^1_2P^2_2P^3_2$ cluster, we apply tomographic method for this system that permit a 3D probing of individual clusters. We acquired a series of TEM images from -60° to $+60^\circ$ with 10° intervals for twelve $P^1_2P^2_2P^3_2$ clusters. The projected positions of the particles were measured and fitted to a tilting model to extract 3D coordinates of the NP, which permitted to reconstruct the cluster structure (Fig. 6.12B). The TEM image inserted in Figure 6.12A shows the untilted picture of the cluster which corresponds to reconstructed particles positions (Fig. 6.12B), while 5C presents a few selected tilted images of the reconstruction at -20° , -10° , 20° , 40° , 60° tilt angles. The projections of the reconstructed clusters agreed well with the raw EM images. The averaged surface-to-surface distances, d_7 , d_{10} and d_{15} , between nanoparticles of the same sizes, 7 nm, 10 nm and 15 nm respectively were obtained from twelve reconstructed clusters (Figure 6.12D). Small but progressive decrease of

interparticle distances by about 4 nm is observed when NP diameter decreases from 15 nm to 7 nm. This change may result from different curvature of particles due to the dependence of DNA length in a shell on particle size ¹⁷³. Also, due to a larger attachment area of apex's DNA for bigger particles, a strain might be imposed on the octahedron resulting in its distortion. Averaged basal (α) and apex (β , for 15 nm NP) angles, as noted in Figure 6.12B, exhibit the well-defined positions of all NPs attached to octahedral frame, as shown in Figure 6.12E. Ideal basal angle is around 90° which matches our experimental data; while the apex angle ($54.5^\circ \pm 10.0^\circ$) is close to the expected value of $\sim 56^\circ$. Thus, we conclude that even attachment of larger particles (15 nm Au core) introduce practically no distortion on the frame; this further support the potential use of the approach for assembly of various designer hetero-cluster.

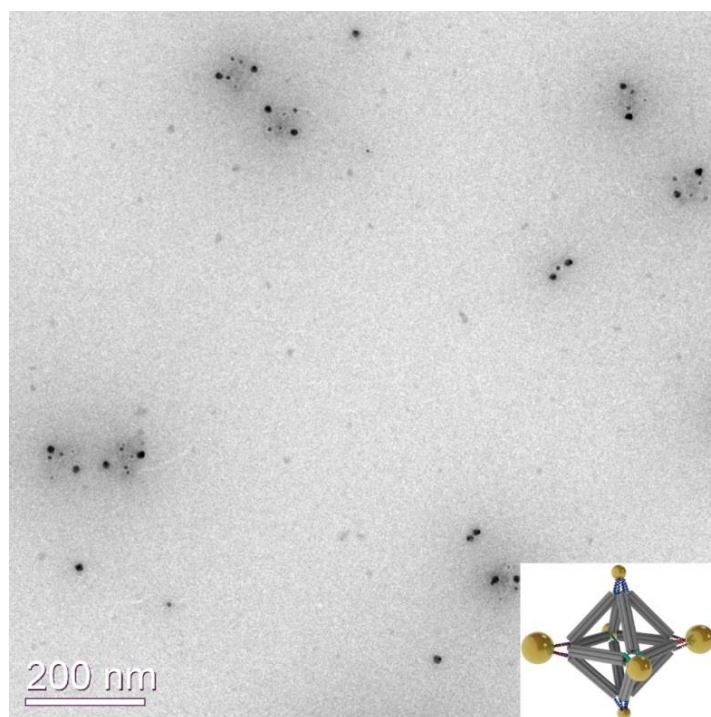


Figure 6.13 A representative electron micrograph of the cluster $P^1_2(12)P^2_2(34)P^3_2(56)$. This picture contains six fully assembled clusters. Each intact cluster has two small (7 nm), two

middle (10 nm), and two large (15 nm) NPs. Isolated individual NPs and partially assembled clusters are also visible.

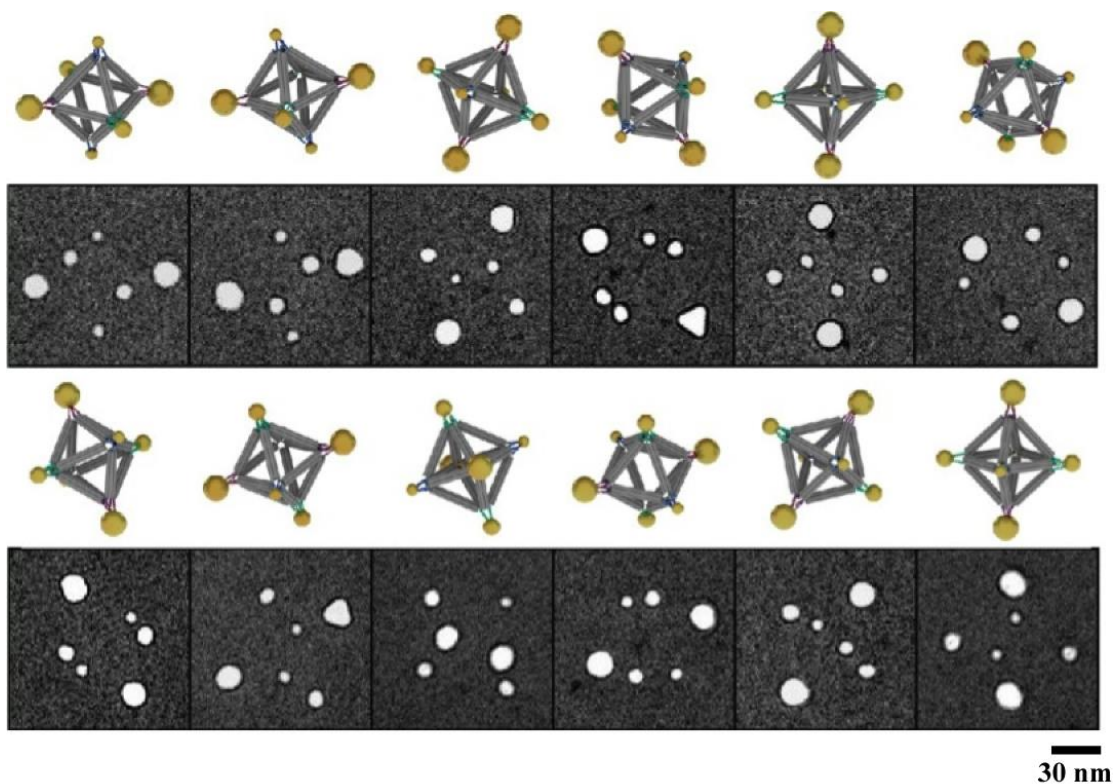


Figure 6.14 Twelve selected raw EM images of the $P^1_2(12)P^2_2(34)P^3_2(56)$ clusters in comparison with the design model in the corresponding views. The coordinating DNA octahedra (gray bars in the 3D model) are virtually invisible in the EM images. The shape of the 15-nm NPs can significantly deviate from the ideal sphere to the elongated or even triangular shapes.

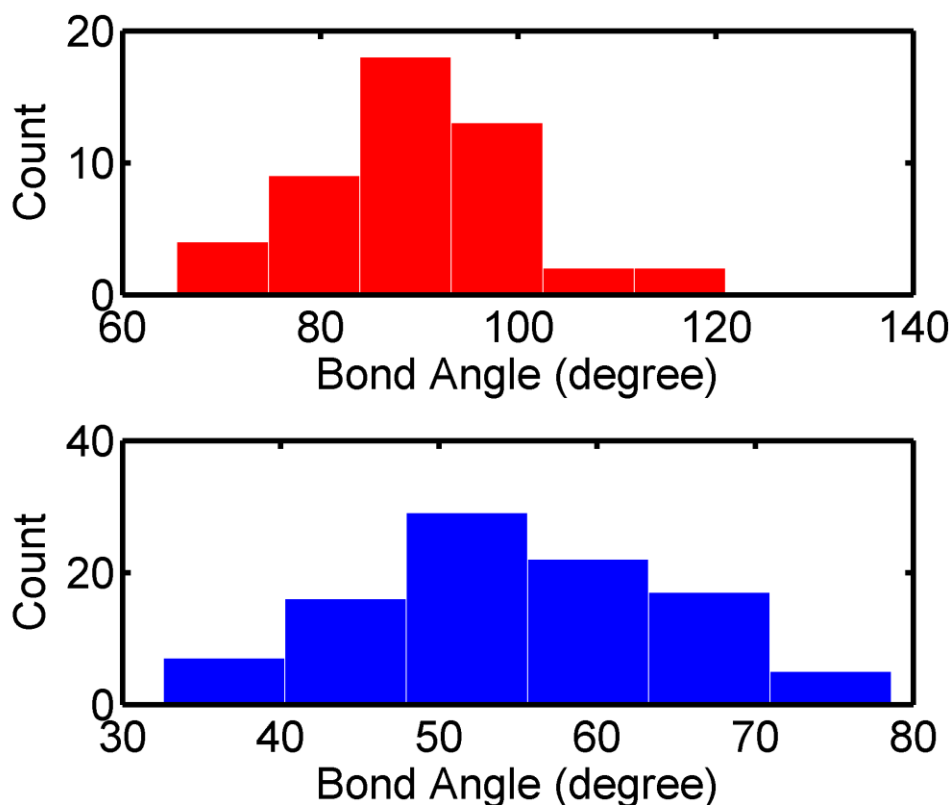


Figure 6.15 Variation of the basal and apex bond angles, α (red) and β (blue) respectively (defined in the Figure 6.12), in the assembled cluster $P^1_2P^2_2P^3_2$, as measured from the 3D cryo-EM tomograms.

The ability to assemble nanoparticle clusters in the designed manner opens new opportunities for creating materials with regulated functions. For example, the chiroptical activity might be induced for plasmonically coupled spherical nanoparticles placed on the chiral⁸³ or tetrahedral scaffold¹⁷⁴. However, as we show here, even the center-symmetric frame, like octahedron, allows producing a chiroptical response if particles of different sizes are placed accordingly. In this case, the chirality is determined by the position of specifically encoded vertices that, in turn, prescribe the placement of different particles. More specifically, depending on the arrangement of nanoparticles of three sizes on the vertices of octahedron, either in the

symmetric fashion, similar to $P^1_2P^2_2P^3_2$ (Figure 6.12) or in the non-symmetric way, non-chiral or chiral architectures can be formed (Figure 6.16a and b). Thus, from the same set of particles and the same, but differently encoded, octahedron frame different chiroptical signatures can be generated.

To realize this idea experimentally, we have substituted the 5 nm P_1 particle in $P^1_2P^2_2P^3_2$ with 20nm gold nanoparticle (P_4) in order to increase the cluster plasmonic response. Such new cluster $P^2_2(36)P^3_2(25)P^4_2(14)$, denoted as $P^2_2P^3_2P^4_2$ (Figure 6.16A), has the same-size particles placed symmetrically (see also the cluster top view in Figure 6.16A). Representative TEM image of the $P^2_2P^3_2P^4_2$ cluster with the correspondingly oriented model are shown on the top right inset of Figure 6C. No circular dichroism (CD) signal was detected in the plasmonic region of the spectrum (Figure 6.16C, red line) for such cluster. However, when the 3 pairs of NPs are positioned in the asymmetric arrangement (Figure 6.16B), the resulting cluster is chiral. Indeed, the cluster, $P^2_2(26)P^3_2(35)P^4_2(14)$, denoted as $P^2_{c2}P^3_{c2}P^4_{c2}$, contains three NP pairs with the same kinds of NPs placed at the edge ends. Representative TEM image and the corresponding model are shown at the bottom left inset of Figure 6.16C. For this $P^2_{c2}P^3_{c2}P^4_{c2}$ cluster a negative CD signal was observed (Figure 6.16c, black line), with its center at the plasmonic peak of the gold cluster (the absorption curves are shown on Figure 6.17). We note that only a very small difference, <1 nm, between plasmonic peak positions for both cases was observed, while, the dramatically different chiroptical responses are exhibited for the symmetric and asymmetric clusters. Thus, we demonstrated that the same set of nanoparticles and the same center-symmetric frame could be used to produce clusters with optically different CD responses via a simple, but precise, spatial placements of NPs in the 3D cluster.

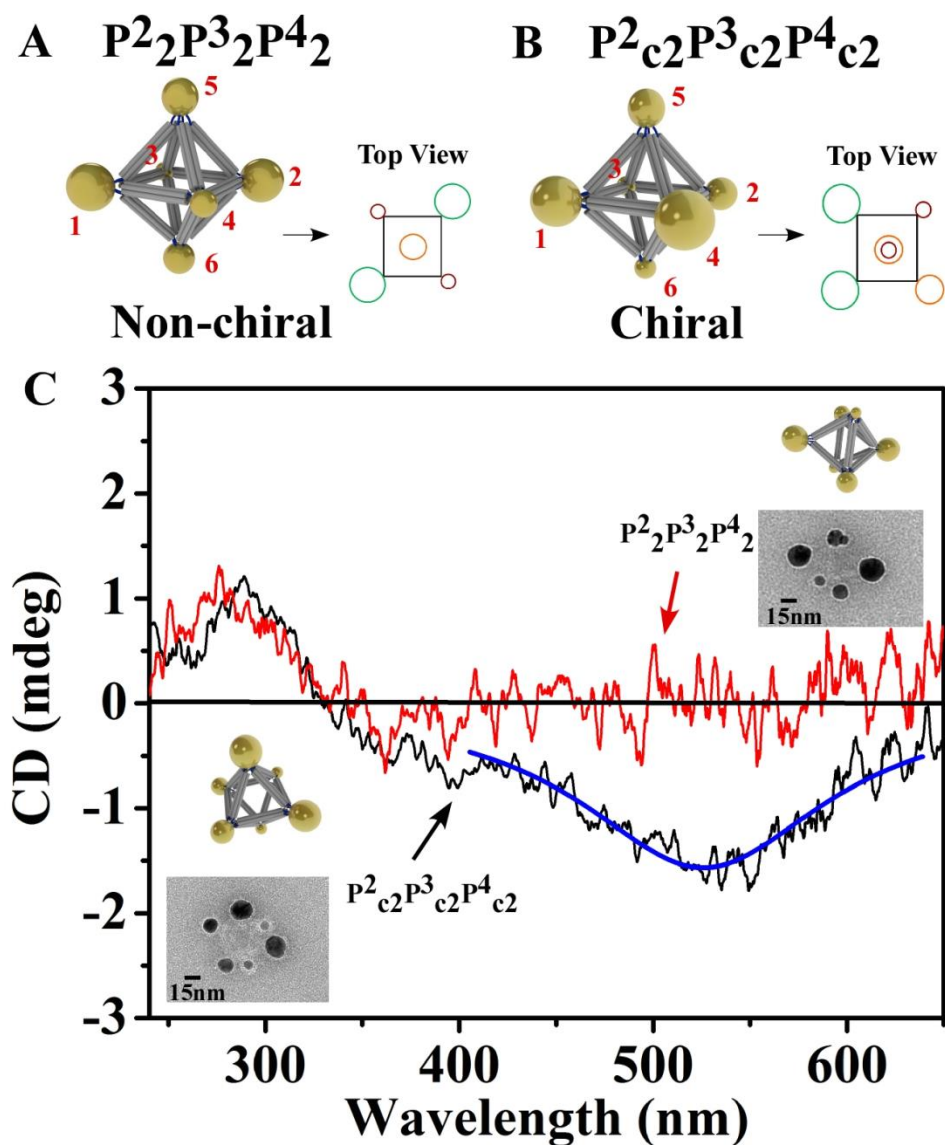


Figure 6.16 CD spectra of octahedron based non-chiral cluster $P^2_2(34)P^3_2(56)P^4_2(12)$ (denoted as $P^2_2P^3_2P^4_2$) and chiral cluster $P^2_2(26)P^3_2(35)P^4_2(14)$ (denoted as $P^2_{c2}P^3_{c2}P^4_{c2}$). (A). Model of non-chiral cluster $P^2_2P^3_2P^4_2$ with its top view. (B). Model of chiral cluster $P^2_{c2}P^3_{c2}P^4_{c2}$ with its top view. (C). Red line is the CD spectrum for cluster $P^2_2P^3_2P^4_2$. The representative TEM image and the model with same orientation are shown at the right top corner. Black line is the CD spectrum for cluster $P^2_{c2}P^3_{c2}P^4_{c2}$ and the blue line is the Lorentzian fit. The representative TEM image and model with same orientation are shown at the low left corner. The CD peaks for both clusters at about 270 nm are from DNA.

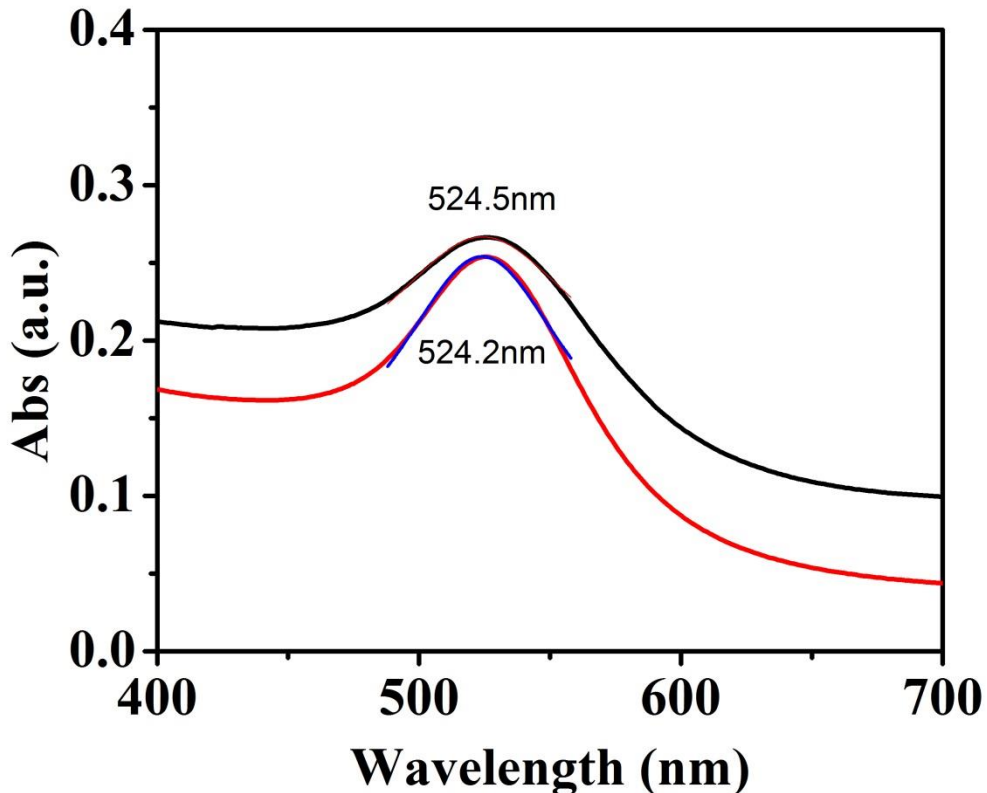


Figure 6.17 UV-vis spectra of the cluster ‘ $P_1P_2P_3$ ’ (red line) and ‘ $P_1^cP_2^cP_3^c$ ’ (black line). Lorentz fitting was applied to obtain the peak positions of the two curves.

We have further explored the use of the specifically encoded octahedron frame as linking element between NPs for building low-dimensional, 1D and 2D, nanoparticle arrays. In this case the linking symmetry and the resulting structure of the array are determined by the choice of octahedron vertices utilized for inter-particle connections. We prescribe these 1D and 2D arrays by encoding the octahedron to carry 2-fold (Figure 6.18A) and 4-fold (Figure 6.18D) symmetries, respectively. More specifically, the frame with 2-fold symmetry contains two vertices with encoding for particle recognition at two ends of the major octahedron diagonal; consequently, this design should result in the linear arrangements of NPs linked by the 2-fold

linking frame. Expanding this approach, we can direct the assembly of a 2D square array (D4 symmetry) by encoding the four octahedron vertices, lying in the same plane, for NPs binding. To realize this idea for assembly of low-dimensional arrays we mixed octahedra with 10nm gold NPs at the ratio of 1:1. After careful annealing (0.3 °C /h from 50 °C to 20 °C) red loose precipitates or black aggregates appeared gradually for 1D and 2D cases, respectively. The samples were then loaded into a glass capillaries and probed by Small Angle X-ray Scattering (SAXS), as previously described^{44,100}. Two-dimensional scattering patterns were collected from the assemblies, and structure factors, $S(q)$, where q is the wave vector, were obtained by the radial integration and normalization by NP form factor.

The structure factor for the NP assembly induced by the two-fold encoded octahedron (Figure 6.18C) exhibits five peaks, with peak position located at $q/q_1 \sim 1, 1.8, 2.7, 3.5, 4.3$ (q_1 is the position of the first peak). Such structure factor can be reasonably well described (Figure 6.18C, blue curve) by dumbbell model^{175,176} with functional form $S(q) \sim \sin(dq)/dq$, where d is a distance between the NP centers, thus, indicating scattering signature of the NP pairs. The flexibility of 1D array at the points of octahedron attachment to NPs and the large angle over which the attachment can occur, contribute to the non-collinearity of 1D array. The fit yields $d=67.4$ nm which is close to the expected value based on the design parameters. We further confirmed (Figure 6.18B) the structure of this array by TEM imaging, which shows the morphology and inter-NP distance ($d=63$ nm), in agreement with the in-situ SAXS results.

The structure of assembly induced by the octahedron with 4-fold symmetry NP connection was initially revealed by SAXS. The observed $S(q)$ peaks signify a 2D NP square array (Figure 6.18F) with interparticle distance of 47.5nm, which is in agreement with 46.4nm obtained from the model (see supporting information). The deviation of higher order peaks towards larger q

from the calculated values can be attributed to the flexibility of 2D NP-octahedron sheet in the solution. Such structure agrees with the array design (Figure 6.18E, left model). Indeed, in the formed 2D square arrays the four in-plane vertices (Figure 6.18D) are bound to four gold NPs, while each NP binds four octahedra (the vertices below and above the plane are silent). The size of 2D crystallites is 0.2 μm , as estimated from the scattering peak width, and their melting temperature is about 39 $^{\circ}\text{C}$, as detected by DLS measurements (Figure 6.19). The ex-situ visualization with TEM (Figure 6.18E, right) concurs with the SAXS results, and it closely resembles the model arrangement: a 2D square array of NPs in which they are linked by 4-fold binding octahedron.

6.4 Conclusion

The presented studies demonstrate that three-dimensional nanoparticle clusters can be effectively created using the strategy based on the rigid 3D DNA frame with encoded sites for nanoparticles positioning. The example of such approach based on the octahedron, allows for arranging particles in 3D with nearly nanometer precision in the designed non-periodic structure, as confirmed by our detailed visualization using cryo-EM methods. Based on such precise cluster assembly, nano-architectures with different chiroptical activities were created using the same set of nanoparticles but different frame encodings. Moreover, we demonstrated that the designed arrangement of NPs in 1D and 2D arrays could be achieved by prescribing specific vertices of octahedron as NP connecting sites. The structural integrity of DNA frame ensures proper nanoparticles coordination, while DNA origami methodology provides a predictable frame fabrication. Our work opens up numerous exciting opportunities for high-yield precise assembly of tailored 3D mesoscale building blocks, in which multiple nanoparticles of different structures and functions can be integrated.

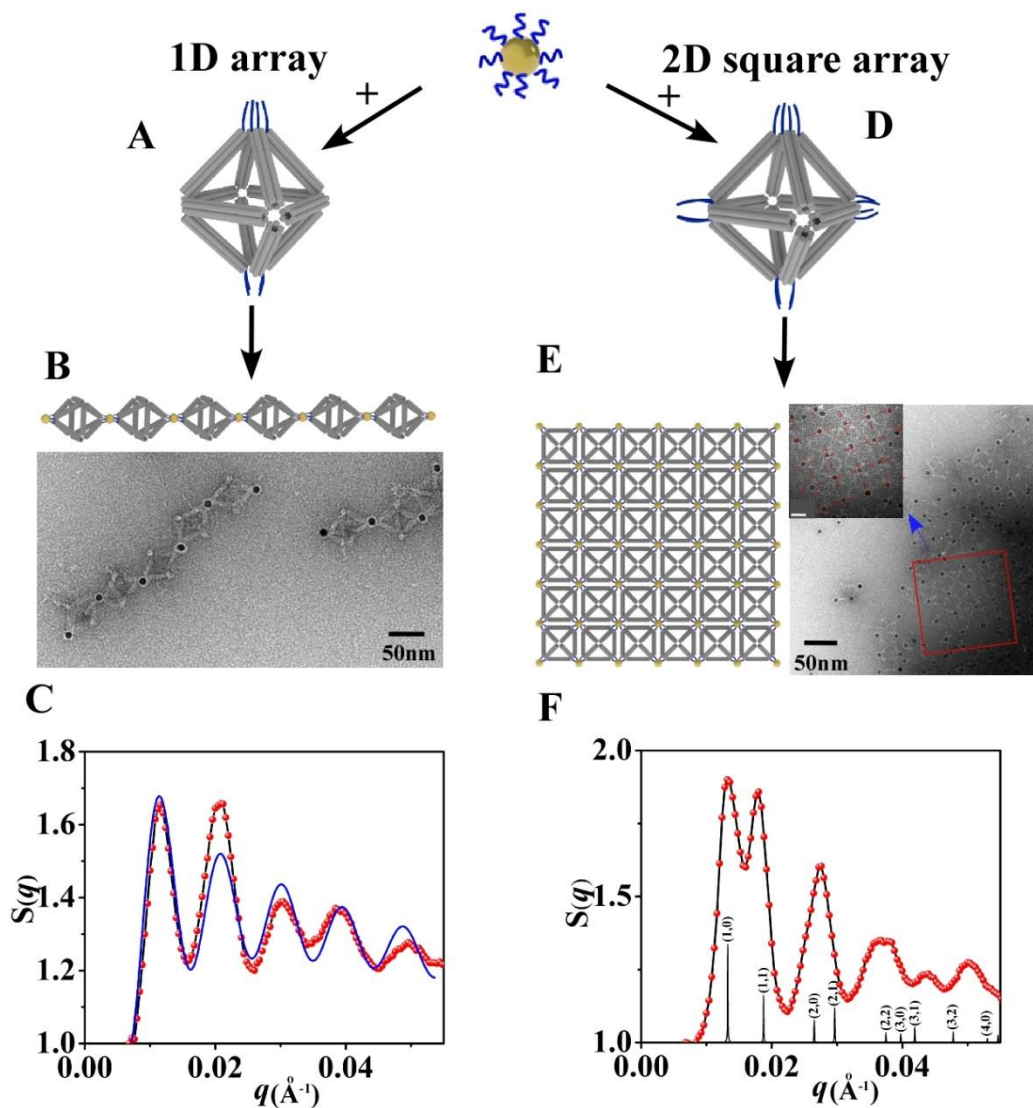


Figure 6.18 Encoded octahedra link NPs with 2-fold or 4-fold symmetries for corresponding assembly of low-dimensional, linear 1D and square 2D, NP arrays. (A). Model of octahedral DNA origami with 2-fold symmetry NP binding for assembly of 1D array. (B). The model of 1D array (upper) and the representative negative stained TEM image of formed 1D array (below). (C). Extracted structure factor $S(q)$ for 1D array from in-situ SAXS pattern (red points is a measurement, and the blue line is fitting as described in the text). (D). The model of octahedral DNA origami with 4-fold symmetry NP binding for assembly of 2D square array. (E). The model of 2D square array and the representative negative stained TEM image of formed 2D NP-

octahedra array (inset is a zoomed picture of selected area; bar scale is 20nm). (F). Extracted structure factor $S(q)$ for 2D NP array (red line) and the simulated 2D scattering pattern (black lines with diffraction peak indexes).

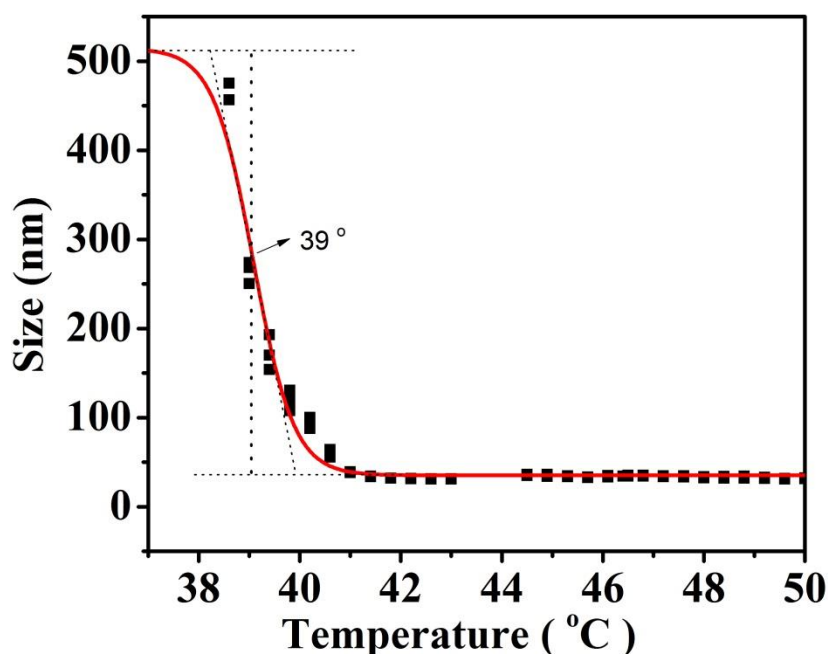


Figure 6.19. Dynamic process by detecting the size of participants after mixing NPs and octahedron for the formation of 2D array crystals by DLS. Sample was annealed from 50 °C to room temperature with the rate of 4 °C /h. Melting temperature was around 39 °C for the 2D array system.

6.5 Methods

Octahedron origami was prepared by mixing 20 nM scaffold (M13mp18), 100 nM of each staple oligonucleotide, buffer and salts. Buffer solution contains 1 mM EDTA, 12.5 mM $MgCl_2$, 5 mM Tris (pH=7.9 at 20°C). Folding of octahedron origami was carried out by carefully annealing the mixed sample. Briefly, the sample was rapidly heated from room temperature to 90 °C, followed by slow cooling from 80 °C to 61 °C over 80 min, then 60°C to 24°C over 12 h. Samples were

then electrophoresed on 1% agarose gels ($0.5 \times$ TBE, 11 mM MgCl_2 , 0.5 $\mu\text{g/ml}$ cyber gold) at 100 V for 2 h in cold room (4°C). Bands of target structures were visualized in ultraviolet light, as shown in Figure 6.2. The target bands were then cut, crushed and filtered through a cellulose-acetate spin column for 3 min at $15,000 \times g$ in cold room (4°C).

The mixing ratio of gold nanoparticles and octahedral DNA origami was different for each of the three studied systems. Briefly, the molar ratio of NPs and the octahedral apexes with particle encoding ssDNA was 2.5:1. The mixture was then diluted in $1 \times$ TAE (1 mM EDTA, 5 mM Tris with $\text{pH}=7.9$ at 20°C) buffer solution with 12.5 mM MgCl_2 and annealed in a PCR device from 50°C to room temperature in 3 hr. This mixture solution was also electrophoresed in 1% agarose gels ($0.5 \times$ TBE, 11 mM MgCl_2 , 0.5 $\mu\text{g/ml}$ cyber gold) at 100 V for 2 h in cold room (4°C). The gel bands containing target structure were visualized in ultraviolet light and white light, as shown in Figure 6.2. The target band was then cut out, crushed and filtered through the cellulose-acetate spin column for 3 min at $15,000 \times g$ in cold room (4°C) to retrieve the fully assembled clusters for EM.

Transmission electron microscopy (TEM) is often used to capture of image at a significantly high resolution than light scattering. When a beam of electrons transmitted through an ultra-thin specimen, for example, single layer of carbon, the image is formed by the interaction of electrons which have transmitted through the specimen. It was then magnified and focused to be detected by CCD camera. In our specific case, in order to get the clear information of DNA, we should be stained it because of its low contraction compared with the background and gold nanoparticles.

To prepare negative staining EM grids, a layer of carbon film (~ 20 nm thick) was evaporated on a piece of freshly cleaved mica in the Edwards vacuum evaporator ($< 10^{-5}$ Torr). Carbon film was

then peeled off of mica by floating it on the surface of deionized water, deposited on the 300 mesh copper grids. Cryo-EM grids were either purchased from Ted Pella, Inc. (Prod # 01824) or prepared in a similar way as for the negative staining grids: a thin layer of carbon film (~ 2 nm thickness) was prepared and deposited on the lacey carbon coated EM grids. All homemade continuous carbon coated grids were air-dried before usage.

All carbon coated grids were first glow discharged in 100 mT argon atmosphere for 1 min. A drop of 4-5 μl of sample solution was applied to the glow-discharged continuous carbon coated grid and incubated for 3-5 min. Excess solution was removed by blotting the grid with a piece of filter paper. The grid was then washed by a drop of ddH₂O and stained by 4 μl 2% (w/v) uranyl acetate aqueous solution for 15 s. After blotting excess stain solution the grid was left for air-dry. The negatively stained sample was imaged in a JEOL JEM-2010F TEM operating at 200 kV or in a JEOL JEM-1400 TEM operating at 120 kV. Cryo-EM grids were prepared in an FEI Vitrobot at 11 °C (DNA only) or 21 °C (DNA-NP conjugates) with the relative humidity set to 90% and the blotting pad height offset to -1.0 mm. 3.5 μl of DNA specimen was pipetted onto a freshly glow-discharged lacey carbon grid covered with an additional thin layer of continuous carbon film. The sample solution was incubated on EM grid for 3 min, blotted for 5 s before being plunged into liquid ethane that was pre-cooled by liquid nitrogen. The cryo-EM grids were then transferred to and stored in liquid nitrogen. The cryo-EM grids were transferred in liquid nitrogen into a Gatan 626 cryo-specimen holder and then inserted into the microscope. The specimen temperature was maintained at -170 °C during data collection. Cryo-EM imaging was performed in JEOL JEM-2010F TEM operating at 200 kV. Cryo-EM images were recorded in the low-dose mode ($15 \text{ e}^-/\text{\AA}^2$) at 30,000 \times microscope magnification on a Gatan UltraScan 4000 CCD camera ($4,096 \times 4,096$ pixel), corresponding to 3.52 \AA /pixel sampling at the specimen

level. To collect data for Electron tomography, series of cryo-EM images tilted from -60° to $+60^\circ$ with 10° intervals were obtained under the same condition as described above except that the microscope magnification is $20,000\times$, corresponding to $5.29 \text{ \AA}/\text{pixel}$ sampling at the specimen level.

Negatively stained sample were prepared for checking the sample quality and for calculating the particle statistics. Only cryo-EM images were used for further processing and 3D reconstruction. Particle selection and image processing were done using EMAN and EMAN2 software package. For 3D reconstruction of the DNA octahedral which would be discussed in chapter 6, raw particle images were selected in a semi-automatic manner with *e2boxer.py* in EMAN2. The pooled raw images were manually inspected in order to remove “bad” particles (partially assembled, of low contrast, or contacting other particles). The contrast transfer function (CTF) was first determined with raw images and corrected for by flipping the phases in EMAN2. The phase-flipped data were then subject to 2D image classification in an iterative manner. Particle images assigned to the same class are mutually aligned and averaged to generate a set of high-contrast class averages that are representative views of the particle structure. Reference-based and reference-free 2D classifications of image data set were done by *classesbymra* and *e2refine2d.py*, respectively. Reference-free 2D averages were used to calculate starting models by *e2initialmodel.py*. The starting model was low-pass filtered and used for 3D refinement against the phase-flipped raw image dataset by *e2refine.py* in EMAN2. The resolution of the final 3D map was estimated by the so-called “Gold standard” Fourier shell correlation method at the threshold of 0.143. For 3D reconstruction of the DNA-NP complexes, a similar procedure was used except that we simply inverted the image contrast without going through the full CTF correction route. This is justified because the gold particle images are largely of scattering

contrast and that the DNA contrast is overwhelmed by the extremely strong gold scattering. Separation of the gold particle images in the raw image of the DNA-NP clusters was done by the command “*DU*” or “*DU V*” in the SPIDER software package. All image processing and 3D reconstruction were done on an 8-CPU Dell Linux workstation. 3D density map was displayed and manipulated in Chimera package. Standard B-DNA model (theoretical) with 84 base pairs in length was built by the DNA modeling web server 3D-DART. Six copies of the DNA duplex model were manually put together in a close pack fashion in Chimera to generate our 6HB atomic model. When viewed down the long axis of the bundle, the six DNA duplexes are arranged in a honeycomb shape with a hollow channel in the center. The 6HB atomic model was then docked automatically as a single rigid body into the 3D EM map with the command “Fit in Map” in the Chimera program. We used a model-based method to rapidly reconstruct the three-dimensional architecture of nanoparticle assemblies in real space. The model based tomographic method relies only on the projected centroids of the nanoparticles and bypasses the image intensity. This method requires only 5-10 tilt images and is often useful to calibrate a TEM goniometer or to detect field/scan distortions.

The nominal core sizes of the gold NPs used in this study were 7 nm, 10 nm, and 15 nm. We measured the size of free NPs in EM images using the software ‘Image J’. We found the average sizes of the three types of NPs are 6.6 ± 0.7 nm, 9.8 ± 0.7 nm and 15.4 ± 2.0 nm respectively.

HPLC purified DNA oligonucleotides were purchased as lyophilized powders (Integrated DNA Technologies Inc.). The staple DNA was purified with standard desalting method. The DNA sequences (5’ to 3’) were:

(1) s1 (used for functionalization of the 7 nm gold NPs for assembling the P_6 cluster and the $P^1_2P^2_2P^3_2$ cluster) : HS-C₆H₁₂-TT;

(2) s2 (functionalization for 10nm gold NPs for cluster P_4 and for cluster $P^1_2P^2_2P^3_2$): HS-C₆H₁₂-TTTTTTTTTTTTTTTTATC CTTATCAATATT;

(3) s3 (functionalization for 15nm gold NPs for cluster $P^1_2(12)P^2_2(34)P^3_2(56)$): HS-C₆H₁₂-TTTTTTTTTTTT TTTTAA CCTAACCTTCAT;

(4) Staple sequences for octahedra origami folding:

TCAAAGCGAACCAGACCGTTTTATATAGTC;
GCTTTGAGGACTAAAGAGCAACGGGGAGTT;
GTAAATCGTCGCTATTGAATAACTCAAGAA;
AAGCCTTAAATCAAGACTTGCGGAGCAAAT;
ATTTTAAGAAGCTGGCTTGAATTATCAGTGA;
GTAAAATTTCGCATTATAAACGTAAACTAG;
AGCACCATTACCATTACAGCAAATGACGGA;
ATTGCGTAGATTTTCAAACAGATTGTTTG;
TAACCTGTTTAGCTATTTTCGCATTCATTC;
GTCAGAGGGTAATTGAGAACACCAAATAG;
CTCCAGCCAGCTTTCCCCTCAGGACGTTGG;
GTCCACTATTAAAGAACCAGTTTTGGTTCC;
TAAAGGTGGCAACATAGTAGAAAATAATAA;
GATAAGTCCTGAACAACCTGTTTAAAGAGAA;
GGTAATAGTAAAATGTAAGTTTTACACTAT;

TCAGAACCGCCACCCTCTCAGAGTATTAGC;
AAGGGAACCGAACTGAGCAGACGGTATCAT;
GTAAAGATTCAAAAGGCCTGAGTTGACCCT;
AGGCGTTAAATAAGAAGACCGTGTCGCAAG;
CAGGTCGACTCTAGAGCAAGCTTCAAGGCG;
CAGAGCCACCACCCTCTCAGAACTCGAGAG;
TTCACGTTGAAAATCTTGCGAATGGGATTT;
AAGTTTTAACGGGGTTCGGAGTGTAGAATGG;
TTGCGTATTGGGCGCCCGCGGGGTGCGCTC;
GTCACCAGAGCCATGGTGAATTATCACCAATCAGAAAAGCCT;
GGACAGAGTTACTTTGTCGAAATCCGCGTGTATCACCGTACG;
CAACATGATTTACGAGCATGGAATAAGTAAGACGACAATAAA;
AACCAGACGCTACGTTAATAAAAACGAACATACCACATTCAGG;
TGACCTACTAGAAAAAGCCCCAGGCAAAGCAATTTTCATCTTC;
TGCCGGAAGGGGACTCGTAACCGTGCATTATATTTTAGTTCT;
AGAACCCCAAATCACCATCTGCGGAATCGAATAAAAATTTTT;
GCTCCATTGTGTACCGTAACACTGAGTTAGTTAGCGTAACCT;
AGTACCGAATAGGAACCCAAACGGTGTAACCTCAGGAGGTTT;
CAGTTTGAATGTTTAGTATCATATGCGTAGAATCGCCATAGC;
AAGATTGTTTTTTAACCAAGAAACCATCGACCCAAAAACAGG;
TCAGAGCGCCACCACATAATCAAAATCAGAACGAGTAGTATG;
GATGGTTGGGAAGAAAAATCCACCAGAAATAATTGGGCTTGA;
CTCCTTAACGTAGAAACCAATCAATAATTCATCGAGAACAGA;

AGACACCTTACGCAGAACTGGCATGATTTTCTGTCCAGACAA;
GCCAGCTAGGCGATAGCTTAGATTAAGACCTTTTTAACCTGT;
CCGACTTATTAGGAACGCCATCAAAAATGAGTAACAACCCCA;
GTCCAATAGCGAGAACCAGACGACGATATTCAACGCAAGGGA;
CCAAAATACAATATGATATTCAACCGTTAGGCTATCAGGTAA;
AACAGTACTTGAAAACATATGAGACGGGTCTTTTTTAATGGA;
TTTCACCGCATTAAAGTCGGGAAACCTGATTTGAATTACCCA;
GAGAATAGAGCCTTACCGTCTATCAAATGGAGCGGAATTAGA;
ATAATTAATTTAAAAAACTTTTTCAAACCTTTTAACAACGCC;
GCACCCAGCGTTTTTTATCCGGTATTCTAGGCGAATTATTCA;
GGAAGCGCCACAAACAGTTAATGCCCCGACTCCTCAAGATA;
GTTTGCCTATTCACAGGCAGGTCAGACGCCACCACACCACCC;
CGCGAGCTTAGTTTTTCCCAATTCTGCGCAAGTGTAAGCCT;
AGAAGCAACCAAGCCAAAAGAATACACTAATGCCAAAACCTCC;
ATTAAGTATAAAGCGGCAAGGCAAAGAACTAATAGGGTACC;
CAGTGCCTACATGGGAATTTACCGTTCCACAAGTAAGCAGAT;
ATAAGGCGCCAAAAGTTGAGATTTAGGATAACGGACCAGTCA;
TGCTAAACAGATGAAGAAACCACCAGAATTTAAAAAAAGGCT;
CAGCCTTGTTTTTGTATTAAGAGGCTGACTGCCTATATCAGA;
CGGAATAATTCAACCCAGCGCCAAAGACTTATTTAACGCAA;
CGCCTGAATTACCCTAATCTTGACAAGACAGACCATGAAAGA;
ACGCGAGGCTACAACAGTACCTTTTACAAATCGCGCAGAGAA;
CAGCGAACATTAAGAGAGAGTACCTTTACTGAATATAATGAA;

GGACGTTTAATTTTCGACGAGAAACACCACCACTAATGCAGAT;
AAAGCGCCAAAGTTTATCTTACCGAAGCCCAATAATGAGTAA;
GAGCTCGTTGTAAACGCCAGGGTTTTCCAAAGCAATAAAGCC;
AATTATTGTTTTTCATGCCTTTAGCGTCAGATAGCACGGAAAC;
AAGTTTCAGACAGCCGGGATCGTCACCCTTCTGTAGCTCAAC;
ACAAAGAAATTTAGGTAGGGCTTAATTGTATACAACGGAATC;
AACAAAAATAACTAGGTCTGAGAGACTACGCTGAGTTTCCCT;
CATAACCTAAATCAACAGTTCAGAAAACGTCATAAGGATAGC;
CACGACGAATTCGTGTGGCATCAATTCTTTAGCAAAATTACG;
CCTACCAACAGTAATTTTATCCTGAATCAAACAGCCATATGA;
GATTATAAAGAAACGCCAGTTACAAAATTTACCAACGTCAGA;
AGTAGATTGAAAAGAATCATGGTCATAGCCGGAAGCATAAGT;
TAGAATCCATAAATCATTAAACAATTTCTCCCGGCTTAGGTT;
AAAGGCCAAATATGTTAGAGCTTAATTGATTGCTCCATGAGG;
CCAAAAGGAAAGGACAACAGTTTCAGCGAATCATCATATTCC;
GAAATCGATAACCGGATACCGATAGTTGTATCAGCTCCAACG;
TGAATATTATCAAATAATGGAAGGGTTAATATTTATCCCAA;
GAGGAAGCAGGATTCGGGTAAAATACGTAAAACACCCCCCAG;
GGTTGATTTTCCAGCAGACAGCCCTCATTCGTCACGGGATAG;
CAAGCCCCACCCTTAGCCCCGAATAGGACGATCTAAAGTTT;
TG TAGATATTACGCGGCGATCGGTGCGGGCGCCATCTTCTGG;
CATCCTATTCAGCTAAAAGGTAAAGTAAAAAGCAAGCCGTTT;
CAGCTCATATAAGCGTACCCCCGGTTGATGTGTCGGATTCTCC;

CATGTCACAAACGGCATTAAATGTGAGCAATTCGCGTTAAAT;
AGCGTCACGTATAAGAATTGAGTTAAGCCCTTTTAAAGAAAG;
TATAAAGCATCGTAACCAAGTACCGCACCGGCTGTAATATCC;
ATAGCCCGCGAAAATAATTGTATCGGTTGCGCGACAATGAGT;
AGACAGTTCATATAGGAGAAGCCTTTATAACATTGCCTGAGA;
AACAGGTCCCGAAATTGCATCAAAAAGATCTTTGATCATCAG;
ACTGCCCTTGCCCCGTTGCAGCAAGCGGCAACAGCTTTTTCT;
TCAAAGGGAGATAGCCCTTATAAATCAAGACAACAACCATCG;
GTAATACGCAAACATGAGAGATCTACAACCTAGCTGAGGCCGG;
GAGATAACATTAGAAGAATAACATAAAAAGGAAGGATTAGGA;
CAGATATTACCTGAATACCAAGTTACAATCGGGAGCTATTTT;
CATATAACTAATGAACACAACATACGAGCTGTTTCTTTGGGG;
ATGTTTTGCTTTTGATCGGAACGAGGGTACTTTTTCTTTGATAAGAGGTCATT;
GGGGTGCCAGTTGAGACCATTAGATACAATTTTCACTGTGTGAAATTGTTATCC;
CTTCGCTGGGCGCAGACGACAGTATCGGGGCACCGTCGCCATTCAGGCTGCGCA;
TCAGAGCTGGGTAAACGACGGCCAGTGCGATCCCCGTAGTAGCATTAAACATCCA;
TTAGCGGTACAGAGCGGGAGAATTAACCTGCGCTAATTTGGAACCTATTATTCT;
GATATTCTAAATTGAGCCGGAACGAGGCCCAACTTGGCGCATAGGCTGGCTGAC;
TGTCGTCATAAGTACAGAACCGCCACCCATTTTACAGTACAACTACAACGCC;
CGATTATAAGCGGAGACTTCAAATATCGCGGAAGCCTACGAAGGCACCAACCTA;
AACATGTACGCGAGTGGTTTGAATACCTAAACACATTCTTACCAGTATAAAGC;
GTCTGGATTTTGCCTTTTAAATGCAATGGTGAGAAATAAATTAATGCCGGAGAG;
GCCTTGAATCTTTTCCGGAACCGCCTCCAGAGCCCAGAGCCGCCGCCAGCATT;

CGCTGGTGCTTTCCTGAATCGGCCAACGAGGGTGGTGATTGCCCTTCACCGCCT;
TGATTATCAACTTTACAATAAAGGAATCCAAAAGTTTGAGTAACATTATCAT;
ACATAACTTGCCCTAACTTTAATCATTGCATTATAACAACATTATTACAGGTAG;
GTAGCGCCATTAAATTGGGAATTAGAGCGCAAGGCGCACCGTAATCAGTAGCGA;
TTATTTTTACCGACAATGCAGAACGCGCGAAAAATCTTTCCTTATCATTCCAAG;
TTTCAATAGAAGGCAGCGAACCTCCCGATTAGTTGAAACAATAACGGATTTCGCC;
GGGCGACCCCAAAGTATGTTAGCAAACCTAAAAGAGTCACAATCAATAGAAAAT;
AGCCGAAAGTCTCTCTTTTGTATGATACAAGTGCCTTAAGAGCAAGAAACAATGA;
GTGGGAAATCATATAAATATTTAAATTGAATTTTTGTCTGGCCTTCCTGTAGCC;
CCCACGCGCAAATGGTTGAGTGTTGTTTCGTGGACTTGCTTTCGAGGTGAATTT;
ATGACCACTCGTTTGGCTTTTGCAAAAGTTAGACTATATTCATTGAATCCCCCT;
TCCAAATCTTCTGAATTATTTGCACGTAGGTTTAACGCTAACGAGCGTCTTTCC;
GGGTTATTTAATTACAATATATGTGAGTAATTAATAAGAGTCAATAGTGAATTT.

(5) Staple strands with sticky end

For cluster P₆:

TTTGCGGATGGCCAACTAAAGTACGGGCTTGCAGCTACAGAGAAAAAAAAAAAA
AAA;
CTTCATCAAGAGAAATCAACGTAACAGAGATTTGTCAATCATAAAAAAAAAAAAA
AAA;
AAAGATTCATCAGGAATTACGAGGCATGCTCATCCTTATGCGAAAAAAAAAAAA
AAA;

ATAAATCATAACATAAATCGGTTGTACTGTGCTGGCATGCCTGAAAAAAAAAAAA
AAA;
GGTAGCTATTTTAGAGAATCGATGAAAACATTAATGTGTAGAAAAAAAAAAAA
AAA;
CAAATGCTTTAAAAAATCAGGTCTTTAAGAGCAGCCAGAGGGAAAAAAAAAAAA
AAA;
TCATATGGTTTACGATTGAGGGAGGGAAACGCAATACATACAAAAAAAAAAAA
AAA;
CAACGCTCAACAGCAGAGGCATTTTCAATCCAATGATAAATAAAAAAAAAAAAA
AAA;
AATAGCAATAGCACCAGAAGGAAACCTAAAGCCACTGGTAATAAAAAAAAAAAAA
AAAA;
GACAGGAGGTTGAAACAAATAAATCCGCCCCCTCCGCCACCCAAAAAAAAAAAA
AAA;
AGCTTTCATCAACGGATTGACCGTAAAATCGTATAATTTTTAAAAAAAAAAAA
AA;
AGAGCCTAATTTGATTTTTTTGTTTAAATCCTGAAATAAAGAAAAAAAAAAAA
AAA;
GCTCACAATTCCGTGAGCTAACTCACTGGAAGTAATGGTCAAAAAAAAAAAAA
AAA;
CTTAAACAGCTTATATATTCGGTCGCTTGATGGGGAACAAGAAAAAAAAAAAA
AAA;
AAACGAAAGAGGGCGAAACAAAGTACTGACTATATTCGAGCTAAAAAAAAAAAA

AAAA;
ACTGTTGGGAAGCAGCTGGCGAAAGGATAGGTCAAGATCGCAAAAAAAAAAAAA
AAAA;
GGCCCTGAGAGAAGCAGGCGAAAATCATTGCGTAGAGGCGGTAAAAAAAAAAAA
AAAA;
AACGGGTATTAAGGAATCATTACCGCCAGTAATTCAACAATAAAAAAAAAAAAA
AAA;
CAGAATCAAGTTTCGGCATTTCGGTTAAATATATCACCAGTAAAAAAAAAAAA
AAA;
GAAACATGAAAGCTCAGTACCAGGCGAAAAATGCTGAACAAAAAAAAAAAA
AAAA;
ATCAAATCATATATGTAAATGCTGAACAAACACTTGCTTCTAAAAAAAAAAAA
AAA;
TGATTGCTTTGAGCAAAAAGAAGATGAAATAGCAGAGGTTTTGAAAAAAAAAAAA
AAA;
TTTGCGGAACAATGGCAATTCATCAATCTGTATAATAATTTTAAAAAAAAAAAA
AA;
TGTAGCATTCCAACGTTAGTAAATGAAGTGCCGCGCCACCCTAAAAAAAAAAAA
AAA.

For cluster P₄(1234):

TTTGCGGATGGCCAACATAAAGTACGGGCTTGCAGCTACAGAGAAAAAAAAAAAA

AAA;
CTTCATCAAGAGAAATCAACGTAACAGAGATTTGTCAATCATAAAAAAAAAAAAA
AAA;
AAAGATTCATCAGGAATTACGAGGCATGCTCATCCTTATGCGAAAAAAAAAAAA
AAA;
ATAAATCATAATAAATCGGTTGTACTGTGCTGGCATGCCTG;
GGTAGCTATTTTAGAGAATCGATGAAAACATTAATGTGTAG;
CAAATGCTTTAAAAAATCAGGTCTTTAAGAGCAGCCAGAGGGAAAAAAAAAAAA
AAA;
TCATATGGTTTACGATTGAGGGAGGGAAACGCAATACATACAAAAAAAAAAAA
AAA;
CAACGCTCAACAGCAGAGGCATTTTCAATCCAATGATAAATAAAAAAAAAAAAA
AAA;
AATAGCAATAGCACCAGAAGGAAACCTAAAGCCACTGGTAATAAAAAAAAAAAAA
AAAA;
GACAGGAGGTTGAAACAAATAAATCCGCCCCCTCCGCCACCCAAAAAAAAAAAA
AAA;
AGCTTTCATCAACGGATTGACCGTAAAATCGTATAATATTTT;
AGAGCCTAATTTGATTTTTTTGTTTAAATCCTGAAATAAAGAA;
GCTCACAATTCCGTGAGCTAACTCACTGGAAGTAATGGTCAAAAAAAAAAAAA
AAA;
CTTAAACAGCTTATATATTCGGTCGCTTGATGGGGAACAAGAAAAAAAAAAAA
AAA;

AAACGAAAGAGGGCGAAACAAAGTACTGACTATATTCGAGCTAAAAAAAAAAAA
AAAA;
ACTGTTGGGAAGCAGCTGGCGAAAGGATAGGTCAAGATCGCA;
GGCCCTGAGAGAAGCAGGCGAAAATCATTGCGTAGAGGCGGTAAAAAAAAAAAA
AAAA;
AACGGGTATTAAGGAATCATTACCGCCAGTAATTCAACAATAAAAAAAAAAAAA
AAA;
CAGAATCAAGTTTCGGCATTTCGGTTAAATATATCACCAGTAAAAAAAAAAAA
AAA;
GAAACATGAAAGCTCAGTACCAGGCGAAAAATGCTGAACAAA;
ATCAAATCATATATGTAAATGCTGAACAAACACTTGCTTCTAAAAAAAAAAAA
AAA;
TGATTGCTTTGAGCAAAAGAAGATGAAATAGCAGAGGTTTTGAAAAAAAAAAAA
AAA;
TTTGCGGAACAATGGCAATTCATCAATCTGTATAATAATTTT;
TGTAGCATTCCAACGTTAGTAAATGAAGTGCCGCGCCACCCT.

For cluster $P^1_2(12)P^2_2(34)P^3_2(56)$:

TTTGCGGATGGCCAACTAAAGTACGGGCTTGCAGCTACAGAGAATATTGATAAGGA
T;
CTTCATCAAGAGAAATCAACGTAACAGAGATTTGTCAATCATATGAAGGTTAGGTT
A;

AAAGATTCATCAGGAATTACGAGGCATGCTCATCCTTATGCGATGAAGGTTAGGTT
A;
ATAAATCATACATAAATCGGTTGTACTGTGCTGGCATGCCTGAAAAAAAAAAAAAAAA
A;
GGTAGCTATTTTAGAGAATCGATGAAAACATTAATGTGTAGAAAAAAAAAAAAAAAA
AA;
CAAATGCTTTAAAAAATCAGGTCTTTAAGAGCAGCCAGAGGGATGAAGGTTAGGTT
A;
TCATATGGTTTACGATTGAGGGAGGGAAACGCAATACATACAAATATTGATAAGGA
T;
CAACGCTCAACAGCAGAGGCATTTTCAATCCAATGATAAATAATGAAGGTTAGGTT
A;
AATAGCAATAGCACCAGAAGGAAACCTAAAGCCACTGGTAATAATATTGATAAGG
AT;
GACAGGAGGTTGAAACAAATAAATCCGCCCCCTCCGCCACCCAATATTGATAAGGA
T;
AGCTTTCATCAACGGATTGACCGTAAAATCGTATAATATTTTAAAAAAAAAAAAAAAA
A;
AGAGCCTAATTTGATTTTTTTGTTTAAATCCTGAAATAAAGAAAAAAAAAAAAAAAA
A;
GCTCACAATTCCGTGAGCTAACTCACTGGAAGTAATGGTCAAAATATTGATAAGGA
T;
CTTAAACAGCTTATATATTCGGTCGCTTGATGGGGAACAAGAAATATTGATAAGGA

T;

AAACGAAAGAGGGCGAAACAAAGTACTGACTATATTCGAGCTATGAAGGTTAGGT

TA;

ACTGTTGGGAAGCAGCTGGCGAAAGGATAGGTCAAGATCGCAAAAAAAAAAAAAA

AA;

GGCCCTGAGAGAAGCAGGCGAAAATCATTGCGTAGAGGCGGTAATATTGATAAGG

AT;

AACGGGTATTAAGGAATCATTACCGCCAGTAATTCAACAATAATGAAGGTTAGGTT

A;

CAGAATCAAGTTTCGGCATTTCGGTTAAATATATCACCAGTAATATTGATAAGGAT

;

GAAACATGAAAGCTCAGTACCAGGCGAAAAATGCTGAACAAAAAAAAAAAAAAAAA

AAA;

ATCAAAATCATATATGTAAATGCTGAACAAACACTTGCTTCTATGAAGGTTAGGTT

A;

TGATTGCTTTGAGCAAAAGAAGATGAAATAGCAGAGGTTTTGATGAAGGTTAGGTT

A;

TTTGCAGCAACAATGGCAATTCATCAATCTGTATAATAATTTTAAAAAAAAAAAAAAAAA

A;

TGTAGCATTCCAACGTTAGTAAATGAAGTGCCGCGCCACCCTAAAAAAAAAAAAAAAAA

AA.

Chapter 7

Rational Assembly of 3D Superlattices of Nanoparticle via Symmetric DNA Origami Structures

Abstract

Programmable assembly of a three-dimensional superlattice by soft DNA linkers has been demonstrated in last ten years. Size ratios and shapes of nanoparticles played an important role in determining the final superlattice. However, in order to build more complicated frameworks, the demand for designing more complicated DNA origami structures which could decide the final framework is urgent. Here we reported a general method for building well-ordered structures from simple lattices to complicated crystals by DNA origami frames. Also, by controlling the position of the functional groups on the DNA origami building blocks, more new structures could be generated. Our strategy would bring a novel method for assembly into any nanoparticle superlattice in demand by pre-experimental design.

7.1 Introduction

Organization of individual building blocks into well-ordered structures is obvious in nature within all length scales including atomic systems, organic molecules, polymers and superlattice of colloids. Construction of different building blocks with high packing efficiency and high level of orders could be firstly rationalized and simulated from their different but unique geometries. This could be crucial for understanding the physical properties inside each programmed assembled framework. The shape of the building block is significant in determining the final assembly with growing scale length according to recent simulations¹⁴. So an experimental survey about how to

construct different shapes of polyhedra into well-aligned structures, even crystalline becomes urgent ⁵⁶. DNA origami technology provides a simple way to construct these frames with different shapes^{40,42,167}. One dimensional bundles ¹⁷⁷, two dimensional triangles ^{57,154}, Cube ¹⁶¹, sphere ⁴¹, and even more complicated structures ^{42,162} with certain length scales were produced and reported by DNA origami technique with attractive applications ^{60,61,83,178} within the last ten years after the successful creation of the first DNA origami structure since 2006 ⁴⁰. By careful designing, the functional group on each frame can be precisely controlled for further assembly into more complicated but fantastic frameworks as desired ^{58,60,154}. Special superlattices could be expected by incorporation of some unusual polyhedral structures with reduced symmetry. Also, choosing different positions for the functional group in a certain structure would be expected to form quite different assemblies. Gold nanoparticles would be an excellent helper for construction of these DNA origami polyhedral frameworks by connecting designed functional groups on each DNA origami frame. They could also be utilized as the indicator for the detection of the final superlattice by Small Angle X-ray Scattering (SAXS) ^{44,45}. In this report, we will discuss the rational assembly of 3D framework of origami polyhedral shapes via connection of gold nanoparticles.

7.2 The concept of nanoparticle-DNA framework

From a geometric standpoint, assembly with rigid DNA origami structures can be directed by their specific nano-scaled structures. We designed such DNA origami structures as the ‘frame’ including octahedron, cube and so on (Figure 7.1) using the software of caDNAno (<http://cadnano.org/>). Each edge of the origami structure was composed of a six-helix-bundle (6HB). For octahedral and cubic structures, the length of the 6HB is 28.6nm (84 base pairs); for prism, tetrahedral and hexagonal, the length of the 6HB is 42.8nm (126 base pairs); for elongated

octahedral, the length for four edges in the mid-plane is 28.6nm while the other eight edges have a length of 35.7nm (105 base pairs). Every bundle has one single strand DNA on two ends respectively for further assembly. 10nm gold nanoparticles (NPs) capped with synthetic oligonucleotides which were partly complementary with the sticky ends on each corner of origami structures were mixed with the frames respectively. In order to form 3D superlattice as shown in Figure 7.1 (DNA-NP framework), the ratio of NP and DNA origami should be well controlled. For example, if the ratio of NP and origami is larger than 6:1 for octahedron structures, clusters other than superlattices would be preferred. Binding of NPs on each frame was also shown in Figure 7.1 for the formation of DNA-NP framework. In a typical experiment, DNA origami frames were prepared by mixing 20 nM scaffold (M13mp18), 100 nM of each staple oligonucleotide in buffer solution containing 1 mM EDTA, 12.5 mM MgCl₂, 5 mM Tris (pH=7.9 at 20°C). Then the mixture was slowly annealed by rapid heating from room temperature to 90 °C and maintaining for 10 minutes, followed by slow cooling down from 80 °C to 61 °C over 80 min, then 60°C to 24°C over 12 h to fold the target structures. Samples were then electrophoresed on 1% agarose gels (0.5× TBE, 11 mM MgCl₂, 0.5 µg/ml cyber gold) at 100 V for 2 h in cold room (4°C). The grids for negative stained TEM were purchased from TedPella Cooperation. They were firstly applied to the glow-discharge to make the surface hydrophilic. A drop of 4-5 µl of sample solution was then dropped onto the surface of the grids and incubated for 3-5 min. Excess solution was removed by gently blotting the top solution on the grid with a piece of filter paper. We will then wash the grid by ddH₂O twice and stained by 4 µl 2% (w/v) uranyl acetate aqueous solution for 10 s. The grids were then left for air dry after blotting excess stain solution. The samples were imaged in a JEOL JEM-1400 TEM operating at 120 kV.

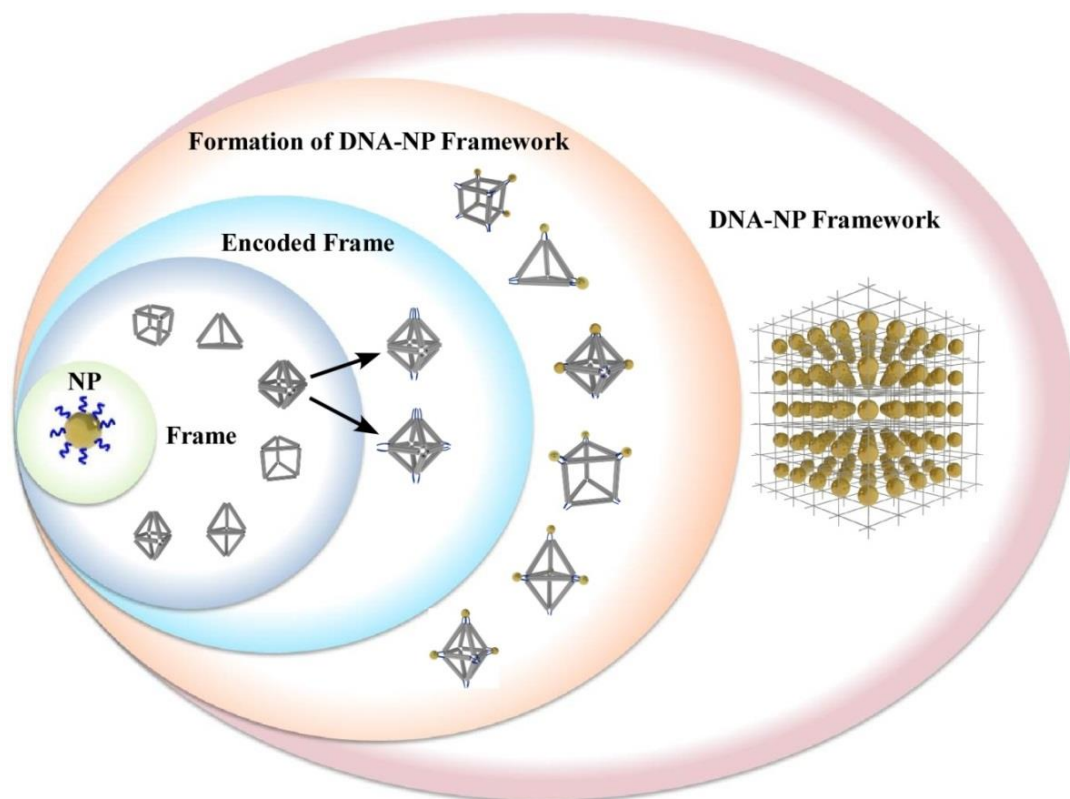


Figure 7.1 10nm gold nanoparticle (NP) assembly with DNA origami polyhedral frames including octahedral, cubic, prism, hexagonal etc. in the position of every corner for each origami shape to form 3D framework. Specially, the octahedral frame was encoded into another two frames with 2-fold and 4-fold symmetry for further assembly.

7.3 Results and discussion

The unique aspect of the assembly of DNA frames with NPs to form 3D superlattices is that NPs will act as a ‘linker’ between these large DNA frames. This concept is quite different from reported short DNA/NP superlattice structures in which the size ratio of NPs determines the final structure⁵⁵. From an energy minimization standpoint, origami structures will decide the final superlattice of the assemblies which will put the frames in a certain order. Table 7.1 described all the frames we would discuss one by one.

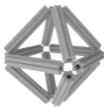

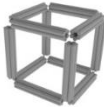



Frame Name	Octahedron	Elongated Square Bipyramid	Cubic	Tetrahedron	Prism	Triangular Bipyramid
Model						

Table 7.1 Summary of all the frames and relevant models discussed in this chapter

7.3.1 Octahedron

Octahedron is a common structure in nature with O_h symmetry. Each corner of the designed octahedral origami frame has four DNA sticky ends for binding with mixed 10nm NPs. Figure 7.2b shows the representative negative stained TEM image of the designed structure without purification. It is obvious from the image that over 99% of the formed structures are octahedral. We start to demonstrate the assembly of octahedron/NP superlattice by mixing them at different ratios ranging from 2:1, 1:1, 1:2, to 1:3. In order to build a well-ordered and close-packed superlattice, weak and reversible interactions are necessary. The sticky ends from each corner of octahedron were composed of eight polyA, while the oligonucleotides functionalized on 10nm NPs had six polyT outside. The melting temperature (T_m) for the binding is around 28° C. Crystal was created by carefully annealing the mixtures from 40° C to room temperature (1° C/h) to make sure that the formation process is thermodynamically controlled. Then the internal structure was probed by *in situ* Small Angle X-ray Scattering (SAXS) measurement. Two-

dimensional data collected from the assemblies were integrated and normalized based on the q value from the first ring. All the samples with different ratio showed the similar pattern (Figure 7.2d, green line), illustrating the structure factor $S(q)$ as a function of scattering vector q for octahedron origami-AuNP assembly and revealing almost thirty orders of resolution limited Bragg's peaks for the 3-D crystalline with remarkable degrees of long-range ordering. Analysis of the peaks reveals a diffraction pattern matching the fitted curve of a face-centered-cubic (f.c.c) structure as shown in Figure 7.2d (black lines). The height of the $S(q)$ peaks also qualitatively follows the intensities ratio predicted for f.c.c arrangement. The measured lattice parameters for the observed f.c.c structure are around 68nm at room temperature, which matches the predicted interparticle distance 66.5nm based on the calculation of the length of the octahedron edge, nanoparticle size, and DNA linker shells.

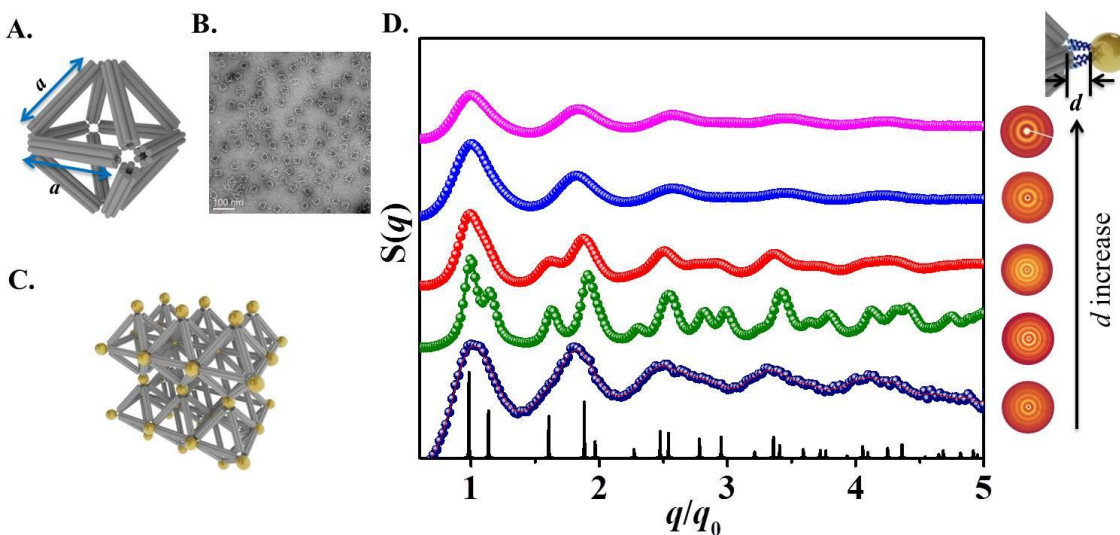


Figure 7.2 Octahedral DNA origami assembled with 10nm NPs to form a crystal and its scattering pattern. (A). Model of DNA origami. Each edge was composed of a six-helix-bundle with the same length. (B). Representative negative stained TEM image of octahedral origami.

(C). Model of the assembled superlattice by octahedral origami and NPs. (D). Extracted structure factors $S(q)$ v.s. q for different octahedral/NP superlattice systems (left). Distance from NP to octahedron (d) decreases from top (pink) to bottom (blue). Black line is the fitted lines for f.c.c structure. Right parts show corresponding SAXS images for each system.

In f.c.c lattice, the O_h symmetry of the octahedron has two different binding modes with nanoparticles, as shown in Figure 7.2c. The in-plane (equatorial) corners (total of four) bind with four nanoparticles and each nanoparticle in this layer also binds with four octahedrons. Each layer assembles with each other by the out-of-plane (axial) connection with another nanoparticle. The particle between layers only binds with two octahedrons in total. The different binding modes may come from different kinetic rate for these two methods. One nanoparticle grasps four octahedrons and because of the electronic repulsion in buffer solution, these four octahedrons will be arranged in a plane. The 1st level assembling leads to different in-plane and out-of-plane constructions, which is also the building block for further assemblies. The 2nd level construction may assemble in two different ways. Equatorial connections elongate the first layer, while axial will bind with another NP which will attract another layer to form a 3-D lattice.

NP-oligonucleotide conjugates and DNA origami frames have many variables that can be adjusted to affect the final structure and resolution, especially the linker parts including sticky ends from DNA origami and oligonucleotides capped on NPs because these are the soft parts of the assembly. We designed five systems accordingly in octahedron/NP system by changing the length of the soft part (d) as shown in Figure 7.2d (right part). The soft linker length was increased from ~6nm to ~12nm from system I to system V, while the order of the 1D peak integrated from SAXS patterns decayed accordingly from system II-V. System I is a special case, while octahedral only have six polyA stretched out which were totally complementary with

oligonucleotides attached on NPs. So the freedom of the movement for the soft linkers was limited which brings low order of the structures. This result illustrates that in order to well orient the arrangement of the NPs for origami structures, the NPs should be close enough to be reached by the DNA origami (except some free bases near the octahedron), which indirectly emphasize the decisive effect of the large DNA structures.

7.3.2 Elongated Square Bipyramid

One of the advantages of DNA origami technology is that we can design DNA frames as desired, even with lower symmetry. We have shown in Figure 7.2 that octahedron can bind with NPs to form f.c.c structure, in which each edge of the unit cell equals to each other ($a=b=c$). This structure was also reported several times by other DNA/NP systems. However, simple DNA linkers cannot be adjusted if we want one parameter (c) in f.c.c unit cell to be different with another two parameters (a and b). Hereby, we designed another DNA frame called ‘elongated square bipyramid (ESB)’ as shown in Figure 7.3a, which is similar to octahedron with difference only in the length of some edges. In this special DNA origami structure, four edges in the mid-plane have the same length (a) while the eight remaining edges are designed with longer six-helix bundles ($b=1.25a$). Figure 7.3b shows the representative TEM image of the designed structure. Compared with Figure 7.2b, these formed structures have different length in different diagonals as designed. Mixing and annealing of these structures with 10nm NPs also brings obvious aggregations with dark black color. Figure 7.3d shows the integrated function of $S(q)$ v.s. q by SAXS measurement which is different from f.c.c. SAXS image shown in Figure 7.3c also had different rings with octahedral system shown in Figure 7.2d. Simulation of the formed superlattice by the same construction method with octahedron (Figure 7.3d, inserted model) shows the same peak position ratios as the experimental data (Figure 7.3d, black line). Analysis

of the peaks reveals body-centered-tetragonal structure (BCT). In this unit cell, $a=b \neq c$ as designed. This is the first report of BCT structure for DNA/NP systems until now because it is hard for simple DNA/NP systems to assemble into this special superlattice which also demonstrate the unique value for DNA origami technology in this area.

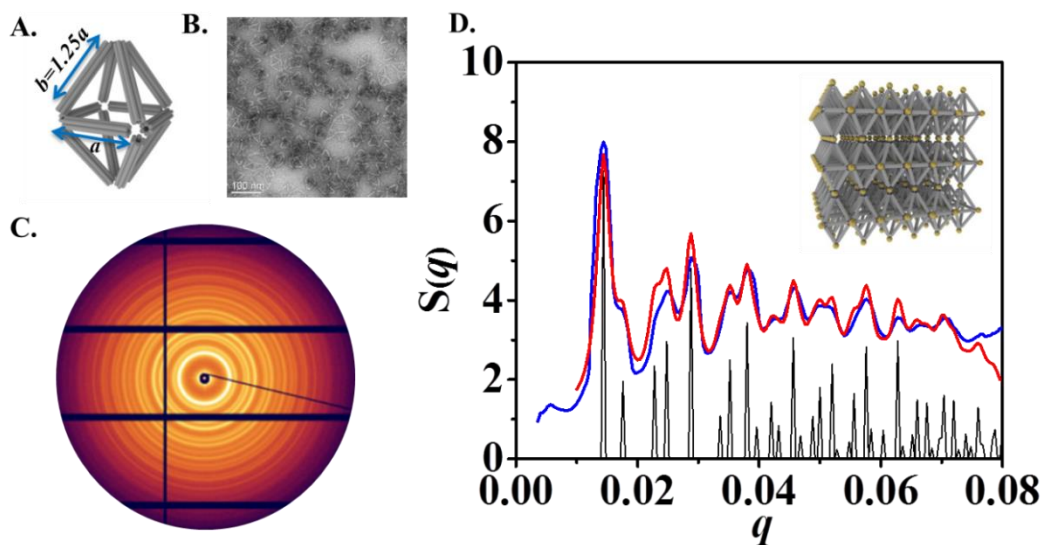


Figure 7.3 Elongated square bipyramid DNA origami (ESB) assembled with 10nm NPs to form crystal and its scattering pattern. (A). Model of ESB with different length as marked. (B). Representative negative stained TEM image of ESB. (C). SAXS image of the scattering. (D). Extracted structure factors $S(q)$ v.s. q for ESB/NP superlattice system. Inserted is the model of the assembled superlattice by ESB and NP.

7.3.3 Cube

Besides octahedron and ESB, we also designed another common structure-cube with same length of the edges (Figure 7.4a, inserted model). Interestingly, most of the cubes in solution are tilted due to the flexibility of the structure which comes from its intrinsic property as shown by the TEM image in Figure 7.4b. More remarkably than the formation of superlattice by rigid frames

(octahedron or ESB), cubes with different tilted states can also form order crystal structure when assembled with NPs (Figure 7.4a, blue line). This was achieved by mixing cubic frames with three sticky ends stretched out from each corner and 10nm NPs with the ratio of 1:1 and annealing slowly from 45° C to room temperature (1° C/h). The integrated data from the rings (Figure 7.4a, inserted) shows around thirty peaks at the position of $q/q_0 = 1: \sqrt{2}: \sqrt{3}: 2 \dots$ which coordinated with the theoretical simple cubic structure (black line in Figure 7.4a). Moreover, the relative height ratios are also consistent with the theoretical calculation. The average size of the single-crystal domain was estimated to be around 0.6 μm according to the Scherrer formula. The model for the formation of cubic and NP assemblies was proposed in Figure 7.4c. Cubic frames were constructed in unbent states when forming the framework because of the synergistic effect of the superlattice which could ‘pull’ from eight directions of the corners. In order to form simple cubic structure, each cubic will bind with eight NPs nearby, while each NP will also connect with eight DNA cubes. Interparticle distance in this system is calculated to be around 53.0nm according to the first peak which also fits the estimated distance well based on the close-packed simple cubic model.

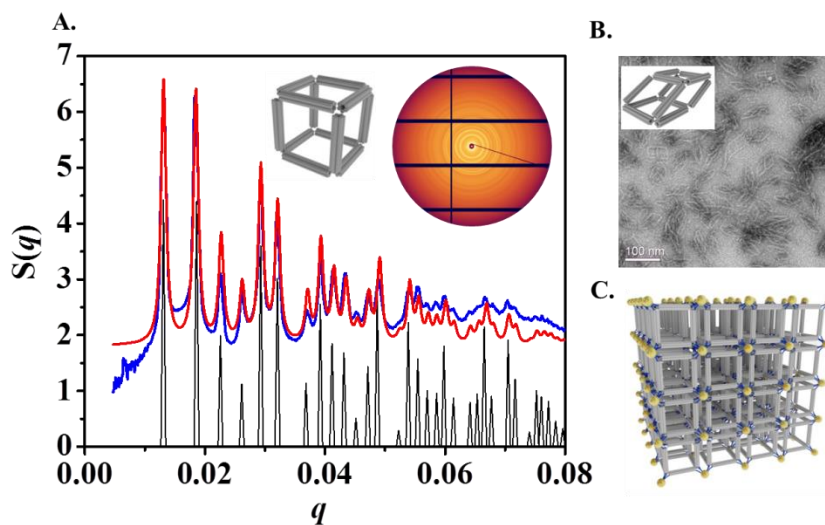


Figure 7.4 Cubic DNA origami assembled with 10nm NPs to form crystal and its scattering pattern. (A). Extracted structure factors $S(q)$ v.s. q for cubic/NP superlattice system. Inserted is the model of the cube (left) and SAXS image for the system (right). (B). Representative negative stained TEM image of octahedral origami. Inserted is the model of tilted cubic model. (C). Model of the assembled superlattice by cubic frames and NPs.

7.3.4 Tetrahedron

In order to complete our big map, we then designed tetrahedral frame since it also has a relatively high symmetry (T_d). Figure 7.5a (inserted above the curve) shows the tetrahedral model we designed. Each edge of the structure has a length of around 43nm (126 bases). Figure 7.5b shows a representative negative stained TEM image of the tetrahedral structure as designed. We then mixed the frames with 10nm NPs in a ratio of 1:1 and slowly annealed as described above. Black aggregations formed with clear supernatant. The precipitates were collected and measured by SAXS. Figure 7.5a (inserted below the curve) showed the 1D images of the result. Extracted structure factors $S(q)$ for tetrahedral system was shown in Figure 7.5a (red line with black cubic points). Less than ten peaks (red line with black rectangular points) were found which also matches the simulated f.c.c peaks (Figure 7.5a, black line). In order to form f.c.c structure, each NP will bind with four tetrahedra from four symmetric directions as shown in Figure 7.5c. The formed crystalline is not as good as other systems because packing tetrahedron to form f.c.c. structure as Figure 7.5c is not as tight as other polyhedra. Many unpaired bases from scaffold DNA may also attribute to the disordered structure.

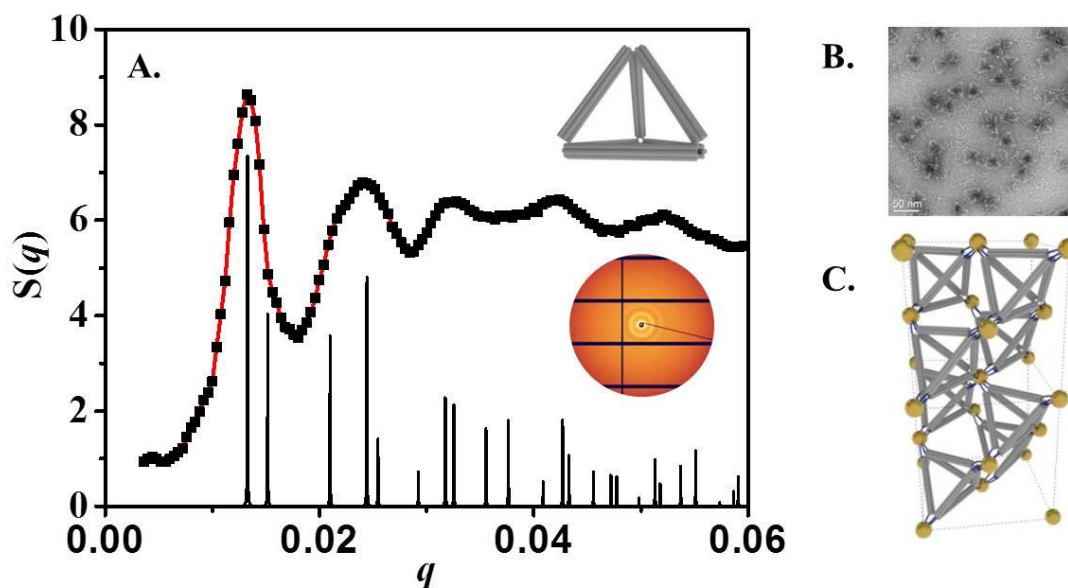


Figure 7.5 Tetrahedron DNA origami structure assembled with 10nm NPs. (A). Extracted structure factor $S(q)$ v.s. q for tetrahedron/NP superlattice system (inserted is the model of the tetrahedron). (B). Representative TEM image for tetrahedron. (C). Model of formed f.c.c. structure by tetrahedron/NP system.

7.3.5 Triangular Bipyramid

The origami structures discussed above, regardless of the ones with relatively high symmetry such as octahedron and cube, or the ones with lower symmetry (ESB), all have the same face structure individually (triangle or cube). We then designed a prism structure as shown in Figure 7.6b which has two triangle faces and three square faces. We mixed this kind of frame with two kinds of ‘faces’ with NPs in a ratio of 2:1 and annealed according to the method discussed above. SAXS result for this sample revealed a new and ordered structure as shown in Figure 7.6a (red line) with more than twenty recognizable peaks. Simulating the possible models for the assembled framework, we found a hexagonal structure was formed (Figure 7.6c) with $a=b \neq c$,

$\alpha=\beta=90^\circ$ while $\gamma=120^\circ$. The difference of $a=b$ and c comes from the different bonding mode compared with cubic for which $a=b=c$.

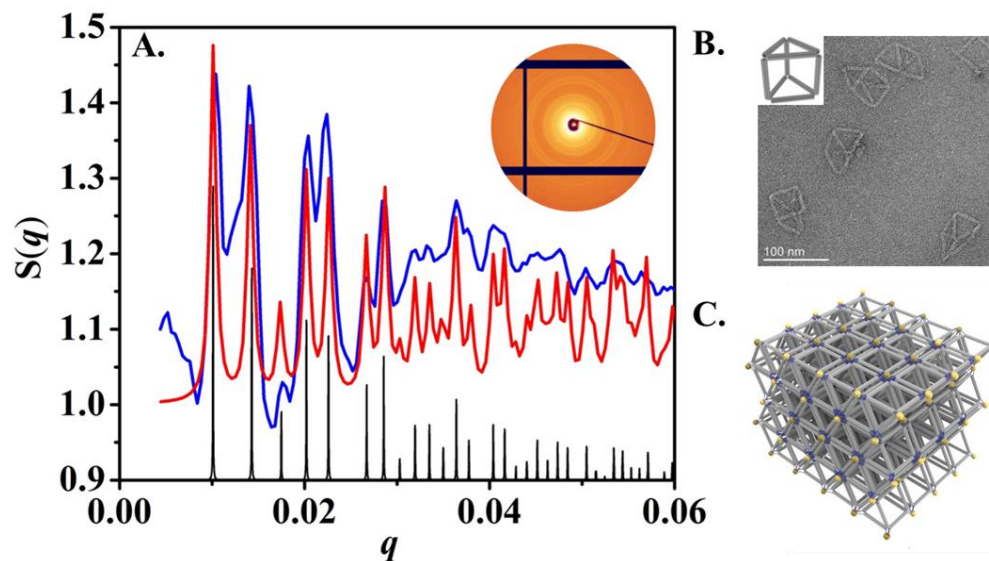


Figure 7.6 Prism DNA origami structure assembled with 10nm NPs. (A). Extracted structure factor $S(q)$ v.s. q for tetrahedron/NP superlattice system (inserted is the 1D ring image of the SAXS result). (B). Representative TEM image for tetrahedron (inserted is the model of the prism). (C). Model of formed hexagonal structure by prism/NP system.

7.4 Conclusion

In all cases, large DNA origami structures can direct the arrangement of NPs in superlattice with the help of NPs as the connector, and in the meanwhile, DNA origami frames can form 3D crystals as designed. This is the first report of the formation of 3D DNA origami structures. All the formed crystal structures and their building blocks are listed in Table 7.2. Because the DNA origami technology has nanometer-scale precision in determining the functional position, simpler and more effective control of different crystal superlattices will be more accessible.

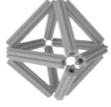
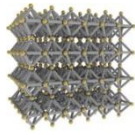
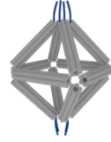


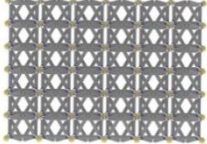

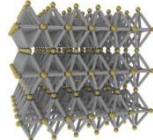
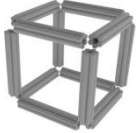
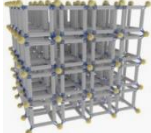

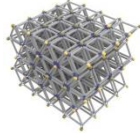

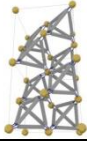

Building Blocks	Frameworks
Octahedral 	FCC 
	1D 
	2D 
ESB 	BCT 
Cubic 	SC 
Prism 	HEX 
Tetrahedral 	FCC 
Triangular Dipyramid 	Disordered

Table 7.2 Summary of building blocks and corresponding assembled frameworks

7.5 Methods

a. DLS results for all the origami structures.

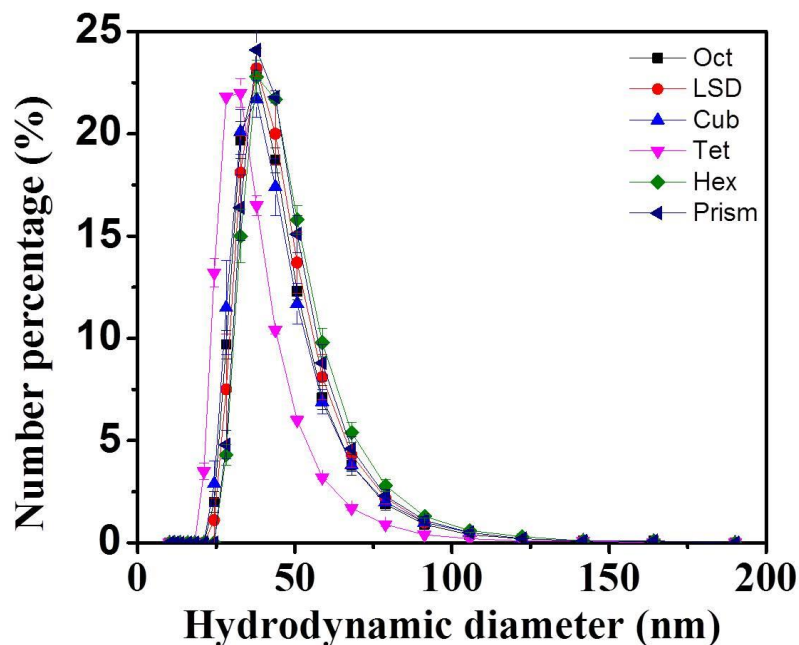


Figure 7.7 DLS results for all the origami structures discussed in this chapter

b. Determination of melting temperature of each system.

We used DLS to determine the melting temperature for each system (Table 7.3). Mixture of NPs and frames was measured 5 mins each while annealing the samples from 50 °C to room temperature over 12 hours.

Polyhedron	Binding method	M.T. (°C)
Octahedron	15polyA/6bind thio-DNA (16mer)	35.5
ESB	15polyA/6bind thio-DNA (16mer)	32.4
Cubic	15polyA/9bind thio-DNA (30mer)	35.9
Prism	10random/8bind thio-DNA (50mer)	37.9
Tetrahedron	15random/9bind thio-DNA (30mer)	39.5
TD	15polyA/6bind thio-DNA (16mer)	37.8

Table 7.3 Summary of melting temperatures for all frames assembly with 10nm NPs by DLS measurement.

c. DNA sequence design

HPLC purified DNA oligonucleotides were purchased as lyophilized powders (Integrated DNA Technologies Inc.). The staple DNA was purified with standard desalting method. The DNA sequences (5' to 3') were:

- (1). S1 (used for system I-III of octahedron, prism system, hexagonal system, elongated square bipyramid system): HS-C₆H₁₂-TTCTCCACTATTTTTT;

Chapter 8

Conclusions and Future Work

The work present in this thesis mainly focuses on DNA templated assembly of nanostructures with metal nanoparticles or quantum dots as the units and exploration of their inner structures and optical properties. Simple nano-clusters, core-shell structures and more complicated nanocrystal frameworks are discussed throughout the entire thesis with different DNA nanotechnology.

In chapter 2, I demonstrated that a pH sensitive DNA i-motif sequence can be used as a linker for dimer clusters produced by step-wise method. By careful design of a third NP with attached DNA complementary to this specific linker, trimer clusters can be produced. Interestingly, dimer and trimer cluster can be switched by pH cycling of the solution with the help of this special DNA imotif. When we replaced the third NP into quantum dots, the binding and disassembling of the QDs could result in ON and OFF for fluorescence during pH cycling. More complicated clusters can be generated based on this method in the future work. For example, dimers can be served as building block to build tetramers or even crystals. However, some issues need to be addressed here. First, the yield in forming tetramer would be expected to be lower than 40%. Second, melting temperature for multiple linkers used in dimer system should be carefully controlled before growing crystals. DNA origami technique provides a novel route to build complicate clusters and design nanocrystals, as demonstrated in chapter 6 and 7. However, dynamic control of the cluster structures and nanocrystals is still hard for origami structures because of its rigid cage.

This novel DNA motif was also introduced into three-dimensional nanocrystal systems which was assembled by DNA attached gold nanoparticles as discussed in chapter 3. In the formed BCC structure linked by imotif sequence, pH cycling can cause vibration of the lattice parameter a by SAXS measurement. More complicated i-motif linkage which contains two sections of imotif DNA separated by a short length of double strand DNA was also investigated. Around twice of the vibration effect (a) could be observed without disturbing the formation of BCC crystal. Similar effect was also obtained for dimer systems. However, only control of the interparticle distance is not enough. Since the final structure is greatly dependent on the size ratio of NP1 and NP2, more complicated case could be designed in which pH cycling can generate different crystal structures.

Since DNA single and double strands were demonstrated to be a great distance controller between nanoparticles, we designed a core-shell structure (50nm AuNP as the core and 10nm QDs as the shell) with different core-shell interparticle distance by DNA linker as described in chapter 4. The optical output could be controlled from quenched to enhanced, in a step-wise manner by tuning the interparticle distance. In our work, optical pumping at surface plasmon resonance could result in an overall PL with more than four times enhancement for a separation distance d around 40 nm. More future work could be attributed to increase the maximal PL enhancement by replacing AuNP to silver or designing more rigid linkers such as DNA origami bundles.

Furthermore, in chapter 5, we explored more functions of DNA sequence, from distance controller to chiral origin. As we know, normal B-DNA has a chiral double helix. With binding the double helix to our synthesized silver nanocubes, it can introduce CD response in plasmon nanoparticle region. Remarkably, a single free DNA with its native CD intensity signal can

enhance up to one hundred fold for the silver cube although there is no intrinsic chiral property for single nanocube. Increase the salt concentration of the system could decrease the CD signal which further demonstrated the play role of the orientation of DNA on the surface of the silver cube. Future work could be focused on controlling the placement and orientation of the chiral DNA and investigating more nanoparticle geometries and materials.

DNA origami technology can help us build larger and more complicated DNA structures, which broaden the way to fabricate complicate clusters as demonstrated in chapter 6. Combined with cryo-EM technique and single particle method, we can reconstruction the 3D model of the designed octahedron and clusters in different sizes and positions in nanometer precision. Based on this specific method, we can design different chiroptical activities with same set of nanoparticles but with different encoding. More complicated low dimensional arrays were also designed and observed in TEM. This work provides more opportunities for assembly of high-yield precise 3D mesoscale building blocks which was demonstrated in chapter 7.

Finally, we designed a set of polyhedra including octahedron, cube, and prism et al. with the similar method shown in chapter 6. These frames can be assembled with nanoparticles to form different frameworks. More remarkably, if we slightly change the edge length of the frame, different and more complicated structures could be obtained. This work opens an opportunity to design the framework we desire. In the future, this work can be extended to construction of different shaped origami structures together; building 3D DNA origami structures without the help of NP or fulfil the dynamic control of the final framework by changing or external environments.

References

- 1 Hartling, T., Reichenbach, P. & Eng, L. M. Near-field coupling of a single fluorescent molecule and a spherical gold nanoparticle. *Optics Express* **15**, 12806-12817 (2007).
- 2 Anger, P., Bharadwaj, P. & Novotny, L. Enhancement and quenching of single-molecule fluorescence. *Physical Review Letters* **96** (2006).
- 3 Grzybowski, B. A., Wilmer, C. E., Kim, J., Browne, K. P. & Bishop, K. J. M. Self-assembly: from crystals to cells. *Soft Matter* **5**, 1110–1128 (2009).
- 4 Grzelczak, M., Vermant, J., Furst, E. M. & Liz-Marzan, L. M. Directed Self-Assembly of Nanoparticles. *ACS Nano* **4**, 3591-3605 (2010).
- 5 Whitesides, G. M. & Grzybowski, B. Self-Assembly at All Scales. *Science* **295**, 2418-2421 (2002).
- 6 Gong, J., Li, G. & Tang, Z. Self-assembly of noble metal nanocrystals: Fabrication, optical property, and application. *Nano Today* **7**, 564-585 (2012).
- 7 Gang, O. & Zhang, Y. Shaping Phases by Phasing Shapes. *ACS Nano* **5**, 8459–8465 (2011).
- 8 Egelstaff, P. A. *An introduction to the liquid state*. (Clarendon Press, Oxford, 1992).
- 9 McDonald, J. *Theory of Simple Liquids*. (Academic Press, 1986).
- 10 Rechtsman, M., Stillinger, F. H. & Torquato, S. Designed Interaction Potentials via Inverse Methods for Self-Assembly. *Physical Review E* **73**, 011406 (2006).
- 11 Rechtsman, M. C., Stillinger, F. H. & Torquato, S. Self-Assembly of the Simple Cubic Lattice via an Isotropic Potential. *Physical Review E* **74**, 021404 (2006).
- 12 Tkachenko, A. V. Morphological diversity of DNA-colloidal self-assembly. *Physical Review Letters* **89** (2002).
- 13 Lu, K. Theoretical analysis of colloidal interaction energy in nanoparticle suspensions. *Ceramics International* **34**, 1353-1360 (2008).
- 14 Damasceno, P. F., Engel, M. & Glotzer, S. C. Predictive Self-Assembly of Polyhedra into Complex Structures. *Science* **337**, 453-457 (2012).
- 15 Chen, Q., Bae, S. C. & Granick, S. Directed self-assembly of a colloidal kagome lattice. *Nature* **469**, 381-384 (2011).
- 16 Wang, Y., Wang, Y., Breed, D. R., Manoharan, V. N., Feng, L., Hollingsworth, A. D., Weck, M. & Pine, D. J. Colloids with valence and specific directional bonding. *Nature* **491**, 51-56 (2012).
- 17 Glotzer, S. C. & Solomon, M. J. Anisotropy of building blocks and their assembly into complex structures. *Nature Materials* **6**, 557-562 (2007).
- 18 Pawar, A. B. & Kretzschmar, I. Fabrication, Assembly, and Application of Patchy Particles. *Macromolecular Rapid Communication* **31**, 150-168 (2010).
- 19 Perro, A., Reculosa, S., Ravaine, S., Bourgeat-Lami, E. & Duguet, E. Design and synthesis of Janus micro- and nanoparticles. *Journal of Material Chemistry* **15**, 3745-3760 (2005).
- 20 Crowley, J. M., Sheridan, N. K. & Romano, L. Dipole moments of gyricon balls. *Journal of Electrostatics* **55**, 247-259 (2002).
- 21 Kopelman, R., McNaughton, B. H., Agayan, R. R. & Wang, J. X. Physiochemical microparticle sensors based on nonlinear magnetic oscillations. *Sensors and Actuators B* **121**, 330-340 (2007).

- 22 Anker, J. N. & Kopelman, R. Magnetically modulated optical nanoprobe. *Applied Physics Letters* **82**, 1102-1104 (2003).
- 23 Watson, J. D. & Crick, F. H. A Structure for Deoxyribose Nucleic Acid. *Nature* **171**, 737-738 (1953).
- 24 Seeman, N. C. Nucleic Acid Junctions and Lattices *Journal of Theoretical Biology* **99**, 237-247 (1982).
- 25 Kallenbach, N. R., Ma, R.-I. & Seeman, N. C. An immobile nucleic acid junction constructed from oligonucleotides. *Nature* **305**, 829-831 (1983).
- 26 Chen, J. & Seeman, N. C. Synthesis from DNA of a molecule with the connectivity of a cube. *Nature* **350**, 631 - 633 (1991).
- 27 Winfree, E., Liu, F., Wenzler, L. A. & Seeman, N. C. Design and self-assembly of two-dimensional DNA crystals. *Nature* **394**, 539-544 (1998).
- 28 Zheng, J., Birktoft, J. J., Chen, Y., Wang, T., Sha, R., Constantinou, P. E., Ginell, S. L., Mao, C. & Seeman, N. C. From molecular to macroscopic via the rational design of a self-assembled 3D DNA crystal. *Nature* **461**, 74-77 (2009).
- 29 Cohen, S. N., Chang, A., Boyer, H. W. & Helling, R. B. Construction of biologically functional bacterial plasmids in vitro. *Proceedings of the National Academy of Sciences of the United States of America* **70**, 3240-3244 (1973).
- 30 Seeman, N. C., Wang, H., Yang, X., Liu, F., Mao, C., Sun, W., Wenzler, L., Shen, Z., Sha, R., Yan, H., Wong, M. H., Sa-Ardyen, P., Liu, B., Qiu, H., Li, X., Qi, J., Du, S. M., Zhang, Y., Mueller, J. E., Fu, T.-J., Wang, Y. & Chen, J. New motifs in DNA nanotechnology. *Nanotechnology* **9**, 257-273 (1998).
- 31 Kimball, A., Guo, Q., Lu, M., Conningham, R., Kallenbach, N., Seeman, N. & Tullius, T. Construction and Analysis of Parallel and Antiparallel Holliday Junctions. *Journal of Biological Chemistry* **265**, 6544-6547 (1990).
- 32 Lo, P. K., Mettera, K. L. & Sleiman, H. F. Self-assembly of three-dimensional DNA nanostructures and potential biological applications. *Current Opinion in Chemical Biology* **14**, 597-607 (2010).
- 33 He, Y., Su, M., Fang, P.-a., Ribbe, A. E., Jiang, W. & Mao, C. On the Chirality of Self-Assembled DNA Octahedra. *Angewandte Chemie International Edition* **49**, 748-751 (2010).
- 34 Zhang, C., Tian, C., Guo, F., Liu, Z., Jiang, W. & Mao, C. DNA-Directed Three-Dimensional Protein Organization. *Angewandte Chemie International Edition* **51**, 3382-3385 (2012).
- 35 Zhang, C., Wu, W., Li, X., Tian, C., Qian, H., Wang, G., Jiang, W. & Mao, C. Controlling the Chirality of DNA Nanocages. *Angewandte Chemie International Edition* **51**, 7999-8002 (2012).
- 36 Zhang, C., Ko, S. H., Su, M., Leng, Y., Ribbe, A. E., Jiang, W. & Mao, C. Symmetry Controls the Face Geometry of DNA Polyhedra. *Journal of American Chemical Society* **131**, 1413 (2009).
- 37 Zhang, C., Tian, C., Li, X., Qian, H., Hao, C., Jiang, W. & Mao, C. Reversibly Switching the Surface Porosity of a DNA Tetrahedron. *Journal of American Chemical Society* **134**, 11998-12001 (2012).
- 38 He, Y., Ye, T., Su, M., Zhang, C., Ribbe, A. E., Jiang, W. & Mao, C. Hierarchical self-assembly of DNA into symmetric supramolecular polyhedra. *Nature* **452**, 198-201 (2008).

- 39 Zhang, C., Su, M., He, Y., Zhao, X., Fang, P.-a., Ribbe, A. E., Jiang, W. & Mao, C. Conformational flexibility facilitates self-assembly of complex DNA nanostructures. *Proceedings of the National Academy of Sciences of the United States of America* **105**, 10665-10669 (2008).
- 40 Rothmund, P. W. K. Folding DNA to create nanoscale shapes and patterns. *Nature* **440**, 297-302 (2006).
- 41 Han, D., Pal, S., Nangreave, J., Deng, Z., Liu, Y. & Yan, H. DNA Origami with Complex Curvatures in Three-Dimensional Space. *Science* **332**, 342-346 (2011).
- 42 Dietz, H., Douglas, S. M. & Shih, W. M. Folding DNA into Twisted and Curved Nanoscale Shapes. *Science* **325**, 725-730 (2009).
- 43 Douglas, S. M., Marblestone, A. H., Teerapittayanon, S., Vazquez, A., Church, G. M. & Shih, W. M. Rapid prototyping of 3D DNA-origami shapes with caDNAo. *Nucleic Acids Research* **37**, 5001-5006 (2009).
- 44 Nykypanchuk, D., Maye, M. M., van der Lelie, D. & Gang, O. DNA-guided crystallization of colloidal nanoparticles. *Nature* **451**, 549-552, doi:10.1038/Nature06560 (2008).
- 45 Park, S. Y., Lytton-Jean, A. K. R., Lee, B., Weigand, S., Schatz, G. C. & Mirkin, C. A. DNA-programmable nanoparticle crystallization. *Nature* **451**, 553-556 (2008).
- 46 Hurst, S. J., Lytton-Jean, A. K. R. & Mirkin, C. A. Maximizing DNA loading on a range of gold nanoparticle sizes. *Analytical Chemistry* **78**, 8313-8318 (2006).
- 47 Niemeyer, C. M. & Simon, U. DNA-Based Assembly of Metal Nanoparticles. *European Journal of Inorganic Chemistry* **2005**, 3641-3655 (2005).
- 48 Loweth, C., Caldwell, W., Peng, X., Alivisatos, A. & Schultz, P. DNA-based assembly of gold nanocrystals. *Angewandte Chemie International Edition* **38**, 1808-1812 (1999).
- 49 Braun, E., Eichen, Y., Sivan, U. & Ben-Yoseph, G. DNA-templated assembly and electrode attachment of a conducting silver wire. *Nature* **391**, 775-778 (1998).
- 50 Fu, A. H., Micheel, C. M., Cha, J., Chang, H., Yang, H. & Alivisatos, A. P. Discrete nanostructures of quantum dots/Au with DNA. *Journal of the American Chemical Society* **126**, 10832-10833 (2004).
- 51 Maye, M. M., Gang, O. & Cotlet, M. Photoluminescence enhancement in CdSe/ZnS-DNA linked-Au nanoparticle heterodimers probed by single molecule spectroscopy. *Chemical Communications* **46**, 6111-6113 (2010).
- 52 Alivisatos, A. P., Johnsson, K. P., Peng, X., Wilson, T. E., Loweth, C. J., Bruchez Jr, M. P. & Schultz, P. G. Organization of 'nanocrystal molecules' using DNA. *Nature* **382**, 609-611 (1996).
- 53 Maye, M. M., Nykypanchuk, D., Cuisinier, M., van der Lelie, D. & Gang, O. Stepwise surface encoding for high-throughput assembly of nanoclusters. *Nature Materials* **8**, 388-391, doi:10.1038/nmat2421 (2009).
- 54 Sun, D. & Gang, O. Binary Heterogeneous Superlattices Assembled from Quantum Dots and Gold Nanoparticles with DNA. *Journal of American Chemical Society* **133**, 5252-5254 (2011).
- 55 Macfarlane, R. J., Lee, B., Jones, M. R., Harris, N., Schatz, G. C. & Mirkin, C. A. Nanoparticle Superlattice Engineering with DNA. *Science* **334**, 204-208 (2011).
- 56 Jones, M. R., Macfarlane, R. J., Lee, B., Zhang, J., Young, K. L., Senesi, A. J. & Mirkin, C. A. DNA-nanoparticle superlattices formed from anisotropic building blocks. *Nature Materials* **9** (2010).

- 57 Hung, A. M., Micheel, C. M., Bozano, L. D., Osterbur, L. W., Wallraff, G. M. & Cha, J. N. Large-area spatially ordered arrays of gold nanoparticles directed by lithographically confined DNA origami. *Nature Nanotechnology* **5**, 121 (2010).
- 58 Ding, B., Deng, Z., Yan, H., Cabrini, S., Zuckermann, R. N. & Bokor, J. Gold Nanoparticle Self-Similar Chain Structure Organized by DNA Origami. *Journal of American Chemical Society* **132**, 3248–3249 (2010).
- 59 Zhao, Z., Jacovetty, E. L., Liu, Y. & Yan, H. Encapsulation of Gold Nanoparticles in a DNA Origami Cage. *Angewandte Chemie International Edition* **50**, 2041-2044 (2011).
- 60 Shen, X., Song, C., Wang, J., Shi, D., Wang, Z., Liu, N. & Ding, B. Rolling Up Gold Nanoparticle-Dressed DNA Origami into Three-Dimensional Plasmonic Chiral Nanostructures. *Journal of American Chemical Society* **134**, 146–149 (2012).
- 61 Acuna, G. P., Bucher, M., Stein, I. H., Steinhauer, C., Kuzyk, A., Holzmeister, P., Schreiber, R., Moroz, A., Stefani, F. D., Liedl, T., Simmel, F. C. & Tinnefeld, P. Distance Dependence of Single-Fluorophore Quenching by Gold Nanoparticles Studied on DNA Origami. *ACS Nano* **6**, 3189–3195 (2012).
- 62 Lee, J., Hernandez, P., Govorov, A. O. & Kotov, N. A. Exciton–plasmon interactions in molecular spring assemblies of nanowires and wavelength-based protein detection. *Nature Materials* **6**, 291-295 (2007).
- 63 Redl, F. X., Cho, K. S., Murray, C. B. & O'Brien, S. Three-dimensional binary superlattices of magnetic nanocrystals and semiconductor quantum dots. *Nature* **423**, 968-971 (2003).
- 64 Csaki, A., Garwe, F., Steinbruck, A., Maubach, G., Festag, G., Weise, A., Riemann, I., König, K. & Fritzsche, W. A parallel approach for subwavelength molecular surgery using gene-specific positioned metal nanoparticles as laser light antennas. *Nano Letters* **7**, 247 (2007).
- 65 J. Su, F. C., Cryns, V. L. & Messersmith, P. B. Catechol Polymers for pH-Responsive, Targeted Drug Delivery to Cancer Cells. *Journal of American Chemical Society* **133**, 11850-11853 (2011).
- 66 Vial, S., Nykypanchuk, D., Yager, K. G. & Gang, O. Linear Mesostructures in DNA-Nanorod Self-Assembly. *ACS Nano* **7**, 5437-5445 (2013).
- 67 Sun, D., Stadler, A. L., Gurevich, M., Palma, E., Stach, E., Lelie, D. v. d. & Gang, O. Heterogeneous nanoclusters assembled by PNA-templated double-stranded DNA. *Nanoscale* **4**, 6722-6725 (2012).
- 68 Kim, J.-W., Kim, J.-H. & Deaton, R. DNA-Linked Nanoparticle Building Blocks for Programmable Matter. *Angewandte Chemie International Edition* **50**, 9185 –9190 (2011).
- 69 Sherman, W. B. & Seeman, N. C. A precisely controlled DNA biped walking device. *Nano Letters* **4**, 1203-1207 (2004).
- 70 Feng, L. P., Park, S. H., Reif, J. H. & Yan, H. A two-state DNA lattice switched by DNA nanoactuator. *Angewandte Chemie International Edition* **42**, 4342-4346 (2003).
- 71 Tian, Y. & Mao, C. Molecular gears: a pair of DNA circles continuously rolls against each other. *Journal of American Chemical Society* **126**, 11410-11411 (2004).
- 72 Maye, M. M., Kumara, M. T., Nykypanchuk, D., Sherman, W. B. & Gang, O. Switching binary states of nanoparticle superlattices and dimer clusters by DNA strands. *Nature Nanotechnology* **5**, 116-120 (2010).

- 73 Xiong, H., Sfeir, M. Y. & Gang, O. Assembly, Structure and Optical Response of Three-Dimensional Dynamically Tunable Multicomponent Superlattices. *Nano Letters* **10**, 4456-4462 (2010).
- 74 Choi, J., Kim, S., Tachikawa, T., Fujitsuka, M. & Majima, T. pH-induced intermolecular folding dynamics of i-motif DNA. *Journal of American Chemical Society* **133**, 16146-16153 (2011).
- 75 Giannini, V., Fernandez-Dominguez, A. I., Sonnefraud, Y., Roschuk, T., Fernandez-Garcia, R. & Maier, S. A. Controlling Light Localization and Light-Matter Interactions with Nanoplasmonics. *Small* **6**, 2498-2507 (2010).
- 76 Govorov, A. O., Bryant, G. W., Zhang, W., Skeini, T., Lee, J., Kotov, N. A., Slocik, J. M. & Naik, R. R. Exciton-plasmon interaction and hybrid excitons in semiconductor-metal nanoparticle assemblies. *Nano Letters* **6**, 984-994 (2006).
- 77 Zhang, X., Marocico, C. A., Lunz, M., Gerard, V. A., Gun'ko, Y. K., Lesnyak, V., Gaponik, N., Susha, A. S., Rogach, A. L. & Bradley, A. L. Experimental and Theoretical Investigation of the Distance Dependence of Localized Surface Plasmon Coupled Forster Resonance Energy Transfer. *ACS Nano* **8**, 1273-1283 (2014).
- 78 Kuzyk, A., Schreiber, R., Zhang, H., Govorov, A. O., Liedl, T. & Liu, N. Reconfigurable 3D plasmonic metamolecules. *Nature Materials* **13**, 862-866 (2014).
- 79 Jin, Y. D. & Gao, X. H. Plasmonic fluorescent quantum dots. *Nature Nanotechnology* **4**, 571-576 (2009).
- 80 Song, J. H., Atay, T., Shi, S. F., Urabe, H. & Nurmikko, A. V. Large enhancement of fluorescence efficiency from CdSe/ZnS quantum dots induced by resonant coupling to spatially controlled surface plasmons. *Nano Letters* **5**, 1557-1561 (2005).
- 81 Lunz, M., Gerard, V. A., Gun'ko, Y. K., Lesnyak, V., Gaponik, N., Susha, A. S., Rogach, A. L. & Bradley, A. L. Surface Plasmon Enhanced Energy Transfer between Donor and Acceptor CdTe Nanocrystal Quantum Dot Monolayers. *Nano Letters* **11**, 3341-3345 (2011).
- 82 Kulakovich, O., Strekal, N., Yaroshevich, A., Maskevich, S., Gaponenko, S., Nabiev, I., Woggon, U. & Artemyev, M. Enhanced luminescence of CdSe quantum dots on gold colloids. *Nano Letters* **2**, 1449-1452 (2002).
- 83 Kuzyk, A., Schreiber, R., Fan, Z., Pardatscher, G., Roller, E.-M., Högele, A., Simmel, F. C., Govorov, A. O. & Liedl, T. DNA-based self-assembly of chiral plasmonic nanostructures with tailored optical response. *Nature* **483**, 311-314 (2012).
- 84 Mastroianni, A. J., Claridge, S. A. & Alivisatos, A. P. Pyramidal and Chiral Groupings of Gold Nanocrystals Assembled Using DNA Scaffolds. *Journal of the American Chemical Society* **131**, 8455-8459 (2009).
- 85 Park, S. Y., Lytton-Jean, A. K. R., Lee, B., Weigand, S., Schatz, G. C. & Mirkin, C. A. DNA-programmable nanoparticle crystallization. *Nature* **451**, 553-556 (2008).
- 86 Xu, P. F., Lee, J. H., Ma, K., Choi, C., Jin, S., Wang, J. & Cha, J. N. Enhanced Raman signals from switchable nanoparticle probes. *Chemical Communications* **49**, 8994-8996 (2013).
- 87 Pal, S., Dutta, P., Wang, H., Deng, Z., Zou, S., Yan, H. & Liu, Y. Quantum Efficiency Modification of Organic Fluorophores Using Gold Nanoparticles on DNA Origami Scaffolds. *Journal of Physical Chemistry C* **117**, 12735-12744 (2013).

- 88 Dutta, P. K., Varghese, R., Nangreave, J., Lin, S., Yan, H. & Liu, Y. DNA-Directed Artificial Light-Harvesting Antenna. *Journal of the American Chemical Society* **133**, 11985-11993 (2011).
- 89 Pilo-Pais, M., Watson, A., Demers, S., LaBean, T. H. & Finkelstein, G. Surface-Enhanced Raman Scattering Plasmonic Enhancement Using DNA Origami-Based Complex Metallic Nanostructures. *Nano Letters* **14**, 2099-2104 (2014).
- 90 Xiong, H., Sfeir, M. Y. & Gang, O. Assembly, Structure and Optical Response of Three-Dimensional Dynamically Tunable Multicomponent Superlattices. *Nano Letters* **10**, 4456-4462 (2010).
- 91 Young, K. L., Ross, M. B., Blaber, M. G., Rycenga, M., Jones, M. R., Zhang, C., Senesi, A. J., Lee, B., Schatz, G. C. & Mirkin, C. A. Using DNA to Design Plasmonic Metamaterials with Tunable Optical Properties. *Advanced Materials* **26**, 653-659 (2013).
- 92 Acuna, G. P., Bucher, M., Stein, I. H., Steinhauer, C., Kuzyk, A., Holzmeister, P., Schreiber, R., Moroz, A., Stefani, F. D., Liedl, T., Simmel, F. C. & Tinnefeld, P. Distance Dependence of Single-Fluorophore Quenching by Gold Nanoparticles Studied on DNA Origami. *Acs Nano* **6**, 3189-3195, doi:10.1021/nn2050483 (2012).
- 93 Sun, D. Z. & Gang, O. Binary Heterogeneous Superlattices Assembled from Quantum Dots and Gold Nanoparticles with DNA. *Journal of the American Chemical Society* **133**, 5252-5254 (2011).
- 94 Seelig, J., Leslie, K., Renn, A., Kuhn, S., Jacobsen, V., van de Corput, M., Wyman, C. & Sandoghdar, V. Nanoparticle-induced fluorescence lifetime modification as nanoscopic ruler: Demonstration at the single molecule level. *Nano Letters* **7**, 685-689 (2007).
- 95 Jennings, T. L., Singh, M. P. & Strouse, G. F. Fluorescent lifetime quenching near d=1.5 nm gold nanoparticles: Probing NSET validity. *Journal of the American Chemical Society* **128**, 5462-5467 (2006).
- 96 Yun, C. S., Javier, A., Jennings, T., Fisher, M., Hira, S., Peterson, S., Hopkins, B., Reich, N. O. & Strouse, G. F. Nanometal surface energy transfer in optical rulers, breaking the FRET barrier. *Journal of the American Chemical Society* **127**, 3115-3119 (2005).
- 97 Yu, W. W., Wang, Y. A. & Peng, X. G. Formation and stability of size-, shape-, and structure-controlled CdTe nanocrystals: Ligand effects on monomers and nanocrystals. *Chemistry of Materials* **15**, 4300-4308 (2003).
- 98 Zang, H. D., Routh, P. K., Alam, R., Maye, M. M. & Cotlet, M. Core size dependent hole transfer from a photoexcited CdSe/ZnS quantum dot to a conductive polymer. *Chemical Communications* **50**, 5958-5960 (2014).
- 99 Xiong, H. M., van der Lelie, D. & Gang, O. Phase Behavior of Nanoparticles Assembled by DNA Linkers. *Physical Review Letters* **102** (2009).
- 100 Zhang, Y., Lu, F., Yager, K. G., van der Lelie, D. & Gang, O. A general strategy for the DNA-mediated self-assembly of functional nanoparticles into heterogeneous systems. *Nature Nanotechnology* **8**, 865-872 (2013).
- 101 Reineck, P., Gomez, D., Ng, S. H., Karg, M., Bell, T., Mulvaney, P. & Bach, U. Distance and Wavelength Dependent Quenching of Molecular Fluorescence by Au@SiO₂ Core-Shell Nanoparticles. *ACS Nano* **7**, 6636-6648 (2013).
- 102 Gueroui, Z. & Libchaber, A. Single-molecule measurements of gold-quenched quantum dots. *Physical Review Letters* **93** (2004).

- 103 Pons, T., Medintz, I. L., Sapsford, K. E., Higashiya, S., Grimes, A. F., English, D. S. & Mattoussi, H. On the quenching of semiconductor quantum dot photoluminescence by proximal gold nanoparticles. *Nano Letters* **7**, 3157-3164 (2007).
- 104 Li, M., Cushing, S. K., Wang, Q. Y., Shi, X. D., Hornak, L. A., Hong, Z. L. & Wu, N. Q. Size-Dependent Energy Transfer between CdSe/ZnS Quantum Dots and Gold Nanoparticles. *Journal of Physical Chemistry Letters* **2**, 2125-2129 (2011).
- 105 Stryer, L. & Haugland, R. P. ENERGY TRANSFER - A SPECTROSCOPIC RULER. *Proceedings of the National Academy of Sciences of the United States of America* **58**, 719-& (1967).
- 106 Medintz, I. L. & Mattoussi, H. Quantum dot-based resonance energy transfer and its growing application in biology. *Physical Chemistry Chemical Physics* **11**, 17-45 (2009).
- 107 Patra, D., Gregor, I., Enderlein, J. & Sauer, M. Defocused imaging of quantum-dot angular distribution of radiation. *Applied Physics Letters* **87**, doi:10.1063/1.2037194 (2005).
- 108 Bharadwaj, P., Anger, P. & Novotny, L. Nanoplasmonic enhancement of single-molecule fluorescence. *Nanotechnology* **18** (2007).
- 109 Kuhn, S., Hakanson, U., Rogobete, L. & Sandoghdar, V. Enhancement of single-molecule fluorescence using a gold nanoparticle as an optical nanoantenna. *Physical Review Letters* **97** (2006).
- 110 Peng, B., Li, Z. P., Mutlugun, E., Martinez, P. L. H., Li, D. H., Zhang, Q., Gao, Y., Demir, H. V. & Xiong, Q. H. Quantum dots on vertically aligned gold nanorod monolayer: plasmon enhanced fluorescence. *Nanoscale* **6**, 5592-5598 (2014).
- 111 Tam, F., Goodrich, G. P., Johnson, B. R. & Halas, N. J. Plasmonic enhancement of molecular fluorescence. *Nano Letters* **7**, 496-501 (2007).
- 112 Sun, D. Z. & Gang, O. DNA-Functionalized Quantum Dots: Fabrication, Structural, and Physicochemical Properties. *Langmuir* **29**, 7038-7046 (2013).
- 113 Wagnière, G. H. *On chirality and the universal asymmetry : reflections on image and mirror image*. (VHCA [with] Wiley-VCH, 2007).
- 114 Kadhane, U., Holm, A. I. S., Hoffmann, S. V. & Nielsen, S. B. Strong coupling between adenine nucleobases in DNA single strands revealed by circular dichroism using synchrotron radiation. *Physical Review E* **77** (2008).
- 115 Fasman, G. D. *Circular dichroism and the conformational analysis of biomolecules*. (Plenum Press, 1996).
- 116 Berova, N., Woody, R. W. & Nakanishi, K. *Circular dichroism : principles and applications*. 2nd ed. edn, (Wiley-VCH, 2000).
- 117 Barron, L. D. *Molecular light scattering and optical activity*. 2nd ed., rev. and enl. edn, (Cambridge University Press, 2004).
- 118 Ren, M. X., Plum, E., Xu, J. J. & Zheludev, N. I. Giant nonlinear optical activity in a plasmonic metamaterial. *Nature Communications* **3** (2012).
- 119 Helgert, C., Pshenay-Severin, E., Falkner, M., Menzel, C., Rockstuhl, C., Kley, E. B., Tunnemann, A., Lederer, F. & Pertsch, T. Chiral Metamaterial Composed of Three-Dimensional Plasmonic Nanostructures. *Nano Letters* **11**, 4400-4404 (2011).
- 120 Hentschel, M., Schaferling, M., Weiss, T., Liu, N. & Giessen, H. Three-Dimensional Chiral Plasmonic Oligomers. *Nano Letters* **12**, 2542-2547 (2012).
- 121 Moskovits, M. Surface-Enhanced Spectroscopy. *Reviews of Modern Physics* **57**, 783-826 (1985).

- 122 Nie, S. M. & Emery, S. R. Probing single molecules and single nanoparticles by surface-enhanced Raman scattering. *Science* **275**, 1102-1106 (1997).
- 123 Lakowicz, J. R. Radiative decay engineering: Biophysical and biomedical applications. *Analytical Biochemistry* **298**, 1-24 (2001).
- 124 Jeanmaire, D. L. & Vanduyne, R. P. Surface Raman Spectroelectrochemistry .1. Heterocyclic, Aromatic, and Aliphatic-Amines Adsorbed on Anodized Silver Electrode. *Journal of Electroanalytical Chemistry* **84**, 1-20 (1977).
- 125 Zeng, J., Zheng, Y. Q., Rycenga, M., Tao, J., Li, Z. Y., Zhang, Q. A., Zhu, Y. M. & Xia, Y. N. Controlling the Shapes of Silver Nanocrystals with Different Capping Agents. *Journal of the American Chemical Society* **132**, 8552-+ (2010).
- 126 Xia, X., Zeng, J., Zhang, Q., Moran, C. H. & Xia, Y. Recent Developments in Shape-Controlled Synthesis of Silver Nanocrystals. *Journal of Physical Chemistry C* **116**, 21647-21656 (2012).
- 127 Zhang, Q. A., Li, W. Y., Moran, C., Zeng, J., Chen, J. Y., Wen, L. P. & Xia, Y. N. Seed-Mediated Synthesis of Ag Nanocubes with Controllable Edge Lengths in the Range of 30-200 nm and Comparison of Their Optical Properties. *Journal of the American Chemical Society* **132**, 11372-11378 (2010).
- 128 Johnson, P. B. & Christy, R. W. Optical Constants of Noble Metals. *Physical Review B* **6**, 4370-4379 (1972).
- 129 Govorov, A. O. Plasmon-Induced Circular Dichroism of a Chiral Molecule in the Vicinity of Metal Nanocrystals. Application to Various Geometries. *Journal of Physical Chemistry C* **115**, 7914-7923 (2011).
- 130 Govorov, A. O., Fan, Z. Y., Hernandez, P., Slocik, J. M. & Naik, R. R. Theory of Circular Dichroism of Nanomaterials Comprising Chiral Molecules and Nanocrystals: Plasmon Enhancement, Dipole Interactions, and Dielectric Effects. *Nano Letters* **10**, 1374-1382 (2010).
- 131 Govorov, A. O. & Fan, Z. Y. Theory of Chiral Plasmonic Nanostructures Comprising Metal Nanocrystals and Chiral Molecular Media. *Chemphyschem* **13**, 2551-2560 (2012).
- 132 Jones, M. R., Macfarlane, R. J., Lee, B., Zhang, J. A., Young, K. L., Senesi, A. J. & Mirkin, C. A. DNA-nanoparticle superlattices formed from anisotropic building blocks. *Nature Materials* **9**, 913-917, doi:Doi 10.1038/Nmat2870 (2010).
- 133 Artemyev, M., Kisiel, D., Abmiotko, S., Antipina, M. N., Khomutov, G. B., Kislov, V. V. & Rakhnyanskaya, A. A. Self-organized, highly luminescent CdSe nanorod-DNA complexes. *Journal of the American Chemical Society* **126**, 10594-10597 (2004).
- 134 Cao, Y. W., Jin, R. & Mirkin, C. A. DNA-modified core-shell Ag/Au nanoparticles. *Journal of the American Chemical Society* **123**, 7961-7962 (2001).
- 135 Lee, J. S., Lytton-Jean, A. K. R., Hurst, S. J. & Mirkin, C. A. Silver nanoparticle-oligonucleotide conjugates based on DNA with triple cyclic disulfide moieties. *Nano Letters* **7**, 2112-2115 (2007).
- 136 Lu, F., Zhang, Y., Zhang, L. H., Zhang, Y. G., Wang, J. X., Adzic, R. R., Stach, E. A. & Gang, O. Truncated Ditetragonal Gold Prisms as Nanofacet Activators of Catalytic Platinum. *Journal of the American Chemical Society* **133**, 18074-18077 (2011).
- 137 Israels, R., Leermakers, F. A. M., Fleer, G. J. & Zhulina, E. B. Charged Polymeric Brushes - Structure and Scaling Relations. *Macromolecules* **27**, 3249-3261 (1994).
- 138 Slocik, J. M., Govorov, A. O. & Naik, R. R. Plasmonic Circular Dichroism of Peptide-Functionalized Gold Nanoparticles. *Nano Letters* **11**, 701-705 (2011).

- 139 Ha, J. M., Solovyov, A. & Katz, A. Synthesis and Characterization of Accessible Metal Surfaces in Calixarene-Bound Gold Nanoparticles. *Langmuir* **25**, 10548-10553 (2009).
- 140 Rivetti, C., Walker, C. & Bustamante, C. Polymer chain statistics and conformational analysis of DNA molecules with bends or sections of different flexibility. *Journal of Molecular Biology* **280**, 41-59 (1998).
- 141 Flatau, P. J. & Draine, B. T. Fast near field calculations in the discrete dipole approximation for regular rectilinear grids. *Optics Express* **20**, 1247-1252 (2012).
- 142 Fan, F. R., Liu, D. Y., Wu, Y. F., Duan, S., Xie, Z. X., Jiang, Z. Y. & Tian, Z. Q. Epitaxial growth of heterogeneous metal nanocrystals: From gold nano-octahedra to palladium and silver nanocubes. *Journal of the American Chemical Society* **130**, 6949 (2008).
- 143 Maye, M. M., Nykypanchuk, D., van der Lelie, D. & Gang, O. A simple method for kinetic control of DNA-induced nanoparticle assembly. *Journal of the American Chemical Society* **128**, 14020-14021 (2006).
- 144 Hurst, S. J., Lytton-Jean, A. K. R. & Mirkin, C. A. Maximizing DNA loading on a range of gold nanoparticle sizes. *Anal Chem* **78**, 8313-8318, doi:Doi 10.1021/Ac0613582 (2006).
- 145 Halverson, J. D. & Tkachenko, A. V. DNA-programmed mesoscopic architecture. *Physical Review E* **87**, 062310 (2013).
- 146 Zeravcic, Z. & Brenner, M. P. Self-replicating colloidal clusters. *Proceedings of the National Academy of Sciences of the United States of America* **111**, 1748-1753 (2013).
- 147 Yan, W., Xu, L., Xu, C., Ma, W., Kuang, H., Wang, L. & Kotov, N. A. Self-Assembly of Chiral Nanoparticle Pyramids with Strong R/S Optical Activity. *Journal of the American Chemical Society* **134**, 15114–15121 (2012).
- 148 Fan, J. A., Bao, K., Sun, L., Bao, J., Manoharan, V. N., Nordlander, P. & Capasso, F. Plasmonic Mode Engineering with Templated Self-Assembled Nanoclusters. *Nano Letters* **12**, 5318-5324 (2012).
- 149 Hiroi, K., Komatsu, K. & Sato, T. Superspin glass originating from dipolar interaction with controlled interparticle distance among gamma-Fe₂O₃ nanoparticles with silica shells. *Physical Review B* **83**, 224423 (2011).
- 150 Ruzicka, B., Zaccarelli, E., Zulian, L., Angelini, R., Sztucki, M., Moussa ïl, A., Narayanan, T. & Sciortino, F. Observation of empty liquids and equilibrium gels in a colloidal clay. *Nature Materials* **10**, 56-60 (2011).
- 151 Chen, Q., K. Whitmer, J., Jiang, S., Bae, S. C., Luijten, E. & Granick, S. Supracolloidal Reaction Kinetics of Janus Spheres. *Science* **331**, 199-202 (2011).
- 152 Mastroianni, A. J., Claridge, S. A. & Alivisatos, A. P. Pyramidal and Chiral Groupings of Gold Nanocrystals Assembled Using DNA Scaffolds. *Journal of the American Chemical Society* **131**, 8455–8459 (2009).
- 153 Klinkova, A., Thérien-Aubin, H., Choueiri, R. M., Rubinstein, M. & Kumacheva, E. Colloidal analogs of molecular chain stoppers. *Proceedings of the National Academy of Sciences of the United States of America* **110**, 18775-18779 (2013).
- 154 Pal, S., Deng, Z., Ding, B., Yan, H. & Liu, Y. DNA-Origami-Directed Self-Assembly of Discrete Silver-Nanoparticle Architectures. *Angewandte Chemie International Edition* **49**, 2700–2704 (2010).

- 155 Zhang, C., Macfarlane, R. J., Young, K. L., Choi, C. H. J., Hao, L., Auyeung, E., Liu, G., Zhou, X. & Mirkin, C. A. A general approach to DNA-programmable atom equivalents. *Nature Materials* **12**, 741-746 (2013).
- 156 Seeman, N. C. DNA in a material world. *Nature* **421**, 427-431 (2003).
- 157 Shih, W. M., Quispe, J. D. & Joyce, G. F. A 1.7-kilobase single-stranded DNA that folds into a nanoscale octahedron. *Nature* **427**, 618-621 (2004).
- 158 Zheng, J., Birktoft, J. J., Chen, Y., Wang, T., Sha, R., Constantinou, P. E., Ginell, S. L., Mao, C. & Seeman, N. C. From molecular to macroscopic via the rational design of a self-assembled 3D DNA crystal. *Nature* **461**, 74-77 (2009).
- 159 Zhang, C., Li, X., Tian, C., Yu, G., Li, Y., Jiang, W. & Mao, C. DNA Nanocages Swallow Gold Nanoparticles (AuNPs) to Form AuNP@DNA Cage Core-Shell Structures. *ACS Nano* **8**, 1130-1135 (2014).
- 160 Sharma, J., Chhabra, R., Cheng, A., Brownell, J., Liu, Y. & Yan, H. Control of Self-Assembly of DNA Tubules Through Integration of Gold Nanoparticles. *Science* **323**, 112-116 (2009).
- 161 Andersen, E. S., Dong, M., Nielsen, M. M., Jahn, K., Subramani, R., Mamdouh, W., Golas, M. M., Sander, B., Stark, H., Oliveira, C. L. P., Pedersen, J. S., Birkedal, V., Besenbacher, F., Gothelf, K. V. & Kjems, J. Self-assembly of a nanoscale DNA box with a controllable lid. *Nature* **459**, 73-76 (2009).
- 162 Bai, X., Martin, T. G., Scheres, S. H. W. & Dietz, H. Cryo-EM structure of a 3D DNA-origami object. *Proceedings of the National Academy of Sciences of the United States of America* **149**, 20012-20017 (2012).
- 163 Midgley, P. A. & Dunin-borkowski, R. e. electron tomography and holography in materials science. *Nature Materials* **8**, 271-280 (2009).
- 164 Kourkoutis, L. F., Plitzko, J. M. & Baumeister, W. Electron Microscopy of Biological Materials at the Nanometer Scale. *Annual Review of Materials Research* **42**, 33-58 (2012).
- 165 De-Rosier, D. & Klug, A. Reconstruction of three dimensional structures from electron micrographs. *Nature* **217**, 130-134 (1968).
- 166 Mathieu, F., Liao, S., Kopatsch, J., Wang, T., Mao, C. & Seeman, N. C. Six-Helix Bundles Designed from DNA. *Nano Letters* **5**, 661-665 (2005).
- 167 Douglas, S. M., Dietz, H., Liedl, T., Hogberg, B., Graf, F. & Shih, W. M. Self-assembly of DNA into nanoscale three-dimensional shapes. *Nature* **459**, 414-418 (2009).
- 168 Douglas, S. M., Chou, J. J. & Shih, W. M. DNA-nanotube-induced alignment of membrane proteins for NMR structure determination. *Proceedings of the National Academy of Sciences of the United States of America* **104**, 6644-6648 (2006).
- 169 Scheres, S. H. & Chen, S. Prevention of overfitting in cryo-EM structure determination. *Nature Methods* **9**, 853-854 (2012).
- 170 Hagerman, P. J. Flexibility of DNA. *Annual Review of Biophysics and Biophysical Chemistry* **17**, 265-286 (1988).
- 171 Wang, T., Schiffels, D., Cuesta, S. M., Fygenson, D. K. & Seeman, N. C. Design and characterization of 1D nanotubes and 2D periodic arrays self-assembled from DNA multi-helix bundles. *Journal of the American Chemical Society* **134**, 1606-1616 (2012).
- 172 Sa-Ardyen, P., Vologodskii, A. V. & Seeman, N. C. The flexibility of DNA double crossover molecules. *Biophysical Journal* **84**, 3829-3837 (2003).

- 173 Hill, H. D., Millstone, J. E., Banholzer, M. J. & Mirkin, C. A. The Role Radius of Curvature Plays in Thiolated Oligonucleotide Loading on Gold Nanoparticles. *ACS Nano* **3**, 418-424 (2009).
- 174 Yan, W., Xu, L., Xu, C., Ma, W., Kuang, H., Wang, L. & Kotov, N. A. Self-Assembly of Chiral Nanoparticle Pyramids with Strong R/S Optical Activity. *Journal of American Chemical Society* **134**, 15114-15121 (2012).
- 175 Chi, C., Vargas-Lara, F., Tkachenko, A. V., Starr, F. W. & Gang, O. Internal Structure of Nanoparticle Dimers Linked by DNA. *ACS Nano* **6**, 6793-7802 (2012).
- 176 Kaya, H. Scattering from Cylinders with Globular End-Caps. *Journal of Applied crystallography* **37**, 223-230 (2004).
- 177 Schreiber, R., Do, J., Roller, E.-M., Zhang, T., Schüller, V. J., Nickels, P. C., Feldmann, J. & Liedl, T. Hierarchical Assembly of Metal Nanoparticles, Quantum Dots and Organic Dyes Using DNA Origami Scaffolds. *Nature Nanotechnology* **9**, 74-78 (2013).
- 178 Ko, S. H., Du, K. & Liddle, J. A. Quantum-Dot Fluorescence Lifetime Engineering with DNA Origami Constructs. *Angewandte Chemie International Edition* **52**, 1193-1197 (2012).